

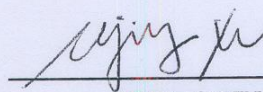
**Synthesis, Characterization and Functionalization of Silicon
Nanoparticle based Hybrid Nanomaterials for Photovoltaic
and Biological Applications**

AN ABSTRACT

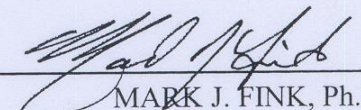
SUBMITTED ON TWENTY-SEVENTH DAY OF AUGUST, 2014

TO THE DEPARTMENT OF CHEMISTRY
IN PARTIAL FULFILMENT OF THE REQUIRMENTS
OF THE SCHOOL OF SCIENCE AND ENGINEERING
OF TULANE UNIVERSITY

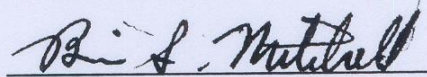
FOR THE DEGREE OF
DOCTOR OF PHILOSOPHY
BY

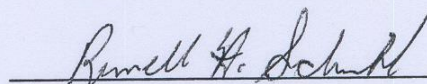

ZEJING XU

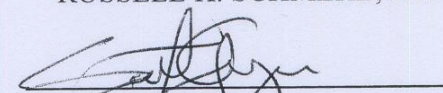
APPROVED BY:


MARK J. FINK, Ph.D

DIRECTOR OF DISSERTATION COMMITTEE


BRIAN S. MITCHELL, Ph.D


RUSSELL H. SCHMEHL, Ph.D


SCOTT MICHAEL GRAYSON, Ph.D


J. J.

JANARTHANAN JAYAWICKRAMARAJAH, Ph.D

Abstract

Silicon nanoparticles are attractive candidates for biological, photovoltaic and energy storage applications due to their size dependent optoelectronic properties. These include tunable light emission, high brightness, and stability against photo-bleaching relative to organic dyes (see Chapter 1). The preparation and characterization of silicon nanoparticle based hybrid nanomaterials and their relevance to photovoltaic and biological applications are described.

The surface-passivated silicon nanoparticles were produced in one step from the reactive high-energy ball milling (RHEBM) of silicon wafers with various organic ligands. The surface structure and optical properties of the passivated silicon nanoparticles were systematically characterized. Fast approaches for purifying and at the same time size separating the silicon nanoparticles using a gravity GPC column were developed. The hydrodynamic diameter and size distribution of these size-separated silicon nanoparticles were determined using GPC and Diffusion Ordered NMR Spectroscopy (DOSY) as fast, reliable alternative approaches to TEM.

Water soluble silicon nanoparticles were synthesized by grafting PEG polymers onto functionalized silicon nanoparticles with distal alkyne or azide moieties. The surface-functionalized silicon nanoparticles were produced from the reactive high-energy ball milling (RHEBM) of silicon wafers with a mixture of either 5-chloro-1-pentyne in 1-pentyne or 1,7 octadiyne in 1-hexyne to afford air and water stable chloroalkyl or alkynyl terminated nanoparticles, respectively. Nanoparticles with the ω -chloroalkyl substituents were easily converted to ω -azidoalkyl groups through the reaction of the silicon

nanoparticles with sodium azide in DMF. The azido terminated nanoparticles were then grafted with monoalkynyl-PEG polymers using a copper catalyzed alkyne-azide cycloaddition (CuAAC) reaction to afford core-shell silicon nanoparticles with a covalently attached PEG shell. Covalently linked silicon nanoparticle clusters were synthesized via the CuAAC “click” reaction of functional silicon nanoparticles with α,ω -functional PEG polymers of various lengths. Dynamic light scattering studies show that the flexible globular nanoparticle arrays undergo a solvent dependent change in volume (ethanol > dichloromethane > toluene) similar in behavior to hydrogel nanocomposites.

A novel light-harvesting complex and artificial photosynthetic material based on silicon nanoparticles was designed and synthesized. Silicon nanoparticles were used as nanoscaffolds for organizing the porphyrins to form light-harvesting complexes thereby enhancing the light absorption of the system. The energy transfer from silicon nanoparticles to porphyrin acceptors was investigated by both steady-state and time-resolved fluorescence spectroscopy. The energy transfer efficiency depended on the donor-acceptor ratio and the distance between the nanoparticle and the porphyrin ring. The addition of C₆₀ resulted in the formation of silicon nanoparticle-porphyrin-fullerene nanoclusters which led to charge separation upon irradiation of the porphyrin ring. The electron-transfer process between the porphyrin and fullerene was investigated by femto-second transient absorption spectroscopy.

Finally, the water soluble silicon nanoparticles were used as nanocarriers in photodynamic therapeutic application, in which can selectively deliver porphyrins into human embryonic kidney 293T (HEK293T) cells. In particular, the PEGylated alkynyl-porphyrins were conjugated onto the azido-terminated silicon nanoparticles via a CuAAC

“click” reaction. The resultant PEGylated porphyrin grafted silicon nanoparticles have diameters around 13.5 ± 3.8 nm. The cryo-TEM and conventional TEM analysis proved that the PEGylated porphyrin grafted silicon nanoparticle could form the micelle-like structures at higher concentration in water via self-assembly. The UV-Vis absorption analysis demonstrated that the silicon nanoparticle could reduce the porphyrin aggregation in water which can reduce the photophysical activity of porphyrin. In addition, the nanoparticle complex was capable of producing singlet oxygen when the porphyrin units were excited by light. The cell studies demonstrated that the silicon nanoparticle could deliver the porphyrin drugs into HEK293T cells and accumulate in the mitochondria where the porphyrin could serve as an efficient photosensitizer to kill the cells via mitochondrial apoptotic pathway.

Synthesis, Characterization and Functionalization of Silicon Nanoparticle based Hybrid Nanomaterials for Photovoltaic and Biological Applications

A DISSERTATION

SUBMITTED ON TWENTY-SEVENTH DAY OF AUGUST, 2014

TO THE DEPARTMENT OF CHEMISTRY

IN PARTIAL FULFILLMENT OF THE REQUIREMENTS

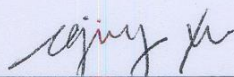
OF THE SCHOOL OF SCIENCE AND ENGINEERING

OF TULANE UNIVERSITY

FOR THE DEGREE OF

DOCTOR OF PHILOSOPHY

BY



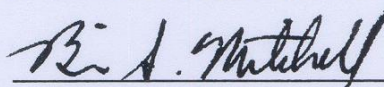
ZEJING XU

APPROVED BY:

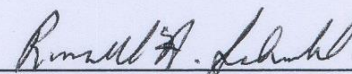


MARK J. FINK, Ph.D

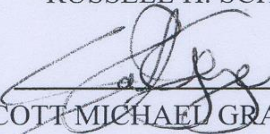
DIRECTOR OF DISSERTATION COMMITTEE



BRIAN S. MITCHELL, Ph.D



RUSSELL H. SCHMEHL, Ph.D



SCOTT MICHAEL GRAYSON, Ph.D



JANARTHANAN JAYAWICKRAMARAJAH, Ph.D

DEDICATION

TO MY PARENTS, GRANDPARENTS AND MY WIFE

FOR ALL YOUR LOVE AND SUPPORT

© Copyright by Zejing Xu, 2014

All Rights Reserved

ACKNOWLEDGEMENTS

This dissertation would not have been completed without the guidance of my committee members, help from friends, and support from my family.

First, I would like to express my deepest gratitude to my advisor, Prof. Mark J Fink, for his excellent guidance, stimulating attitude, constant encouragement and endless patience throughout my graduate studies. I greatly appreciate all his kind support which helped me to enjoy my research and achieve my goals.

I would like to thank Prof. Brian S Mitchell for his guidance as my co-advisor. His knowledge in mechanical processing and chemical engineering were great assets for my research. I also would like to thank the members of my dissertation committee, Prof. Russell H Schmehl, Prof. Scott Michael Grayson, and Prof. Janarthanan Jayawickramarajah for their valuable suggestions and efforts in helping to review this work, and also for their collaboration and support in my graduate research.

I am also thankful to Prof. Mark Sulkes for his kind support in time-resolved emission spectroscopy. I would like to thank Prof. Igor V. Rubtsov, Dr. Qi Zhao, Dr. Jibao He, Dr. Alina Alb, Dr. James Bolinger, Dr. Carol Zhang for their very helpful advice in my graduate study and research. I sincerely thank other members of the faculty and staffs of the chemistry department for their support throughout my graduate study.

I want to thank my previous lab mates Tapas for his kind help and I am grateful to work with my current lab mates Li, Ted, Yuxi and Jamie. I am extremely grateful to Nan Zhang, Yejia Li, Fading Chen, Xiaozhu Chu, Boyu Zhang, Hong Zhang, Yuankai Yue, Zifu Zhu and so many others for their constant support and friendship.

Personally, I would like to thank my parents, Qinghe Xu and Yuzhen Xu, my wife, Manyao Yi, and other family members for their unwavering confidence and support. Most importantly, I give my gratitude to my wife for her love, patience and belief. She was always there cheering me up and stood by me through the good times and bad.

Table of Contents

Chapter 1: Introduction and Significance	1
1.1 Introduction.....	1
1.2 Silicon nanoparticles	2
1.3 Optical properties	3
1.3.1 Origin of optical properties: band gap	3
1.3.2 Optical properties	5
1.4 Synthesis of silicon nanoparticles	7
1.4.1 Bottom-up methods	8
1.4.2 Top-down methods.....	15
1.5 Surface passivation and functionalization of silicon nanoparticles	18
1.5.1 Hydrosilylation reactions.....	21
1.5.2 Silanization reactions.....	24
1.5.3 Alkylation of halide-terminated surfaces.....	26
1.5.4 “Click” Chemistry	27
1.6 Characterization of silicon nanoparticles size distribution	28
1.6.1 Transmission electron microscopy.....	28
1.6.2 Atomic force microscopy	29
1.6.3 Hydrodynamic diameter of silicon nanoparticles	30

1.6.3.1	Dynamic light scattering	31
1.6.3.2	Gel permeation chromatography	32
1.6.3.3	Diffusion-ordered NMR spectroscopy.....	33
1.7	Application of silicon nanoparticles	33
1.7.1	Photovoltaic application	34
1.7.2	Biological applications	35
1.7.2.1	Cytotoxicity	35
1.7.2.2	Bioimaging	36
1.7.2.3	Drug delivery	38
1.7.3	Nanocatalysis	39
1.7.4	Application to Li-ion batteries	40
1.8	Motivation and summary	42
Chapter 2: Mechanochemical Synthesis and Size Distribution of Passivated Silicon Nanoparticles.....		46
2.1	Introduction.....	46
2.2	Results and Discussion	49
2.2.1	Octenyl-passivated silicon nanoparticles	49
2.2.2	Size separation and purification of silicon nanoparticles using GPC column ..	55
2.2.3	Size determination of separated silicon nanoparticles using GPC analysis	61
2.2.4	Size determination of separated silicon nanoparticles using DOSY-NMR	65

2.2.4.1 Size determination of octenyl-passivated silicon nanoparticles	66
2.2.4.2 Synthesis and size determination of pentenyl-passivated silicon nanoparticles.....	74
2.2.4.3 Synthesis and size determination of dodecenyl-passivated silicon nanoparticle	81
2.3 Conclusion	90
2.4 Experimental Section	91
2.4.1 Materials.....	91
2.4.2 Synthesis of passivated silicon nanoparticles.....	91
2.4.3 Purification and size separation of passivated silicon nanoparticles	93
2.4.4 Analytical methods	93
2.4.4.1 NMR sample preparation and acquisition	93
2.4.4.2 Infrared spectroscopy	94
2.4.4.3 UV-vis absorption and photoluminescence spectroscopy	94
2.4.4.4 Transmission electron microscopy.....	94
2.4.4.5 GC-MS.....	95
2.4.4.6 Gel-permeation chromatography	95
Chapter 3: Water soluble PEGylated silicon nanoparticles and their assembly into swellable nanoparticle arrays	96
3.1 Introduction.....	96

3.2 Results and Discussion	97
3.2.1 Synthesis and characterization of initially functionalized silicon nanoparticles	97
3.2.2 PEGylated water soluble silicon nanoparticles	105
3.2.3 PEGylated silicon nanoparticle arrays	110
3.3 Conclusion	122
3.4 Experimental Section	123
3.4.1 Materials and methods	123
3.4.2 Synthesis of ω -alkynyl-octenyl (20%)-Si nanoparticles	123
3.4.3 Synthesis of ω -azido-pentenyl (20%)-Si nanoparticles and ω -azido-pentenyl (50%)-Si nanoparticles	124
3.4.4 Synthesis of functionalized PEG polymers	125
3.4.5 Synthesis of PEGylated water soluble silicon nanoparticles	125
3.4.6 Synthesis of silicon nanoparticle arrays	126
3.4.7 Analytical methods	126
3.4.7.1 NMR sample preparation and acquisition	126
3.4.7.2 Infrared spectroscopy	127
3.4.7.3 UV-vis absorption and photoluminescence spectroscopy	127
3.4.7.4 Transmission electron microscopy	127
3.4.7.5 Dynamic light scattering	128

3.4.7.6 Thermal Gravimetric Analysis	128
Chapter 4: Energy and electron transfer in silicon nanoparticle-based light-harvesting complexes	129
4.1 Introduction.....	129
4.2 Results and Discussion	131
4.2.1 Synthesis and characterization of initially functionalized silicon nanoparticles	131
4.2.1.1 Synthesis and characterization of ω -azidopentenyl Si nanoparticles	132
4.2.1.2 Synthesis and characterization of ω -azidoheptyl Si nanoparticles.....	132
4.2.1.3 Synthesis of 11-bromo-1-undecene.....	134
4.2.1.4 Synthesis and characterization of ω -azidoundecyl Si nanoparticles	137
4.2.2 The donor-acceptor ratio dependence of energy transfer efficiency	139
4.2.3 The distance dependence of energy transfer efficiency	150
4.2.4 Photoinduced electron transfer in Si nanoparticle-porphyrin-fullerene nanocluster	157
4.3 Conclusion	166
4.4 Experimental Section	168
4.4.1 Materials and methods	168
4.4.2 Synthesis of 11-bromo-1-undecene	168
4.4.3 Synthesis of ω -azidopentenyl (5%, 20%, 35%, 50%)-Si nanoparticles	169

4.4.4 Synthesis of ω -azidoheptyl (35%)-Si nanoparticles	170
4.4.5 Synthesis of ω -azidoundecyl (35%)-Si nanoparticles.....	171
4.4.6 Synthesis of 5-(4-(prop-2-yn-1-yloxy))phenyl-10,15,20-triphenyl-Zincporphyrin.....	172
4.4.7 Functionalization of Azide-terminated Si NPs with Zn-porphyrin	172
4.4.8 Analytical methods	172
4.4.8.1 NMR sample preparation and acquisition	172
4.4.8.2 Infrared spectroscopy	173
4.4.8.3 UV-vis absorption and photoluminescence spectroscopy	173
4.4.8.4 GC-MS.....	173
4.4.8.5 Time-resolved emission spectroscopy.....	173
4.4.8.6 Femtosecond transient absorption spectroscopy.....	174
4.5 Model of Si nanoparticles.....	175
Chapter 5: Silicon Nanoparticle-based Nanocarriers for Porphyrin Delivery in Photodynamic Therapy	178
5.1 Introduction.....	178
5.2 Results and Discussion	181
5.2.1 Synthesis and characterization of PEGylated porphyrin grafted silicon nanoparticles	181
5.2.2 Cellular uptake and subcellular localization of the PEGylated porphyrin grafted silicon nanoparticles	190

5.2.3 <i>In vitro</i> photodynamic therapy	196
5.3 Conclusion	201
5.4 Experimental Section	202
5.4.1 Materials and methods	202
5.4.2 Synthesis of ω -azido-pentenyl (50%)-Si nanoparticles	202
5.4.3 Synthesis of PEGylated alkyno-zinc(II)porphyrin	203
5.4.4 Synthesis of PEGylated porphyrin grafted silicon nanoparticles	203
5.4.5 Cell culture	204
5.4.6 Quantification of cell internalization	205
5.4.7 Cell imaging	205
5.4.8 Photodynamic therapy experiment	206
5.4.9 MTT assay	207
5.4.10 Analytical methods	207
5.4.10.1 NMR sample preparation and acquisition	207
5.4.10.2 Infrared spectroscopy	208
5.4.10.3 UV-vis absorption spectroscopy	208
5.4.10.4 Transmission electron microscopy and Cryo-TEM	208
5.4.10.5 AFM experiments	209
Chapter 6: Miscellaneous Projects	210
6.1 Synthesis of water soluble silicon nanoparticles	210

6.1.1 Synthesis of amino-PEGylated silicon nanoparticles	210
6.1.2 Synthesis of the amino-terminated silicon nanoparticles via “click” reaction	215
6.1.3 Synthesis of the amino-terminated silicon nanoparticles via Staudinger Reduction	218
6.1.4 Synthesis of carboxylic acid-functionalized silicon nanoparticles	219
6.1.5 Synthesis of methyl viologen-functionalized silicon nanoparticles via “click” reactions	222
6.1.6 Synthesis of methyl viologen-functionalized silicon nanoparticles via nucleophilic displacement reaction	225
6.2 Synthesis of silicon nanoparticle arrays via “host-guest” self-assembly	227
6.2.1 Synthesis of adamantane grafted silicon nanoparticles	228
6.2.2 Synthesis of β -cyclodextrin grafted silicon nanoparticles	231
6.2.3 Synthesis of silicon nanoparticle arrays via “host-guest” self-assembly	234
6.2.4 Synthesis of water soluble silicon nanoparticle-porphyrin arrays via “host-guest” self-assembly	236
6.3 Experimental Section	240
6.3.1 Materials and methods	240
6.3.2 Synthesis of amino-PEGylated silicon nanoparticles	240
6.3.3 Synthesis of the amino-terminated silicon nanoparticles via “click” reaction	241
6.3.4 Synthesis of the amino-terminated silicon nanoparticles via Staudinger Reduction	242

6.3.5 Synthesis of carboxylic acid-functionalized silicon nanoparticles	242
6.3.6 Synthesis of alkynyl-methyl viologen	243
6.3.7 Synthesis of methyl viologen-functionalized silicon nanoparticles via “click” reaction	243
6.3.8 Synthesis of methyl viologen-functionalized silicon nanoparticles via a nucleophilic displacement reaction	244
6.3.9 Synthesis of adamantane grafted silicon nanoparticles	244
6.3.10 Synthesis of β -cyclodextrin grafted silicon nanoparticles	245
6.3.11 Synthesis of silicon nanoparticle arrays via “host-guest” self-assembly	245
6.3.12 Synthesis of silicon nanoparticle-porphyrin arrays via “host-guest” self- assembly.....	246
6.3.13 Analytical methods	246
6.3.13.1 NMR sample preparation and acquisition	246
6.3.13.2 Infrared spectroscopy	246
6.3.13.3 UV-vis absorption and photoluminescence spectroscopy	247
6.3.13.4 Transmission electron microscopy	247
Chapter 7: Conclusion and Future Direction	248
7.1 Conclusion	248
7.2 Future direction	252
7.2.1 Synthesis of mono-functionalized silicon nanoparticles.....	252

7.2.2 Fabrication of solar cell based on silicon nanoparticle-porphyrin system.....	254
7.2.2.1 Fabrication of solar cell based on silicon nanoparticle-porphyrin-fullerene nanocluster.....	254
7.2.2.2 Layer-by-layer surface modification of TiO ₂ thin films with a silicon nanoparticles-porphyrin system.....	256
7.2.3 Further modification of PEGylated porphyrin-silicon nanoparticle system to enhance their selectivity for photodynamic therapy.....	259
7.2.3.1 Synthesis of PEGylated porphyrin-silicon nanoparticle micelles with controllable size	259
7.2.3.2 Conjugation of PEGylated porphyrin-silicon nanoparticle system with cellular targeting ligands	260
Chapter 8: Reference	262

List of Schemes

Scheme 1.1 Reduction of silicon tetrahalide using sodium naphthalide to produce halogen terminated silicon nanoparticles.....	8
Scheme 1.2 Reduction of silicon tetrahalide using Zintl salts to produce halogen terminated silicon nanoparticles.....	8
Scheme 1.3 Alkylation of halogen terminated silicon nanoparticles	9
Scheme 1.4 Synthesis of alkyl-capped silicon nanoparticles using inverse micelles	10
Scheme 1.5 Oxidation of metal silicide to produce alkyl-capped silicon nanoparticles ...	10
Scheme 1.6 Oxidation of Zintl compounds to produce H-terminated silicon nanoparticles	11
Scheme 1.7 Radical mechanism of formation of silicon nanoparticles.....	11
Scheme 1.8 Thermal decomposition of silane by laser pyrolysis	12
Scheme 1.9 Thermal processing of hydrogen silsesquioxane (HSQ) for preparing silicon nanoparticle/SiO ₂ -like (<i>nc</i> -Si/SiO ₂) nanocomposites	13
Scheme 1.10 Sonochemical synthesis of silicon nanoparticles using reduction reaction .	14
Scheme 1.11 Mechanism of surface etching of silicon by HF.....	15
Scheme 1.12 Sonochemical synthesis of silicon nanoparticles using reactive cavitation erosion.....	17
Scheme 1.13 Copper-catalyzed azide-alkyne cycloaddition reaction	27
Scheme 2.1 Possible bonding modes of passivated silicon surface with alkyne or alkene, and the representation of the alkyl/alkenyl-passivated silicon nanoparticles with different bonding modes.	47
Scheme 2.2 Synthesis of silicon nanoparticles passivated by 1-octyne using RHEBM ...	49

Scheme 2.3 Possible mechanism of forming “ene” structure during RHEBM	51
Scheme 2.4 Synthesis of silicon nanoparticles passivated by 1-pentyne using RHEBM .	74
Scheme 2.5 Synthesis of silicon nanoparticles passivated by 1-dodecyne using RHEBM	81
Scheme 4.1 Synthesis of 11-bromo-1-undecene	134
Scheme 6.1 Schematic of Staudinger Reduction	218

List of Tables

Table 2.1 Hydrodynamic diameter of separated octenyl-passivated silicon nanoparticles from GPC analysis.....	64
Table 2.2 Diffusion coefficients and hydrodynamic diameter of separated octenyl-passivated silicon nanoparticles from the DOSY NMR data in two solvents	72
Table 2.3 Diffusion coefficients and hydrodynamic diameter of separated pentenyl-passivated silicon nanoparticles from the DOSY NMR data in CDCl ₃	80
Table 2.4 Diffusion coefficients and hydrodynamic diameter of separated dodecenyl-passivated silicon nanoparticles from the DOSY NMR data in CDCl ₃	87
Table 2.5 Hydrodynamic diameters of separated silicon nanoparticles with three different surface ligands obtained from DOSY NMR analysis in CDCl ₃	88
Table 3.1 Sizes distribution of PEGylated silicon nanoparticle arrays from DLS.....	119
Table 4.1: Summary data of Si-pentenyl-azide NPs without and with different ratio of attached Zn-porphyrin	150
Table 4.2: Summary data of Si nanoparticle-porphyrin systems without and with attached Zn-porphyrin	155
Table 4.3: Binding Constants (M ⁻¹) of a Varsity of Porphyrin-C ₆₀ Constructs.....	161

List of Figures

Figure 1.1 Quantum size effects of semiconductor quantum dots	3
Figure 1.2 Direct and indirect band gap diagram. E_g , the band gap energy, E_c , the minimum energy of the conduction band, E_v , the maximum energy of the valence band. .	4
Figure 1.3 Illustration showing photoluminescence mechanism in silicon nanoparticles. a) without surface defect states where PL is exclusively due to quantum confinement; b) with surface defect state which reduces the energy gap leading to the red shift of PL; c) with surface defect state which increase the energy gap leading to the blue shift of PL. ...	6
Figure 1.4 Schematic presentation of H-terminated surface of porous silicon layer on the silicon surface after etching process	15
Figure 1.5 Schematic illustration of the mechanochemical synthesis of passivated silicon nanoparticles with alkyne ligands. (alkenes also can be used as passivation ligand)	17
Figure 1.6 Summary of surface tailoring of silicon nanoparticles	20
Figure 1.7 Schematic presentation of the Si(111) and Si(100) silicon-hydride-terminated surfaces on the silicon nanoparticle.	21
Figure 1.8 Schematic the regular mechanism for hydrosilylation of an H-terminated silicon surface with a terminal alkene	23
Figure 1.9 Proposed mechanisms for light-induced hydrosilylation on hydride-terminated silicon surfaces	24
Figure 1.10 Schematic the mechanism for silanization of a hydroxyl-terminated silicon surface with a chlorosilane or alkoxy silane (where $X = Cl, OCH_3, OCH_2CH_3$, etc.).	24
Figure 1.11 Two independent silanization reactions for the formation of siloxane-coated silicon nanoparticles	26

Figure 1.12 (left) (a) and (b) typical TEM image of silicon nanoparticles on a graphite grid. (Right) HRTEM image of the 1.0, 1.67, 2.15, 2.9 and 3.7 nm silicon nanoparticles	29
Figure 1.13 AFM tapping mode tomography of silicon implanted SiO ₂ samples with respect to etching time for (a) $1 \times 10^{17} \text{ cm}^{-2}$ Si ions and for (b) $5 \times 10^{16} \text{ cm}^{-2}$ Si ions	30
Figure 1.14 Illustration showing the hydrodynamic diameter of particles in DLS	31
Figure 1.15 Schematic of the principle of GPC	32
Figure 1.16 Schematic of a Si NCs/P3HT hybrid solar cell (left) and the schematic of electron-hole pair generation in the Si NCs/P3HT hybrid solar cell	34
Figure 1.17 (a) Epifluorescence image of mitosis of BV2 cells stained with silicon nanoparticles under blue light irradiation, (b) and (c) Confocal image of BV2 cells simultaneously stained with silicon nanoparticles and DRAQ5	37
Figure 1.18 Schematic diagram depicting the structure and in vivo degradation process for the biopolymer-coated porous silicon nanoparticles	38
Figure 1.19 Scheme of different sizes silicon nanoparticles for different reactions	40
Figure 1.20 Schematic the illustration of the synthesis route for silicon nanoparticles inserted into graphene. Grey lines (graphene oxide), black lines (thermally reduced grapheme), and purple balls (silicon nanoparticles). (1) Freeze-drying, and (2) thermal reduction	41
Figure 1.21 Development of silicon/carbon nanotube nanocomposites via a phenyl bridge	42
Figure 2.1 300 MHz ¹ H-NMR (top) and ¹³ C-NMR (down) spectra of the octenyl-passivated silicon nanoparticles	50
Figure 2.2 FTIR spectrum of octenyl-passivated silicon nanoparticles	52

Figure 2.3 (a) TEM image of crude octenyl-passivated silicon nanoparticles, (b) the corresponding particle size distribution histograms, and (c) the energy-dispersive X-ray spectra (EDS).	53
Figure 2.4 UV-Vis absorption spectrum and PL emission spectra at various excitation wavelengths of octenyl-passivated silicon nanoparticles.	54
Figure 2.5 Weight distribution of various GPC separated fractions (a), GPC separated various fractions (b) and the Emission of various fractions excited under UV lamp (c) of octenyl-passivated silicon nanoparticles, and the gravity GPC column used to fractionate silicon nanoparticles (d).....	55
Figure 2.6 a) FTIR spectra of various separated fractions of octenyl-passivated silicon nanoparticles; b) Emission maxima vs excitation wavelength of various separated fractions of octenyl-passivated silicon nanoparticles.	57
Figure 2.7 ^1H -NMR (top) and ^{13}C -NMR (down) spectra of octenyl-passivated silicon nanoparticles which contains aromatic impurities	59
Figure 2.8 GC-MS spectra of 30 th fraction of octenyl-passivated silicon nanoparticles which contains mostly aromatic impurities	60
Figure 2.9 (a) TEM image of Fraction 3 octenyl-passivated silicon nanoparticles, (b) the corresponding particle size distribution histograms	61
Figure 2.10 Separated fractions of octenyl-passivated silicon nanoparticles analyzed by GPC	62
Figure 2.11 GPC of various molecular weight polystyrene standards	62
Figure 2.12 The hydrodynamic volume vs. elution volume for polystyrene standards....	63

Figure 2.13 2D DOSY-NMR spectra of separated fractions of octenyl-passivated silicon nanoparticles with ferrocene as internal standard in C_6D_6	68
Figure 2.14 2D DOSY-NMR spectrum of fraction 1 of octenyl-passivated silicon nanoparticles with ferrocene as internal standard in $CDCl_3$	71
Figure 2.15 Hydrodynamic diameters of separated octenyl-passivated silicon nanoparticles obtained from GPC and DOSY NMR analysis.	73
Figure 2.16 1H -NMR (top) and ^{13}C -NMR (down) spectra of the pentenyl-passivated silicon nanoparticles	75
Figure 2.17 FTIR spectrum of pentenyl-passivated silicon nanoparticles.....	76
Figure 2.18 UV-Vis absorption spectrum and PL emission spectra at various excitation wavelengths of pentenyl-passivated silicon nanoparticles	77
Figure 2.19 2D DOSY-NMR spectra of separated fractions of pentenyl-passivated silicon nanoparticles with ferrocene as internal standard in $CDCl_3$	79
Figure 2.20 1H -NMR (top) and ^{13}C -NMR (down) spectra of the dodecenyl-passivated silicon nanoparticles	82
Figure 2.21 FTIR spectrum of dodecenyl-passivated silicon nanoparticles	83
Figure 2.22 UV-Vis absorption spectrum and PL emission spectra at various excitation wavelengths of dodecenyl-passivated silicon nanoparticles.....	84
Figure 2.23 2D DOSY-NMR spectrum of fraction 3 of dodecenyl-passivated silicon nanoparticles with ferrocene as internal standard in $CDCl_3$	86
Figure 3.1 Synthesis and initial functionalization of silicon nanoparticles	98

Figure 3.2 TEM image of ω -alkynyl-octenyl (20%)-Si nanoparticles (a) and ω -azido-pentenyl (20%)-Si nanoparticles (b) and their corresponding particle size distribution histograms	99
Figure 3.3 FTIR spectrum of ω -alkynyl-octenyl (20%)-Si nanoparticles	100
Figure 3.4 ^1H -NMR spectrum of ω -alkynyl-octenyl (20%)-Si nanoparticles.....	101
Figure 3.5 FTIR spectra of ω -chloro-pentenyl (20%)-silicon nanoparticle and ω -azido-pentenyl (20%)-Si nanoparticles	102
Figure 3.6 ^1H -NMR spectrum of ω -chloro-pentenyl (50%)-silicon nanoparticle and ω -azido-pentenyl (50%)-Si nanoparticles.....	103
Figure 3.7 UV-Vis absorption and emission spectra of ω -alkyne-octenyl (20%)-Si nanoparticles (top) and ω -azide-pentenyl (20%)-Si nanoparticles (bottom) in CH_2Cl_2 ..	104
Figure 3.8 Illustration showing the preparation of PEGylated silicon nanoparticles	105
Figure 3.9 FTIR spectrum of ω -azido-pentenyl (50%)-Si nanoparticles, mono-alkylated-PEG and PEGylated silicon nanoparticle	106
Figure 3.10 ^1H NMR spectrum of PEGylated silicon nanoparticles	107
Figure 3.11 TEM image of PEGylated silicon nanoparticles (top) and multimodal particle size distributions from dynamic light scattering (DLS) of ω -azido-pentenyl (50%)-Si nanoparticles and PEGylated silicon nanoparticles (bottom)	108
Figure 3.12 UV-Vis absorbance and PL emission of PEGylated silicon nanoparticles in distilled water	109
Figure 3.13 Illustration showing the preparation of a PEGylated silicon nanoparticle array	110

Figure 3.14 FTIR spectra of ω -azide-pentenyl (20%)-Si nanoparticles and PEGylated silicon nanoparticle arrays from azide terminated silicon nanoparticles and 2 KDa PEG (top), and FT-IR spectra of ω -alkynyl-octenyl (20%)-Si nanoparticles and PEGylated silicon nanoparticle arrays from alkyne terminated silicon nanoparticles and 2KDa PEG	111
Figure 3.15 TEM and HRTEM image of PEGylated silicon nanoparticle arrays from azide terminated silicon nanoparticles with 2 KDa PEG linkers (a,b) and alkyne terminated silicon nanoparticles (c,d) with 2 KDa PEG linkers.	113
Figure 3.16 The size distribution of PEGylated silicon nanoparticle arrays from azide terminated silicon and alkyne terminated silicon nanoparticles from DLS in CH_2Cl_2 . ..	114
Figure 3.17 TEM and HRTEM image of PEGylated silicon nanoparticle arrays from azide terminated silicon nanoparticles with 1 KDa PEG (a,b) and 4.6 KDa PEG (c,d) linkers	115
Figure 3.18 TGA of PEGylated Si nanoparticle arrays with PEG linkers of different sizes	117
Figure 3.19 Multimodal size distribution of PEGylated silicon nanoparticle arrays from azide terminated silicon nanoparticles with 1 KDa PEG (a), 2 KDa PEG (b) and 4.6 KDa PEG (c) linkers in different solvents from DLS.....	119
Figure 3.20 UV-Vis absorption and PL emission of PEGylated silicon nanoparticle arrays with 1 KDa PEG (a), 2 KDa PEG (b) and 4.6 KDa PEG (c) linkers in CH_2Cl_2 ...	121
Figure 4.1 Synthesis of various azide-terminated silicon nanoparticles.....	131
Figure 4.2 FTIR of ω -bromoheptyl Si nanoparticles and ω -azidoheptyl Si nanoparticles	133

Figure 4.3 ^1H -NMR of ω -bromoheptyl Si nanoparticles and ω -azidoheptyl Si nanoparticles in CD_2Cl_2	133
Figure 4.4 UV-Vis absorption and emission spectra of ω -azidoheptyl Si nanoparticles in CH_2Cl_2	134
Figure 4.5 ^1H -NMR spectrum of 11-bromo-1-undecene in CD_2Cl_2	135
Figure 4.6 GC-MS spectrum of 11-bromo-1-undecene	136
Figure 4.7 FTIR of ω -bromoundecyl Si nanoparticles and ω -azido-undecyl Si nanoparticles	137
Figure 4.8 ^1H -NMR of ω -bromoundecyl Si nanoparticles and ω -azidoundecyl Si nanoparticles in CD_2Cl_2	138
Figure 4.9 UV-Vis absorption and emission spectra of ω -azidoundecyl Si nanoparticles in CH_2Cl_2	139
Figure 4.10 Emission of ω -azidopentenyl (20%) Si nanoparticles in CH_2Cl_2 ; absorption and emission of Zn-porphyrin ($\lambda_{\text{exc}}=355\text{ nm}$)	140
Figure 4.11 Synthesis of silicon nanoparticle-porphyrin system	141
Figure 4.12 FTIR of ω -azidopentenyl Si nanoparticles with different azide group surface coverage	141
Figure 4.13 FTIR of Zn-porphyrin, azido-terminated Si nanoparticles and Zn-porphyrin functionalized Si nanoparticles.	142
Figure 4.14 ^1H -NMR of Zn-porphyrin functionalized Si nanoparticles with different donor-acceptor ratios in CD_2Cl_2	144

Figure 4.15 The absorption spectra of Zn-porphyrin and Si-C ₅ -N ₃ NPs without and with different ratio of Zn-porphyrin attached in CH ₂ Cl ₂ (Insert is the zooming range of 530-620 nm)	145
Figure 4.16 The emission spectrum of Zn-porphyrin, and the emission spectra of Si-C ₅ -N ₃ NPs without and with different ratio of Zn-porphyrin attached in CH ₂ Cl ₂ (λ_{exc} =355 nm). The emissions are normalized by absorption at 355 nm	146
Figure 4.17 Time-resolved emission spectra of Si-C ₅ -Por d (6.5%) in CH ₂ Cl ₂ at λ_{exc} =355 nm	147
Figure 4.18 The fluorescence decay curves of Si-C ₅ -N ₃ NPs without and with different ratio of Zn-porphyrin attached in CH ₂ Cl ₂ (λ_{exc} =355 nm, λ_{em} =450 nm).....	148
Figure 4.19. ¹ H-NMR of Zn-porphyrin functionalized Si nanoparticles with different donor-acceptor distance in CD ₂ Cl ₂	151
Figure 4.20 The absorption spectra of Si-C ₅ -N ₃ NPs, Si-C ₇ -N ₃ NPs and Si-C ₁₁ -N ₃ NPs with attached Zn-porphyrin in CH ₂ Cl ₂	152
Figure 4.21 The emission spectra of (a) Si-C ₅ -N ₃ NPs, (b) Si-C ₇ -N ₃ NPs and (c) Si-C ₁₁ -N ₃ NPs with attached Zn-porphyrin in CH ₂ Cl ₂ (λ_{exc} =355 nm). The emissions are normalized by absorption at 355 nm	153
Figure 4.22 The fluorescence decay curves of (a) Si-C ₅ -N ₃ NPs, (b) Si-C ₇ -N ₃ NPs and (c) Si-C ₁₁ -N ₃ NPs with attached Zn-porphyrin in CH ₂ Cl ₂ (λ_{exc} =355 nm, λ_{em} =450 nm).....	154
Figure 4.23 Illustration of the organization of Si nanoparticle-porphyrin-fullerene nanocluster	157
Figure 4.24 UV-Vis absorption spectra of the Si-C ₅ -Por d (blue line) and C ₆₀ (red line) in toluene/acetonitrile (1:1).....	158

Figure 4.25 UV-Vis absorption spectra of the Zn-porphyrin functionalized silicon nanoparticles upon addition of C ₆₀ (0-20 equiv.) in toluene/acetonitrile (1:1).....	159
Figure 4.26 Fluorescence spectra of Zn-porphyrin functionalized silicon nanoparticles upon addition of C ₆₀ (0-20 equiv., 1 equiv. = 8.80 μmol/L) in toluene/acetonitrile (1:1). (λ _{exc} =420 nm)	159
Figure 4.27 A plot of the change in fluorescence intensity of Zn-porphyrin functionalized silicon nanoparticles as a ratio of F/F ₀ versus concentration of C ₆₀ in toluene/acetonitrile (1:1). [K _a =5.4±1.6×10 ³ M ⁻¹ ; R ² =0.99].....	160
Figure 4.28 Fluorescence spectra of the Zn-porphyrin upon addition of C ₆₀ (0-20 equiv., 1 equiv. = 11.7 μmol/L) in toluene/acetonitrile (1:1). (λ _{exc} =420 nm)	163
Figure 4.29 A plot of the change in fluorescence intensity of Zn-porphyrin as a ratio of F ₀ /F versus concentration of C ₆₀ in toluene/acetonitrile (1:1). [K _D =2.0±0.1×10 ³ M ⁻¹ ; R ² =0.99].....	163
Figure 4.30 a) Femtosecond transient absorption spectra of Si-C ₅ -Por d in argon-saturated toluene/acetonitrile (1:1) at 298 K after laser excitation at 575 nm. b) Time profiles of absorption at 643 nm of Si-C ₅ -Por d in argon-saturated toluene/acetonitrile (1:1) at 298 K. c) Femtosecond transient absorption spectra of Si NP-Por-C ₆₀ ([C ₆₀] = 2.01 × 10 ³ μmol/L) in argon-saturated toluene/acetonitrile (1:1) at 298 K after laser excitation at 575 nm. d) Time profiles of absorption at 643 nm of Si NP-Por-C ₆₀ in argon-saturated toluene/acetonitrile (1:1) at 298 K.....	164
Figure 4.31 Illustration of the energy/electron transfer inside the Si NP-Por-C ₆₀ system	166
Figure 4.32 Model of a Si nanoparticle	175

Figure 5.1 The mechanism of action on tumors in photodynamic therapy	178
Figure 5.2 Illustration showing the synthesis of PEGylated porphyrin grafted silicon nanoparticles	181
Figure 5.3 ^1H -NMR spectrum of PEGylated porphyrin grafted silicon nanoparticles in CDCl_3	182
Figure 5.4 FTIR spectra of azido-terminated silicon nanoparticles and PEGylated porphyrin grafted silicon nanoparticles	184
Figure 5.5 AFM image (a) and histogram height distribution (b) of the azido-terminated silicon nanoparticles; AFM image of the PEGylated porphyrin grafted silicon nanoparticles (c) and the height profiles collected at the indicated white lines (labeled 1,2,3 respectively) (d).....	185
Figure 5.6 Cryo-TEM image (a), a zoom in image (b) and the histogram size distribution of the PEGylated porphyrin grafted silicon nanoparticles in water (0.10 mg/mL, 20 μM of porphyrin); (d) Conventional TEM image of PEGylated porphyrin grafted silicon nanoparticles in water.	186
Figure 5.7 (a) UV-Vis absorption spectra of PEGylated porphyrin in water and CH_2Cl_2 and PEGylated porphyrin grafted Si nanoparticles in water (insert is the absorption in 400-460 nm range); Reconstructed Soret peaks of PEGylated porphyrin (b) and PEGylated porphyrin grafted Si nanoparticles (c)	188
Figure 5.8 Near-IR Emission spectra of singlet oxygen phosphorescence in air-saturated solution of PEGylated porphyrin grafted silicon nanoparticles in deuterated acetone at room temperature. Absorbance of the PEGylated porphyrin grafted silicon nanoparticles was ~ 0.5 at $\lambda = 430$ nm.	191

Figure 5.9 Cellular uptake curve of PEGylated porphyrin grafted silicon nanoparticles monitored by UV absorption at $\lambda = 430$ nm (average of two independent experiments).

.....192

Figure 5.10 Confocal microscope images of fixed HEK293T cells. The cells were incubated with PEGylated porphyrin grafted silicon nanoparticles (0.05 mg/mL, 10 μ M in porphyrin) for 24 hours and co-stained with a whole cell stain (Cell Mask green). The stained cells were fixed with 4% PFA (4g paraformaldehyde and 2g sucrose in 100 mL PBS buffer) and then rinsed briefly with PBS buffer. The fixed cells were visualized by 488 nm laser excitation and a 515nm long pass (emission) filter was applied. PEGylated porphyrin grafted silicon nanoparticles were visualized by 633 nm laser excitation, and a 650-715 band pass (emission) filter was applied.193

Figure 5.11 Confocal microscope images of fixed HEK293T cells to determine the subcellular localization of the nanoparticles. The cells were incubated with PEGylated porphyrin grafted Si nanoparticles (0.05 mg/mL, 10 μ M in porphyrin) for 24 hours and stained with a mitochondrial stain (MitoTracker Deep Red). Mitochondria were visualized by 633 nm laser excitation and a 650-715 band pass (emission) filter was applied. PEGylated porphyrin grafted Si nanoparticles were visualized by 554 nm laser excitation, and a 650-715 band pass (emission) filter was applied. The scale bar is 20 μ m.195

Figure 5.12 Fluorescence microscopy image of DAPI stained nucleus. (a) HEK293T cells without PEG-Por-Si NPs and irradiation, (b) HEK293T cells incubated with 0.01 mg/mL PEG-Por-Si NPs for 24 hours without irradiation, (c) HEK293T cell without

PEG-Por-Si NPs and irradiated for 3 hours, (d) HEK293T cells incubated with 0.01 mg/mL PEG-Por-Si NPs for 24 hours and irradiated for 3 hours.	197
Figure 5.13 Efficacy of PEGylated porphyrin grafted silicon nanoparticles in inducing cellular death by a photodynamic process. HEK293T cells were incubated for 24 hours with PEG-Por-Si NPs (10 μ M in porphyrin), PEGylated porphyrin (10 μ M in porphyrin), or PEGylated silicon nanoparticles (no porphyrin, 0.01 mg/mL). Cells were washed and irradiated for 3 hours. Further 12 hours incubation after irradiation, cell death was measured.	198
Figure 5.14 Thermo Oriel 200W Xenon arc light system	206
Figure 6.1 Synthesis of amino-PEGylated silicon nanoparticles	210
Figure 6.2 FTIR of spectra of ω -alkynyl-octenyl (50%)-Si nanoparticles, amino-azido-bifunctional-PEG and amino-PEGylated silicon nanoparticles.	211
Figure 6.3 ^1H NMR spectrum of α,ω -amino-azido-PEG and amino-PEGylated silicon nanoparticles in CD_2Cl_2	212
Figure 6.4 the TEM image of amino-PEGylated silicon nanoparticles in water	213
Figure 6.5 UV-Vis absorbance and PL emission of amino-PEGylated silicon nanoparticles in distilled water.....	214
Figure 6.6 Synthesis of amino-terminated silicon nanoparticles via “click” reaction....	215
Figure 6.7 FTIR spectra of ω -azido-pentenyl (50%)-silicon nanoparticles and amino terminated silicon nanoparticles.....	216
Figure 6.8 ^1H NMR spectrum of amino-terminated silicon nanoparticles in CD_2Cl_2	216
Figure 6.9 UV-Vis absorbance and PL emission of amino-terminated silicon nanoparticles in distilled water.....	217

Figure 6.10 Synthesis of amino-terminated silicon nanoparticles via reduction reaction	218
Figure 6.11 FTIR spectra of ω -azido-pentenyl (50%)-silicon nanoparticles and amino terminated silicon nanoparticles	219
Figure 6.12 Synthesis of carboxylic acid-functionalized silicon nanoparticles via “click” reaction.....	220
Figure 6.13 FTIR spectra of ω -azido-pentenyl (50%)-silicon nanoparticles and carboxylic acid-functionalized silicon nanoparticles	220
Figure 6.14 ^1H NMR spectrum of carboxylic acid-functionalized silicon nanoparticles in CD_2Cl_2	221
Figure 6.15 Schematic of the synthesis of methyl viologen-functionalized silicon nanoparticles via “click” reaction and the possible electron transfer process inside the system	222
Figure 6.16 ^1H -NMR spectra of mono-methyl viologen and alkynyl-methyl viologen in D_2O	223
Figure 6.17 FTIR spectrum of the methyl viologen functionalized silicon nanoparticles	224
Figure 6.18 Synthesis of methyl viologen-functionalized silicon nanoparticles via nucleophilic displacement reaction	225
Figure 6.19 ^1H -NMR spectra of the ω -chloro-terminated silicon nanoparticles in CD_2Cl_2 and the methyl viologen functionalized silicon nanoparticles in $\text{DMSO}-\text{D}_6$	226
Figure 6.20 Structure of adamantane, β -cyclodextrin and their inclusion complexes	227
Figure 6.21 Synthesis of adamantane grafted silicon nanoparticles.....	228

Figure 6.22 FTIR of spectra of ω -alkynyl-octenyl (50%)-Si nanoparticles and adamantane grafted silicon nanoparticles.	229
Figure 6.23 ^1H NMR spectrum of adamantane grafted silicon nanoparticles in CD_2Cl_2	229
Figure 6.24 the TEM image of adamantane grafted silicon nanoparticles in toluene the corresponding particle size distribution histogram	230
Figure 6.25 UV-Vis absorbance and PL emission of adamantane grafted silicon nanoparticles in CH_2Cl_2	231
Figure 6.26 Synthesis of β -cyclodextrin grafted silicon nanoparticles.....	232
Figure 6.27 FTIR of spectra of ω -alkynyl-octenyl (50%)-Si nanoparticles and β -cyclodextrin grafted silicon nanoparticles.	232
Figure 6.28 ^1H NMR spectrum of β -cyclodextrin grafted silicon nanoparticles in $\text{DMSO}-\text{D}_6$	233
Figure 6.29 Synthesis of silicon nanoparticle arrays via “host-guest” self-assembly	234
Figure 6.30 TEM images and EDS spectrum of silicon nanoparticles arrays via “host-guest” self-assembly	235
Figure 6.31 Synthesis of water soluble silicon nanoparticle-porphyrin arrays via “host-guest” self-assembly	236
Figure 6.32 TEM images of silicon nanoparticle-porphyrin arrays in water	237
Figure 6.33 UV-Vis spectrum of silicon nanoparticle-porphyrin arrays in water.....	238
Figure 6.34 PL Emission spectra of silicon nanoparticle-porphyrin arrays in water	239
Figure 7.1 The proposed synthesis approach of mono-functionalized silicon nanoparticles	252

Figure 7.2 Schematic of a silicon nanoparticles-porphyrin-fullerene hybrid solar cell .	254
Figure 7.3 Schematic of charge separation in silicon nanoparticles-porphyrin-fullerene hybrid solar cell	255
Figure 7.4 Proposed synthesis of 4-ethynylphenylacetic acid	256
Figure 7.5 Schematic of layer by layer surface modification of TiO ₂ plate with silicon nanoparticle-porphyrin complex	258
Figure 7.6 Schematic of synthesis PEGylated porphyrin functionalized silicon nanoparticle array	259
Figure 7.7 Schematic of synthesis of amino-PEGylated porphyrin and RGD-PEGylated porphyrin grafted silicon nanoparticles.	261

Chapter 1: Introduction and Significance

1.1 Introduction

Silicon is the second most abundant element in the Earth's crust and occurs in the nature mainly in various forms of silicon dioxide and silicates. As a semiconductor element, silicon does not occur naturally in its elemental form but can be obtained from chemical reduction of silicon dioxide.¹ Silicon has a large impact on modern technology due to its crucial roles in the microelectronics industry. It is the principal component in semiconductor devices, such as integrated circuits.

As the key component in modern technology, silicon is a prime candidate in the newest generation of modern science: nanotechnology. Nanotechnology is an interdisciplinary field which involves chemistry, biology, physics and engineering, which is focused on the synthesis and control of materials on the nanometer scale. When the size of the semiconductor materials scales down to the range of 1-100 nanometer, the materials will display new optical and electronic properties distinct from their bulk materials.² Nanocrystalline silicon and silicon nanoparticles in particular, can exhibit enhanced optical and electronic properties when compared to the bulk phase material, and hence has potential for use in numerous applications. In addition, silicon nanoparticles are more attractive than other types of nanoparticles because they are fully compatible with existing technologies.

This thesis describes the synthesis, characterization and functionalization of silicon nanoparticles and their application in the fields of solar energy materials and photodynamic therapy. Specifically, this work concerns the production of passivated

silicon nanoparticles by a mechanochemical process, new methods for characterization of size distribution and functionalization of silicon nanoparticles with applications as light-harvesting antennas in solar energy materials and as nanocarriers for drug delivery in photodynamic therapy.

1.2 Silicon nanoparticles

Although bulk crystalline silicon is useful as a building block material in semiconductor devices, silicon is not popular in optics and optoelectronics because of its very low luminescence efficiency at room temperatures due to its indirect bandgap.³ As an indirect bandgap material, radiative recombination in silicon requires the simultaneous generation of vibration in the crystal lattice (a phonon) along with the photon. Thus it is much more probable for the electron to release by nonradiative process than for radiative recombination.⁴ However, an intense period of research into the silicon nanostructures was sparked by Canham in 1990, when he first reported the discovery of visible luminescence from porous silicon produced by electrochemical etching of silicon wafers.⁵ In particular, silicon nanoparticles have received great attention due to their efficient and size dependent light emission⁶. In the past decades, a variety of synthesis approaches have been developed to produce silicon nanoparticles with efficient luminescence at room temperature and high quantum yield that can be closer to or even higher than some of other direct-bandgap semiconductor nanoparticles.⁷ Thus, silicon nanoparticles have already shown great potential application in fields of photovoltaics, biology, energy storage, nanocatalysis and memory devices.

1.3 Optical properties

1.3.1 Origin of optical properties: band gap

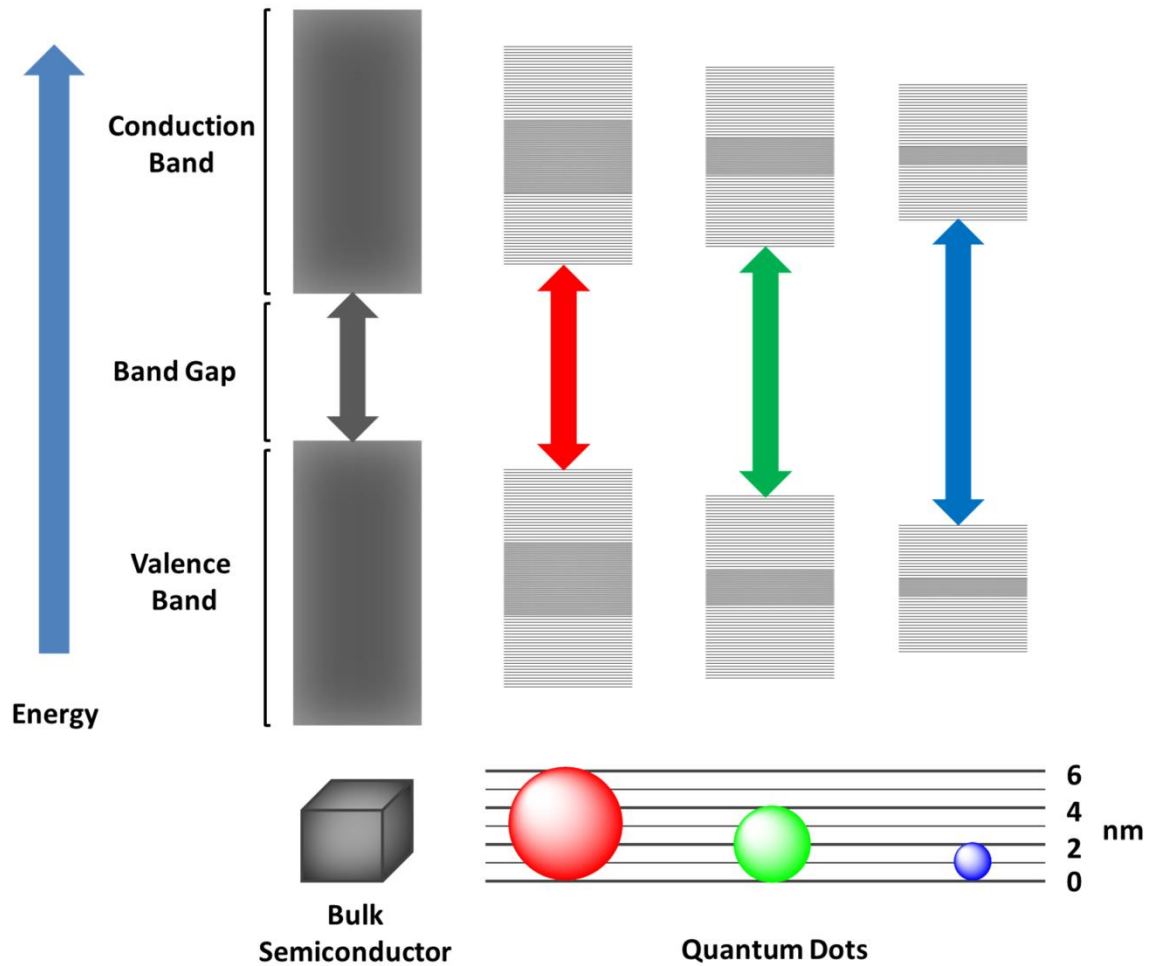


Figure 1.1 Quantum size effects of semiconductor quantum dots

The optical properties of the crystal are determined by the energy band gap of the material due to the quantum confinement: as the cluster size of a semiconductor decreases, the gap between valence and conduction band increases (Figure 1.1).⁸ This basic phenomenon can be understood by considering the movement of the electrons and holes in both free and confined space. Electrons and holes are allowed to move freely throughout the entire crystal in a bulk semiconductor, while their movement becomes

limited in a nanocrystal. When the physical dimension of nanoparticles approaches the Bohr exciton radius, the exciton will be confined, which results in the band gap of the nanoparticle inversely correlating to the particle size.^{2,9}

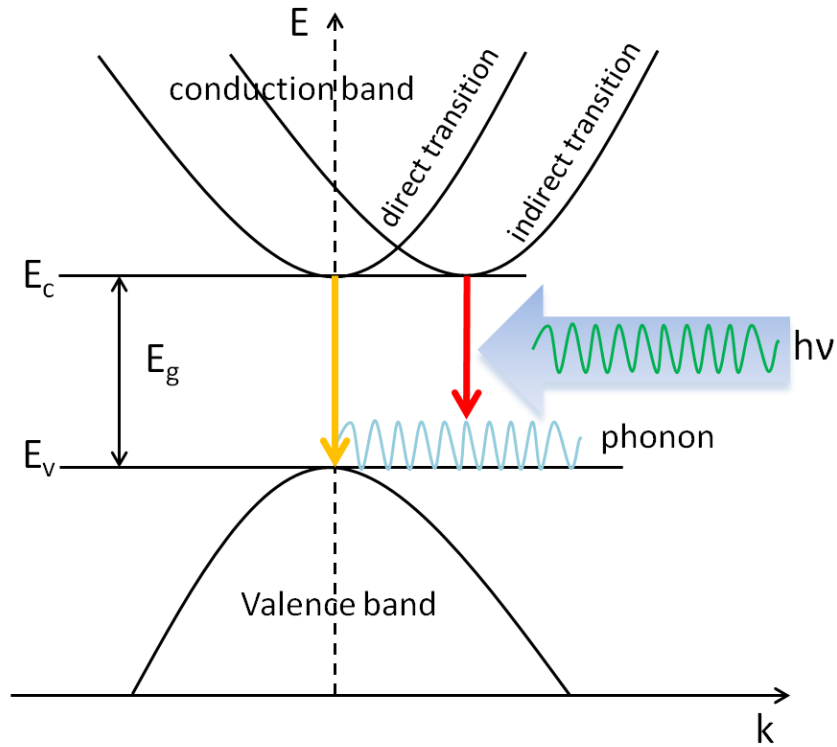


Figure 1.2 Direct and indirect band gap diagram. E_g , the band gap energy, E_c , the minimum energy of the conduction band, E_v , the maximum energy of the valence band.

There are two types of band gaps in semiconductor physics, direct band gap and indirect band gap, which are determined by a certain crystal momentum (k -vector) of the minimal-energy state of the conduction band and the maximal-energy state of the valence band. In a direct band gap material, the k -vector of the conduction band minimum and the valence band maximum are the same, while in an indirect band gap material, like silicon, the k -vector of the conduction band minimum and the valence band maximum are shifted (Figure 1.2). Thus, the direct electronic optical transitions in an indirect band gap are

dipole forbidden because the electron must pass through an intermediate state and transfer momentum to the crystal lattice. However, during the photon absorption or emission in indirect band gap materials, the electronic optical transitions can be assisted by either absorbing or emitting a phonon (a quantum of lattice vibration), which supplies the missing crystal momentum (Figure 1.2).¹⁰

When the size of an indirect band gap semiconductor scales down to nanometer scales and approaches the Bohr exciton radius (about 5 nm for Si), the absorbing and luminescence states will be shifted to higher energies due to the spatial confinement, which leads to increase of band gap energy and the delocalization of carriers in k-vector. This results in the change of absorption and emission properties of the indirect band gap semiconductor by allowing the non-phonon optical transitions,¹¹ which means the nanometer sizes indirect band gap semiconductor like silicon might have a direct or quasi-direct band gap.¹²

1.3.2 Optical properties

In addition to quantum confinement, there are two other factors which can influence optical properties of silicon nanoparticles: surface defects and surface passivation.¹³ Surface defects occur when the surface of silicon nanoparticles are not fully passivated, and lead to the formation of surface dangling bonds which act as traps to lower the surface free energy, increase the nonradiative recombination, and quench the photoluminescence. Figure 1.3 shows the possible photoluminescence mechanism of silicon nanoparticles with and without surface defects. Numerous studies have been reported which claim that the surface defect states, such as P_b-type defects,¹⁴ could decrease the effective band gap of the silicon nanoparticles and resulting in the red shift

of the photoluminescence (showing red emission, Figure 1.3b).^{3, 13b, 15} However, Y. Zhao and coworkers reported that the surface defect states also could increase the band gap of the silicon nanoparticles and lead to a blue shift of the photoluminescence (showing blue emission, Figure 1.3c).¹⁶

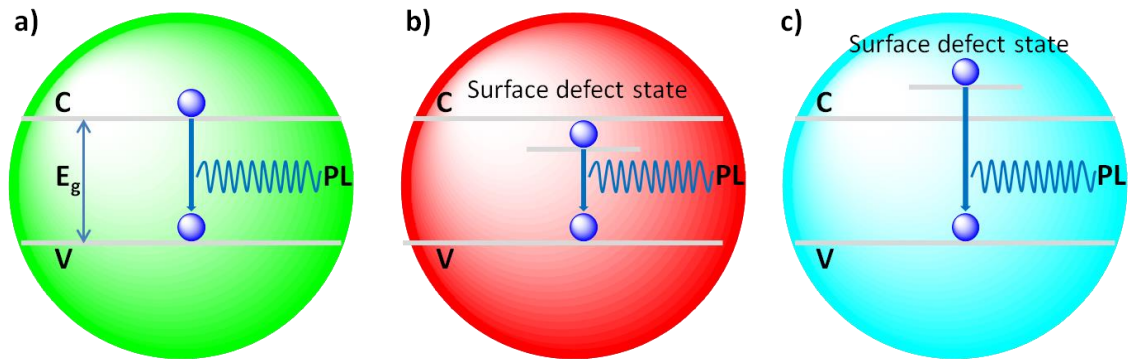


Figure 1.3 Illustration showing photoluminescence mechanism in silicon nanoparticles. a) without surface defect states where PL is exclusively due to quantum confinement; b) with surface defect state which reduces the energy gap leading to the red shift of PL; c) with surface defect state which increase the energy gap leading to the blue shift of PL.

Surface passivation also plays an important role in the optical properties of silicon nanoparticles. Hydrogen is well known to be introduced to the silicon nanoparticles to replace the surface dangling bands during the synthesis process. One study on porous silicon has claimed that hydrogen atoms on the surface can eliminate the irradiative centers and result in increasing blue emission intensity.¹⁶ However, the Si-H bonds in the particle's surface can be very reactive and easily be oxidized to form Si=O bonds. Oxygen passivation on the silicon nanoparticles surface has been shown to cause a considerable red shift of the photoluminescence due to the electron-hole recombination involving a trapped electron or exciton.^{13b} In addition, a Si-C bond on the nanoparticle's

surface, which is much stable than a Si-H bond, has been shown to have similar effect as the Si-H bond on the photoluminescence properties of silicon nanoparticles.¹⁷

The optical properties of silicon nanoparticles, which are determined by their size and surface states, include primarily the absorption and photoluminescence (PL). The typical absorbance of silicon nanoparticles contains a continuous absorbance from the UV to the visible range due to the indirect character of the absorbance. The emission wavelength of the PL can be varied by tuning the excitation wavelength and/or nanoparticle sizes.¹⁸ The width of PL is also related to the polydispersity of the particle size which can be reduced by size separation of the particles.¹⁸⁻¹⁹ Another important optical property of silicon nanoparticles is their relatively high quantum yield. It has been reported that silicon nanocrystals passivated by alkenes shown a quantum yield as high as 0.6 at 789 nm.²⁰ Furthermore, the room temperature PL lifetimes of silicon nanoparticles can be up to the microsecond scale, which are much longer than that of the organic dyes and direct band gap semiconductor nanoparticles.⁴ The photostabilities of silicon nanoparticles have been compared with organic dyes used in biological cell imaging, which clearly indicated that the fluorescence of silicon nanoparticles was stable over 2 hours while the organic dyes quickly lost their intensity.²¹

1.4 Synthesis of silicon nanoparticles

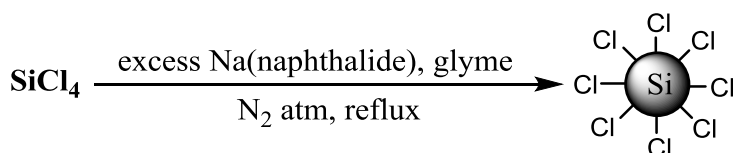
A significant amount of work on synthesis of silicon nanoparticles has been reported in last two decades. Due to the optical quenching effect of the surface termination with oxygen, most of the synthetic approaches are focused on the oxide free alkyl passivated silicon nanoparticles. There are two general routes for synthesizing silicon nanoparticles: a top-down process which nanoparticles are forming by reducing the bulk silicon into the

nanometer size scale, and a bottom-up process which silicon nanoparticles are assembled from molecular precursors.

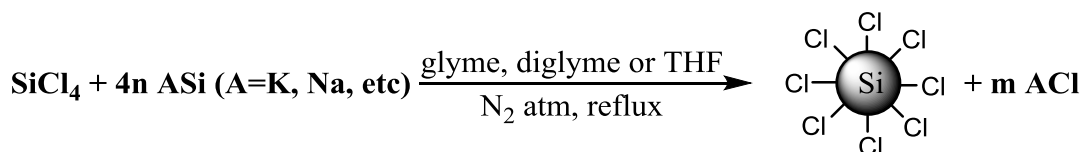
1.4.1 Bottom-up methods

Reduction of halosilanes

Reduction of halosilanes is one of the efficient techniques for producing alkylated silicon nanoparticles, which was developed by Kauzlarich and co-workers.²² The halogen terminated silicon nanoparticles can be obtained from the reduction of silicon tetrachloride with sodium naphthalide at room temperature (Scheme 1.1).



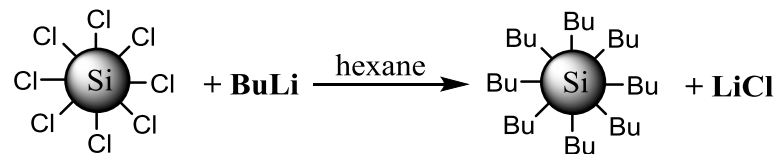
Scheme 1.1 Reduction of silicon tetrahalide using sodium naphthalide to produce halogen terminated silicon nanoparticles



Scheme 1.2 Reduction of silicon tetrahalide using Zintl salts to produce halogen terminated silicon nanoparticles

Another solution synthesis route to halogen terminated silicon nanoparticles at low temperature, which was also developed by Kauzlarich and co-workers, is the reduction of silicon tetrachloride using Zintl salts (ASi, A=K, Na, etc.) to produce the chloro-terminated silicon nanoparticles (Scheme 1.2).²³ These chloro-terminated silicon

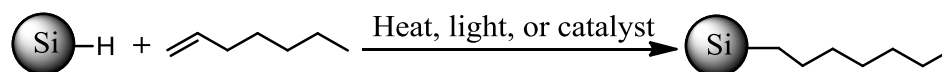
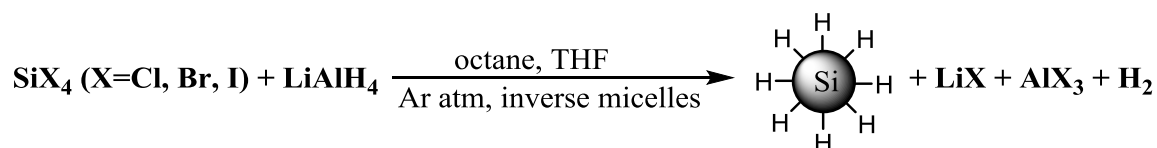
nanoparticles can be used as precursors for obtaining alkylated silicon nanoparticles using an alkyl lithium reagent (Scheme 1.3).²⁴



Scheme 1.3 Alkylation of halogen terminated silicon nanoparticles

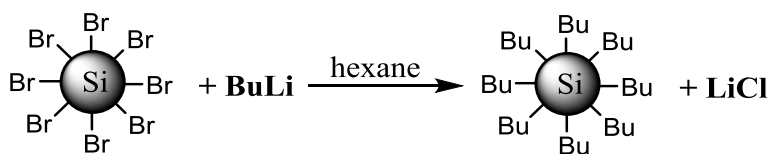
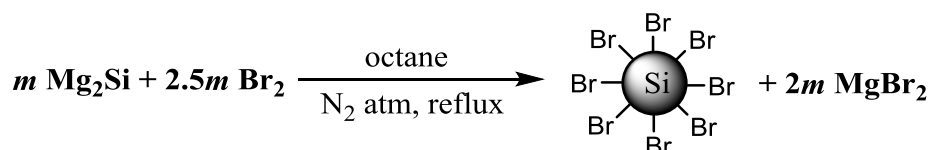
Reduction of halosilanes in inverse micelles

Provencio and co-workers first reported a synthetic method for the production of size-selected silicon nanoparticles using inverse micelles as reaction vessels in 1999.²⁵ In this process, the controlled nucleation and growth of the silicon nanocluster occurs in the interior of nanosize surfactant aggregates. The nucleation and growth of silicon nanoparticles is restricted to the micelle interior, since the anhydrous halosilanes (*e.g.* SiX_4 , where $\text{X}=\text{Cl}, \text{Br}, \text{I}$) only disperses in the hydrophilic solution inside the micelles and is completely insoluble in the continuous oil medium used (*e.g.* octane). The anhydrous silicon salts are reduced from Si(IV) to Si(0) using an anhydrous metal hydride (usually 1 M LiAlH_4 in THF). The resulting silicon nanoparticles exhibit hydrogen termination which can be further functionalized by a hydrosilylation reaction.²⁶ The advantage of this approach is that the silicon nanoparticle size can be controlled by the micelle size, intermicellar interactions and the reaction chemistry.^{25, 27} However, due to the encapsulation by the interior of micelles, the hydrosilylation of the hydrogen terminated silicon nanoparticles is difficult and the further purification steps are necessary.



Scheme 1.4 Synthesis of alkyl-capped silicon nanoparticles using inverse micelles

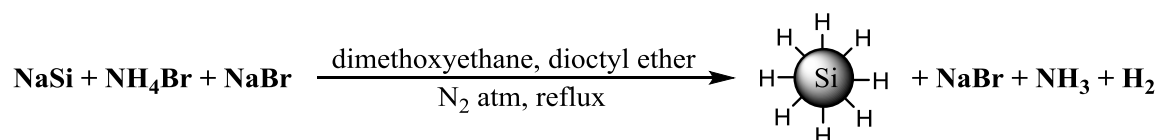
Oxidation of metal silicides



Scheme 1.5 Oxidation of metal silicide to produce alkyl-capped silicon nanoparticles

Halogen terminated silicon nanoparticles can be produced from oxidation reaction of metal silicides. One of the methods to produce alkyl-capped silicon nanoparticles involves the oxidation of metal silicide with bromine resulting in bromine terminated silicon nanoparticles. These nanoparticles are usually followed by the further functionalization with alkyl lithiums (Scheme 1.5).²⁸

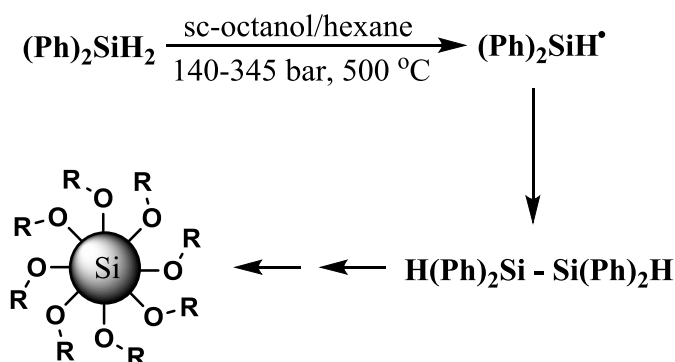
Another similar approach used to obtain silicon nanoparticles is the oxidation of Zintl salts. Oxidation is accomplished with ammonium bromide in a solution of dimethoxyethane and dioctyl ether under nitrogen atmosphere, resulting in H-terminated silicon nanoparticles (Scheme 1.6).²⁹



Scheme 1.6 Oxidation of Zintl compounds to produce H-terminated silicon nanoparticles

The H-terminated surface on silicon nanoparticles is highly reactive and can be further functionalized via a hydrosilylation reaction to obtain air-stable alkyl-capped silicon nanoparticles.

Thermal decomposition of silanes in supercritical conditions



Scheme 1.7 Radical mechanism of formation of silicon nanoparticles

Thermal decomposition of silanes in supercritical fluids is a successful approach to yield passivated silicon nanoparticles. Korgel and co-workers developed an approach involving the thermal degradation of diphenylsilane in supercritical octanol to produce passivated silicon nanoparticles.³⁰ The thermal degradation of diphenylsilane was performed in a mixture of octanol and hexane at high temperatures (500°C) and high pressure (345 bar) to produce silicon nanoparticles with a stable organic monolayer passivation. The authors claimed that the formation of silicon nanoparticles followed a

radical mechanism because the benzene ring could help to stabilize the silane radical intermediates, and at the end of the reaction the octanol can replace the phenyl groups while forming the passivated surface.³⁰⁻³¹

Thermal decomposition of silanes using laser pyrolysis

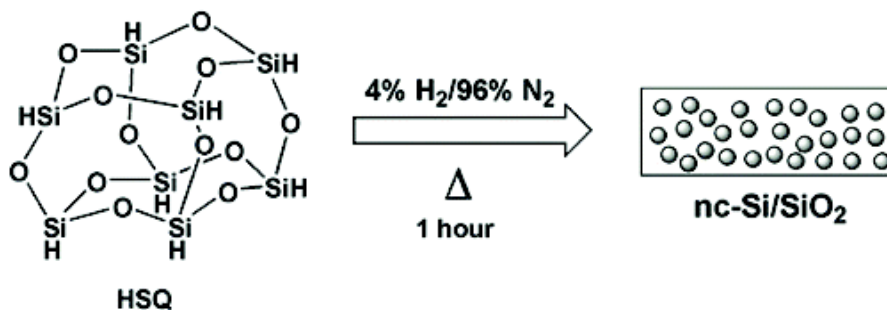


Scheme 1.8 Thermal decomposition of silane by laser pyrolysis

Another approach to synthesize passivated silicon nanoparticles using laser induced heating to dissociate the silanes to produce silicon powder.^{18, 32} In this method, silicon powders were synthesized by laser-induced heating of silanes to the temperatures where the silanes dissociates. A continuous CO₂ laser beam was focused to a gas stream which contains silane (SiH₄), sulfur hexafluoride (SF₆), hydrogen and helium (Scheme 1.8). Oxide terminated silicon nanoparticles were obtained in a continuous fashion with a rate of 20-200 mg/h.

In order to produce alkyl-capped silicon nanoparticles, the oxide terminated silicon nanoparticles need to be treated with HF etching to obtain hydrogen terminated silicon nanoparticles which is followed by a hydrosilylation reaction. Alternatively, the nanoparticles can be treated with HNO₃ to obtain hydroxyl terminated silicon nanoparticles which then is followed by a rapid thermal oxidation to produce the blue-emitting particles.

Reductive thermal annealing of hydrogen silsesquioxane



Scheme 1.9 Thermal processing of hydrogen silsesquioxane (HSQ) for preparing silicon nanoparticle/SiO₂-like (*nc*-Si/SiO₂) nanocomposites

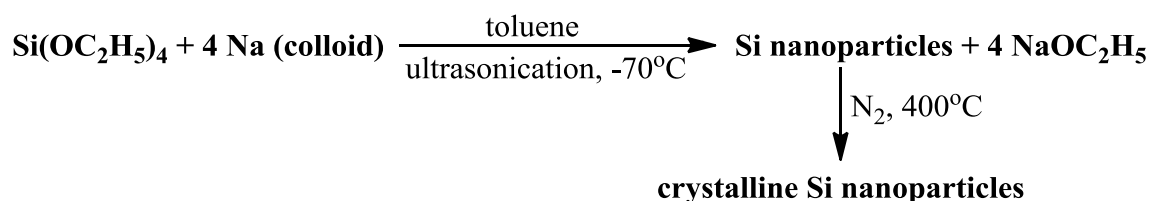
In 2006, Veinot and co-workers reported the bulk preparation of nanocrystalline Si-SiO₂ (*nc*-Si/SiO₂) composites via a straightforward reductive thermal annealing of a well-defined molecular precursor, hydrogen silsesquioxane (Scheme 1.9).³³ In this process, hydrogen silsesquioxane was thermally processed in a 4% H₂:96% N₂ atmosphere at 1100 °C to produce silicon nanocrystallites encapsulated in a SiO₂-like matrix. The freestanding hydride-surface-terminated silicon nanocrystals could be liberated from the *nc*-Si/SiO₂ composites powders upon etching in ethanol-water solutions of hydrofluoric acid.

Plasma synthesis

Kortshagen and co-workers reported a single-step synthesis process for oxygen terminated silicon nanoparticles based on a low-pressure nonthermal plasma in 2005.³⁴ The synthesis approach based on a nonthermal plasmas which was a partially ionized gas with electrons possessing temperatures of 20,000-50,000K and thus a significantly hotter than the gaseous atoms and ions, which remain close to room temperature. During the

processing, the free electrons and ions can recombine at the particle surface which may contribute to heating the particles to high temperatures which is significantly above the temperature of the surrounding gas.³⁴ Kortshagen and Swihart reported that the silicon nanoparticles are created by the electron impact dissociation of SiH₄ and subsequent clustering of the fragments.³⁵ However, this method results in the production of oxide terminated silicon nanoparticles which need to be further functionalized to obtain alkyl-capped silicon nanoparticles.

Sonochemical synthesis



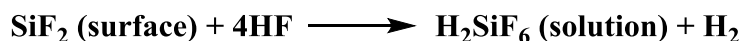
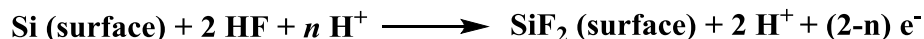
Scheme 1.10 Sonochemical synthesis of silicon nanoparticles using reduction reaction

Sonochemical synthesis is another technique that has been used for synthesizing passivated silicon nanoparticles. Gedanken and co-workers first reported a sonochemical approach to produce silicon nanoparticles from tetraethyl orthosilicate in 1998.³⁶ In this approach, tetraethyl orthosilicate was reduced by colloidal sodium under sonication in toluene at -70°C which resulted in the oxygen passivated silicon nanoparticles. However, the oxygen passivated silicon nanoparticles needed to be treated with HF in order to obtain hydrogen terminated silicon nanoparticles which could be further functionalized by a hydrosilylation reaction.

1.4.2 Top-down methods

Chemical and electrochemical etching

Many groups have reported that the H-terminated silicon nanoparticles can be synthesized via anodic HF etching of silicon, followed by ultrasonication.³⁷ Porous silicon with H-terminated surface can be obtained after exposing the crystalline silicon wafer to HF and current (Figure 1.4). After the etching process, the porous surface of the silicon wafer is extremely fragile due to ultra-small substructures on the surface. The ultra-small silicon nanoparticles with H-terminated surface can leach out from the porous surface and be suspended in the carrier solution, such as toluene, over several hours using sonification.



Scheme 1.11 Mechanism of surface etching of silicon by HF

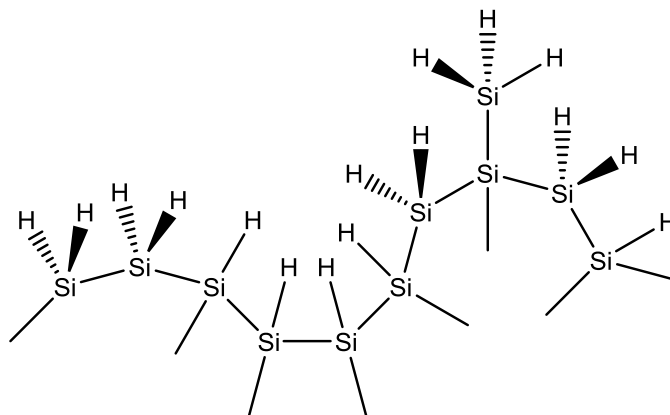


Figure 1.4 Schematic presentation of H-terminated surface of porous silicon layer on the silicon surface after etching process

The H-terminated silicon nanoparticles can be used as starting materials to produce alkylated silicon nanoparticles via hydrosilylation reactions. Additionally, some groups have reported that the size of the silicon nanoparticles can be influenced by the applied current during the etching process.³⁸

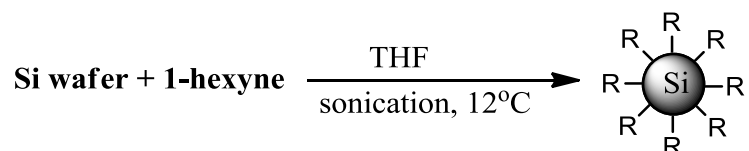
Laser ablation

Since 1994, several groups have reported that silicon nanoparticles with oxide terminated or hydrogen terminated surface can be generated via laser ablation.^{35, 39} The generation of silicon nanoparticles is caused by a laser induced degradation of silicon wafers in vacuum^{39b} or inert atmosphere^{39c} resulting in a oxide terminated surface, whereas in a hydrogen atmosphere^{39f} a hydrogen terminated surface is obtained. The generation rate and average particle size depend on the variation of process parameters, which including ablation pulse, gas valve timing and nozzle length. Silicon nanoparticles are produced using femtosecond laser ablation in vacuum due to the sudden expansion of the extreme material state induced by ultra-short laser irradiation of the target surface,^{39a} while the generation of silicon nanoparticles in argon gas using a nanosecond laser followed a mechanism of a condensation based process.^{39e} The size of the resulted silicon nanoparticles in this method ranges from 1-10 nm, and further functionalization is necessary due to the oxide and hydrogen terminated surfaces.

Sonochemical synthesis

Recently, Mitchell and co-workers developed a novel approach for preparing silicon nanoparticles with organic surface functional groups in a one-step reaction using sonochemical synthesis.⁴⁰ This synthesis approach involves a combination of acoustic

cavitation erosion of a single-crystalline silicon surface coupled with simultaneous reaction with an organic ligand. Functionalized silicon nanoparticles with ultra-small sized and blue-green photoluminescence have been formed at the end of the reactive cavitation erosion.



Scheme 1.12 Sonochemical synthesis of silicon nanoparticles using reactive cavitation erosion

Mechanochemical synthesis of silicon nanoparticles

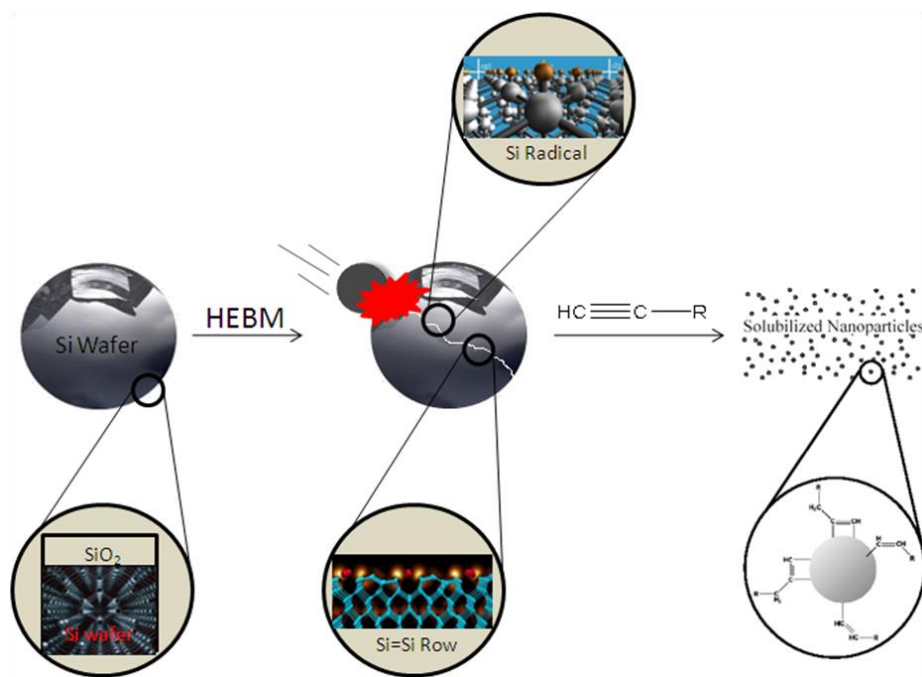


Figure 1.5 Schematic illustration of the mechanochemical synthesis of passivated silicon nanoparticles with alkyne ligands. (alkenes also can be used as passivation ligand)

As previously discussed, passivated silicon nanoparticles can be produced via different approaches. However, all of those pathways exhibit similar disadvantages which require either the use of highly reactive or corrosive chemicals, or require of further modification of unstable hydrogen or halogen terminated surfaces. An approach of producing silicon nanoparticles with organic passivation surface in a one-step reaction under mild reaction conditions with the possibility of scale-up is highly desirable.

Mechanochemical synthesis of passivated silicon nanoparticles via Reactive High Energy Ball Milling (RHEBM) is a one-step reaction which has been proved to be an efficient and simple pathway to produce alkylated silicon nanoparticles.⁴¹ The alkylated silicon nanoparticles are obtained via ball milling with a reactive organic liquid, such as alkyne or alkene, and silicon wafer under nitrogen atmosphere. During the RHEBM, the mechanical energy causes the silicon wafer to fracture and creates fresh silicon surface which contain reactive silicon-silicon double bonds (-Si=Si-) and silicon surface radicals (Figure 1.5). The newly-created surface is highly reactive and can react with alkynes or alkenes resulting in the formation of strong covalent Si-C bonds which can prevent further oxidation of the silicon surface.^{22a} After RHEBM, the alkylated silicon nanoparticles are soluble in the organic liquid and can be easily separated out from the reaction mixture by centrifugation.

1.5 Surface passivation and functionalization of silicon nanoparticles

All the synthetic approaches to silicon nanoparticles involve surface passivation and/or functionalization. The surface atoms of the nanoparticles play a very important role in the optoelectronic properties of nanoparticles compared to their bulk atoms due to the enormous surface area-to-volume that is one of the important attributes of

nanoparticles.⁴² Compared to other compound semiconductors, the significant advantage of silicon nanoparticles is their surface chemistry because of the formation of strong covalent bonds between silicon and carbon or oxygen, which can covalently link organic entities onto a silicon surface.⁴ Passivation of the silicon nanoparticle surfaces with organic groups can increase the resistance of surface oxidation, control the particle's interaction and hence control the particle's arrangement on surfaces, stabilizes the electronic and optical properties of the particles, prevent bulk aggregation and improve the solubility in various solvents.⁶ Also, further functionalization of silicon nanoparticles can provide intriguing properties, such as water solubility and biocompatibility, and lead to numerous applications including bioimaging, drug delivery and electronic devices. Figure 1.6 shows the summary of surface tailoring methods of silicon nanoparticles.

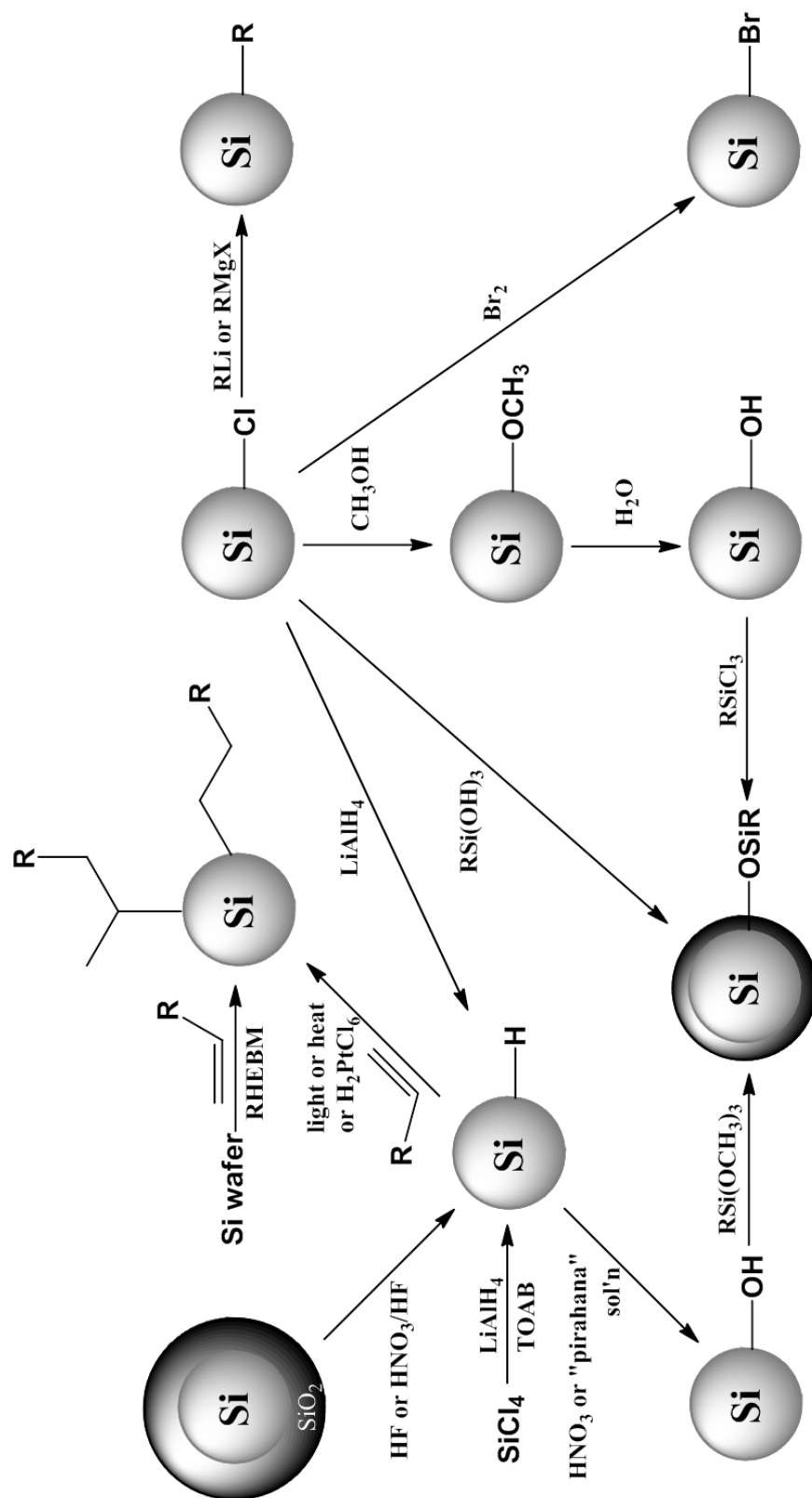
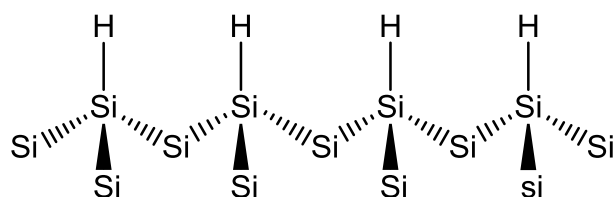


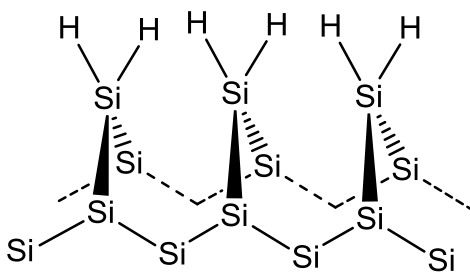
Figure 1.6 Summary of surface tailoring of silicon nanoparticles

1.5.1 Hydrosilylation reactions

One of the primary means of attaching organic molecules to a silicon surface is hydrosilylation reactions which form the silicon-carbon bonds on the hydrogen terminated silicon surface. Most of the synthetic approaches of silicon nanoparticles result in the generation of hydrogen terminated silicon nanoparticles (Figure 1.7 shows two typical silicon-hydrogen-terminated surfaces on the silicon nanoparticle), which means a second step reaction for further functionalization with organic molecules via hydrosilylation reactions is necessary. Although the hydrogen terminated silicon nanoparticles are very sensitive to oxygen which requires more complex handling and equipment, the high reactivity of the silicon-hydrogen bond makes the hydrosilylation reactions easier and more efficient.



Monohydride terminated flat Si(111)-(1×1)



Dihydride terminated flat Si(100)-(1×1)

Figure 1.7 Schematic presentation of the Si(111) and Si(100) silicon-hydride-terminated surfaces on the silicon nanoparticle. ⁴³

In 1993, Linford and co-workers first reported that the hydrosilylation reactions can be used for attaching alkenes to a silicon surface.⁴⁴ In this reaction, a silicon-hydrogen bond on the silicon surface reacts with a double bond in an alkene (or triple bond in an alkyne) to form a direct silicon-carbon bond resulting in an organic layer on the silicon nanoparticle surface. Figure 1.8 shows the regular mechanism for the hydrosilylation of a hydrogen-terminated silicon surface with a terminal alkene.⁴ The hydrosilylation reaction can be initiated by heating, light irradiation or a catalyst which can induce the generation of silicon surface radicals by removing a hydrogen atom. The silicon surface radical can react with a double bond to form a silicon-carbon bond and generate a free radical at the other carbon in the double bond. The carbon radical can then take a hydrogen from the neighboring silicon atom and generate a new silicon surface radical which can repeat the process (Figure 1.8). In 2013, Buriak reported that there were plural mechanisms of the light-promoted hydrosilylation besides the regular radical mechanism, such as exciton-driven hydrosilylation, photoemission-driven hydrosilylation and surface plasmon-assisted hydrosilylation (Figure 1.9).⁴⁵

It has been demonstrated that hydrogen terminated silicon nanoparticles can be further functionalized with more complex functional alkenes or alkynes, including biocompatible molecules, using the hydrosilylation reaction. For example, Sato and coworkers have used acrylic acid to synthesis propionic acid functionalities in 2006,⁴⁶ Rogozhina and coworker used methyl-4-pentenoate to prepare methyl ester carboxyl functionalities in 2006,⁴⁷ Choi and coworkers reported the attachment of streptavidin in a four step procedure in 2008,⁴⁸ Zachariah et al. and Rosso-Vasic et al. reported the attachment of acryl amine and acrylthiol in 2008 and 2009,⁴⁹ Sudeep and coworkers used

3-aminopropyltriethoxysilane to yield amino functionalities in 2009,⁵⁰ Zhao and coworkers used octene and hexane for activation with 4'-[3-trifluoromethyl-3H-diazirin-3-yl]-benzoic acid and N-hydroxysuccinimide for DNA labeling in 2009,⁵¹ and Nelles and coworkers reported the attachment of alkene terminated PEG 1100 in 2010.⁵²

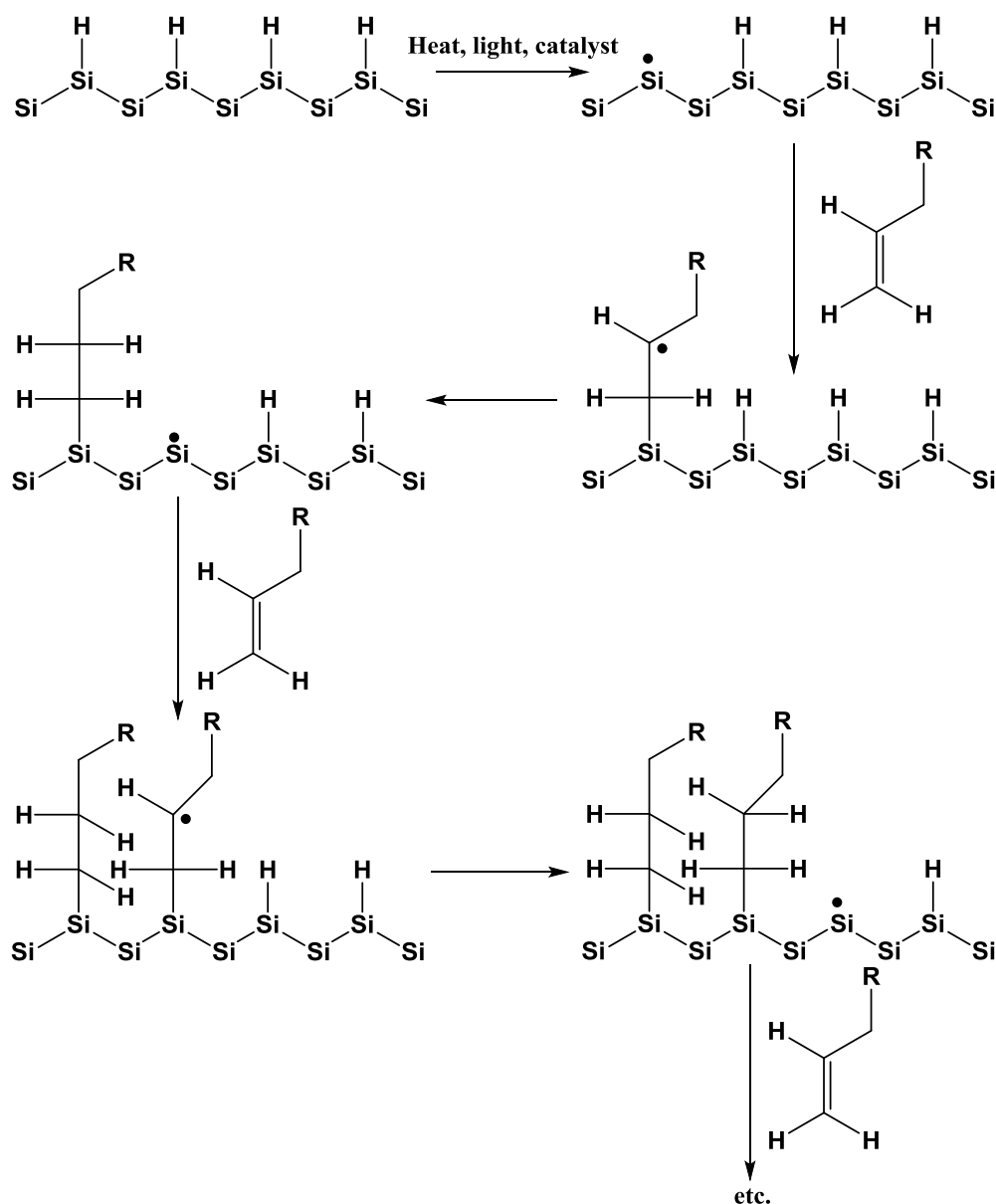


Figure 1.8 Schematic the regular mechanism for hydrosilylation of an H-terminated silicon surface with a terminal alkene.⁴

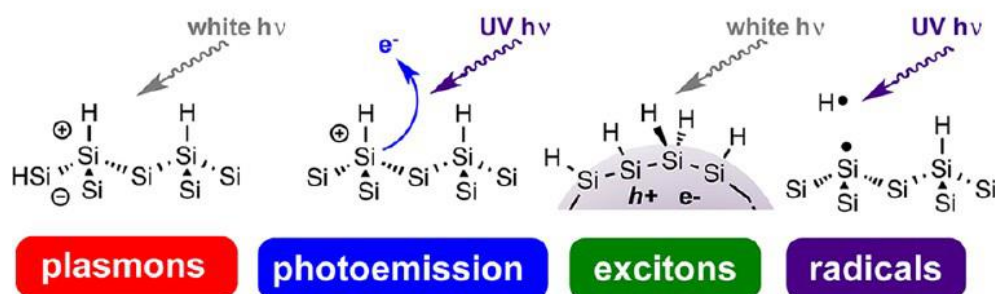


Figure 1.9 Proposed mechanisms for light-induced hydrosilylation on hydride-terminated silicon surfaces⁴⁵

1.5.2 Silanization reactions

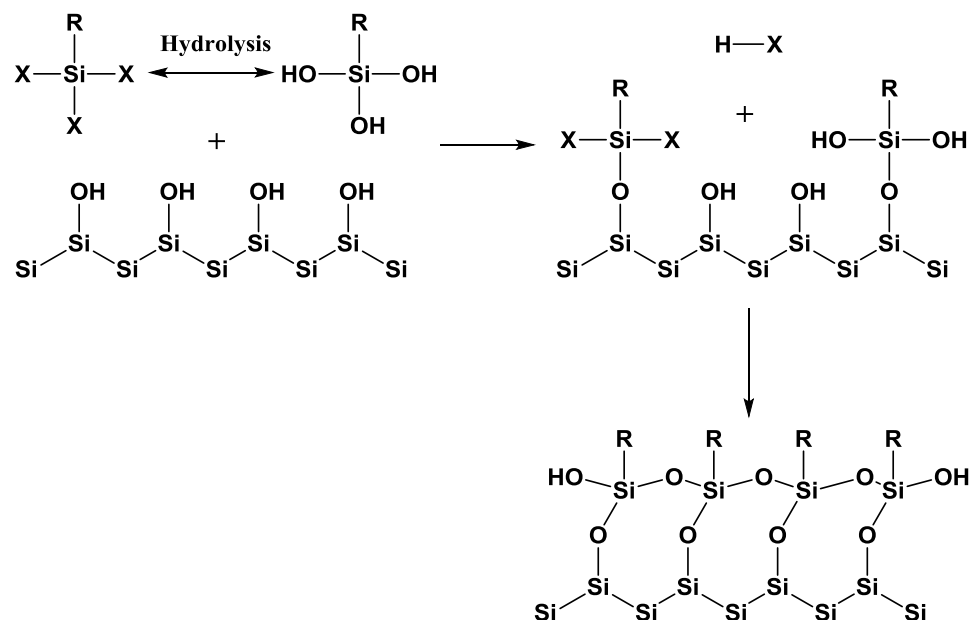


Figure 1.10 Schematic the mechanism for silanization of a hydroxyl-terminated silicon surface with a chlorosilane or alkoxy silane (where X = Cl, OCH₃, OCH₂CH₃, etc.).⁴

Silanization is another general method of attaching organic molecules to silicon surfaces which forms the silicon-oxygen-silicon link on the hydroxyl-terminated silicon surfaces. As shown in Figure 1.10, the alkoxy or chlorine groups on the silanizing agent, which typically has one organic group and three alkoxy or chlorine groups attached to it,

react with the surface hydroxyls on silicon to form the Si-O-Si linkages. The linkages then condense with each other to form a cross-linked siloxane layer on the surface. During the reaction, the silane can partially or fully hydrolyzed in solution before reacting with hydroxyl groups on the silicon surface. The condensation reactions can lead to a siloxane layer on the surface, however, the condensation reactions can also occur in solution in the presence of more than trace amounts of water and lead to the polymerization of the silane which is undesirable.⁴

Some examples of silanization reactions applied to attach organic molecules to silicon nanoparticles have been reported by Swihart's group. They prepared silicon nanoparticles with -OH group on the surface, and then the nanoparticles were reacted with octadecyltrimethoxysilane to produce alkyl termination.¹⁸ In another study, they reacted the hydroxyl-terminated silicon nanoparticles with 3-bromopropyltrichlorosilane to generate the bromo-terminated silicon nanoparticles, and then used the bromine groups as sites to attach aniline and initiate graft polymerization of polyaniline on the particle surface.⁵³

Kauzlarich and coworkers also reported the modification of chloride-terminated silicon nanoparticles to yield the "ultrastable" siloxane-coated silicon nanoparticles using two independent silanization reactions (Figure 1.11).^{22b} In one case, the chlorine terminated groups on the nanoparticle surface were converted to methoxy groups upon exposure to methanol. Then the methoxy terminated silicon nanoparticles reacted with water and finally alkyl trichlorosilanes to obtain the silicon nanoparticles with cross-linked siloxane surfaces. The same siloxane-coated silicon nanoparticles were generated

via a second approach in which the methoxy terminated silicon nanoparticles were reacted directly with trihydroxysilanes.

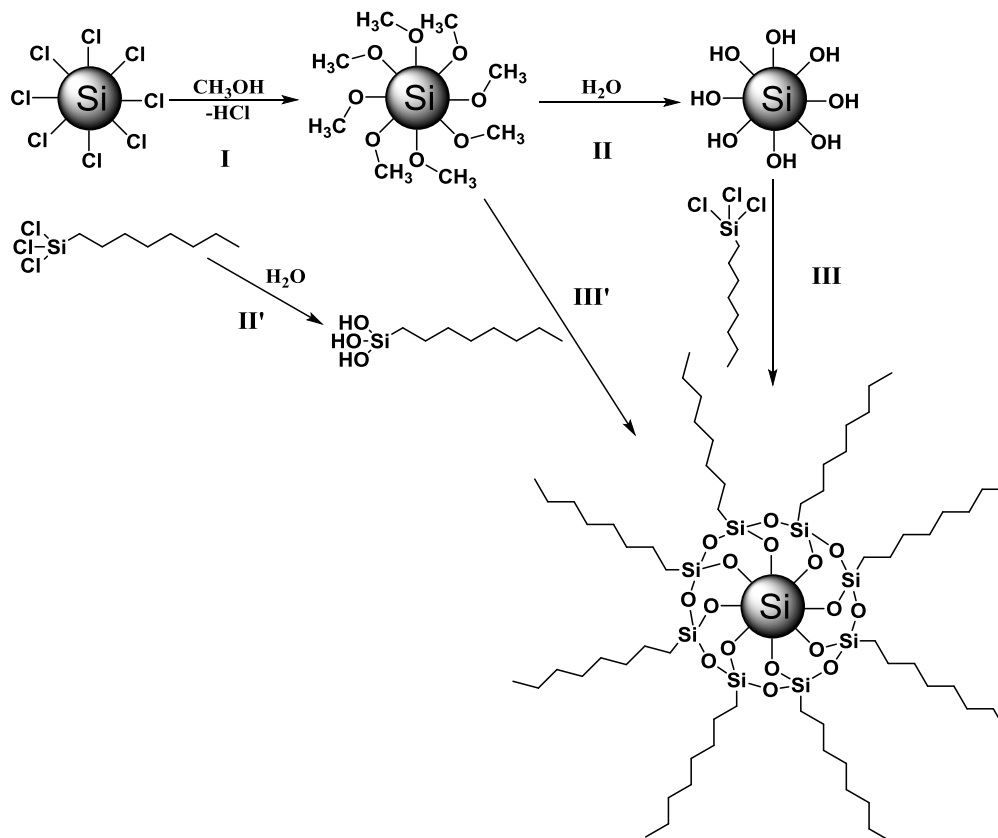


Figure 1.11 Two independent silanization reactions for the formation of siloxane-coated silicon nanoparticles.^{22b}

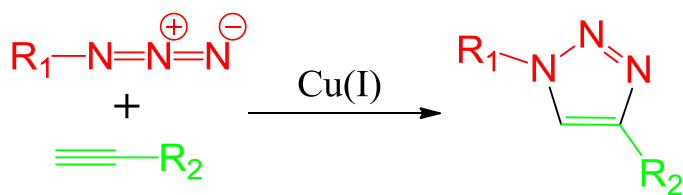
1.5.3 Alkylation of halide-terminated surfaces

Chlorine terminated silicon nanoparticles, which have a chemically active surface, can be further functionalized with alkyl groups using an alkyl Grignard (RMgBr) or an alkyl lithium reagent (RLi).²⁴ In 1996, Bely and Kauzlarich first reported an unexpected reaction occurred between the chloride surface-terminated silicon nanoparticles and the methanol which used to remove the salt impurities resulting in the passivation of -OMe

groups on the silicon nanoparticle surfaces.²³ Kauzlarich's group extended the modification of the chlorine terminated silicon nanoparticles using alkyl lithium, Grignard reagents, lithium aluminum hydride or bromine.^{28, 54} Similarly, Rogozhina and coworkers reported that the chlorine terminated silicon nanoparticles can react with butyl amine to obtain a Si-N bonded organic surface layer.⁵⁵

1.5.4 "Click" Chemistry

The previous discussed methods to produce stable silicon nanoparticles with specific functionalization are very time consuming and limited by the choice of capping agents. An alternative approach to functionalize silicon nanoparticles with specific surface ligands is "click" chemistry. "Click" chemistry is an attractive tool for functionalizing silicon nanoparticles because of its high yields, modular approach, and broad functional group tolerance.⁵⁶ The copper catalyzed azide-alkyne cycloaddition (CuAAC)⁵⁷ and the thiol-ene reaction⁵⁸ are two major "click" reactions that have been broadly used. The CuAAC in particular is one of the most efficient "click" reactions due to its high selectivity and mild reaction conditions (Scheme 1.13).^{57, 59}



Scheme 1.13 Copper-catalyzed azide-alkyne cycloaddition reaction

In addition, azides and alkynes are essentially inert to molecular oxygen, various solvents including water, and common reaction conditions in organic synthesis, while the formed triazole is very stable which is nearly impossible to oxidize or reduce.⁶⁰ Therefore,

alkyne-azide “click” chemistry has been performed to functionalize various nanostructure materials, including gold nanoparticles,⁶¹ metal oxide nanoparticles,⁶² silica nanoparticles⁶³ and silicon surfaces.⁶⁴

1.6 Characterization of silicon nanoparticles size distribution

The size and size distribution of silicon nanoparticles is very crucial for their applications due to quantum size effects exhibited by the silicon nanoparticles. Therefore, characterizing the size of silicon nanoparticles, which is usually done by transmission electron microscopy (TEM) and atomic force microscopy (AFM), plays a central role in the silicon nanoparticle investigation. In addition, the hydrodynamic diameter of silicon nanoparticles can be measured by dynamic light scattering (DLS), gel permeation chromatography (GPC) and diffusion-order NMR spectroscopy (DOSY).

1.6.1 Transmission electron microscopy

Transmission electron microscopy (TEM) is one of the most powerful tools to determine and directly image the size of silicon nanoparticles. Many investigations of the silicon nanoparticle size distribution have been done using TEM technique. The size distribution of a silicon nanoparticle sample can be obtained from a typical TEM image, which usually shows the nearly spherical particles with several nm-sizes (Figure 1.13 left). Furthermore, the accurate sizes of individual silicon nanoparticles can be monitored by high resolution TEM (HRTEM) (Figure 1.12 right).⁶⁵ However, the quantification of the characterization by TEM techniques assumes that the imaged sample is homogenous and the imaged area is a representative of the whole sample.

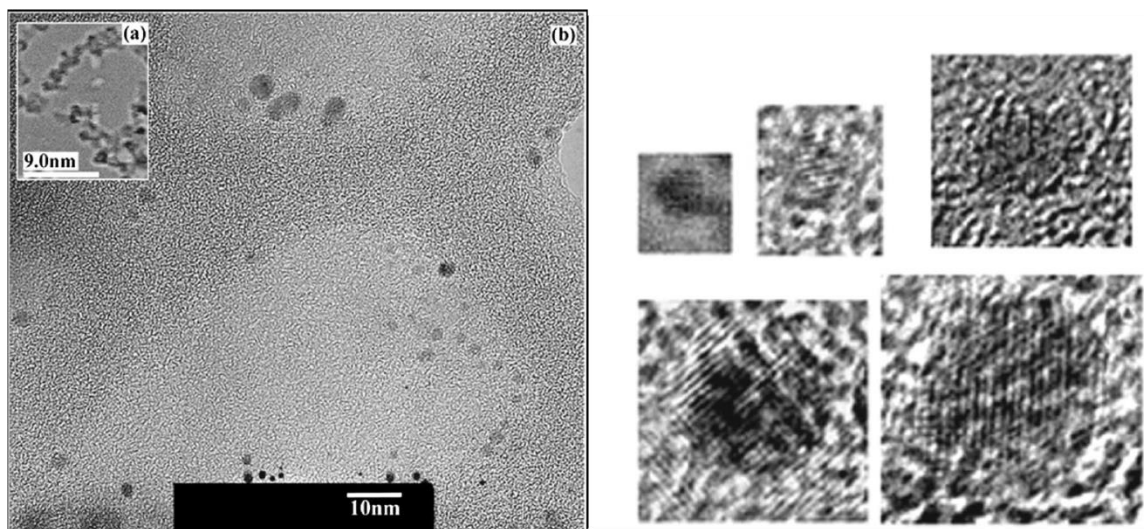


Figure 1.12 (left) (a) and (b) typical TEM image of silicon nanoparticles on a graphite grid. (Right) HRTEM image of the 1.0, 1.67, 2.15, 2.9 and 3.7 nm silicon nanoparticles.⁶⁵

1.6.2 Atomic force microscopy

Atomic force microscopy (AFM) is an alternative method, even an easier method in some cases, to probe silicon nanoparticles compared to TEM, especially when the partition of nanoparticles is low in the matrix or precipitates in the amorphous state.⁶⁶ In this case, AFM is a useful tool to indirectly image the silicon nanoparticles in a matrix and investigate their size variation. AFM can provide higher resolution than SEM, even up to atomic resolution (~ 0.1 nm) in ultra-high vacuum.⁶⁷ Generally, the distribution of heights can be measured as an integral function of the size distribution of silicon nanoparticles in an AFM image. For example, Mayandi and coworkers studied the size variation of silicon nanoparticles in SiO_2 matrix using AFM (Figure 1.13).⁶⁸ As shown in Figure 1.13 (a), the particle-like features which are signatures of regions with silicon nanoparticles appear in the AFM image after 20 s etching. They are also present for longer etching times and then disappear again as the SiO_2 is etched away. Figure 1.13 (b)

shows a similar variation of particle-like features under a different etching rate. Therefore, AFM is a promising tool, in some cases a much more convenient, easier, and cheaper way, for the investigation of the silicon nanoparticles and their size variation compared to TEM.

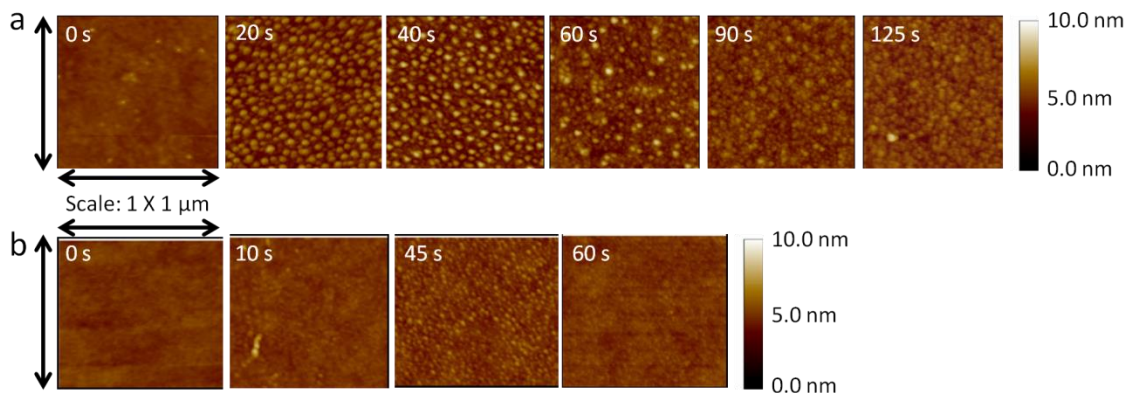


Figure 1.13 AFM tapping mode tomography of silicon implanted SiO_2 samples with respect to etching time for (a) $1 \times 10^{17} \text{ cm}^{-2}$ Si ions and for (b) $5 \times 10^{16} \text{ cm}^{-2}$ Si ions.⁶⁸

1.6.3 Hydrodynamic diameter of silicon nanoparticles

In addition to the quantum size effects, surface passivation is another impact factor of the optical properties of silicon nanoparticles. However, since the organic ligands on the silicon nanoparticle surface can be either indiscernible by TEM due to the insufficient contrast, or have been burned off due to the electron beam, the TEM image of the silicon nanoparticles usually only shows the core size of the particles.⁶⁹ Consequently, fast, reliable and cost-effective approaches for determining the entire size, such as hydrodynamic diameter, of silicon nanoparticles are highly desired. Here, a brief review of the techniques that can be used for determining the hydrodynamic diameter of silicon nanoparticles is discussed.

1.6.3.1 Dynamic light scattering

Dynamic light scattering (DLS) is a non-invasive, well-established technique that can be used for determining the size of particles and macromolecules typically in the range of 1 nanometer to several micrometers.⁷⁰ It can be used to measure the size of small particles, such as nanoparticles, biomolecules and polymers, suspended in a liquid medium.

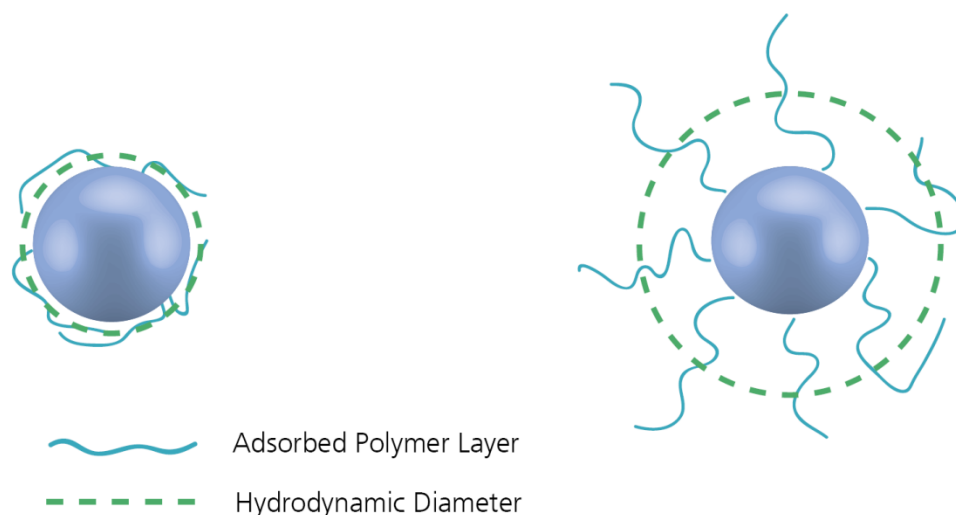


Figure 1.14 Illustration showing the hydrodynamic diameter of particles in DLS

The diameter obtained by DLS is hydrodynamic diameter which is based on the translational diffusion coefficient of the particle (Figure 1.14). Translational diffusion coefficients depend on the size of particle core, the surface structure and the concentration and type of ions in the medium, which means the size obtained from this technique will be closer to the entire size of the particle. However, due to the limitation of this technique, DLS is more efficient to measure the size of polymer grafted nanoparticles, but not sensitive enough to the small size (< 10 nm) nanoparticles.⁶⁹

1.6.3.2 Gel permeation chromatography

Gel permeation chromatography (GPC) is one type of size exclusion chromatography (SEC), which separates the analytes based on their size or hydrodynamic volume. Once the analytes are injected into the GPC column, the smaller analytes can enter the pores on the stationary phase more easily and therefore spend more time in these pores, while the larger analytes spend less time in the pores or even cannot enter these pores (Figure 1.15). As a result, the larger analytes elute first and the smaller analytes come out later.

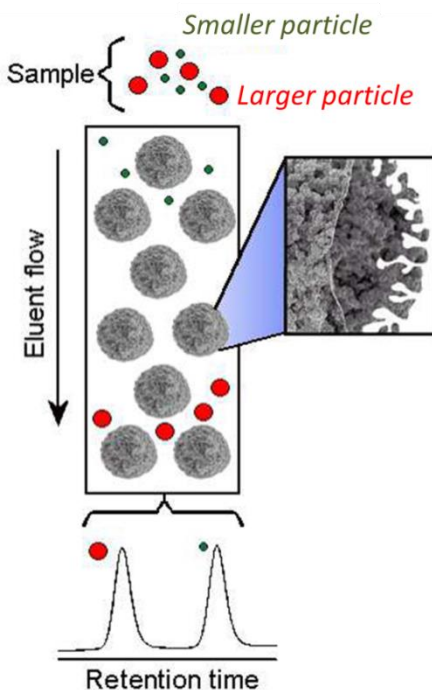


Figure 1.15 Schematic of the principle of GPC

GPC is usually used to determine the relative molecular weight of polymers and the distribution of their molecular weights. It also can be used to screen and estimate the size of nanoparticles. For example, Burda and coworkers have reported to use a gravity GPC column to separate the PEGylated gold nanoparticles based on the grafting density of the

PEG and the core size of the nanoparticles.⁷¹ Nayfeh and coworkers have reported that the GPC was used to characterize the solubility and aggregation of H-terminated and alkylated silicon nanoparticles, while using a polystyrene standard for calibration. The dispersion of the silicon nanoparticles in THF was measured by a UV detector at 365 nm.⁶

1.6.3.3 Diffusion-ordered NMR spectroscopy

Diffusion-ordered NMR spectroscopy (DOSY) was recently used as a reliable alternative to TEM for determining the size of gold nanoparticles in organic solutions. Wang and coworkers first used diffusion NMR to estimate the size of Au nanoclusters in 2010.⁷² Kubiak and coworkers reported that the 2D DOSY NMR was used to calculate the diffusion constants and the diameter of solubilized gold nanoparticles capped with alkyl thiol in different deuterated solvents, and they claimed that the distribution of nanoparticles sizes obtained from DOSY strongly correlated with the TEM image analysis.⁷³ Hakkinen and coworkers have used DOSY to estimate the hydrodynamic sizes of three monodisperse thiol-stabilized gold nanoclusters which the sizes of those gold nanoclusters were already known. The average cluster diameters obtained this technique were shown to agree well with the average cluster diameters reported in the literature.⁷⁴

1.7 Application of silicon nanoparticles

Size dependent optical and electronic properties⁷⁵ such as broad tunable light emission,^{31, 65, 76} high brightness,⁵⁵ stability against photo-bleaching relative to organic dyes,^{17, 22b, 27} and low toxicity *in vitro and in vivo* compared to traditional II/VI semiconductor quantum dots,⁷⁷ are attractive properties for silicon nanoparticles making them as ideal candidates in biological, photovoltaic and other device applications.

1.7.1 Photovoltaic application

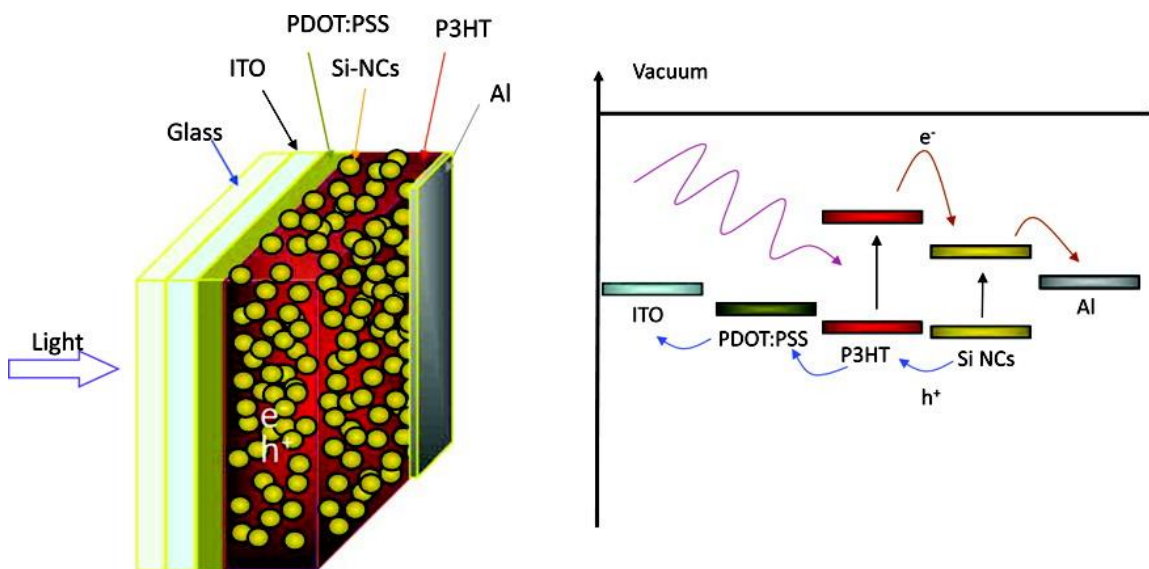


Figure 1.16 Schematic of a Si NCs/P3HT hybrid solar cell (left) and the schematic of electron-hole pair generation in the Si NCs/P3HT hybrid solar cell.⁷⁸

Silicon has enjoyed years of success because of its crucial roles in the solar cell and microelectronics industries, and also is a prime candidate for organic-nanocrystal hybrid solar cells due to its abundance, non-toxicity and strong UV absorption.⁷⁸ The band gap of bulk silicon is 1.12 eV, but the band gap of silicon nanoparticles can be increased and tuned by changing the particle size and surface functionalization, which makes the electronic properties of silicon nanoparticles more attractive.⁷⁹ Gowrishankar and coworkers have assembled two hybrid bilayer solar cells which consisting of either hydrogenated amorphous silicon (*a*-Si:H)/ poly(3-hexylthiophene) (P3HT) or *a*-Si:H/ poly(2-methoxy-5-(2'-ethyl-hexyloxy)-1,4-phenylenevinylene) (MEH-PPV), and have achieved efficiencies of 0.16%.⁸⁰ Adikaari and coworkers reported an improvement on these results by replacing the *a*-Si:H by nanocrystalline silicon and increased the efficiency up to 0.87%.⁸¹ Kortshagen and coworkers used blends of free-standing silicon

nanocrystals (Si NCs) and regioregular P3HT to form nanocrystal-polymer hybrid solar cells (Figure 1.16).⁷⁸ They explored different Si NC sizes and Si NCs/P3HT ratios to optimize the solar cell performance, and achieved the power conversion efficiency as high as 1.15%. Kortshagen and coworkers also have studied the effects of annealing and different metal electrodes on Si NCs/P3HT solar cells to further optimize the performance of the solar cell, and produced a device with an improved power conversion efficiency of 1.47%.⁸²

1.7.2 Biological applications

Unlike traditional II/VI semiconductor quantum dots, silicon nanoparticles exhibit low toxicity *in vitro* and *in vivo*.⁷⁷ Moreover, silicon nanoparticles provide intriguing properties such as water solubility and biocompatibility with further functionalization, and therefore show great potential application in bioimaging and drug delivery.^{4, 83}

1.7.2.1 Cytotoxicity

The first concern when silicon nanoparticles are used in life sciences *in vivo* is the cytotoxicity or biocompatibility. Yamamoto and coworkers have used the passively oxidized 6.5 nm silicon quantum dots which emit green light in living HeLa cell imaging, while the toxicity of silicon quantum dots was not observed at 112 $\mu\text{g mL}^{-1}$ concentration.⁸⁴ This indicates that silicon quantum dots are over ten times safer under UV exposure when compare to CdSe quantum dots. Horrocks and Datta have reported intracellular internalization and toxicity of alkyl-capped silicon nanocrystals in human neoplastic and normal primary cells.⁸⁵ The uptake of silicon nanocrystals by cells was via cholesterol-dependent endocytosis, which means the internalization of silicon nanoparticles by cells is dependent on the membrane cholesterol levels.⁸⁶ When assessed

by cell morphology, apoptosis, and cell viability assays, there was no evidence of *in vitro* cytotoxicity. Zuilhof and coworkers have systematically investigated the cytotoxicity of a broad series of surface functionalized silicon nanoparticles and demonstrated that the toxicity of silicon nanoparticles was dominated by their surface chemistry.⁸⁷ The results showed that the positively charged silicon nanoparticles displayed some toxicity, while the carboxylic acid-coated, dextran-coated and PEG-coated silicon nanoparticles displayed no toxicity in a rat lung and human colon cell lines. Thus, silicon nanoparticles are highly attractive materials for biological and medical applications given the right coating.

1.7.2.2 Bioimaging

Silicon nanoparticles are suitable for bioimaging application due to several features. First, the surface of silicon nanoparticles can be made reactive and easy to functionalize with versatile biocompatible ligands. Secondly, silicon nanoparticles are benign to cells and tissues, and wouldn't release toxic heavy metal ions.⁸⁸ Finally, silicon nanoparticles have broad tunable light emission^{31, 65, 76} with very high quantum yields which can be up to 0.6.²⁰

Many studies on the silicon nanoparticles have been done to demonstrate the excellent potential application of the modified silicon nanoparticles in bioimaging. For example, Cola and Zuilhof have prepared very stable and bright emitting amine-terminated silicon nanoparticles with different alkyl chain lengths between silicon core and amine end-group.^{49a} These functionalized silicon nanoparticles, which had ~12% emission quantum yields, were used in BV2 cells (a murine cell) imaging (Figure 1.17). These silicon nanoparticles were readily taken up by BV2 cells and appeared to relocate

to the newly formed cells indicating their good biocompatibility and minimal toxicity. Compared to the organic dye, these silicon nanoparticles are located in the cytosol and did not tend to relocate to the nuclei.^{49a}

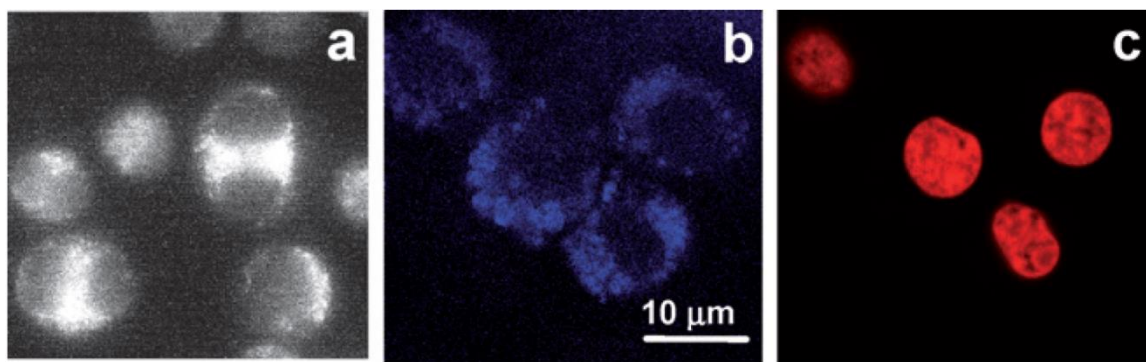


Figure 1.17 (a) Epifluorescence image of mitosis of BV2 cells stained with silicon nanoparticles under blue light irradiation, (b) and (c) Confocal image of BV2 cells simultaneously stained with silicon nanoparticles and DRAQ5.^{49a}

Swihart and coworkers have reported silicon nanoparticles encapsulated in amine-functionalized phospholipid micelles, with 50-120 nm diameters and 2-4% luminescence quantum yield, were used as luminescent labels for human pancreatic cancer cells.⁸⁹ Fan and Lee also have reported a novel kind of 25 nm oxidized silicon nanospheres, with excellent water dispersibility, high photoluminescent quantum yield and ultra photostability, were conjugated with antibody and applied in immunofluorescent cell imaging.⁹⁰ Reipa and co-workers have prepared conjugation of multiple photoluminescent silicon nanoparticles to streptavidin molecules using the multistage photoassisted procedure, which provided a convenient pathway for biomolecule labeling in biotin-streptavidin affinity based assays.⁴⁸

All of the above reports show that the silicon nanoparticles with stable luminescence, especially their antibody bioconjugates, are promising fluorescent biological probes for long-term and real-time cellular labeling.^{48-49, 89-90}

1.7.2.3 Drug delivery

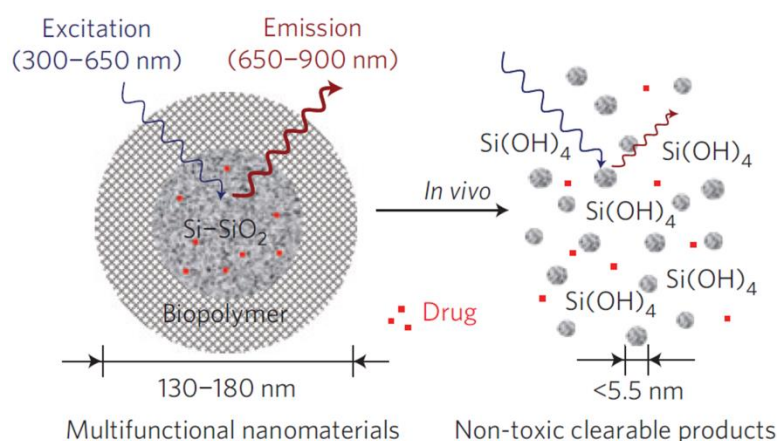


Figure 1.18 Schematic diagram depicting the structure and in vivo degradation process for the biopolymer-coated porous silicon nanoparticles.⁹¹

Nanomaterials which can circulate in the body have great potential to diagnose and treat disease.⁹² Porous silicon nanoparticles have been established as excellent candidates of drug delivery devices because of their excellent biocompatibility, biodegradability and their numerous pores which can accommodate drugs.⁹³ Sailor and coworkers have reported the 126 nm luminescent porous silicon nanoparticles with the pore size of 5-10 nm can carry a drug payload and of which the intrinsic near-infrared photoluminescence enables monitoring of both accumulation and degradation in vivo.⁹¹ The luminescent porous silicon nanoparticles can self-destruct via hydrolysis of surface silicon dioxide into orthosilicic acid Si(OH)₄ in a mouse renally, and then can be excreted from the body through urine (Figure 1.18). For *in vivo* studies, the luminescent porous silicon

nanoparticles injected intravenously were observed to accumulate mainly in mononuclear phagocytic-system related organs, and could degrade within a few days and then be removed from the body.

Vaccari and coworkers have investigated the potential applications of porous silicon as drug-carrier. The delivery of doxorubicin via porous silicon into human colon showed cytotoxic effects on the carcinoma cells.⁹⁴ Chondroitin sulphate, lactoferrin, and N-butyldeoxynojirimycin also can be delivered into tumoral cells using porous silicon nanoparticles, and shown significant effect on decreasing the tumoral cells density.⁹⁵ Recently, Brinker and coworkers have demonstrated that a single drug-loaded porous silica nanoparticle which modified with a targeting peptide can specifically bound to human hepatocellular carcinoma and killed the drug-resistant human carcinoma.⁹⁶

1.7.3 Nanocatalysis

The objective of nanocatalysis is the design of a new generation catalyst, nanocatalysts, which have strong and tunable chemical activity, specificity and selectivity.⁹⁷ Silicon nanoparticle photocatalysts with the capability to utilize visible and/or near UV light can be especially photo-stable, inexpensive and non-toxic.⁹⁷ It has been reported that porous silicon and silicon nanoparticles were good photosensitizers for singlet oxygen generation in solution.^{97c, d, 97i} Size controlled silicon nanoparticles are promising candidates as photocatalysts duo to their tunable emissions from near-infrared to blue wavelength.^{97f}

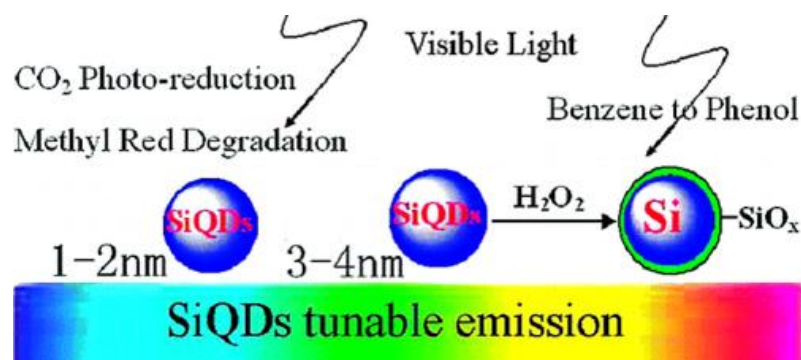


Figure 1.19 Scheme of different sizes silicon nanoparticles for different reactions.^{97g}

Kang and coworkers have used different sizes silicon nanoparticles as photocatalysts for specific reactions.^{97g} For example, the 1-2 nm silicon nanoparticles were excellent photocatalysts for reducing CO₂ to formaldehyde (CH₂O) and formic acid (HCOOH), and the degradation of methyl red, while the 3-4 nm silicon nanoparticles could selectively photocatalyzed the hydroxylation of benzene by H₂O₂ (Figure 1.19). The photocatalysis capabilities of silicon nanoparticles are due to their tunable band gap and excellent photoconductivity properties.

1.7.4 Application to Li-ion batteries

One of the attractive alternatives for increasing the specific energy and energy density of the lithium ion battery is to replace the standard graphite electrodes by silicon-based negative electrodes due to their larger volumetric and gravimetric capacities (2190 mAh cm⁻³ and 3580 mAh g⁻¹, respectively for silicon versus 830 mAh cm⁻³ and 372 mAhg⁻¹ for graphite).⁹⁸ However, silicon still suffers from huge volume changes (>300%) and low intrinsic electrical conductivity during lithium uptake and release from silicon, which seriously hindered the practical application of silicon as an anode material in lithium ion battery.⁹⁹ One pertinent way to overcome these disadvantages and improve

the overall electrochemical performance of silicon anodes is to use a mixture of carbon additives, binders and silicon nanoparticles. These additives can not only restrict the large volume change of silicon to keep the electrode stable, but also enhance the electrical conductivity of the electrode.¹⁰⁰ For example, Zhou et al. have successfully prepared silicon nanocomposites by inserting the silicon nanoparticles into graphene sheets via a novel method combining freeze-drying and thermal reduction (Figure 1.20).^{100b} The obtained silicon nanocomposites exhibit improved cycling performance (ca. 1153 mAh g⁻¹ after 100 cycles) and rate performance in comparison with bare silicon nanoparticles.

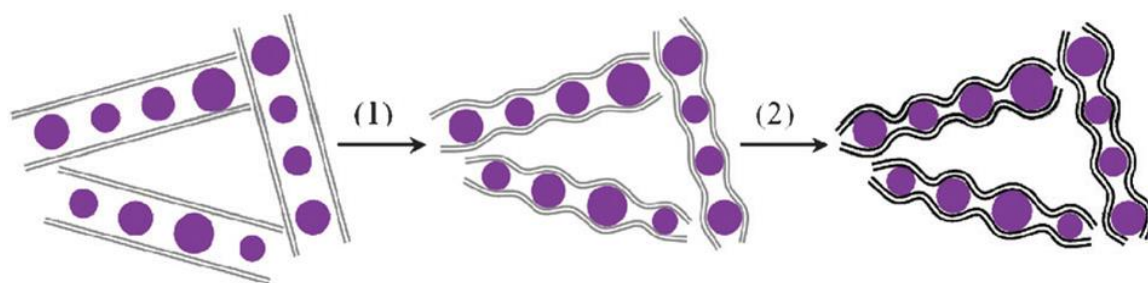


Figure 1.20 Schematic the illustration of the synthesis route for silicon nanoparticles inserted into graphene. Grey lines (graphene oxide), black lines (thermally reduced grapheme), and purple balls (silicon nanoparticles). (1) Freeze-drying, and (2) thermal reduction.^{100b}

Martin et al. have prepared multi-walled carbon nanotube/silicon nanoparticle hybrid nanocomposites as silicon negative electrodes for lithium ion batteries.^{100a} The covalent bonding of the carbon nanotube and silicon nanoparticle was obtained via a phenyl bridge (Figure 1.21). In this system, the carbon nanotube is close enough to the silicon nanoparticle which can enhance the electronic pathway to the active material particles and prevent the large volume change of silicon. The as-achieved

nanocomposites lead to the enhancement of cycling ability and capacity of the battery compared to a simple mixture of the two compounds.

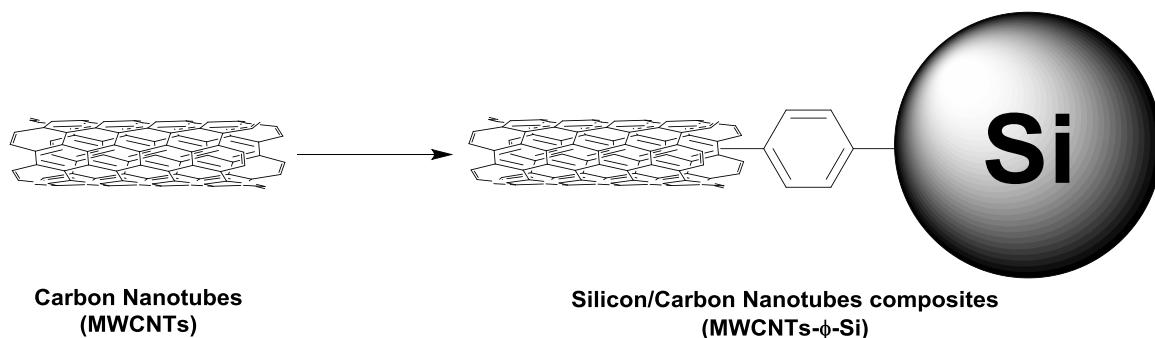


Figure 1.21 Development of silicon/carbon nanotube nanocomposites via a phenyl bridge.^{100a}

1.8 Motivation and summary

In summary, this thesis has the primary aim to investigate the surface structure, optical properties and size distribution of the passivated silicon nanoparticles produced by reactive high energy ball milling (RHEBM), and to probe and enhance their potential application in the fields of light harvesting and drug delivery by functionalizing with organic photosensitizers and water soluble polymers.

RHEBM has the advantage of producing high yields of passivated silicon nanoparticles with polydisperse size distribution in a one-step procedure.⁴¹ Various functionalized alkynes and alkenes, such as mono-alkyne, bis-alkyne, halo-alkyne or halo-alkene, can be used as the surface passivation ligands for ball milling with silicon wafer to obtain alkyl/alkenyl-passivated silicon nanoparticles with different terminal groups. The mono-alkynes are simply used as surface passivation ligands while the bi-functional organic ligands are used as coreactants to form terminated functional groups

for further functionalization. The passivated silicon nanoparticles with terminal alkyne groups or halogen groups (which can be easily converted to azide groups) can be further modified with specific functional ligands via “click” reactions to increase their water solubility or enhance their application as light harvesting materials and drug delivery carriers.

Chapter 2 of this thesis presents the mechanochemical synthesis of various passivated silicon nanoparticles based on the method developed by Heintz.^{41b} The surface structure and optical properties of the passivated silicon nanoparticles were systematically characterized and discussed. The methods of purification and size separation of those silicon nanoparticles with polydisperse size distribution using a gravity GPC column were presented. The size determination of the separated silicon nanoparticles using GPC and DOSY-NMR analysis were discussed.

Chapter 3 illustrates the synthesis of PEGylated water soluble silicon nanoparticles via a Huisgen 2+3 alkyne-azide “click” reaction between appropriately functionalized silicon nanoparticles and PEG polymers. The PEGylated silicon nanoparticles have strong emission in water, and their biocompatibility and non-cytotoxicity has promising biological application. Additionally, the synthesis of flexible globular PEGylated silicon nanoparticle arrays with strong covalent bonding, stable uniform 3D structure, tunable spacer between particles and strong PL emission were also discussed.

In Chapter 4, silicon nanoparticles were used as nanoscaffolds for organizing the porphyrins to form light-harvesting complexes thereby enhancing the light absorption of the system. The energy transfer from silicon nanoparticles to porphyrin acceptors was

investigated by both steady-state and time-resolved fluorescence spectroscopy. The energy transfer efficiency depended on the donor-acceptor ratio and the distance between the nanoparticle and the porphyrin ring. In addition, silicon nanoparticle-porphyrin-fullerene nanocluster was obtained via self-assembly based on the π - π interaction between the porphyrin and fullerene upon adding C₆₀. The formation of nanoclusters resulted in charge separation by irradiating the porphyrin ring. The electron-transfer process between porphyrin and fullerene was investigated by femto-second transient absorption spectroscopy.

Chapter 5 describes the synthesis, characterization, photochemical properties, and photodynamic therapeutic applications of water soluble porphyrin grafted silicon nanoparticles. Silicon nanoparticles were used as nanocarriers for delivery of porphyrin drugs into human embryonic kidney 293T (HEK293T) cells. The nanoparticle is capable of producing singlet oxygen when the porphyrin units are excited by light. The cell studies demonstrated that the silicon nanoparticle can deliver the porphyrin drugs into HEK293T cells and accumulate in the mitochondria where the porphyrin could serve as an efficient photosensitizer to kill the cells via mitochondrial apoptotic pathway.

Chapter 6 describes the investigation of various approaches to produce water soluble silicon nanoparticles via functionalization of the nanoparticle surface with water soluble ligands, and to obtain silicon nanoparticle arrays via “host-guest” self-assembly which rely on the interaction between β -cyclodextrin and adamantane.

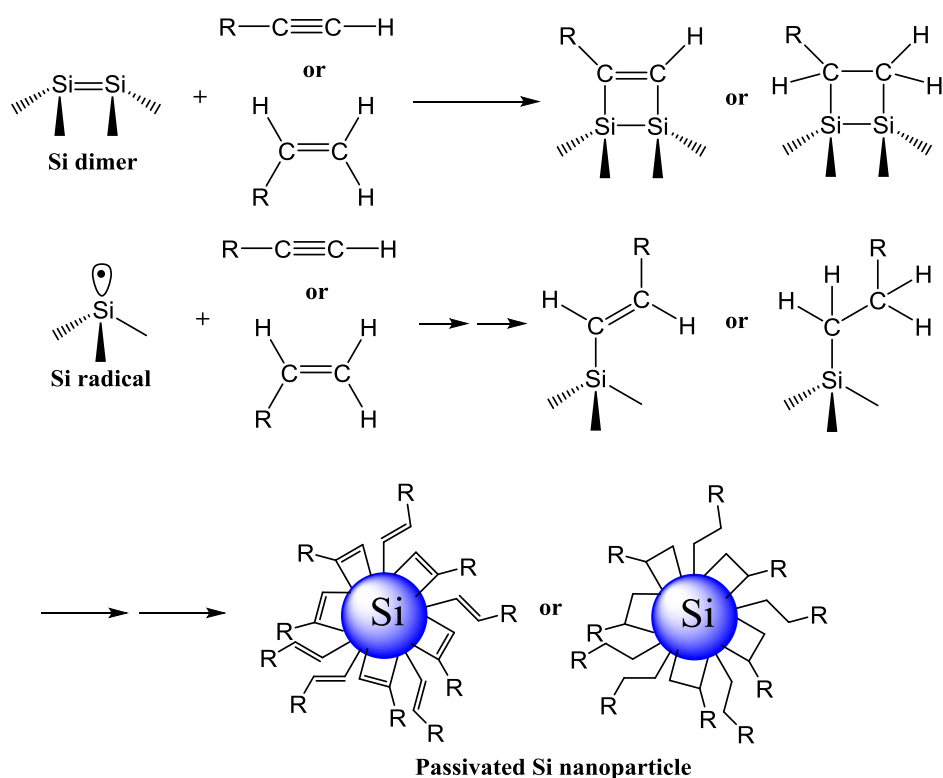
In all cases, the primary work was carried out by the candidate under the guidance of the advisor Prof. Mark J Fink at the Department of Chemistry (Tulane University), and

the co-advisor Prof. Brian S Mitchell at the Department of Chemical and Biomolecular Engineering (Tulane University), and collaborations with other research groups were also critical. In this regard, the author acknowledges the fruitful collaboration with Prof. Janarthanan Jayawickramarajah's group (and Dr. Nan Zhang, Hong Zhang in particular) at the Department of Chemistry (Tulane University), especially for providing the precursor functionalized porphyrins. The author also acknowledges the collaboration with Prof. Scott Grayson's group (and Dr. Yejia Li, Boyu Zhang in particular) at the Department of Chemistry (Tulane University), especially for providing the precursor functionalized PEG polymers. The author also thanks Prof. Benjamin Hall's group (Fading Chen in particular) at the Department of Cell and Molecular Biology (Tulane University) for conducting the relevant cell studies.

Chapter 2: Mechanochemical Synthesis and Size Distribution of Passivated Silicon Nanoparticles

2.1 Introduction

A significant number of studies of functionalized silicon nanoparticles have been reported in the last two decades. Silicon nanoparticles have been prepared by a variety of methods, including electrochemical or chemical etching of bulk silicon³⁷⁻³⁸, oxidation of metal silicides²⁸⁻²⁹, reduction of halosilanes with alkali naphthalide or Zintl salts,^{22b, 23} and thermal decomposition of silanes^{18, 21, 30, 101}. However, all of these pathways are challenging as they require either use of highly reactive or corrosive chemicals, or require further modification of unstable hydrogen or halogen terminated surfaces. The mechanochemical synthesis of passivated silicon nanoparticles via Reactive High Energy Ball Milling (RHEBM), first reported by Heintz et. al in 2007, provides an efficient and simple pathway to produce alkylated silicon nanoparticles.^{41b, c, 102} The alkyl/alkenyl-passivated silicon nanoparticles are obtained via ball milling with a reactive alkene or alkyne, and silicon wafer under nitrogen atmosphere. During the RHEBM, the mechanical energy causes the silicon wafer to fracture and creates a highly reactive silicon surface which contains silicon-silicon double bonds and silicon surface radicals. The fresh silicon surface reacts with alkynes or alkenes resulting in a covalent Si-C bond and finally resulting in a passivated organic surface on the silicon nanoparticle (Scheme 2.1). Hence, various alkynes and alkenes can be used as surface passivation ligands for ball milling with silicon wafer to obtain alkyl/alkenyl-passivated silicon nanoparticles with different terminal groups.



Scheme 2.1 Possible bonding modes of passivated silicon surface with alkyne or alkene, and the representation of the alkyl/alkenyl-passivated silicon nanoparticles with different bonding modes.

Silicon nanoparticles are promising candidates in various applications due to their size dependent electronic and optical properties.⁷⁵ This often requires precise control over the sizes and size distributions of the silicon nanoparticles. However, one weakness of the mechanochemical synthesis approach of silicon nanoparticles, as with any top-down approach, is the polydispersity of the nanoparticle size. Size separation is often achieved in the post processing stage using technique such as gel permeation chromatography (GPC). GPC has been used to separate nanoparticles based on their size (i.e. hydrodynamic volume) with the larger nanoparticles eluting first and the smaller nanoparticles eluting later. For example, Lu et al. have used a gravity GPC column to

separate the PEGylated gold nanoparticles based on the grafting density of the PEG and the core size of the nanoparticles.⁷¹ We have developed a simple and fast process to separate and purify passivated silicon nanoparticles using a gravity GPC column with Bio-beads S-X1 beads as a stationary phase.

The size of nanoparticles is principally characterized by TEM. However, obtaining TEM images and subsequent extraction of the size information of silicon nanoparticles is challenging due to the relatively low contrast of silicon in the electron beam. Furthermore, it is almost impossible to get TEM images of nanoparticles with size of less than 1 nm. Even obtaining high-quality TEM images of nanoparticles smaller than 2 nm is difficult.¹⁰³ Additionally, TEM images usually only show the core size of silicon nanoparticles because of the organic layers on the surface are either indiscernible by TEM due to insufficient contrast, or have been burned off by the electron beam. Other size determination methods, which can measure the full size of particles, such as dynamic light scattering (DLS), are nearly impossible to accurately determine the small size nanoparticles less than 5 nm.¹⁰⁴ Hence, fast and simple alternatives for determining the full size of silicon nanoparticles are desirable.

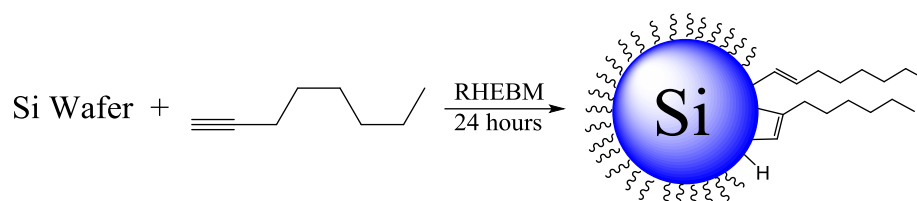
In this chapter, two reliable approaches for determining the size of silicon nanoparticles using gel permeation chromatography (GPC) analysis and diffusion-ordered NMR spectroscopy (DOSY) will be presented. GPC is a type of size-exclusion chromatography (SEC), which is usually used to determine the relative molecular weight and molecular weight distribution of polymers. Using a series of polymers with known hydrodynamic volume as standards, GPC analysis can be used to estimate the hydrodynamic volume of silicon nanoparticles and finally obtain the hydrodynamic

diameter of those nanoparticles. DOSY-NMR was recently used as a reliable alternative to TEM for determining the size of gold nanoparticles in organic solutions.⁷²⁻⁷⁴ 2D DOSY-NMR can be used to calculate the diffusion constants, which is based on the hydrodynamic volume, of the solubilized nanoparticles. By comparing with the diffusion constants of an internal standard with known size, the size of the nanoparticles can be obtained.⁷³ However, no study on GPC or DOSY-NMR applied to the determination of the size of silicon nanoparticles has been reported so far. Therefore, GPC and DOSY-NMR were performed on a series of size-separated silicon nanoparticles with various surface ligands to emphasize and validate the applicability of these techniques.

2.2 Results and Discussion

2.2.1 Octenyl-passivated silicon nanoparticles

Octenyl-passivated silicon nanoparticles were synthesized via the method developed by Heintz,^{41b} as a simple system for studying the passivated surface structure and optical properties of silicon nanoparticles produced by RHEBM (Scheme 2.2).



Scheme 2.2 Synthesis of silicon nanoparticles passivated by 1-octyne using RHEBM

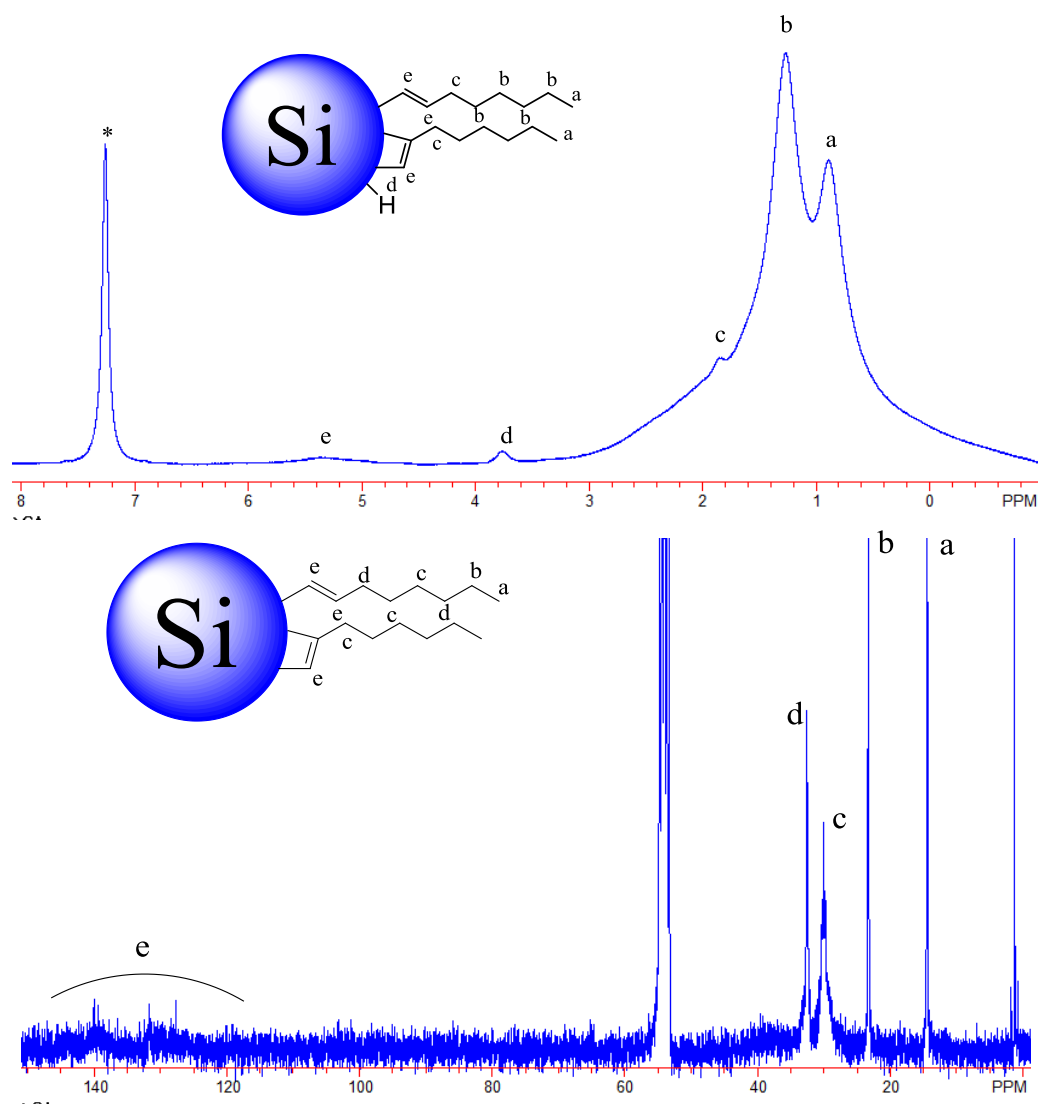
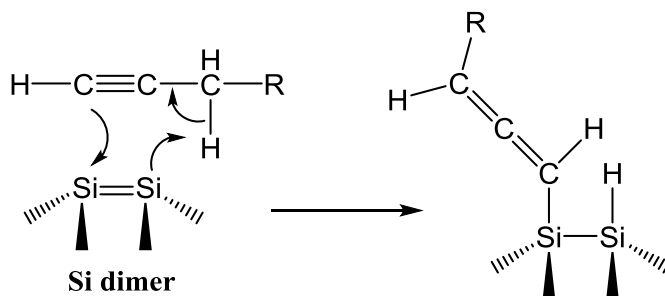


Figure 2.1 300 MHz ^1H -NMR (top) and ^{13}C -NMR (down) spectra of the octenyl-passivated silicon nanoparticles

The octenyl-passivated silicon nanoparticles were first characterized by NMR spectroscopy to determine the surface structure of the silicon nanoparticles. As shown in Figure 2.1, the ^1H -NMR spectrum shows a broad intense peak around 0-1 ppm which indicates the protons in the terminal $-\text{CH}_3$ groups, while the broad peak at 1.1 ppm shows the protons in the $-\text{CH}_2$ groups on the alkyl chain. Resonances at 1.8 ppm and 5.4 ppm

are assigned to the $\text{CH}_2\text{-C=C}$ and H-C=C respectively. Moreover, the peak at 3.8 ppm demonstrates the Si-H passivated surface on the nanoparticle which may be due to the reactive silicon radical abstracting a hydrogen from a surrounding organic ligand, or the result of an “ene” reaction involving a silicon-silicon double bond and the alkyne (Scheme 2.3)¹⁰⁵ in the ball milling process. Correspondingly, in the ^{13}C -NMR spectrum, there are the intense peaks at 14 ppm, 23 ppm, 30 ppm, 33 ppm and the weak peaks in the 120-140 ppm range due to the octenyl passivation.



Scheme 2.3 Possible mechanism of forming “ene” structure during RHEBM

More evidence for the existence of an octenyl-passivated surface on the silicon nanoparticle was obtained by the Fourier transform infrared (FTIR) spectrum shown in Figure 2.2. The strong band in the $2800\text{-}3020\text{ cm}^{-1}$ range indicates the C-H stretching vibration, while the peaks at 1466 cm^{-1} and 1376 cm^{-1} demonstrate the C-H bending vibration. The two peaks around 1597 cm^{-1} and 1690 cm^{-1} are due to the C=C stretching vibration. The Si-C-H and Si-C vibration peaks at 1250 cm^{-1} and 840 cm^{-1} indicate the 1-octyne passivated to the silicon nanoparticle surface. Furthermore, the broad peak at $980\text{-}1130\text{ cm}^{-1}$ due to the Si-O stretch shows the oxygen passivated surface on the nanoparticle,¹⁰⁶ while the Si-H stretching peak at 2120 cm^{-1} correlates with the ~ 3.8 ppm peak in the ^1H -NMR spectrum. The Si-O species are primarily attributed from the silicon

dioxide on the silicon wafer, but also may due to the oxidation reaction of the reactive silicon surface with a trace amount of water in the milling medium.¹⁰⁷

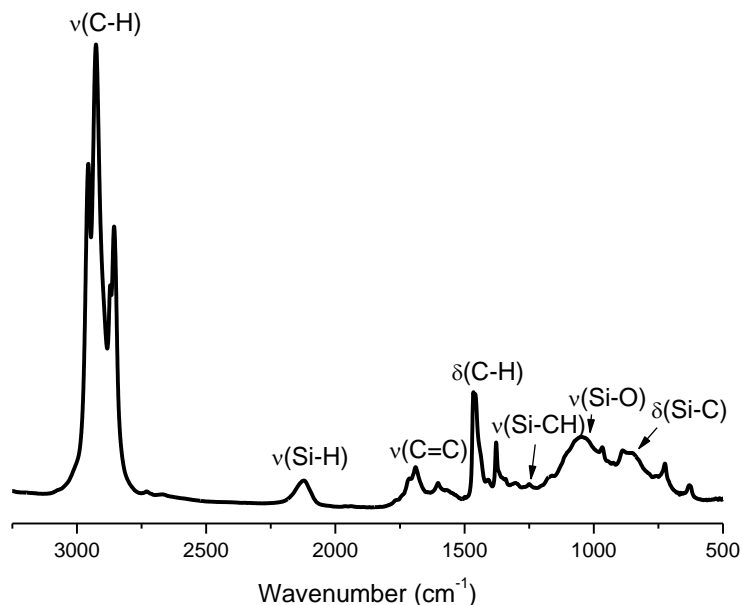


Figure 2.2 FTIR spectrum of octenyl-passivated silicon nanoparticles.

The particle size distribution of the octenyl-passivated silicon nanoparticles was obtained by TEM (Figure 2.3 a). The TEM image of the crude silicon nanoparticles shows the broad size distribution ranging from 1 to 10 nm, as well as some aggregation of the bigger particles. It was from the size distribution that most of the nanoparticles are smaller than 5 nm. The TEM image also shows that the shape of some larger nanoparticles was non-spherical, which might due to strain induced in those particles during high energy ball-milling.¹⁰⁸ Energy dispersive X-ray spectroscopy (EDS) (Figure 2.3 c) of the nanoparticles exhibits a pronounced peak at 1.8 KeV (for $\text{SiK}\alpha$) which confirms silicon in the nanoparticles. The copper peaks which appear in the EDS spectrum are from the Cu grid.

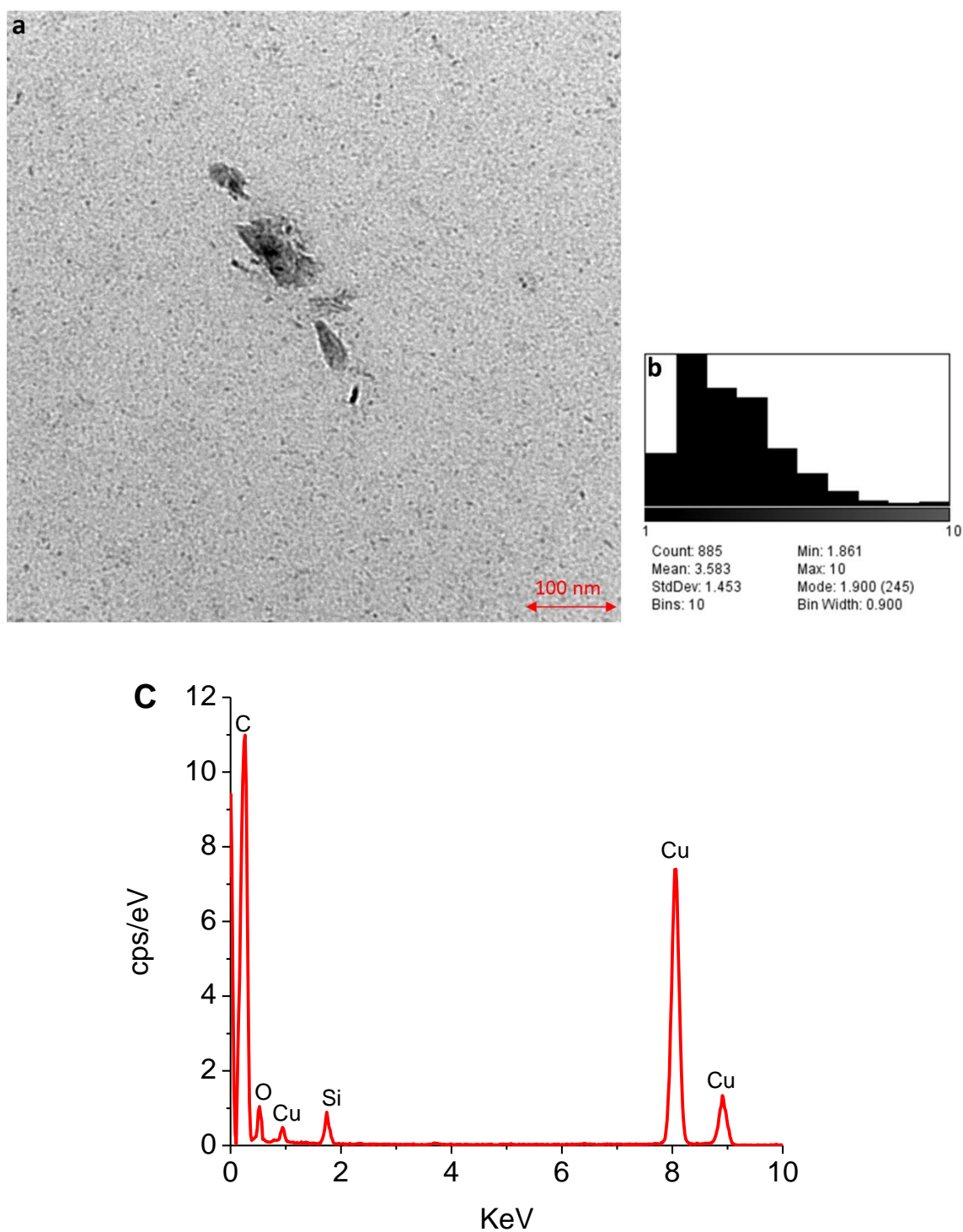


Figure 2.3 (a) TEM image of crude octenyl-passivated silicon nanoparticles, (b) the corresponding particle size distribution histograms, and (c) the energy-dispersive X-ray spectra (EDS).

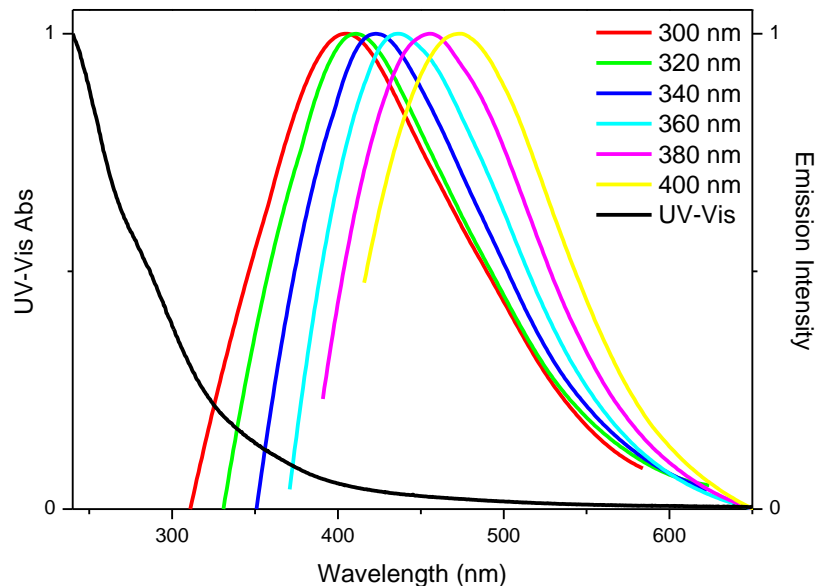


Figure 2.4 UV-Vis absorption spectrum and PL emission spectra at various excitation wavelengths of octenyl-passivated silicon nanoparticles.

The octenyl-passivated silicon nanoparticles show a broad, continuous UV-Vis absorption tailing at around 600 nm (Figure 2.4). The PL emission spectra of the silicon nanoparticles, recorded with various excitation wavelengths ranging from 300 to 400 nm in CH_2Cl_2 , show a strong broad emission in the range of 300 to 650 nm. The strong blue photoluminescence can be either from the decay of quantum confinement excitations or can be attributed to the surface defect state.^{2, 8-10, 13} With increasing the excitation wavelength, the PL emission maxima were found to shift to longer wavelength, which may due to only larger nanoparticles were excited under longer excitation wavelength. Furthermore, the broadness of the emission spectra is consistent with the polydispersity of the silicon nanoparticles.

2.2.2 Size separation and purification of silicon nanoparticles using GPC column

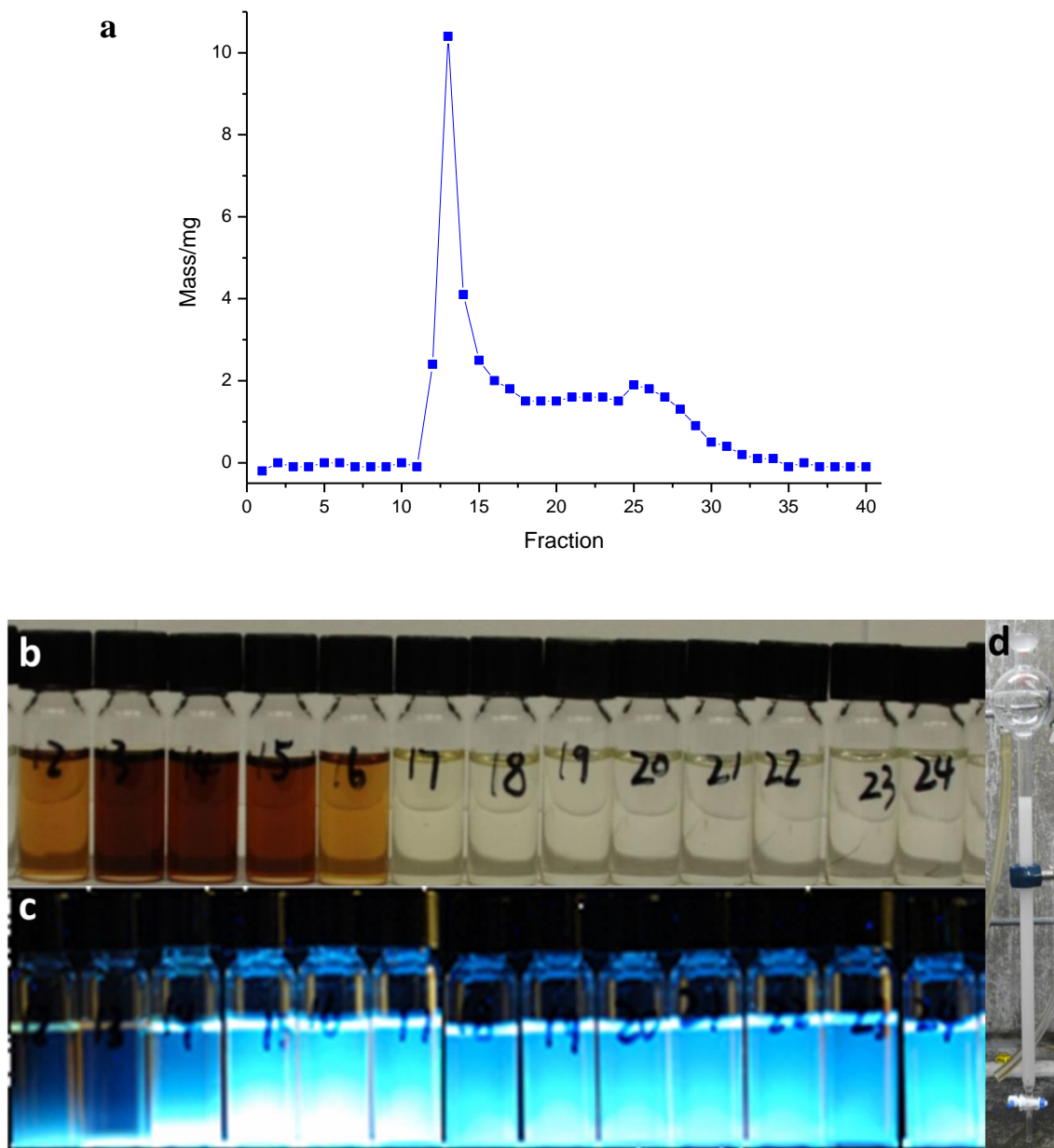


Figure 2.5 Weight distribution of various GPC separated fractions (a), GPC separated various fractions (b) and the Emission of various fractions excited under UV lamp (c) of octenyl-passivated silicon nanoparticles, and the gravity GPC column used to fractionate silicon nanoparticles (d).

Verdoni et al. have reported that alkenyl-passivated silicon nanoparticles produced by RHEBM could be separated based on the surface polarity using a silica gel column.¹⁰⁹ The result indicated that retained portions of alkenyl-passivated silicon nanoparticles possessed an increase in polar species on the surface, compared to eluted fractions which display more alkyl bound species.

In this study, gel permeation chromatography (GPC) column were used to separate the passivated silicon nanoparticles based on their size. A gravity GPC column using Bio-beads S-X1 beads as a stationary phase was used to fractionate the octenyl-passivated silicon nanoparticles (Figure 2.5d). During the separation by GPC, larger size nanoparticles pass through the column faster than the smaller size nanoparticles. Methylene chloride was used as an elution solvent. Fractions were collected in 1.5 ml increments in separate vials for further characterization (Figure 2.5b). The first fraction was collected when the silicon nanoparticle sample was added into the GPC column, and the 12th fraction was found to be the first fraction (**F1**) which contains silicon nanoparticles (Figure 2.5a). All the fractions that contain silicon nanoparticles show bright blue emission under UV lamp (Figure 2.5c). Most of the silicon nanoparticles were contained in the first four fractions (12th fraction to 15th fraction). Molecular impurities were also separated out from the nanoparticle solution and appeared in the later fractions (after 25th fraction) (Figure 2.5 a). Those molecular impurities were generated by the cyclotrimerization of the reactive alkynes, which might be catalyzed by the iron compound inside the ball milling system.¹¹⁰

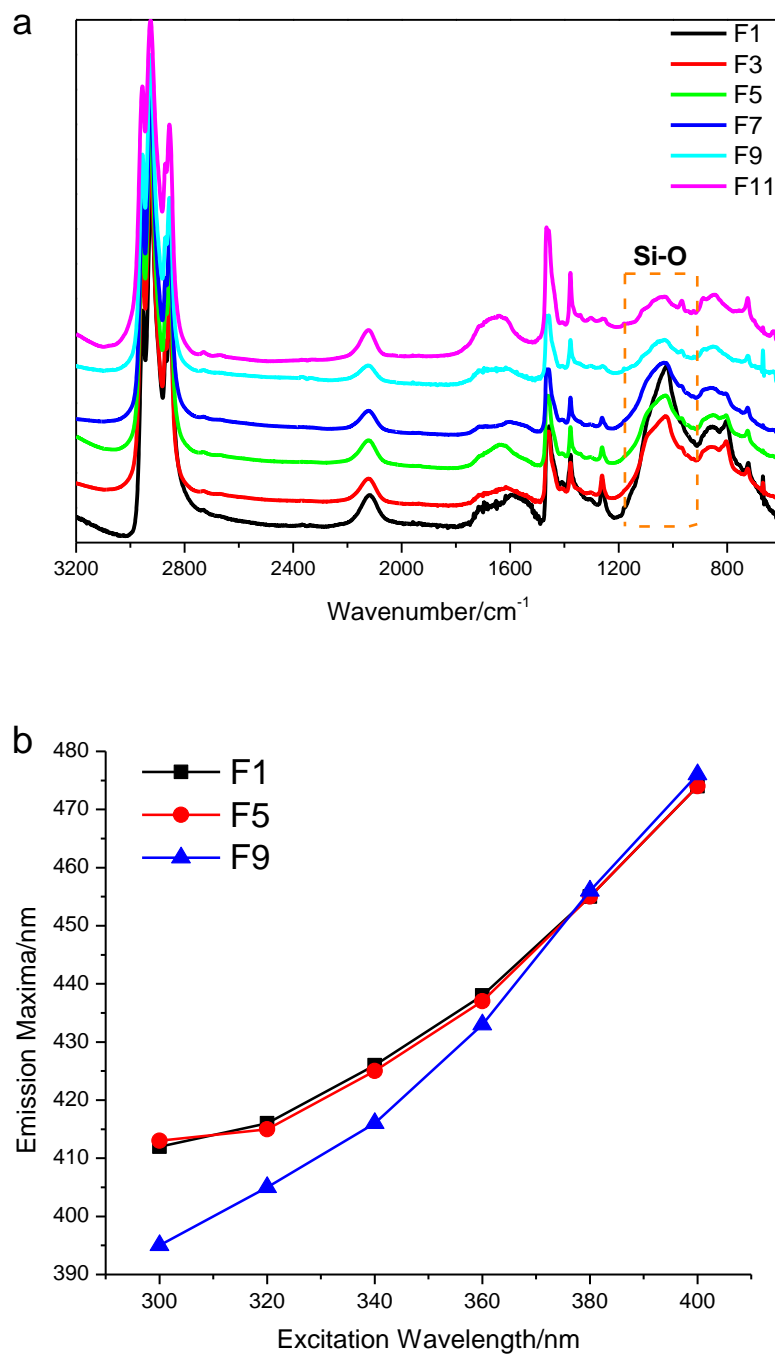


Figure 2.6 a) FTIR spectra of various separated fractions of octenyl-passivated silicon nanoparticles; b) Emission maxima vs excitation wavelength of various separated fractions of octenyl-passivated silicon nanoparticles.

The separated fractions of octenyl-passivated silicon nanoparticles were first characterized by FTIR. The FTIR spectra show the relative intensity of Si-O stretching peaks decrease with the size of nanoparticles (Figure 2.6a), which indicates that there is more oxygen passivated surface on the large size nanoparticles. All the fractions of separated silicon nanoparticles show similar PL emission as the unseparated silicon nanoparticles. For each fraction, the PL emission maxima were shifted to longer wavelength with increasing the excitation wavelength (Figure 2.6b). Comparing the PL emission of F1 and F9 of the separated silicon nanoparticles, the emission maxima of F9 (excited under 300-360 nm) showed blue shift, which due to the decreasing of the nanoparticle size. However, the emission maxima of F9 excited under 380-400 nm didn't show any blue shift. The reason is still unknown, but may be related to the surface-state of the silicon nanoparticles. Furthermore, the F5 of separated silicon nanoparticles showed almost the same PL emission as the F1 of separated silicon nanoparticles, and the PL emission maxima were found to be no blue shift. This is because the PL emission of silicon nanoparticles is not only dependent on the particle size, but also dependent on the surface-state. It has been reported that the oxide surface would cause the blue shift of the PL emission of silicon nanoparticles.¹¹¹ Since the F1 of separated silicon nanoparticles has more oxide surface than that of the F5 of separated silicon nanoparticles (Figure 2.6a), the PL emission maxima of the F1 of separated silicon nanoparticles may have more blue shift which results in the similar PL emission maxima as the F5 of separated silicon nanoparticles.

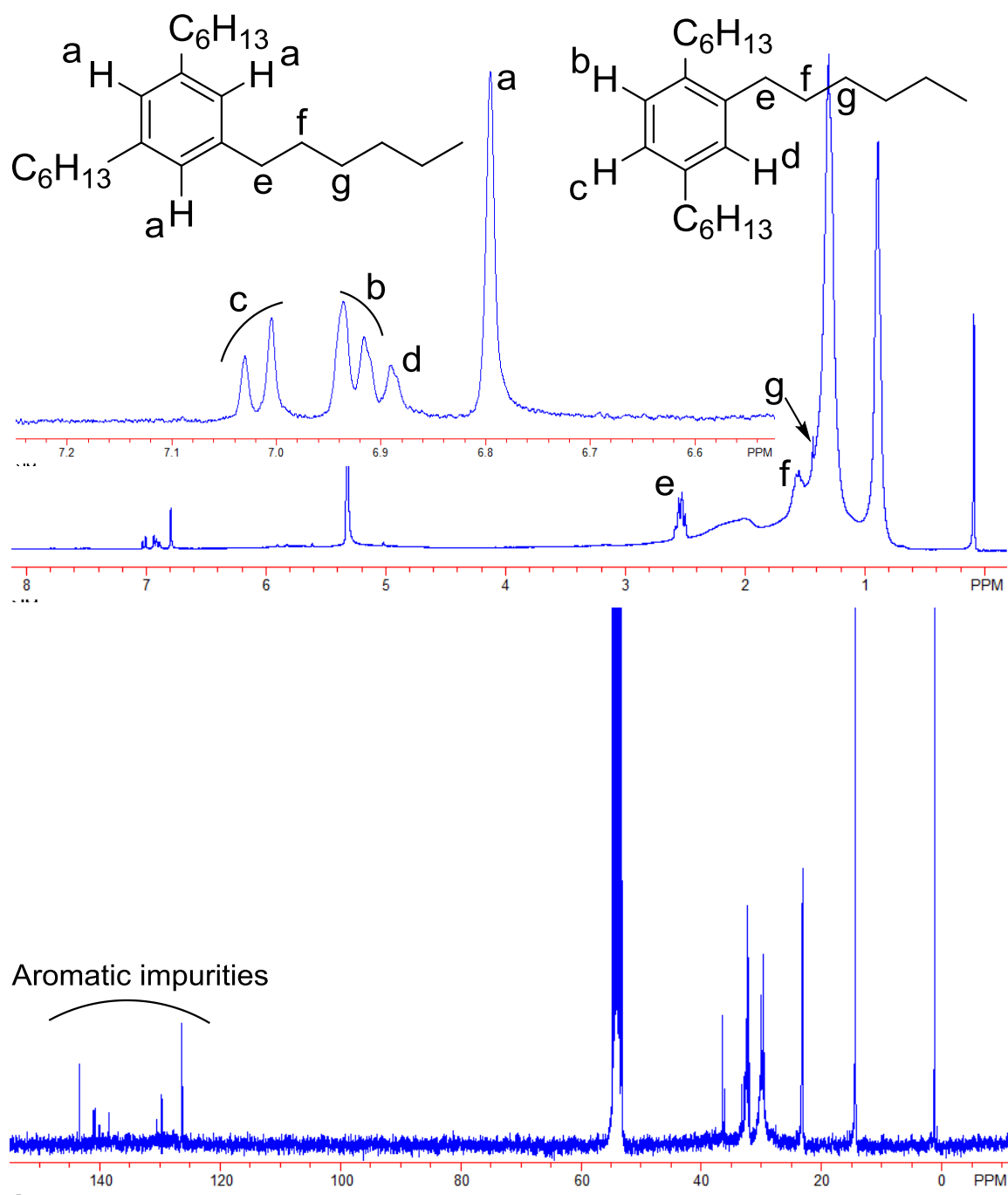


Figure 2.7 ^1H -NMR (top) and ^{13}C -NMR (down) spectra of octenyl-passivated silicon nanoparticles which contains aromatic impurities

The presence of aromatic impurities in the nanoparticle sample was first observed from the ^1H -NMR and ^{13}C -NMR spectra of the crude octenyl-passivated silicon

nanoparticles (Figure 2.7). GC-MS studies (Figure 2.8) of the later GPC fractions confirmed the identity of the aromatic impurities as 1, 2, 4-trihexylbenzene and 1, 3, 5-trihexylbenzene. The two geometrical isomers were generated from the cyclotrimerization of 1-octyne with the ratio of 3:2. Together, the isomers comprise about 10% the mass of the total crude nanoparticles. Moreover, the molecular impurities eluted at the end of the separation, which indicates that GPC can be used for the purification of silicon nanoparticles from molecular impurities.

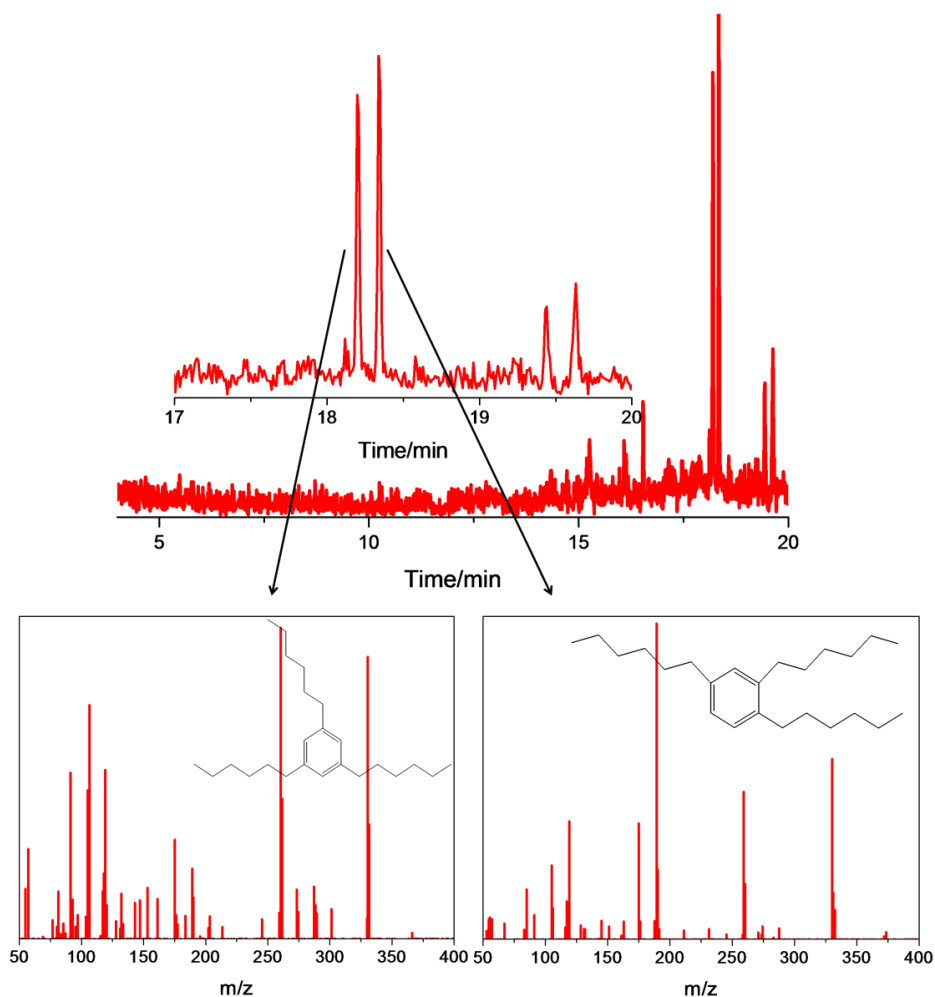


Figure 2.8 GC-MS spectra of 30th fraction of octenyl-passivated silicon nanoparticles which contains mostly aromatic impurities

Figure 2.9a shows the TEM images of an earlier fraction (i.e. fraction 3) of octenyl-passivated silicon nanoparticles after separation by a gravity GPC column. The TEM image shows the spherical particles with the average diameter of 3.5 ± 0.9 nm, and the size distribution is much narrower than that of the crude silicon nanoparticles.

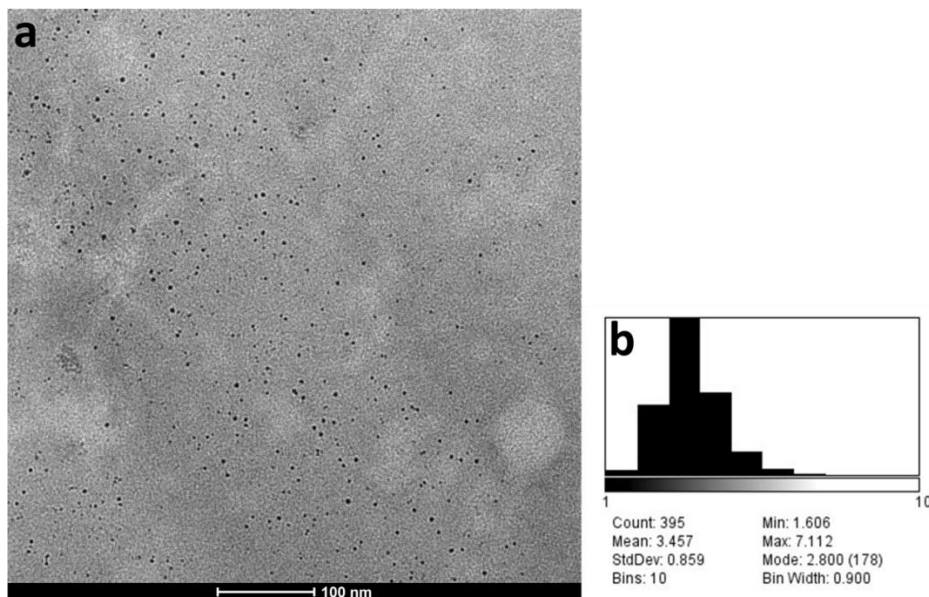


Figure 2.9 (a) TEM image of Fraction 3 octenyl-passivated silicon nanoparticles, (b) the corresponding particle size distribution histograms

2.2.3 Size determination of separated silicon nanoparticles using GPC analysis

GPC analysis was first performed to confirm the size separation of silicon nanoparticles by the gravity GPC column, as well as to characterize the size distribution of the separated silicon nanoparticles. The GPC analysis, using refractive index (RI) detector, of various separated fractions of octenyl-passivated silicon nanoparticles in THF clearly confirms the size separation and roughly shows the size distribution of each of the separated fractions (Figure 2.10). The elution volume of fraction 1 to fraction 11 increases from 7.1 ml to 8.2 ml indicating the decreasing size of the separated silicon nanoparticles.

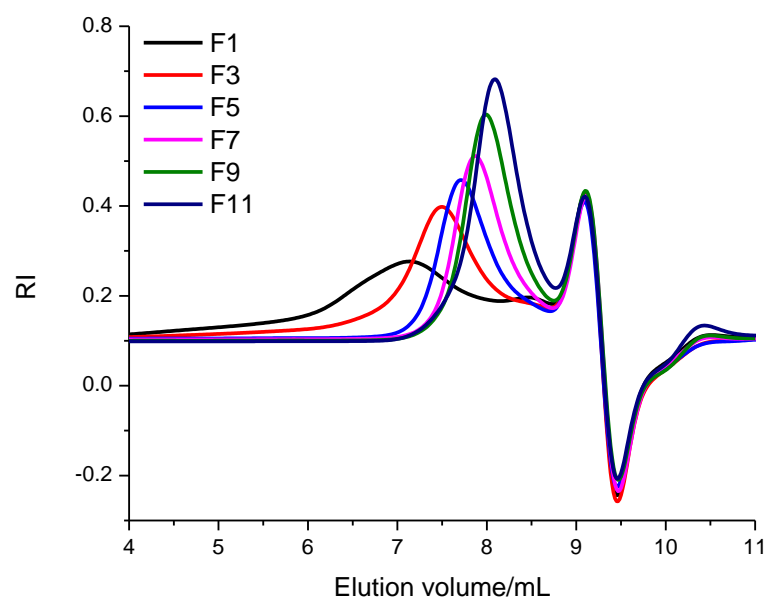


Figure 2.10 Separated fractions of octenyl-passivated silicon nanoparticles analyzed by GPC

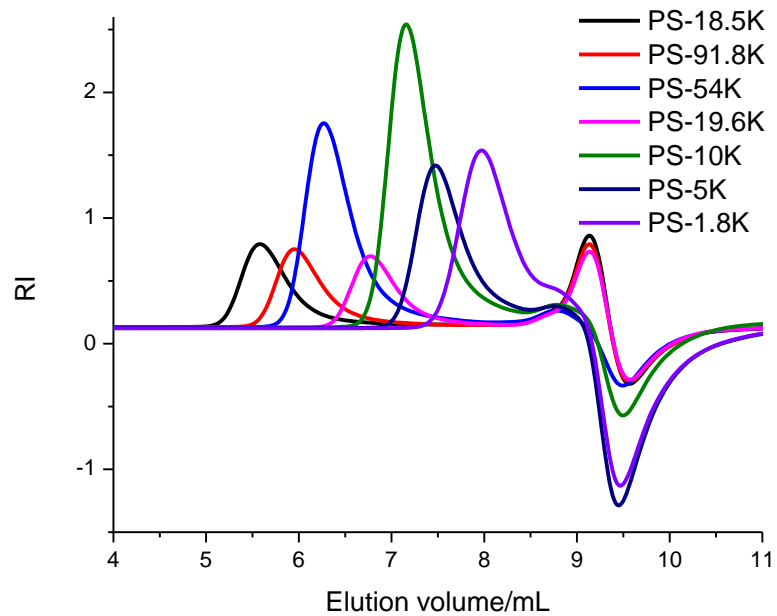


Figure 2.11 GPC of various molecular weight polystyrene standards

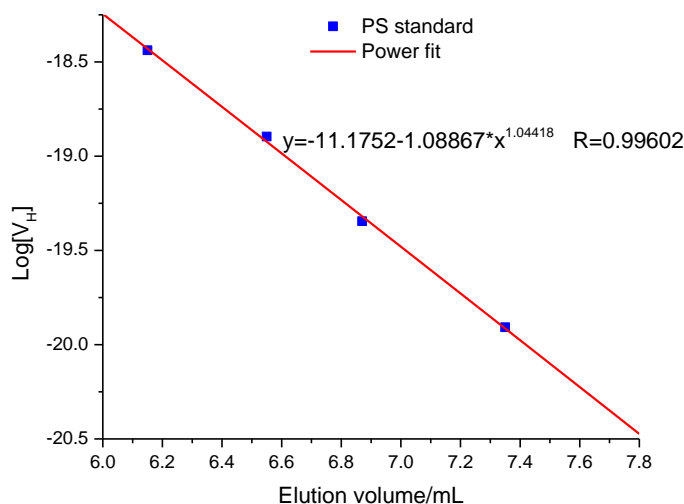


Figure 2.12 The hydrodynamic volume vs. elution volume for polystyrene standards.

GPC systems with multiple detectors (UV, RI, viscosity and multi-angle dynamic light scattering detectors) are usually used to characterize the molecular weight and molecular weight distribution of polymer samples based on their hydrodynamic volumes. However, the absolute sizes of the silicon nanoparticles cannot be directly obtained from the GPC analysis due to the limitation of the detectors. The viscosity of the silicon nanoparticles solution is too low to be monitored by the viscosity detector, while the hydrodynamic volume of the silicon nanoparticle reaches the lower limit of the multi-angle dynamic light scattering detector. Therefore, a series of standards with known hydrodynamic volume are required in order to find out the relationship between the hydrodynamic volume and elution time of the GPC analysis, and subsequently calculate the size of the silicon nanoparticles based on the principle that samples with same hydrodynamic volume elute at the same volume from the same GPC column.

Consequently, a series of polystyrene standards with known hydrodynamic volume were used to estimate the hydrodynamic volume of the silicon nanoparticles. The elution

volumes of the polystyrene standards were obtained using the same GPC system with the same column (Figure 2.11). A power-law relationship was established between hydrodynamic volume and elution volume in this GPC system (Figure 2.12). Then the hydrodynamic volume of the separated silicon nanoparticles can be calculated based on their elution volumes using Equation 1,

$$\text{Log}[V_H] = -11.1752 - 1.08867 \times V_E^{1.04418} \quad (1)$$

where V_H is the hydrodynamic volume and V_E is the elution volume. Therefore, the hydrodynamic diameter of the separated silicon nanoparticles can be obtained using Equation 2,

$$r_H = [3 \times V_H / (4\pi)]^{1/3} \quad (2)$$

where r_H is the hydrodynamic radius, and the results are shown on the Table 2.1. As can be seen, the hydrodynamic diameter of the separated octenyl-passivated silicon nanoparticles decreases from 6.1 nm to 2.5 nm from fraction 1 to fraction 11. This shows that the size separation of silicon nanoparticles is accomplished by gravity GPC and demonstrates that the GPC analysis can be a fast, simple and reliable approach for obtaining the size of ultra-small nanoparticles with appropriate standards.

Table 2.1 Hydrodynamic diameter of separated octenyl-passivated silicon nanoparticles from GPC analysis

Fraction	1	3	5	7	9	11
Diameter/nm	6.1±2.8	4.3±2.1	3.5±1.5	3.0±1.3	2.7±1.2	2.5±1.1

2.2.4 Size determination of separated silicon nanoparticles using DOSY-NMR

An alternative for characterizing the hydrodynamic volume of silicon nanoparticles is by directly measuring the diffusion coefficient of the nanoparticle obtained from 2D DOSY-NMR. DOSY is a NMR technique based on pulsed field gradient spin or stimulated echo measurements, in which the measured signal intensity depends on time, diffusion coefficient, and gradient amplitude.¹¹² If the measurements were made with a range of gradient strengths, the diffusion coefficients of different signals can be determined based on signal intensity. The diffusion coefficient is related to the size and shape of individual species followed the commonly known Stokes-Einstein equation.¹¹³

$$D = \frac{k_b T}{c \pi \eta r_H} \quad (3)$$

where k_b is the Boltzmann constant; T is the temperature reported in Kelvin; c is a parameter that approaches 6 as the hydrodynamic radius reaches 1 nm;¹¹⁴ η is viscosity of the solvent used; and r_H is the hydrodynamic radius. The hydrodynamic radius of the silicon nanoparticles can be obtained using the Stokes-Einstein equation based on the assumption that all the species are spherical.

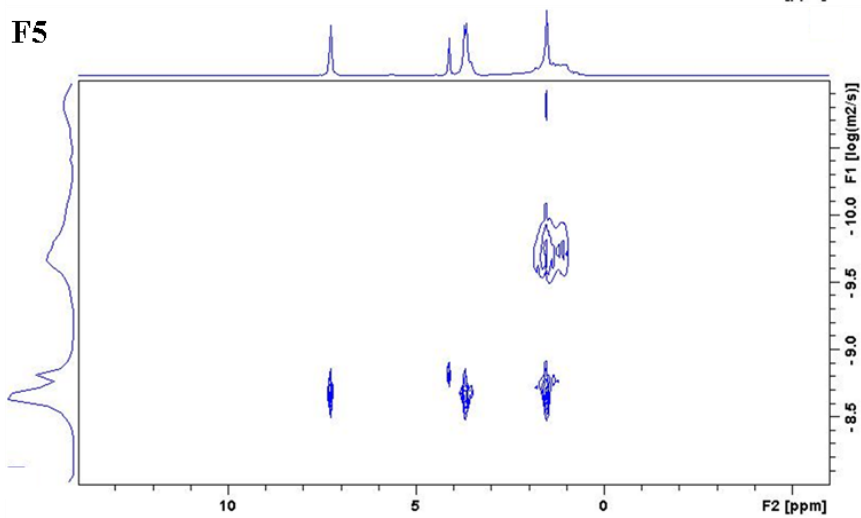
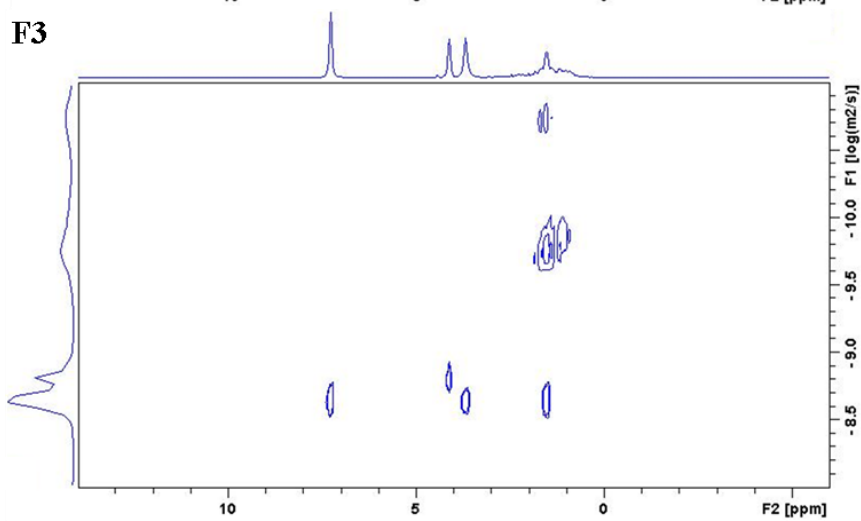
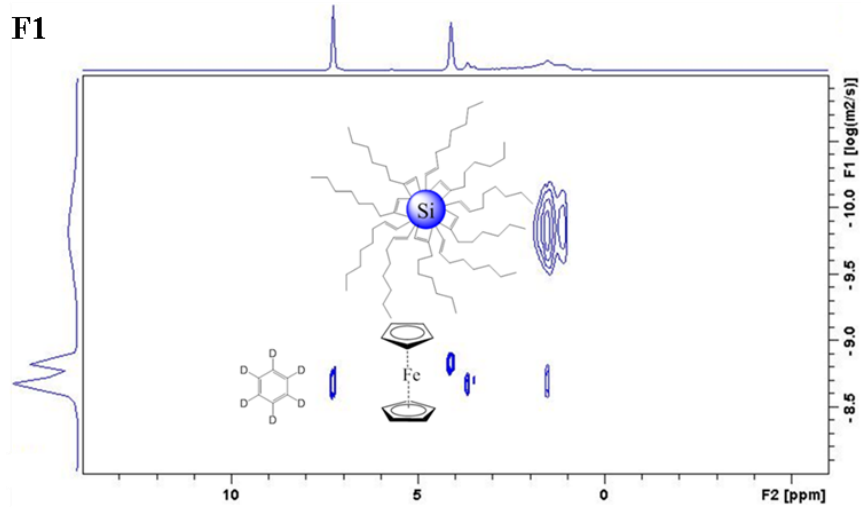
By using an internal standard with known hydrodynamic radius, the hydrodynamic radius of silicon nanoparticles can be calculated using the ratio of standard's diffusion coefficient to that observed for the signals of the silicon nanoparticles (Equation 4).

$$r_{H_{NP}} = \frac{D_{sd}}{D_{NP}} r_{H_{sd}} \quad (4)$$

where $r_{H_{NP}}$ is the hydrodynamic radius of the nanoparticles; $r_{H_{sd}}$ is the hydrodynamic radius of the standard; D_{sd} is the diffusion coefficient of the standard; D_{NP} is the diffusion coefficient of the silicon nanoparticles. Ferrocene was chosen as the standard in this study due to its known hydrodynamic radius of 0.3 nm,¹¹⁵ and its distinct ¹H-NMR resonance which is located in an area that is well isolated from the alkenyl-passivated silicon nanoparticles and solvent resonances.

2.2.4.1 Size determination of octenyl-passivated silicon nanoparticles

2D DOSY-NMR was first performed to determine the hydrodynamic diameters of the size separated octenyl-passivated silicon nanoparticle fractions which were characterized by the GPC analysis. Figure 2.13 shows the 2D DOSY-NMR spectra of the separated fractions of octenyl-passivated silicon nanoparticles, with ferrocene as internal standard, in deuterated benzene. The ferrocene signal at 4.16 ppm, as well as the signal of alkyl groups of the silicon nanoparticles at 1.1 and 0.9 ppm, is clearly labeled.



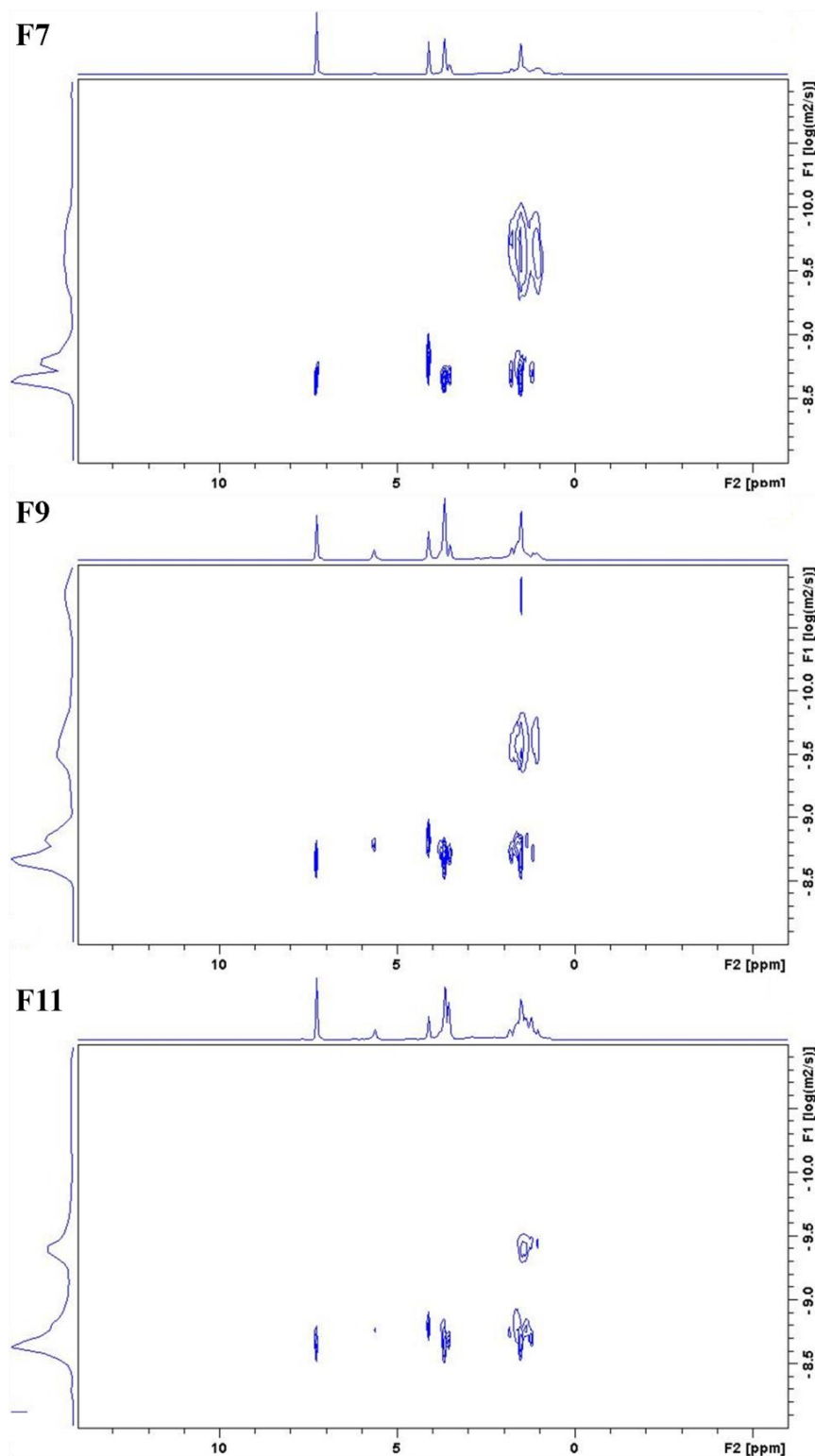
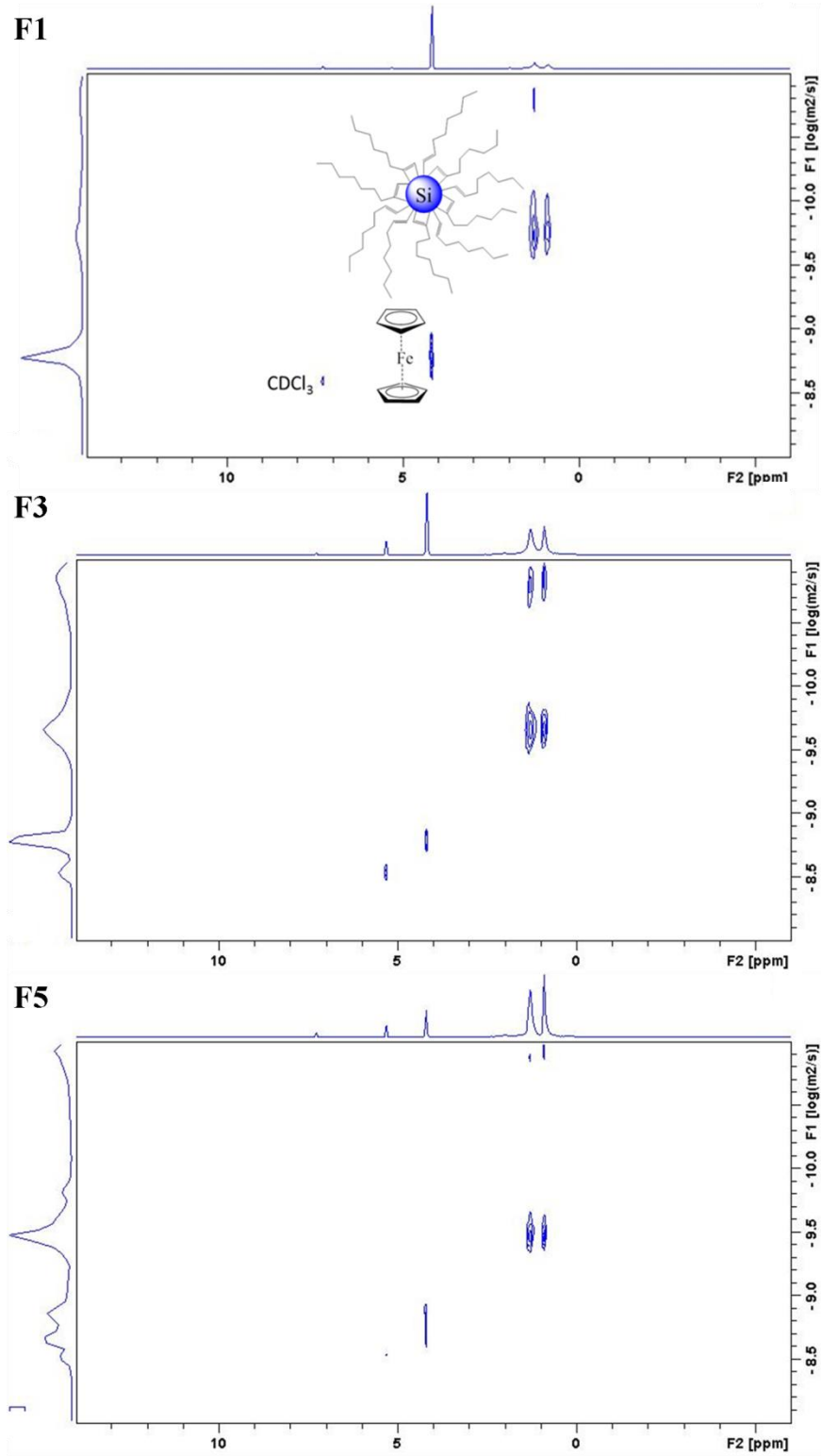


Figure 2.13 2D DOSY-NMR spectra of separated fractions of octenyl-passivated silicon nanoparticles with ferrocene as internal standard in C_6D_6 .

All the DOSY data were processed using the CONTIN algorithm available in the Bruker TOPSPIN 2.1 software. TOPSPIN's CONTIN implementation is directly derived from Provencher's algorithm based on the Inversion of Laplace Transform.¹¹⁶ It must be noted that CONTIN yields generally more broad peaks than the discrete DOSY fitting while giving the continuous distribution of exponents. The diffusion coefficients of the separated silicon nanoparticles and ferrocene, as well as the hydrodynamic diameters of these nanoparticles are shown in the Table 2.2. A distinct decrease of diffusion coefficients from larger to smaller nanoparticles (from F1 to F11) is observed, which indicates decreasing nanoparticle size. By comparing the diffusion coefficient of the silicon nanoparticles to that of the ferrocene, the size of the silicon nanoparticles, which presented in Table 2.2, can be calculated using equation 4. The results show that the hydrodynamic diameters of the separated octenyl-passivated silicon nanoparticles decrease from 6.0 nm to 2.4 nm from fractions 1 to fraction 11, which are in good agreement with the GPC measurements on the same samples.



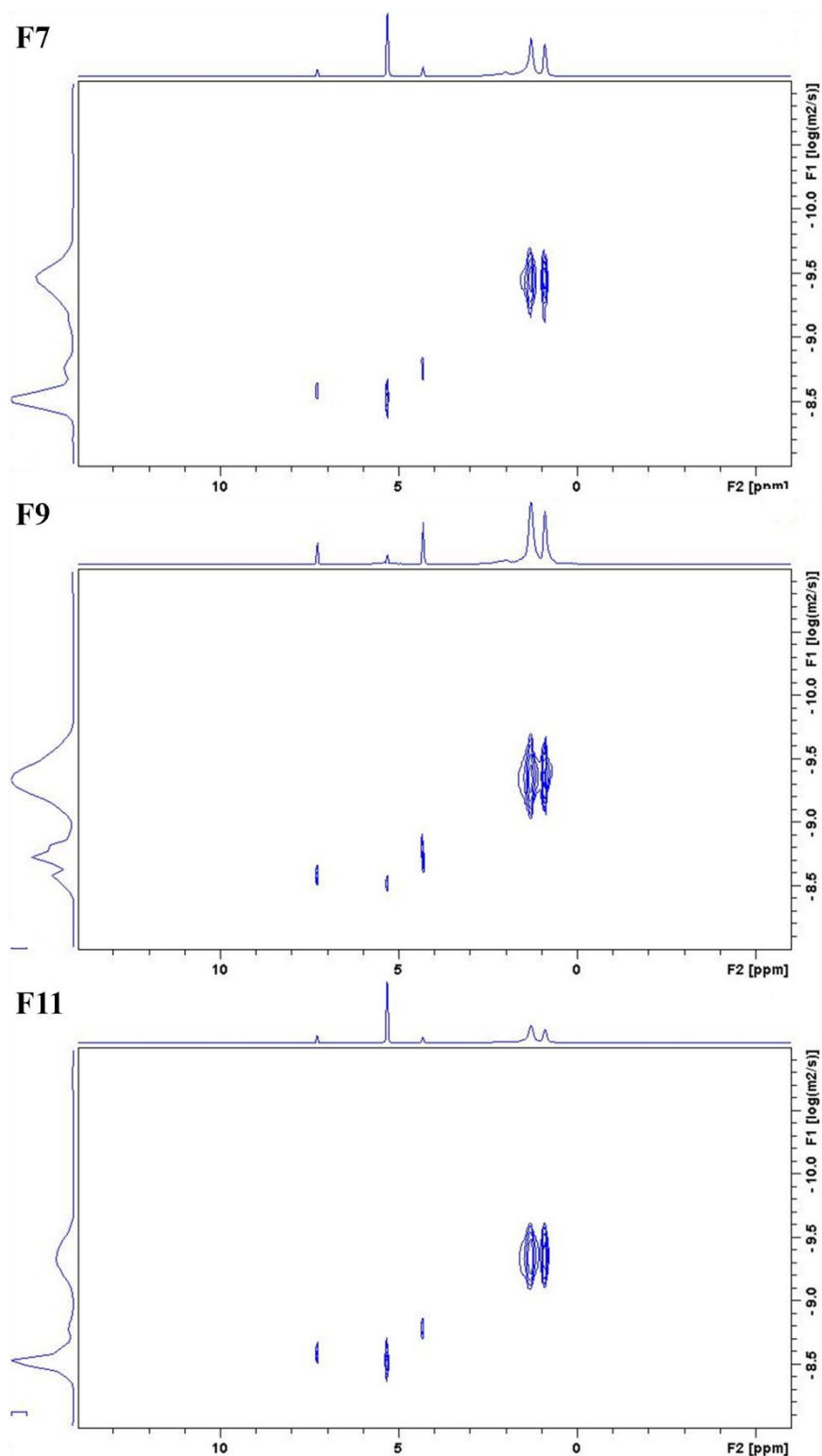


Figure 2.14 2D DOSY-NMR spectrum of fraction 1 of octenyl-passivated silicon nanoparticles with ferrocene as internal standard in CDCl_3 .

Table 2.2 Diffusion coefficients and hydrodynamic diameter of separated octenyl-passivated silicon nanoparticles from the DOSY NMR data in two solvents

Fraction	1	3	5	7	9	11
D_{Fc} in C_6D_6 / m^2s^{-1}	$10^{-8.82}$	$10^{-8.82}$	$10^{-8.82}$	$10^{-8.80}$	$10^{-8.83}$	$10^{-8.81}$
D_{NP} in C_6D_6 / m^2s^{-1}	$10^{-9.82\pm0.25}$	$10^{-9.77\pm0.21}$	$10^{-9.68\pm0.19}$	$10^{-9.60\pm0.19}$	$10^{-9.54\pm0.19}$	$10^{-9.40\pm0.15}$
Diameter in C_6D_6 /nm	6.0 ± 1.5	5.3 ± 1.1	4.4 ± 0.8	3.8 ± 0.7	3.0 ± 0.6	2.4 ± 0.3
D_{Fc} in $CDCl_3$ / m^2s^{-1}	$10^{-8.78}$	$10^{-8.78}$	$10^{-8.66}$	$10^{-8.75}$	$10^{-8.72}$	$10^{-8.77}$
D_{NP} in $CDCl_3$ / m^2s^{-1}	$10^{-9.76\pm0.17}$	$10^{-9.66\pm0.13}$	$10^{-9.48\pm0.11}$	$10^{-9.48\pm0.15}$	$10^{-9.36\pm0.21}$	$10^{-9.36\pm0.15}$
Diameter in $CDCl_3$ /nm	5.8 ± 1.0	4.6 ± 0.7	4.0 ± 0.5	3.2 ± 0.6	2.6 ± 0.6	2.3 ± 0.3

In order to evaluate the effect of solvent on the DOSY-NMR measurement, 2D DOSY-NMR was performed in the more polar deuterated chloroform solvent. Figure 2.14 shows the 2D DOSY-NMR spectra of the separated fractions of octenyl-passivated silicon nanoparticles with ferrocene as internal standard in deuterated chloroform which is similar as the spectrum obtained in deuterated benzene. After analyzing all the DOSY data using the CONTIN algorithm, the diffusion coefficients of the separated silicon nanoparticles and ferrocene, as well as the hydrodynamic diameters of nanoparticles in deuterated chloroform are presented in the Table 2.2. The results show a similar decreasing of diffusion coefficient from fraction 1 to fraction 11 of the octenyl-passivated

silicon nanoparticles, while the calculated hydrodynamic diameters of these silicon nanoparticles decrease from 5.8 nm to 2.3 nm.

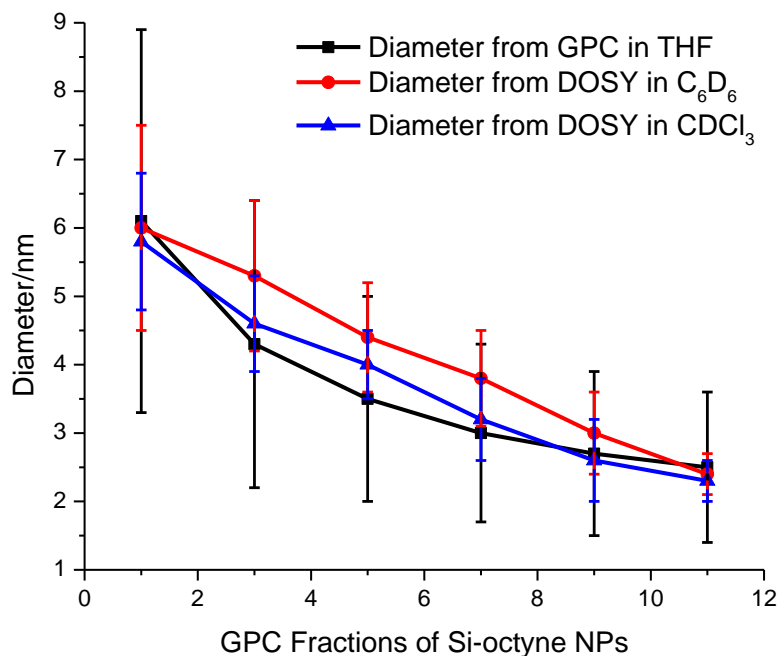
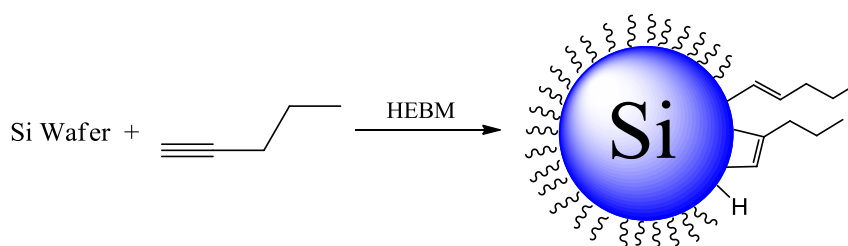


Figure 2.15 Hydrodynamic diameters of separated octenyl-passivated silicon nanoparticles obtained from GPC and DOSY NMR analysis.

Figure 2.15 compares the hydrodynamic diameters of separated octenyl-passivated silicon nanoparticles obtained from the GPC analysis in THF and the DOSY NMR analysis in deuterated benzene and chloroform. The hydrodynamic diameters of the separated silicon nanoparticles obtained from DOSY NMR in the two solvents are comparable with each other. The hydrodynamic diameter of the silicon nanoparticles in deuterated benzene is slightly bigger than the diameter of the nanoparticles in deuterated chloroform, which may due to the greater ability of benzene molecules to interdigitate between the organic chains on the nanoparticle's surface, thereby expanding the particle

volume. The hydrodynamic diameters of the separated silicon nanoparticles obtained from GPC are more similar to the results obtained from DOSY NMR in deuterated chloroform, which may due to the similar polarity of the deuterated chloroform and THF. In addition, compared the hydrodynamic diameter of the fraction 3 of octenyl-passivated silicon nanoparticles (4.3~5.3 nm) to their core size obtained from TEM (3.5 nm, Figure 2.9), it was found that the organic shell on the silicon nanoparticles is around 1 nm which is very reasonable for the octenyl passivated surface. The hydrodynamic diameters of the separated octenyl-passivated silicon nanoparticles obtained from the two techniques are consistent with each other, and show the effectiveness of the DOSY NMR, as well as the GPC analysis, to be reliable methods for determining the size of silicon nanoparticles.

2.2.4.2 Synthesis and size determination of pentenyl-passivated silicon nanoparticles



Scheme 2.4 Synthesis of silicon nanoparticles passivated by 1-pentyne using RHEBM

Pentenyl-passivated silicon nanoparticles were synthesized via ball milling with silicon wafer and 1-pentyne (Scheme 2.4). The ^1H -NMR and ^{13}C -NMR spectra of the pentenyl-passivated silicon nanoparticles presented in Figure 2.16 clearly show similar surface structure to the octenyl-passivated silicon nanoparticles. In the ^1H -NMR spectrum, a broad intense peak at 0.9 ppm indicates the protons in the terminal $-\text{CH}_3$ groups, while the broad peak at 1.4 ppm shows the protons in the $-\text{CH}_2$ group which is next to the terminal $-\text{CH}_3$ group. Resonance at 2.0 ppm and the weak broad peak at 5.4 ppm are

assigned to the $\text{CH}_2\text{-C=C}$ and H-C=C respectively. Furthermore, the peak at 3.5 ppm demonstrates there is also Si-H passivated surface on the nanoparticle. Additionally, the intense peaks at 15 ppm, 23 ppm, and the broad peaks in the 27-43 ppm and 120-140 ppm range shown in the ^{13}C -NMR spectrum are also assigned to the pentenyl surface structure.

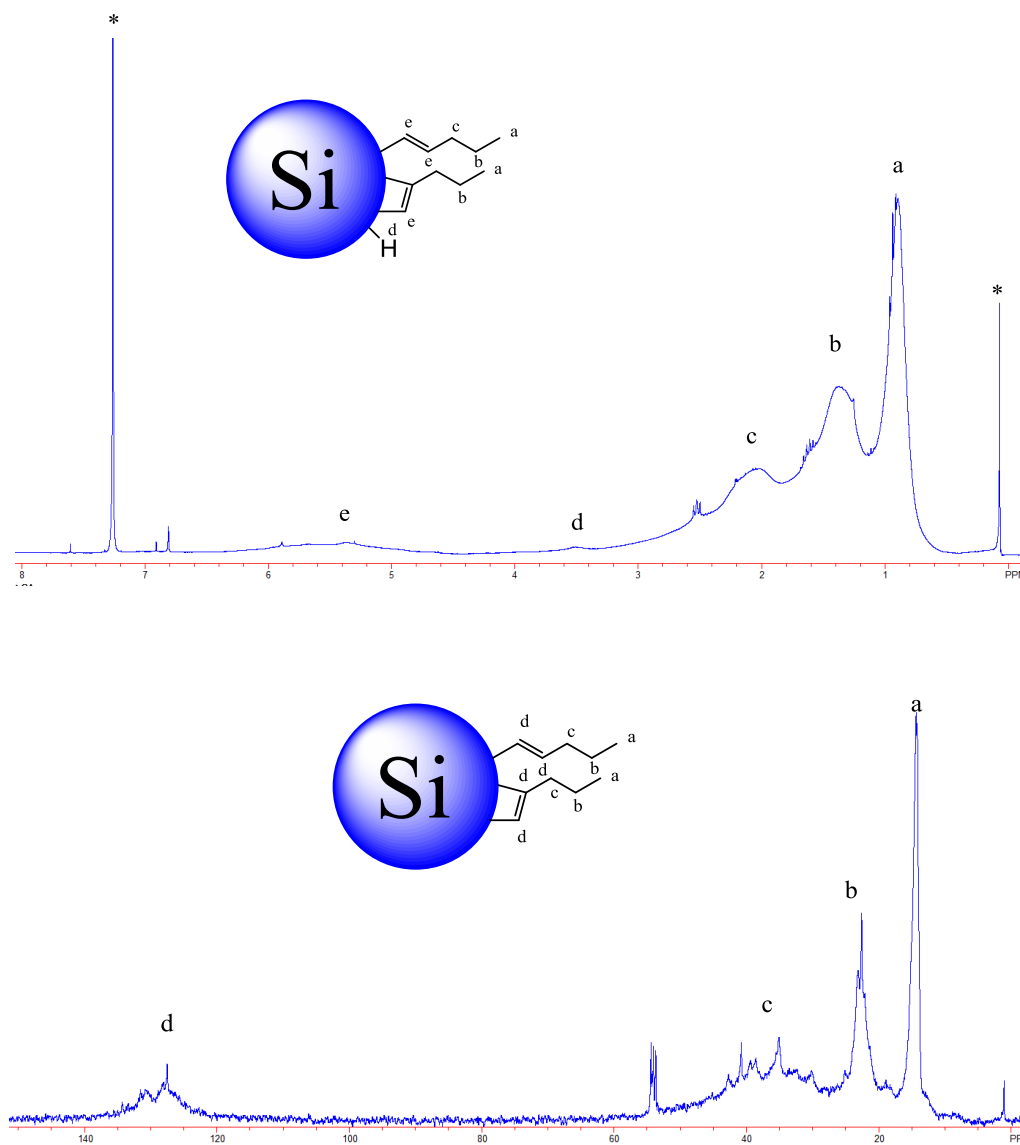


Figure 2.16 ^1H -NMR (top) and ^{13}C -NMR (down) spectra of the pentenyl-passivated silicon nanoparticles

The pentenyl-passivated silicon nanoparticles showed a similar FTIR spectrum to the octenyl-passivated silicon nanoparticles, which further confirmed the pentenyl-passivated surface of the silicon nanoparticles (Figure 2.17). Similarly, the strong band in the 2800-3020 cm^{-1} range indicates the C-H stretching vibration, while the peaks at 1466 cm^{-1} and 1376 cm^{-1} demonstrate the C-H bending vibration. Those two peaks around 1597 cm^{-1} and 1690 cm^{-1} due to the C=C stretching vibration, and the Si-C-H and Si-C vibration peaks at 1250 cm^{-1} and 840 cm^{-1} indicate the 1-pentyne passivated to the silicon nanoparticle surface. Moreover, the broad peak at 980-1130 cm^{-1} is due to the Si-O stretch shows the oxygen passivated surface on the nanoparticle, while the peak at 2120 cm^{-1} is due to a Si-H stretching vibration.

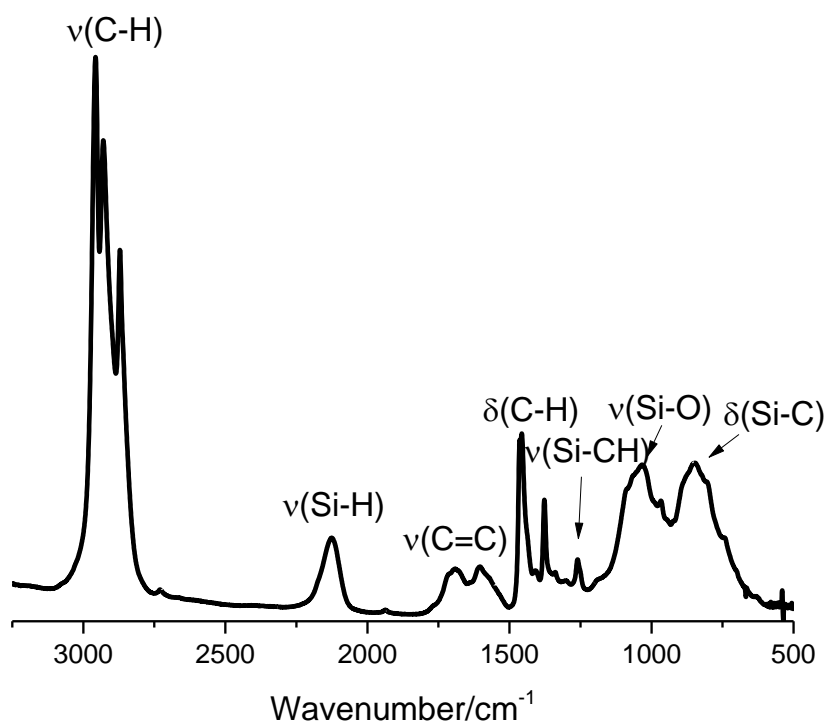


Figure 2.17 FTIR spectrum of pentenyl-passivated silicon nanoparticles

The pentenyl-passivated silicon nanoparticles also show the similar optical properties as that of the octenyl-passivated silicon nanoparticles, including a broad, continuous UV-Vis absorption tailing at 550 m, and the strong broad PL emission in the range of 300 to 650 nm (Figure 2.18). The PL emission spectra of the silicon nanoparticles were recorded with various excitation wavelengths, ranging from 300 to 400 nm in CH_2Cl_2 . With increasing the excitation wavelength, the PL emission maxima were found to shift to longer wavelength. The broadness of the emission spectra indicates that the pentenyl-passivated silicon nanoparticles also have broad size distribution.

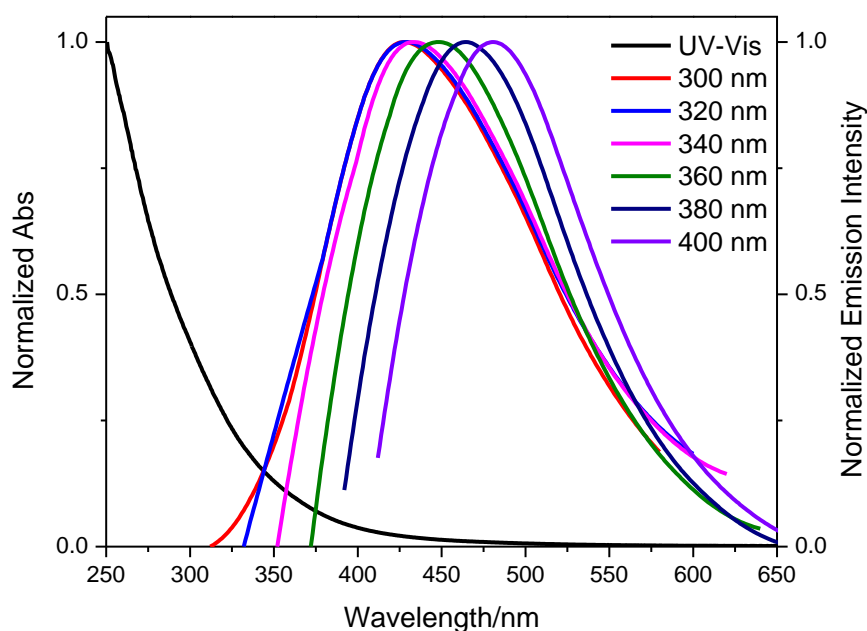
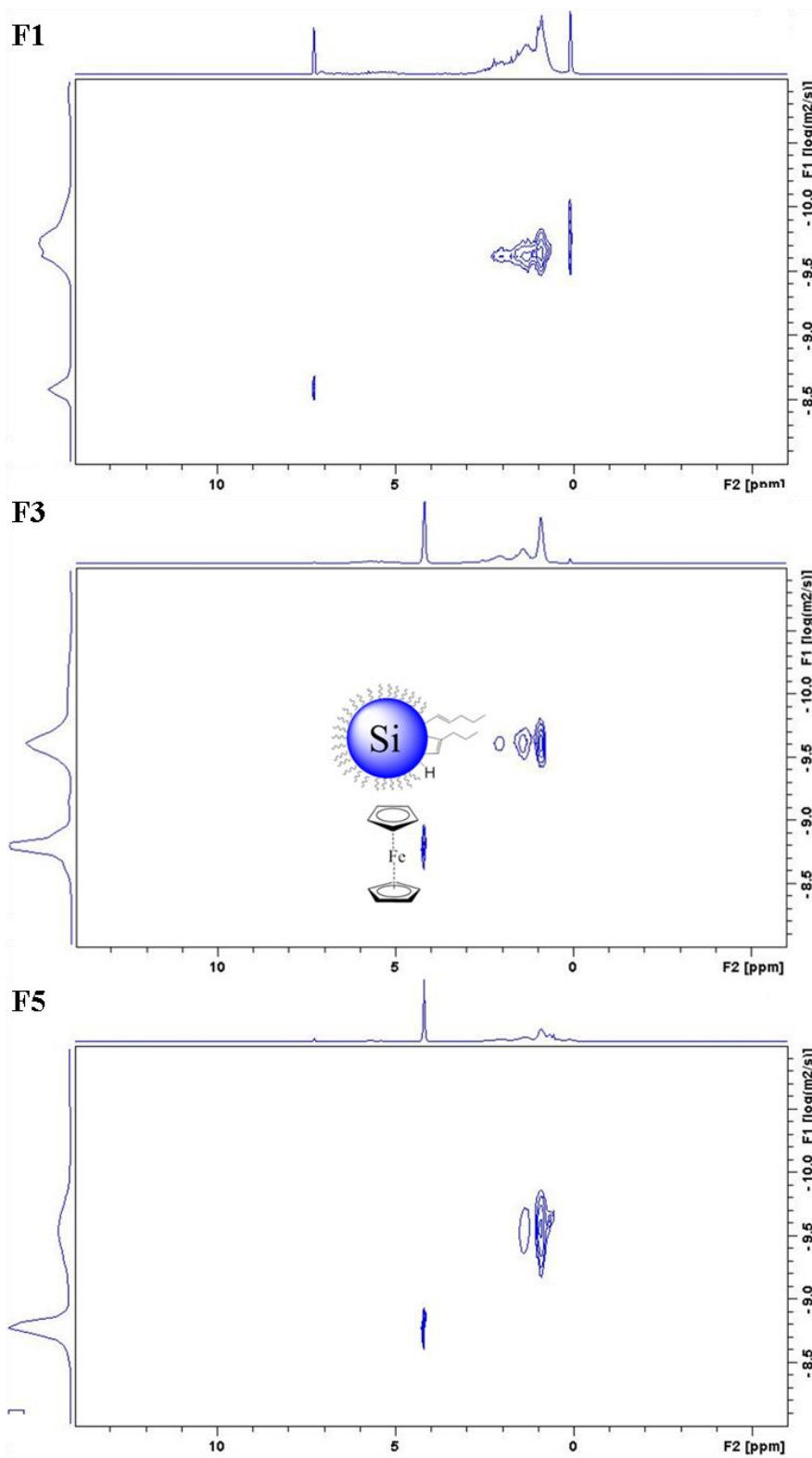


Figure 2.18 UV-Vis absorption spectrum and PL emission spectra at various excitation wavelengths of pentenyl-passivated silicon nanoparticles



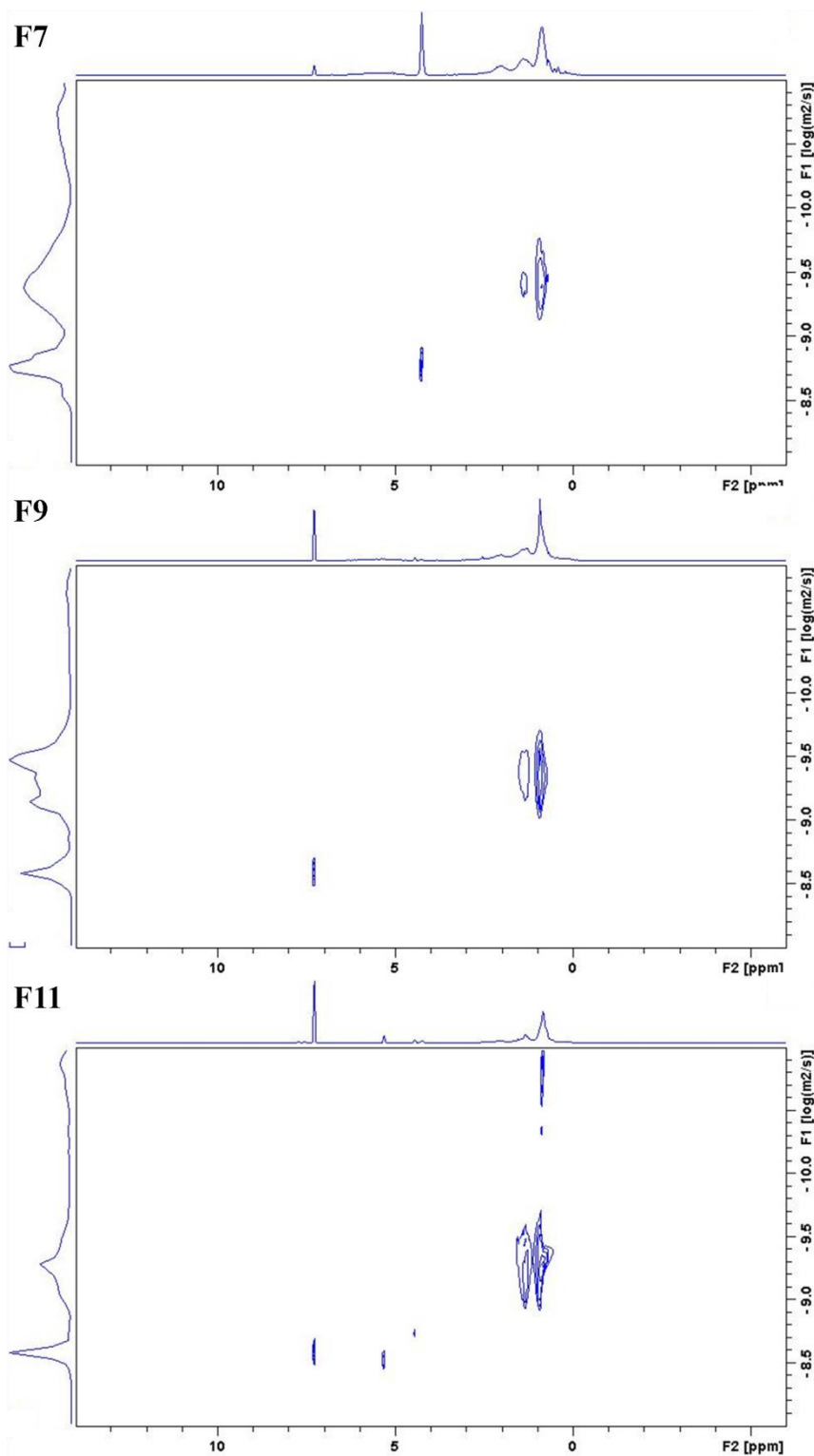


Figure 2.19 2D DOSY-NMR spectra of separated fractions of pentenyl-passivated silicon nanoparticles with ferrocene as internal standard in CDCl_3 .

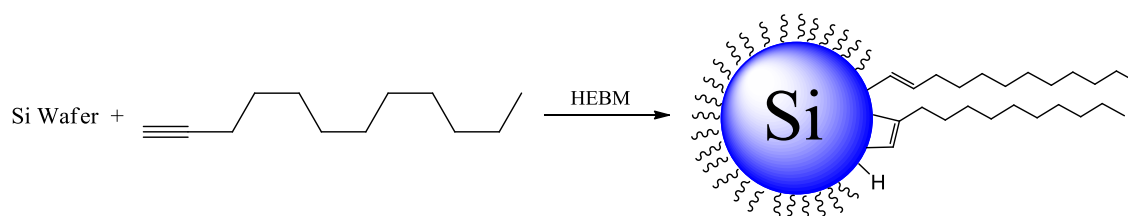
The pentenyl-passivated silicon nanoparticles were separated by a gravity GPC column, and the hydrodynamic diameters of the pentenyl-passivated silicon nanoparticles in each fraction were also characterized using 2D DOSY NMR. Figure 2.19 shows the 2D DOSY-NMR spectra of the separated fractions of pentenyl-passivated silicon nanoparticles with ferrocene as internal standard in deuterated chloroform. Similarly, all of the DOSY data were analyzed using the CONTIN algorithm, and the diffusion coefficients of the separated silicon nanoparticles and the ferrocene, as well as the hydrodynamic diameters of these nanoparticles in deuterated chloroform are presented in the Table 2.3. The results show an expected decreasing of diffusion coefficient from fraction 1 to fraction 11 of the pentenyl-passivated silicon nanoparticles, while the obtained hydrodynamic diameters of the separated pentenyl-passivated silicon nanoparticles decrease from 5.0 nm to 2.0 nm from fraction 1 to fraction 11 which is parallel to that of the separated octenyl-passivated silicon nanoparticles.

Table 2.3 Diffusion coefficients and hydrodynamic diameter of separated pentenyl-passivated silicon nanoparticles from the DOSY NMR data in CDCl₃

Fraction	1	3	5	7	9	11
D_{Fc} in CDCl ₃ /m ² s ⁻¹	10 ^{-8.72}	10 ^{-8.78}	10 ^{-8.80}	10 ^{-8.77}	10 ^{-8.87}	10 ^{-8.74}
D_{NP} in CDCl ₃ /m ² s ⁻¹	10 ^{-9.62±0.15}	10 ^{-9.60±0.13}	10 ^{-9.55±0.17}	10 ^{-9.43±0.17}	10 ^{-9.46±0.11}	10 ^{-9.28±0.17}
Diameter in CDCl ₃ /nm	5.0±0.7	4.0±0.5	3.4±0.6	2.7±0.5	2.3±0.3	2.0±0.4

2.2.4.3 Synthesis and size determination of dodecenyl-passivated silicon nanoparticle

Similar to the other two passivated silicon nanoparticles, the dodecenyl-passivated silicon nanoparticles were obtained by the ball milling with silicon wafer and 1-dodecyne (Scheme 2.5).



Scheme 2.5 Synthesis of silicon nanoparticles passivated by 1-dodecyne using RHEBM

Figure 2.20 shows the ^1H -NMR and ^{13}C -NMR spectra of the dodecenyl-passivated silicon nanoparticles, which clearly demonstrate the dodecenyl-passivated surface on the silicon nanoparticles. In the ^1H -NMR spectrum, an intense peak at 0.9 ppm indicates the protons in the terminal $-\text{CH}_3$ groups, while the strong broad peak at 1.2 ppm shows the protons in the seven $-\text{CH}_2$ groups in the alkyl chain. The weak broad peaks at 2.0 and 5.4 ppm are assigned to the $\text{CH}_2-\text{C}=\text{C}$ and $\text{H}-\text{C}=\text{C}$ respectively. The weakness of these two peaks may be due to more alkyl protons in this system compares to the pentenyl-passivated and octenyl-passivated silicon nanoparticles. Moreover, the weak peak at 3.3 ppm proves that there is slight $\text{Si}-\text{H}$ passivated surface on the nanoparticle. Furthermore, in the ^{13}C -NMR spectrum, the intense peaks at 14 ppm, 23 ppm, 29 ppm, 32 ppm due to the alkyl chain on the nanoparticle surface are also observed. However, the resonance of the $-\text{C}=\text{C}-$ doesn't show on the spectra which may due to the broadness of the peak.

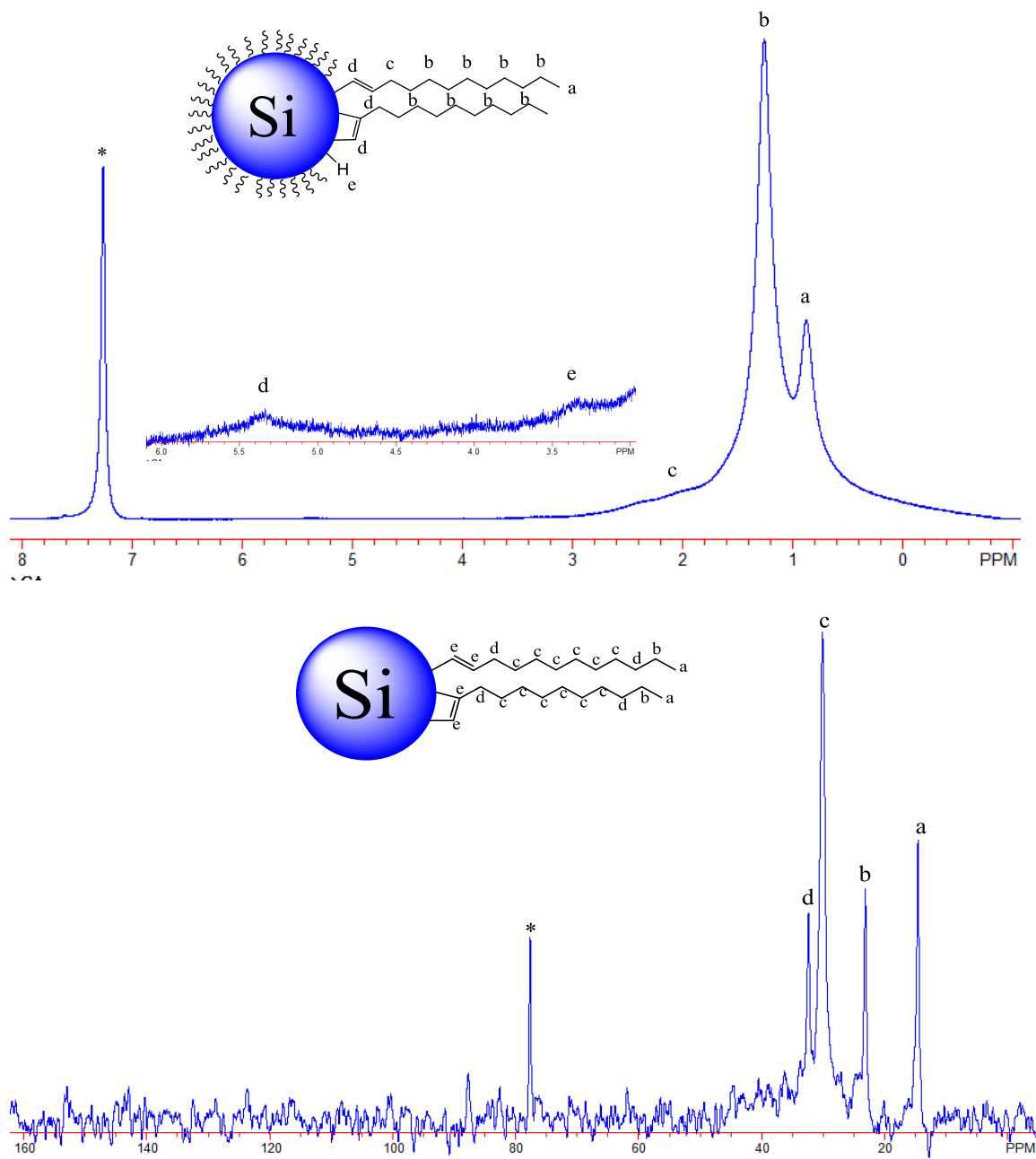


Figure 2.20 ^1H -NMR (top) and ^{13}C -NMR (down) spectra of the dodecenyl-passivated silicon nanoparticles

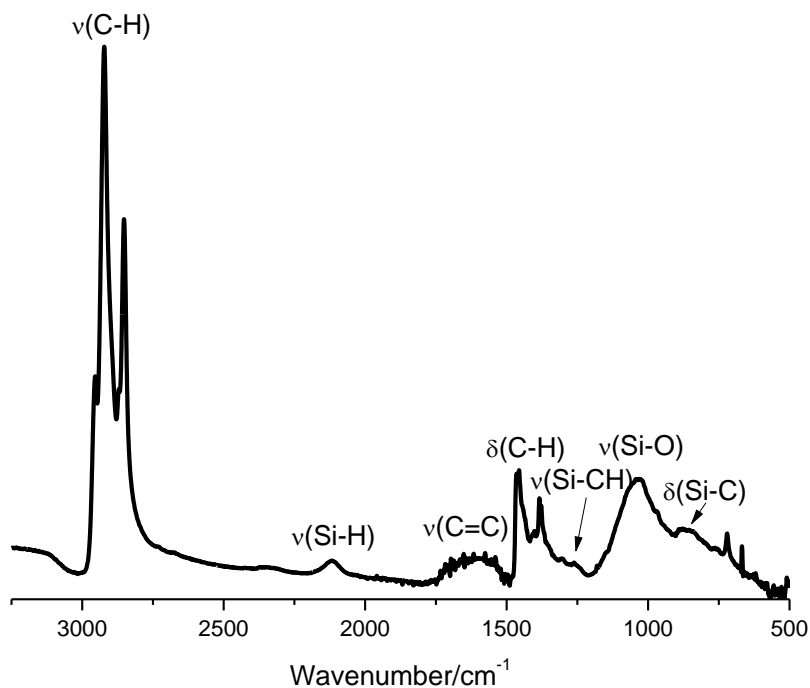


Figure 2.21 FTIR spectrum of dodecenyl-passivated silicon nanoparticles

The FTIR spectrum of the dodecenyl-passivated silicon nanoparticles presented in Figure 2.21, which shows the C-H stretching vibration band in the 2800-3020 cm^{-1} range, the C-H bending vibration peaks at 1466 cm^{-1} and 1376 cm^{-1} , the C=C stretching vibration peaks around 1597 cm^{-1} and 1690 cm^{-1} , and the Si-C-H and Si-C vibration peaks at 1250 cm^{-1} and 840 cm^{-1} . Those vibration peaks further confirmed the dodecenyl-passivated structure of the silicon nanoparticles. Additionally, the broad peak at 980-1130 cm^{-1} due to the Si-O stretch and a weak Si-H stretching vibration at 2120 cm^{-1} shows the oxygen and hydrogen passivated surface on the nanoparticle.

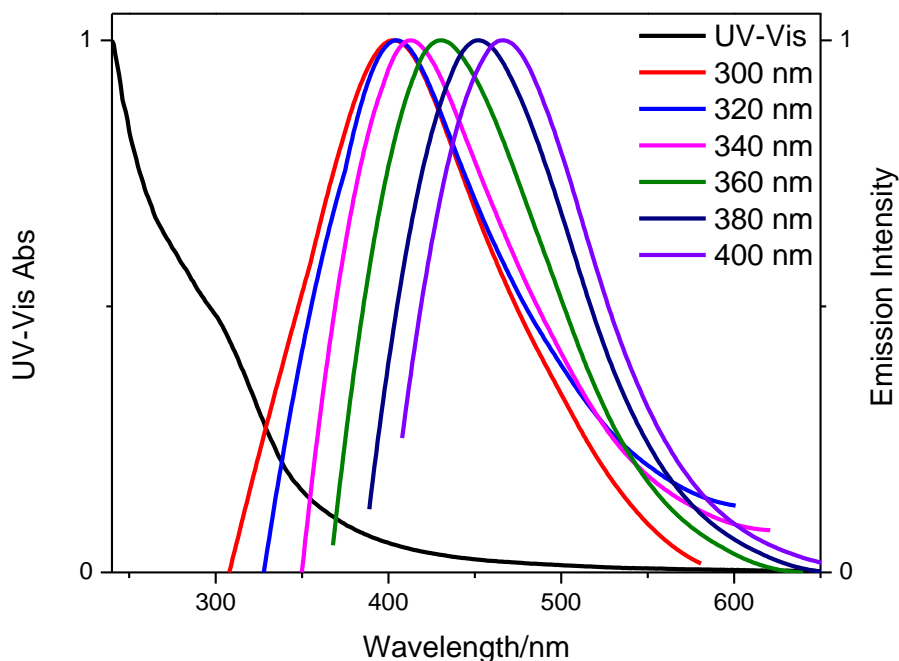
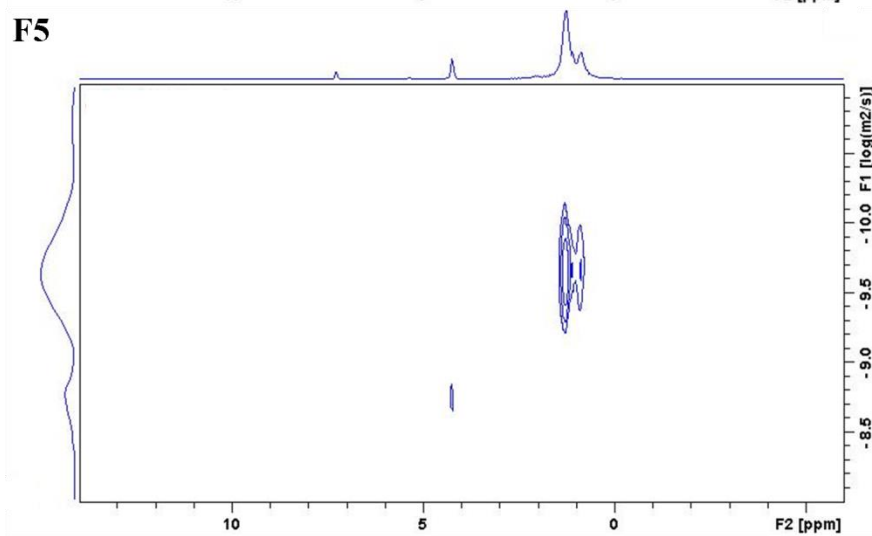
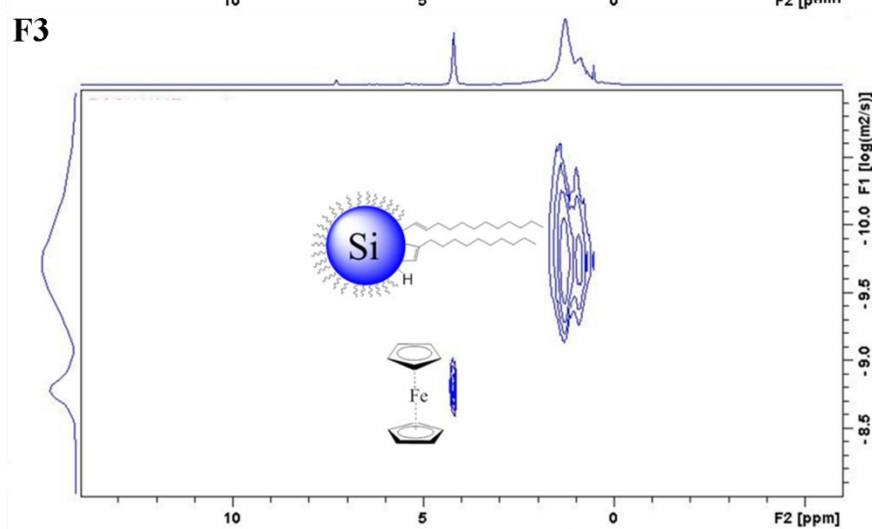
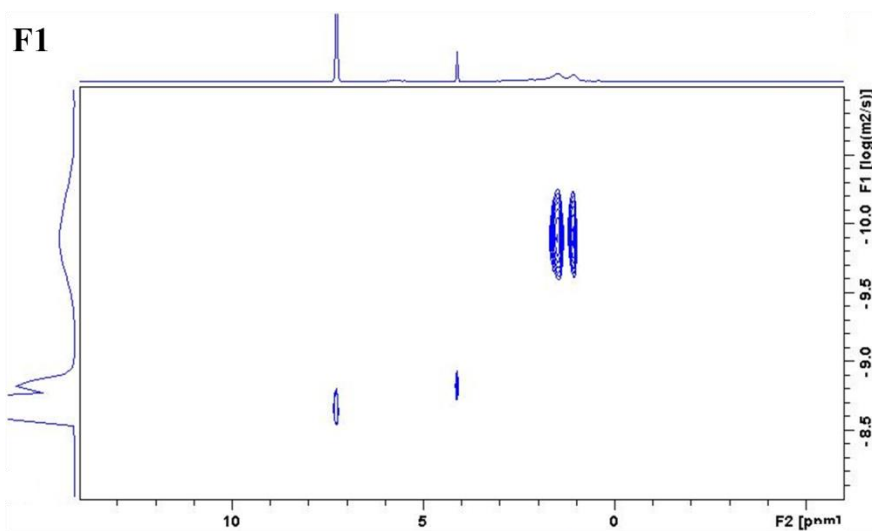


Figure 2.22 UV-Vis absorption spectrum and PL emission spectra at various excitation wavelengths of dodecenyl-passivated silicon nanoparticles

The dodecenyl-passivated silicon nanoparticles also showed the similar optical properties as those of the other two silicon nanoparticles, including a broad, continuous UV-Vis absorption tailing at 600 m, and the strong broad PL emission in the range of 300 to 650 nm (Figure 2.22). The PL emission spectra of the silicon nanoparticles were recorded with various excitation wavelengths, ranging from 300 to 400 nm in CH_2Cl_2 . Similarly, with increasing the excitation wavelength, the PL emission maxima were found to shift to longer wavelength, and the broadness of the emission spectra indicates the dodecenyl-passivated silicon nanoparticles also have broad size distribution.



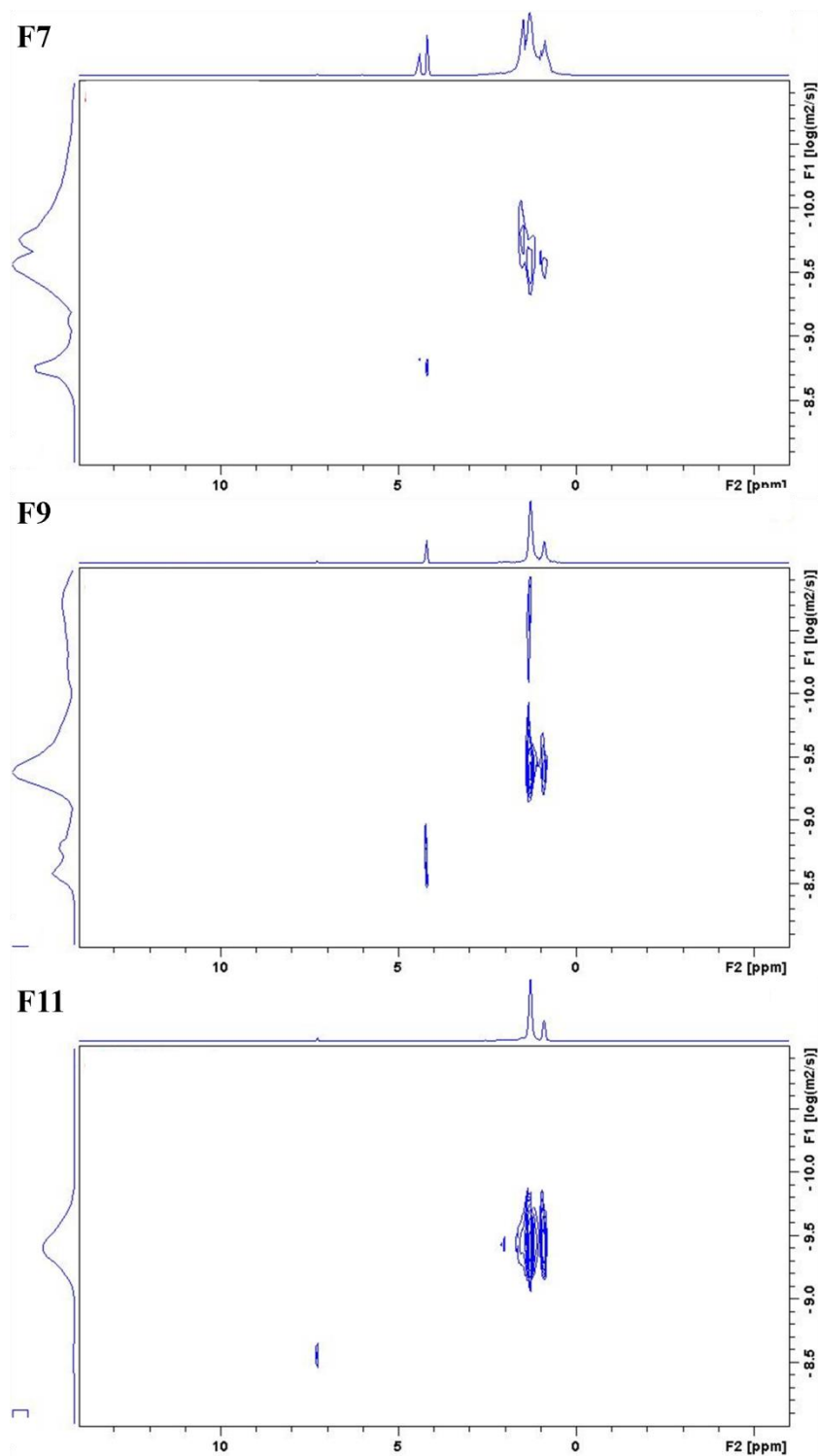


Figure 2.23 2D DOSY-NMR spectrum of fraction 3 of dodeceny-passivated silicon nanoparticles with ferrocene as internal standard in CDCl_3 .

The dodecenyl-passivated silicon nanoparticles were separated by a gravity GPC column, and their hydrodynamic diameters were characterized using 2D DOSY NMR. Figure 2.23 shows the 2D DOSY-NMR spectra of the separated fractions of dodecenyl-passivated silicon nanoparticles with ferrocene as internal standard in deuterated chloroform. After analyzing the DOSY data using the CONTIN algorithm, the diffusion coefficients of the separated silicon nanoparticles and ferrocene, as well as the hydrodynamic diameters of these nanoparticles in deuterated chloroform are presented in the Table 2.4. As expected, the results show a decreasing of diffusion coefficient from fraction 1 to fraction 11 of the dodecenyl-passivated silicon nanoparticles, and the obtained hydrodynamic diameters of the separated dodecenyl-passivated silicon nanoparticles decrease from 6.8 nm to 2.6 nm from fraction 1 to fraction 11 which is parallel to those of the other two separated silicon nanoparticles.

Table 2.4 Diffusion coefficients and hydrodynamic diameter of separated dodecenyl-passivated silicon nanoparticles from the DOSY NMR data in CDCl₃

Fraction	1	3	5	7	9	11
D _{FC} in CDCl ₃ /m ² s ⁻¹	10 ^{-8.83}	10 ^{-8.77}	10 ^{-8.75}	10 ^{-8.76}	10 ^{-8.77}	10 ^{-8.80}
D _{NP} in CDCl ₃ /m ² s ⁻¹	10 ^{-9.89±0.25}	10 ^{-9.73±0.34}	10 ^{-9.65±0.23}	10 ^{-9.57±0.25}	10 ^{-9.46±0.23}	10 ^{-9.43±0.17}
Diameter in CDCl ₃ /nm	6.8±1.8	5.5±2.0	4.8±1.1	3.9±1.0	3.0±0.7	2.6±0.4

Table 2.5 Hydrodynamic diameters of separated silicon nanoparticles with three different surface ligands obtained from DOSY NMR analysis in CDCl₃

Fraction	1	3	5	7	9	11
Si-C ₅ NPs/nm	5.0±0.7	4.0±0.5	3.4±0.6	2.7±0.5	2.3±0.3	2.0±0.4
Si-C ₈ NPs/nm	5.8±1.0	4.6±0.7	4.0±0.5	3.2±0.6	2.6±0.6	2.3±0.3
Si-C ₁₂ NPs/nm	6.8±1.8	5.5±2.0	4.8±1.1	3.9±1.0	3.0±0.7	2.6±0.4

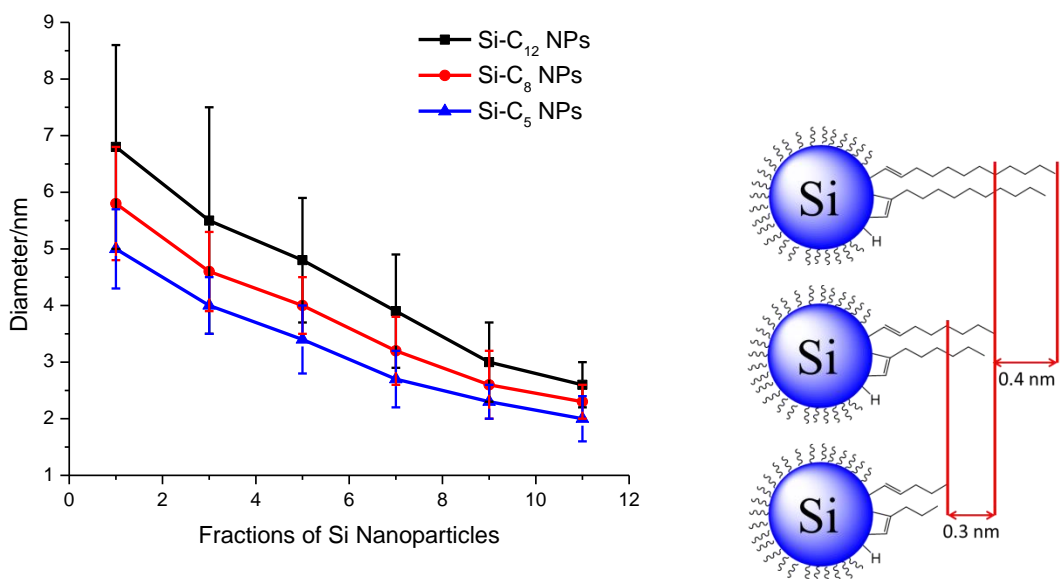


Figure 2.24 Hydrodynamic diameters of separated silicon nanoparticles with three different surface ligands obtained from DOSY NMR analysis in CDCl₃ (left), and the schematic illustration showing the size difference between the three passivated silicon nanoparticles (right).

Table 2.5 and Figure 2.24 compare the hydrodynamic diameters, which were obtained from DOSY NMR analysis in deuterated chloroform, of the separated silicon

nanoparticles with three different surface ligands. Since the silicon core sizes of the nanoparticles obtained from RHEBM are reproducible and independent of the surface ligands,⁶⁹ the difference of the hydrodynamic diameters of these three passivated silicon nanoparticles are only dependent from the chain length of the surface ligands. As shown in Figure 2.24 (right), based on the polarity of the solvent, the organic chain on the particle's surface are more likely to be extended. So the theoretical difference of the hydrodynamic diameters between pentenyl-passivated silicon nanoparticle and octenyl-passivated silicon nanoparticle is around 0.6 nm, while the theoretical difference of the hydrodynamic diameters between dodecenyl-passivated silicon nanoparticle and octenyl-passivated silicon nanoparticle is around 0.8 nm. As expected, the experimental results obtained from DOSY NMR analysis shows the actual difference of the hydrodynamic diameters between the early fractions (F1 to F7) of pentenyl-passivated silicon nanoparticles and octenyl-passivated silicon nanoparticles are around 0.6 nm, while the actual difference of the hydrodynamic diameters between the early fractions (F1 to F7) of dodecenyl-passivated silicon nanoparticles and octenyl-passivated silicon nanoparticles are around 0.8 nm (Figure 2.24 left). The experimental differences of the hydrodynamic diameters between the later fractions (F9 to F11) of three passivated silicon nanoparticles are around 0.3 nm, which are smaller than the expected values. This may due to the lower passivated density on the smaller silicon nanoparticles. In summary, all of these results show that DOSY NMR gives the size of silicon nanoparticles that are in excellent agreement with the changing of the surface ligands and the size separation of the silicon nanoparticles by the gravity GPC column, which further demonstrate the effectiveness of DOSY NMR as a reliable alternative for obtaining the nanoparticle sizes.

2.3 Conclusion

Alkenyl-passivated silicon nanoparticles have been produced in one step from the reactive high-energy ball milling of silicon wafer and the relevant alkynes. The surface structure and optical properties of these passivated silicon nanoparticles have been systematically characterized to confirm the successful production of the nanoparticles and the surface passivation. Due to the polydispersity of the silicon nanoparticles and the fact that alkynes may undergo cyclotrimerization to generate the relevant substituted benzene during the ball milling process, a fast approach for purify and at the same time size separating the silicon nanoparticles using a gravity GPC column has been developed. The hydrodynamic diameters of the separated silicon nanoparticles have been characterized using the GPC and DOSY NMR analysis. The results demonstrate the excellent effectiveness of the GPC and DOSY NMR as reliable approaches for determining the nanoparticle sizes, and these two methods are faster and more cost-effective compared to TEM.

2.4 Experimental Section

2.4.1 Materials

All chemicals were purchased from Sigma-Aldrich or Alfa Aesar, and employed without further purification unless specified. Tetrahydrofuran (THF) was distilled over sodium-benzophenone prior to use. Dichloromethane was distilled over CaH_2 before use. Silicon wafer (undoped, mirror finish, orientation [111]) was obtained from Silrac. Bio-beads S-X1 beads, 200 mesh, were purchased from Bio-Rad.

2.4.2 Synthesis of passivated silicon nanoparticles

Silicon wafer (1.0 g) was placed in a stainless steel milling vial along with two stainless steel milling balls (diameter of 1.2 cm, weighing approximately 8.1 g). The vial was filled in a Vacuum Atmospherics dry box under a nitrogen atmosphere with 20 mL alkynes (1-pentyne, 1-octyne or 1-dodecyne) and then tightly sealed. The milling vial was placed in a SPEX 8000-D Dual Mixer/Mill, and the reactive high energy ball milling were performed for 24 hours. After 24 hours of milling, the reaction mixture was centrifuged to remove larger particles. The solution contains alkenyl-passivated silicon nanoparticles which are soluble in non-polar organic solvents. All of the solvents were removed by vacuum distillation to yield dry nanoparticle products. The nanoparticles can be redispersed in organic solvents like THF, methylene chloride, toluene and hexane etc. Crude Yield: 80-120 mg.

Pentenyl-passivated silicon nanoparticles. ^1H -NMR (δ , 300 MHz, CDCl_3): 5-6 (broad and weak peak), 3.5 (broad and weak peak), 2.4-0.5 (multiple broad peaks). $^{13}\text{C}\{^1\text{H}\}$ NMR (δ , 300 MHz, CD_2Cl_2): 140-120 (broad peaks), 50-10 (multiple broad

peaks). FTIR (thin film on KBr plate): 2820-2990 cm^{-1} (ν (C-H)), 2100 cm^{-1} (ν (Si-H)), 1500-1750 cm^{-1} (ν (C=C)), 1465-1376 cm^{-1} (δ (C-H)), 1250 cm^{-1} (ν (Si-C)), 1190-850 cm^{-1} (ν (Si-O)), 830 cm^{-1} (δ (Si-C)). UV-vis Absorption (in CH_2Cl_2): Single absorption with a tail up to 550 nm. PL emission (in CH_2Cl_2): 350-650 nm emission peaks by changing excitation wavelength from 300-400 nm.

Octenyl-passivated silicon nanoparticles. ^1H -NMR (δ , 300 MHz, CDCl_3): 5-6 (broad and weak peak), 3.7 (broad and weak peak), 3-0 (multiple broad peaks). ^{13}C $\{^1\text{H}\}$ NMR (δ , 300 MHz, CD_2Cl_2): 140-120 (broad peaks), 33 (broad), 30 (broad), 23 (broad), 14 (broad). FTIR (thin film on KBr plate): 2820-2990 cm^{-1} (ν (C-H)), 2100 cm^{-1} (ν (Si-H)), 1500-1750 cm^{-1} (ν (C=C)), 1465-1376 cm^{-1} (δ (C-H)), 1250 cm^{-1} (ν (Si-C)), 1190-850 cm^{-1} (ν (Si-O)), 830 cm^{-1} (δ (Si-C)). UV-vis Absorption (in CH_2Cl_2): Single absorption with a tail up to 600 nm. PL emission (in CH_2Cl_2): 310-650 nm emission peaks by changing excitation wavelength from 300-400 nm.

Dodecenyl-passivated silicon nanoparticles. ^1H -NMR (δ , 300 MHz, CDCl_3): 5-6 (broad and weak peak), 3.4 (broad and weak peak), 3-0 (multiple broad peaks). ^{13}C $\{^1\text{H}\}$ NMR (δ , 300 MHz, CD_2Cl_2): 140-120 (broad peaks), 32 (broad), 29 (broad), 23 (broad), 14 (broad). FTIR (thin film on KBr plate): 2820-2990 cm^{-1} (ν (C-H)), 2100 cm^{-1} (ν (Si-H)), 1500-1750 cm^{-1} (ν (C=C)), 1465-1376 cm^{-1} (δ (C-H)), 1250 cm^{-1} (ν (Si-C)), 1190-850 cm^{-1} (ν (Si-O)), 830 cm^{-1} (δ (Si-C)). UV-vis Absorption (in CH_2Cl_2): Single absorption with a tail up to 600 nm. PL emission (in CH_2Cl_2): 310-650 nm emission peaks by changing excitation wavelength from 300-400 nm.

2.4.3 Purification and size separation of passivated silicon nanoparticles

A gravity GPC column was used for the size separation and purification of passivated silicon nanoparticles. Bio-beads S-X1 beads were swelled overnight in dry THF and packed into a 40 cm \times 1.3 cm glass column. Dichloromethane was used as an elution solvent. A concentrated nanoparticle solution (\sim 50 mg in 1 ml CH₂Cl₂) was added into the column and eluted into various fractions collected in 1.5 mL increments in separate vials. The first fraction was collected when the silicon nanoparticle sample was added into the GPC column, and the 12th fraction was the first fraction (**F1**) which contains silicon nanoparticles. Later fractions (after 25th fraction) contain mostly impurities.

2.4.4 Analytical methods

2.4.4.1 NMR sample preparation and acquisition

NMR samples were prepared by vacuum drying each fraction (\sim 1.5 mL) of the silicon nanoparticle solution, adding 0.8 mL of the deuterated solvent, and then transferring the solution to a 5 mm NMR tube. ¹H-NMR and ¹³C-NMR measurements were performed on a Bruker Avance 300 spectrometer equipped with a 5 mm BBO probe. All DOSY NMR experiments were performed on the same spectrometer equipped with a 5 mm inverse broadband BBI probe at 298 K, which provides a z-direction gradient strength of up to 53.5 G/cm. The PFG NMR pulse sequence with bipolar-gradient pair (BPP) and longitudinal eddy current delay (LED) was used to acquire DOSY spectra with 32768 and 32 points in t₂ and t₁, respectively. The resonance frequency of ¹H nuclei were 300.13 MHz. The corresponding p/2 pulse widths were 7.5 ms and the delay between transients is 2s. A 100 ms diffusion time was used. The gradient pulse widths

varied from 1.3 ms to 2.7 ms, depending on the diffusivity. 384 transients were accumulated. The results are analyzed using CONTIN algorithm available in the Bruker TOPSPIN 2.1 software.

2.4.4.2 Infrared spectroscopy

FTIR spectra were recorded at 1 cm^{-1} resolution with 1000 scans on a Thermo Nicolet NEXUS 670 FTIR instrument. Samples were prepared as a thin film of passivated silicon nanoparticles prepared by depositing dichloromethane solution of silicon nanoparticles on a KBr plate. The FT-IR sample chamber was purged with dry nitrogen before collecting any data.

2.4.4.3 UV-vis absorption and photoluminescence spectroscopy

UV-Vis absorption spectra were recorded in a quartz cuvette (1cm), using a Cary 50 spectrophotometer and were corrected for the solvent absorption. The scan range was 200-800 nm with a 300 nm min^{-1} scan rate. Excitation-emission spectra were recorded in a quartz cuvette (1cm), using a Varian Cary Eclipse spectrofluorometer with a scan rate of 120 nm min^{-1} .

2.4.4.4 Transmission electron microscopy

High-resolution transmission electron microscopy (TEM) studies were performed with a Tecnai G2 TEM using an accelerating voltage of 300 kV. The EDX data were obtained in the TEM using a Bruker attachment, using a 3nm beam spot. TEM samples were prepared by dropping a sonicated diluted solution of silicon nanoparticles in toluene onto a carbon-coated 400 mesh carbon coated copper grid placed on a filter paper. The

filter paper soaked up the excess solution before inserting in grid in the TEM sample holder.

2.4.4.5 GC-MS

GC-MS analysis was performed in GC-MS system (Varian 450 GC, Varian 300 MS) with VF5-MS capillary column. 2 μ L diluted solution in methylene chloride was injected into the GC-MS system.

2.4.4.6 Gel-permeation chromatography

GPC analysis was performed in a multi-detector gel-permeation chromatography (GPC) system with a PL gel 5 μ m, 300 \times 7.5 mm chromatographic column, an injector with a 0.2 mL loop, and UV, RI, viscosity and multi-angle dynamic light scattering detectors. The eluting solvent, THF (>99.9%, HPLC grade) was passed through the detectors and column at 1.0 mL/min. 0.2 mL (2mg/mL) silicon nanoparticles solution in THF, which was pre-filtered by a 0.45 micrometer filter, was injected into the system, and GPC was used to determine size and dispersity.

Chapter 3: Water soluble PEGylated silicon nanoparticles and their assembly into swellable nanoparticle arrays

3.1 Introduction

The solubility of silicon nanoparticles in water is paramount for biological applications. Water soluble silicon nanoparticles have potential use in cellular and assay labeling techniques, as well as in deep-tissue imaging.¹¹⁷ So far, silicon nanoparticles have been made water soluble by functionalizing with various water soluble ligands such as amines,^{17, 26, 117} carboxylic acids,¹¹⁸ poly(acrylic acid),²¹ or by forming micelle-encapsulated silicon nanoparticles using micelles made of phospholipids⁸⁹ or poly(ethylene glycol) (PEG) – based amphiphilies.¹¹⁹

PEG is an ideal polymer for the modification of nanostructured materials based on its intrinsic biocompatibility and water solubility.¹²⁰ PEG grafting has been shown to impart onto a large range of substrates improved properties, including reduced hemolytic toxicity, improved water solubility and increased blood circulation times,¹²¹ and is advantageous in drug delivery systems involving liposomes, nanoparticles and peptides.¹²² PEGylated silicon nanoparticles with strong Si-C attachments have been prepared by Sudeep et al. through the hydrosilylation of H-terminated silicon nanoparticles with alkenyl terminated PEGs.^{49b} Multi-particle assemblies of silicon quantum dots which are physically encapsulated in PEGylated micelles have also been prepared by Erogbogbo et al. for bioimaging applications.¹¹⁹ PEGylated silicon nanoparticle arrays in which the nanoparticles are covalently cross-linked with PEG linkers have yet to be reported.

The mechanochemical synthesis and functionalization of silicon nanoparticles by the reactive high-energy ball milling (RHEBM) of silicon provides a convenient pathway for the covalent attachment of PEG polymers. The freshly prepared silicon surfaces produced by fracturing are highly reactive and undergo “cycloaddition” reactions with unsaturated organic compounds including alkenes and alkynes.¹²³ If the ball milling is performed in a stoichiometric excess of either α, ω -diynes^{41c} or α, ω -chloroalkynes^{41a}, an alkyne end of these molecules attaches covalently with the surface, leaving either an alkyne or chloro group exposed at the perimeter of the ligand shell. The chloro group can be easily converted to an azide group via nucleophilic displacement by the azide ion.^{108b} The PEG polymers can be covalently grafted to the ligand shell of the silicon nanoparticles via a copper catalyzed azide-alkyne cycloaddition (CuAAC) “click” reaction. In this study, the functionalized silicon nanoparticles (alkyne or azide terminated) were reacted with the complementary PEG polymers (azide or alkyne terminated) namely mono-alkynyl-PEG, α, ω -bis-alkynyl-PEG and α, ω -bis-azido-PEG. The use of bifunctional PEG polymers resulted in the formation of covalently cross-linked silicon nanoparticles in the form of colloidal arrays. The colloidal PEGylated silicon nanoparticles display a strong PL emission in water and exhibit promise for a range of biomedical applications, considering the biocompatibility and low cytotoxicity of their components.

3.2 Results and Discussion

3.2.1 Synthesis and characterization of initially functionalized silicon nanoparticles

Functionalized silicon nanoparticles were prepared by a mechanochemical synthesis using reactive high-energy ball milling (see Figure 3.1). Chloro-terminated and alkyne-terminated silicon nanoparticles were directly obtained after reactive high-energy ball

milling of a silicon wafer with a mixture of ω -chloroalkynes or α,ω -diynes, respectively, in the presence of a large amount of a terminal alkyne (1-pentyne or 1-hexyne [1:4 v/v]). The terminal alkyne reacts with the freshly prepared silicon surface in a roughly statistical manner during the RHEBM and thus acts as diluents to the functional groups on the surface. Additionally, the use of a terminal alkyne as the principal component of the reactive mixture reduces the occurrence of “hairpinning”, or the formation of loops, that would result from the reaction of both ends of the α,ω -diynes with the same surface. Azido terminated silicon nanoparticles were easily synthesized through the reactions of chloro-terminated silicon nanoparticles with NaN_3 in DMF.^{108b}

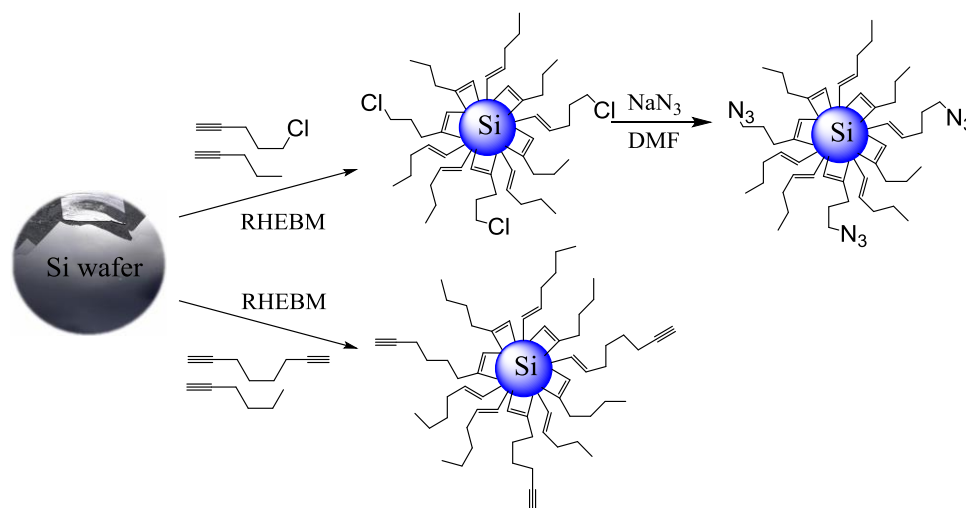


Figure 3.1 Synthesis and initial functionalization of silicon nanoparticles

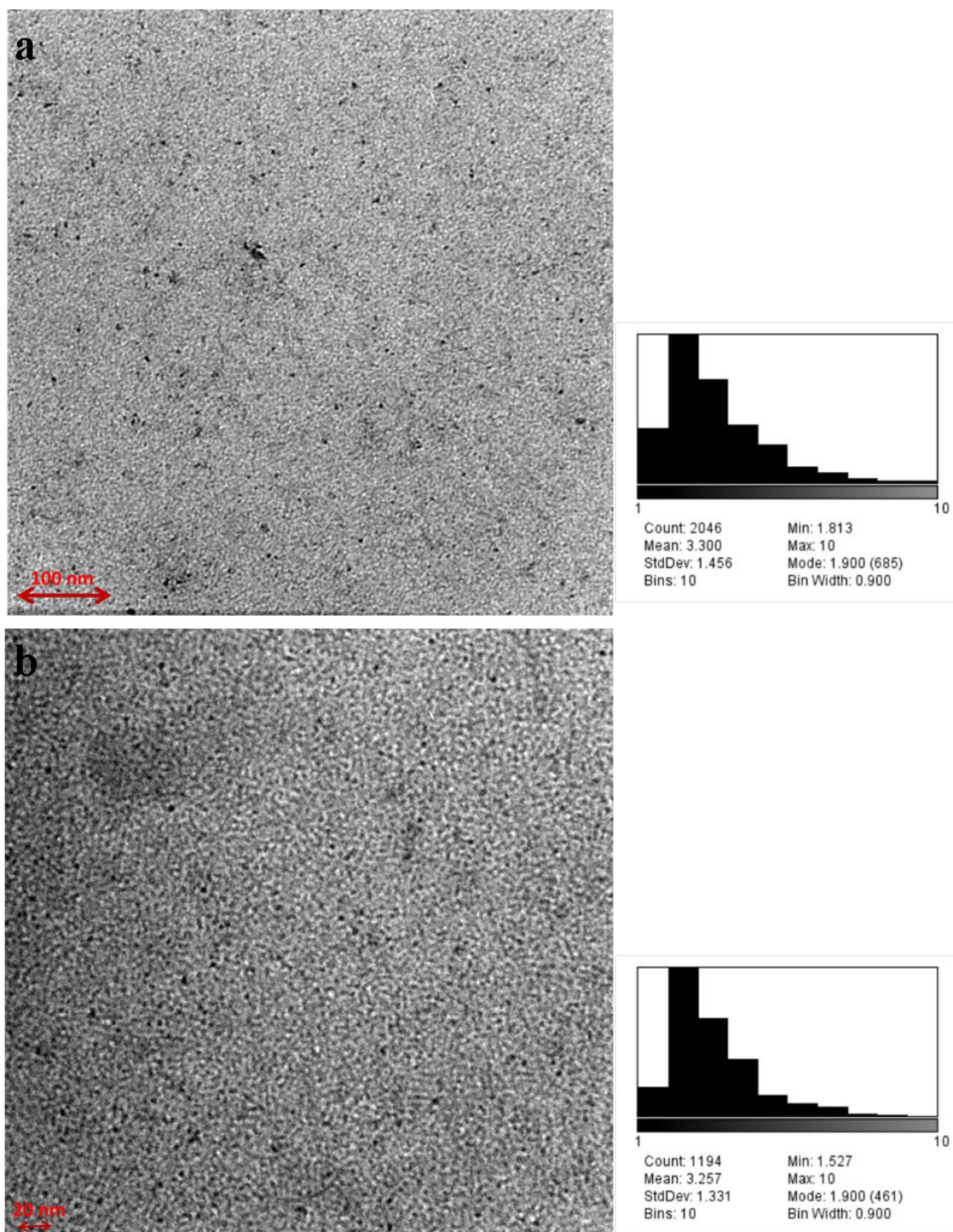


Figure 3.2 TEM image of ω -alkynyl-octenyl (20%)-Si nanoparticles (a) and ω -azido-pentenyl (20%)-Si nanoparticles (b) and their corresponding particle size distribution histograms

The particle size distribution of the ω -alkynyl-octenyl (20%)-silicon nanoparticles (Figure 3.2a) and the ω -azido-pentenyl (20%)-silicon nanoparticles (Figure 3.2b) as obtained from TEM images gave average diameters of 3.3 ± 1.5 nm and 3.3 ± 1.3 nm, respectively. The distributions were obtained from approximately 2050 and 1200 nanoparticles, respectively, from different parts of the TEM grid. Since the short alkyl chains are either indiscernible by TEM due to insufficient contrast, or have been burned off due from the electron beam, these values represent the silicon core alone, and not the shell. The uniform sizes observed when different ligands were employed suggest that the generation of silicon nanoparticles is both reproducible, and independent of the pendant functionalities on the ligands.

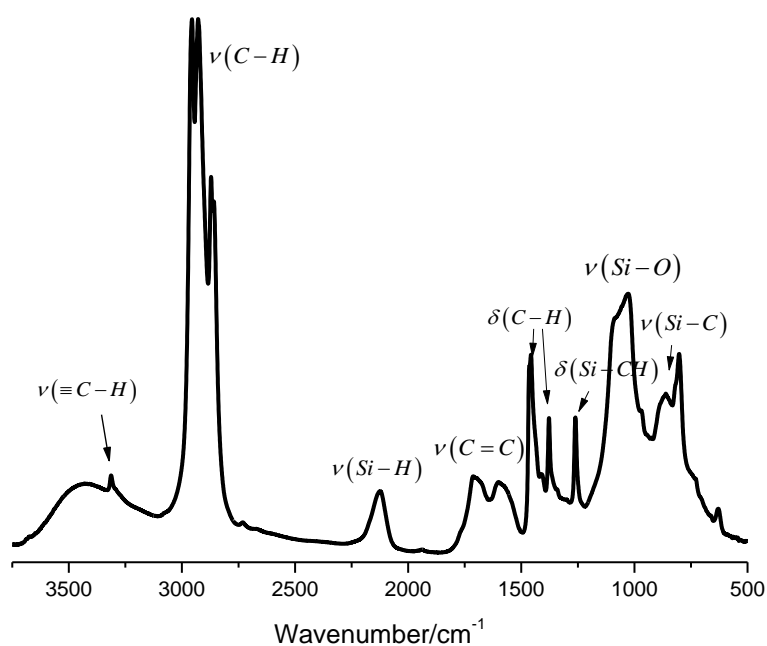


Figure 3.3 FTIR spectrum of ω -alkynyl-octenyl (20%)-Si nanoparticles

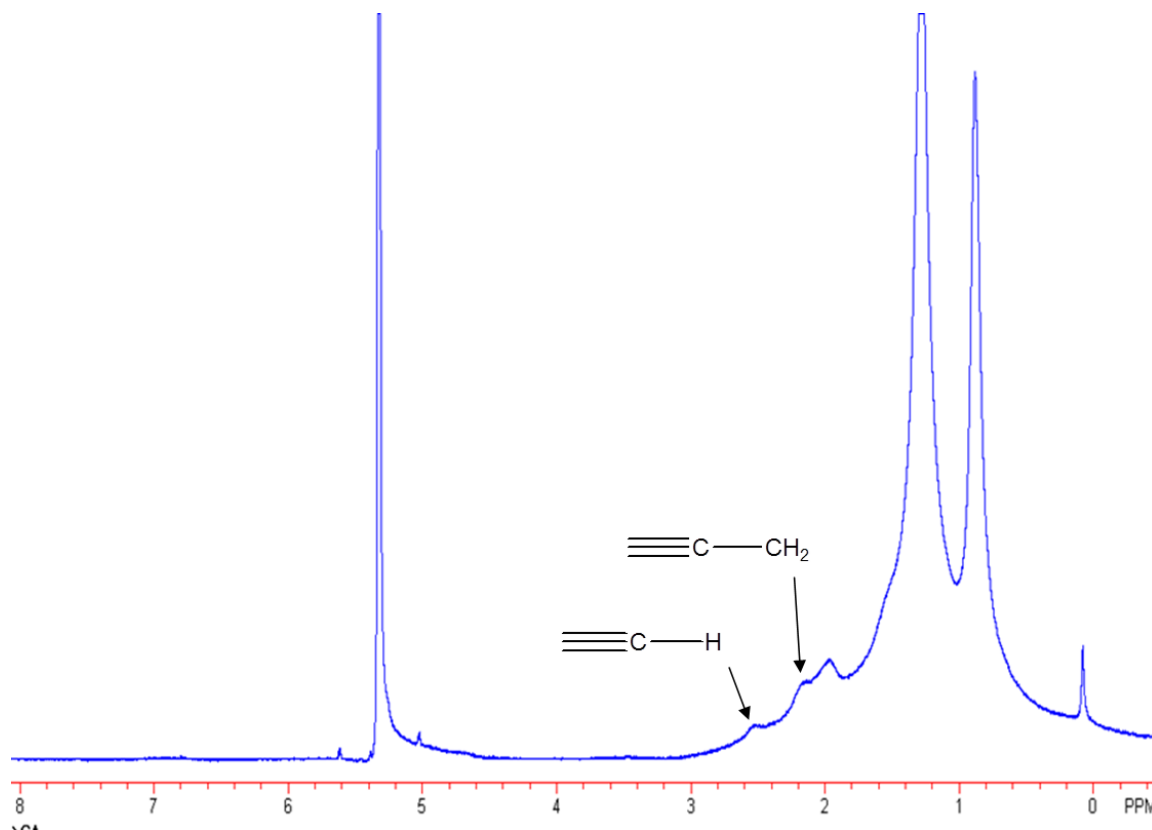


Figure 3.4 ^1H -NMR spectrum of ω -alkynyl-octenyl (20%)-Si nanoparticles

The FTIR (Figure 3.3) and the ^1H -NMR (Figure 3.4) spectra of the ω -alkynyl-octenyl (20%)-Si nanoparticles show evidence for the terminal alkyne group in the silicon nanoparticle shell. The peak at 3315 cm^{-1} in the FTIR spectrum is attributed to $\nu(\text{C-H})$ of the alkyne moiety whereas a weak peak at 2200 cm^{-1} is attributed to the $\nu(\text{C}\equiv\text{C})$ stretch. Resonances in the ^1H NMR spectrum at 2.2 ppm and 2.6 ppm are assigned to the alkyne functionalities, $\text{CH}_2-\text{C}\equiv\text{C}$ and $\text{H}-\text{C}\equiv\text{C}$, respectively.

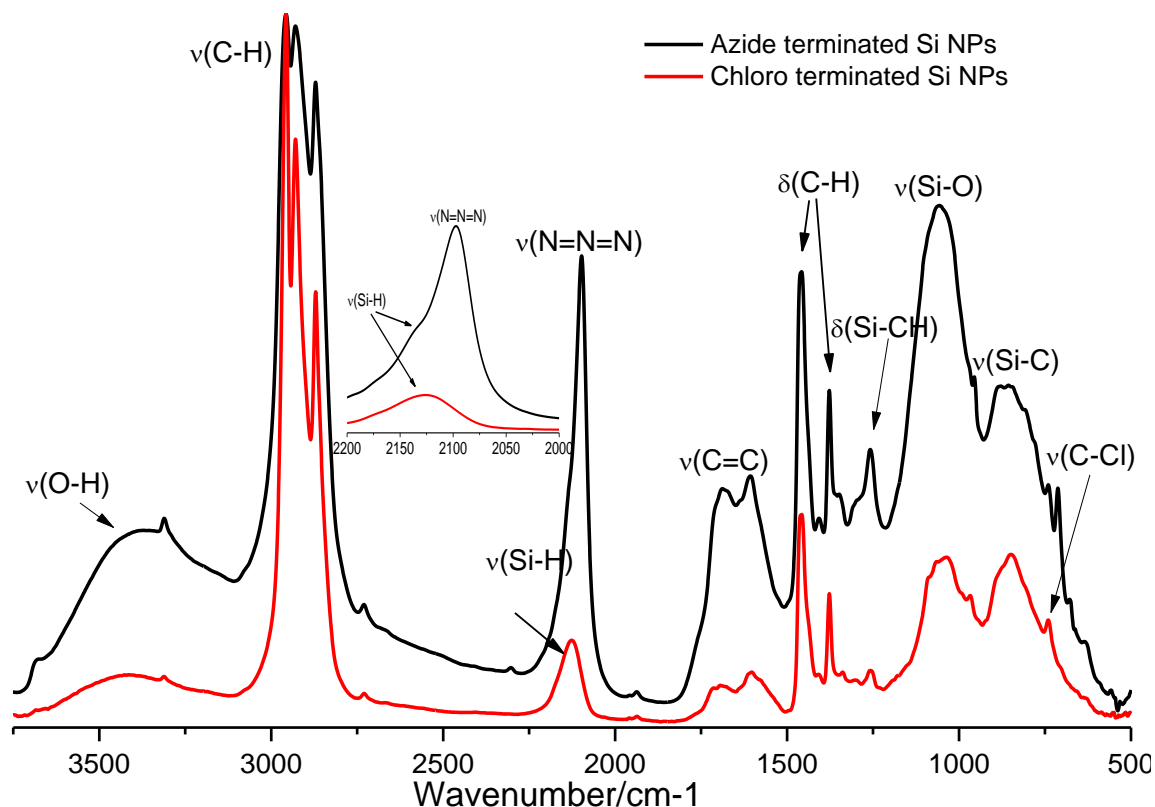


Figure 3.5 FTIR spectra of ω -chloro-pentenyl (20%)-silicon nanoparticle and ω -azido-pentenyl (20%)-Si nanoparticles

Figure 3.5 shows the FTIR spectra of both chloro-terminated and azide-terminated Si nanoparticles. The spectra were normalized to the C-H stretching peaks since both nanoparticles have the same alkenyl chains. A strong absorbance at $\sim 2100\text{cm}^{-1}$ in the FTIR spectrum of azide-terminated Si nanoparticles is assigned to $\nu(\text{N}=\text{N}=\text{N})$. The O-H stretching peak may be due to some of the Si-H were oxidized to Si-OH during the reaction. The ^1H NMR (Figure 3.6) spectra of both functionalized Si nanoparticles are also consistent with the presence of terminal chloro and azide groups in the ligand shell. The electronegative chloro and azide groups result in methylene resonances which are shifted downfield in the ^1H NMR spectra, at 3.4 for the chloro-functionalized nanoparticles and 3.2 ppm for the azido-functionalized nanoparticles.

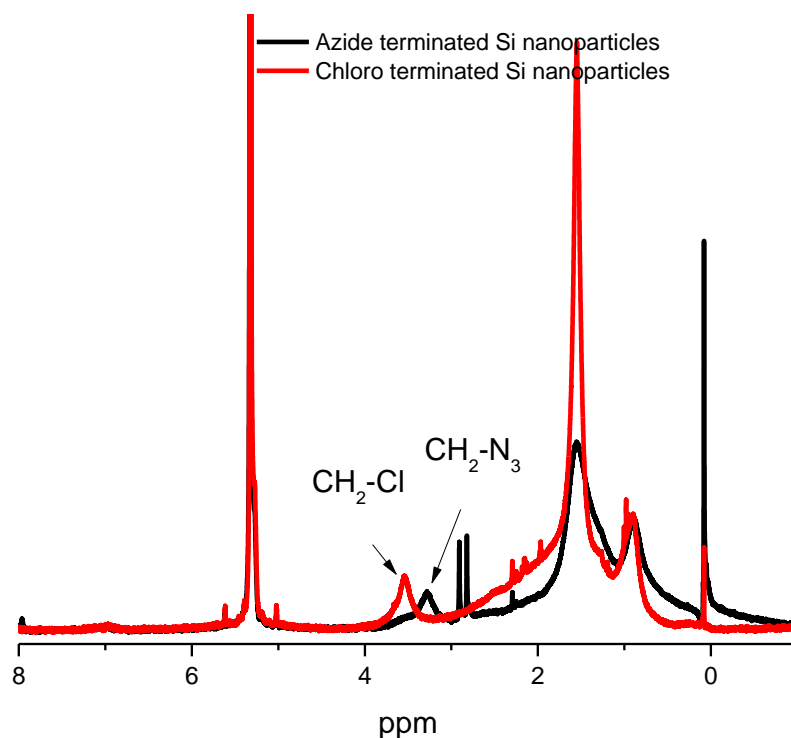


Figure 3.6 ^1H -NMR spectrum of ω -chloro-pentenyl (50%)-silicon nanoparticle and ω -azido-pentenyl (50%)-Si nanoparticles

All of the silicon nanoparticles show a broad, continuous UV-Vis absorption tailing at around 600 nm (Figure 3.7). The emission spectra of alkyne terminated and azido terminated Si nanoparticles were recorded with various excitation wavelengths, ranging from 300 to 400 nm in CH_2Cl_2 . All the nanoparticles being studied show a strong emission in the range of 300 to 700 nm, consistent with the emission spectra of other functionalized silicon nanoparticles formed by RHEBM. The broadness of the emission spectra is consistent with the polydispersity of the silicon nanoparticles.

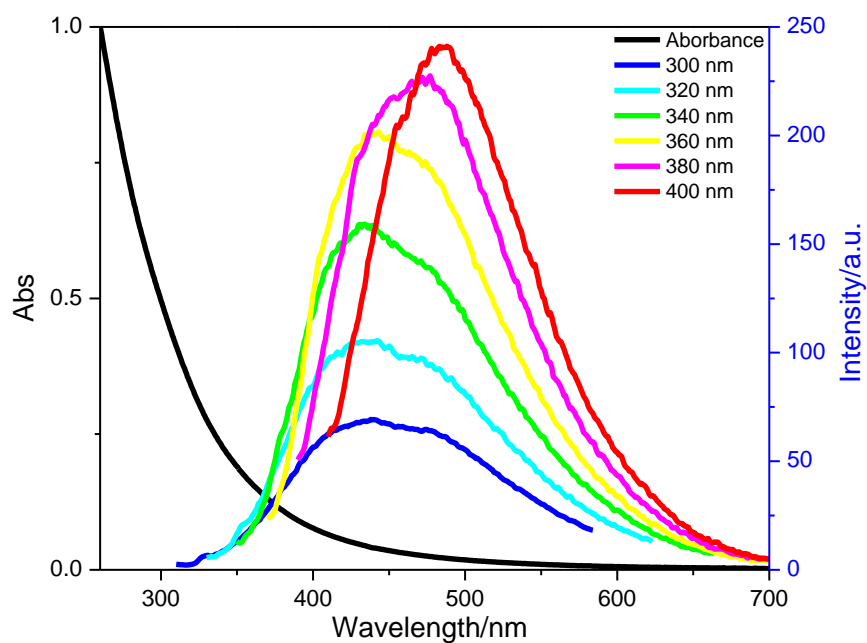
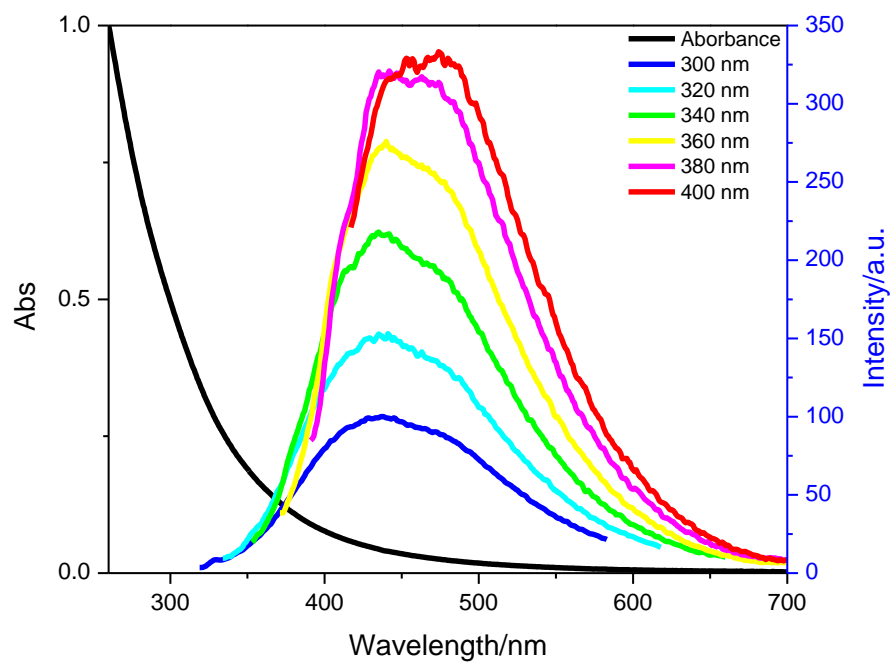


Figure 3.7 UV-Vis absorption and emission spectra of ω -alkyne-octenyl (20%)-Si nanoparticles (top) and ω -azide-pentenyl (20%)-Si nanoparticles (bottom) in CH_2Cl_2

3.2.2 PEGylated water soluble silicon nanoparticles

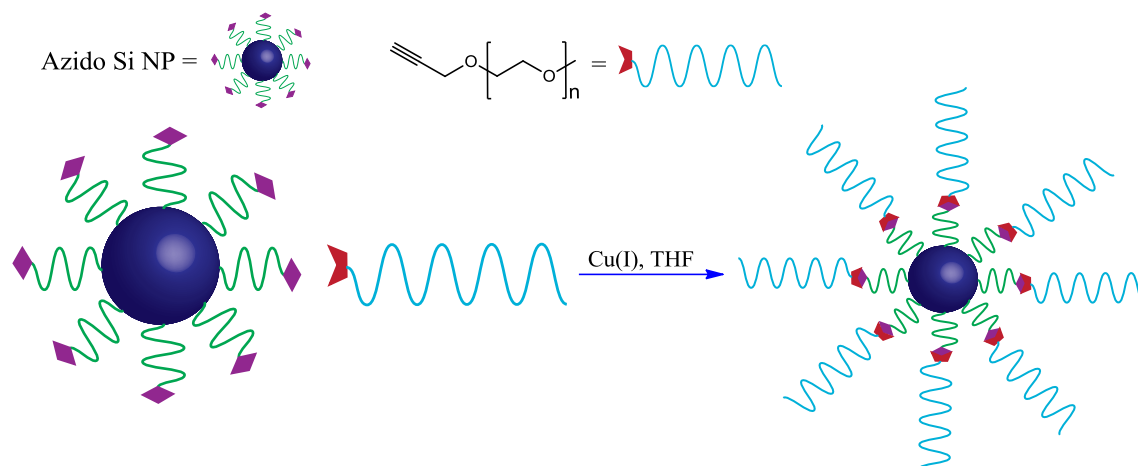


Figure 3.8 Illustration showing the preparation of PEGylated silicon nanoparticles

Water soluble PEGylated core-shell Si nanoparticles were obtained in a CuAAC “click” reaction between ω -azido-pentenyl (50%)-Si nanoparticles and mono-alkynyl PEG (2KDa) (see Figure 3.8). Si nanoparticles with 50% azide surface coverage were used in order to obtain PEGylated Si nanoparticles with maximized grafting PEGs on the surface. “Click” chemistry is an attractive tool for functionalizing silicon nanoparticles because of its high yields, modular approach, and broad functional group tolerance.⁵⁶ The copper catalyzed azide-alkyne cycloaddition (CuAAC) in particular is one of the most efficient “click” reactions due to its high selectivity and mild reaction conditions.^{57, 59}

Changes in the FTIR spectra (Figure 3.9) show that both the $\nu(\text{N}=\text{N}=\text{N})$ from the azide group of the silicon nanoparticles at 2100 cm^{-1} and the alkyne C-H stretch of the reacting PEG at 3250 cm^{-1} disappear during the course of the reaction, while a new peak for the triazole group of the PEGylated silicon nanoparticles appears at 3140 cm^{-1} . Additionally, a new resonance for the triazole proton of the PEGylated silicon nanoparticles is also observed at 7.6 ppm in the ^1H NMR spectrum (Figure 3.10) which is

consistent with the result from the FTIR spectrum. These spectral changes indicate that the “click” reaction of the alkyne-PEG with the azido-capped Si nanoparticles proceeded with high conversion.

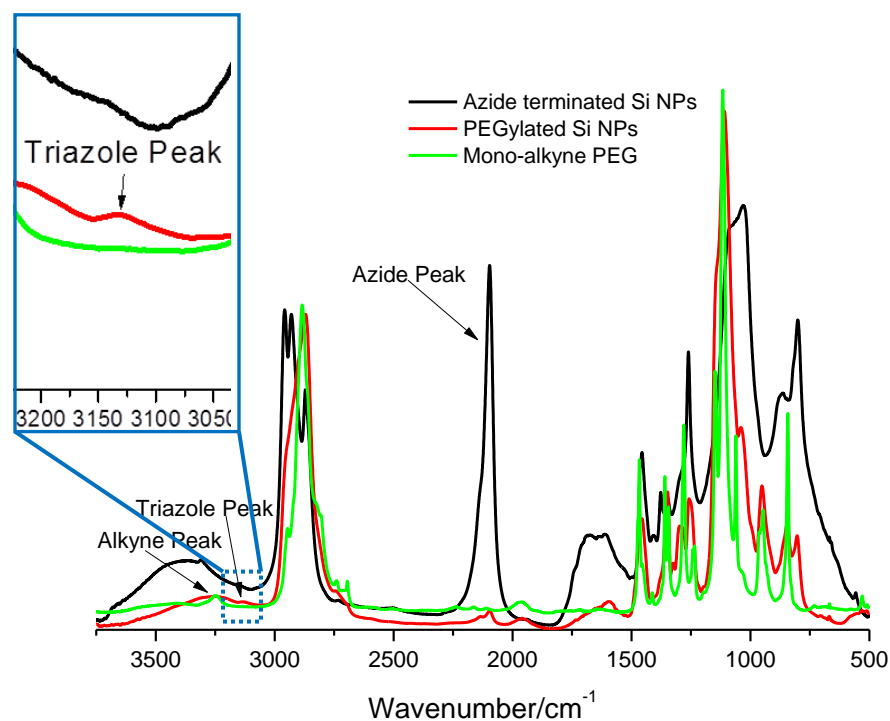


Figure 3.9 FTIR spectrum of ω -azido-pentenyl (50%)-Si nanoparticles, mono-alkyated-PEG and PEGylated silicon nanoparticle

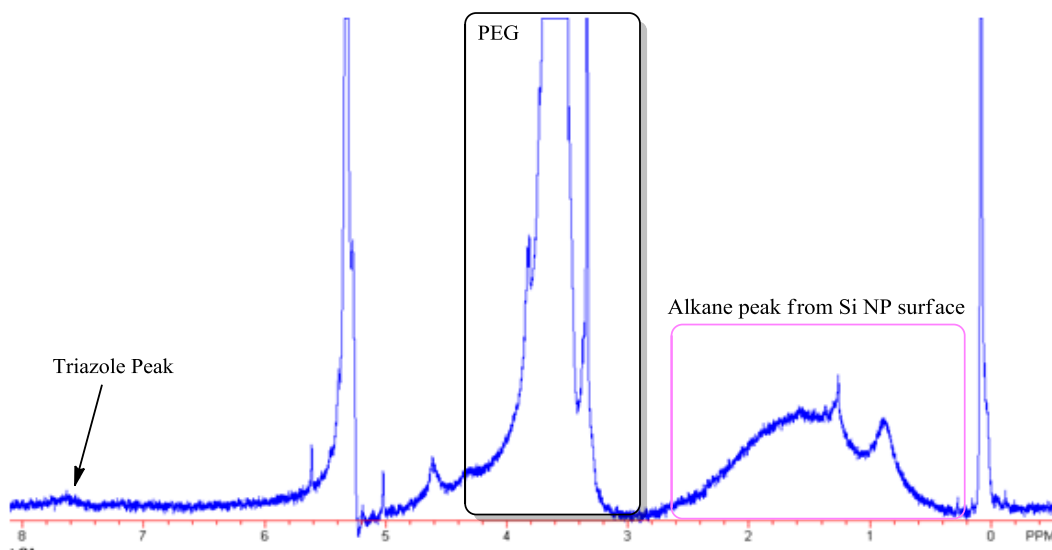


Figure 3.10 ^1H NMR spectrum of PEGylated silicon nanoparticles

A typical TEM image of the PEGylated silicon nanoparticles from a dispersion of the nanoparticles in water shows the contrast between the dark silicon core and light grey PEG shell very clearly (Figure 3.11 top). Many of the particles in the image are clearly isolated nanoparticles, however a number of smaller aggregates are also clearly apparent. The loose aggregates are likely formed through interdigitization of the PEG side chains since intercore distances in the aggregates range from 8-20 nm. In solution, the PEGylated Si nanoparticles show a distribution of hydrodynamic diameters centered at 45 nm as measured by dynamic light scattering (DLS). This compares to an average hydrodynamic diameter in CH_2Cl_2 of 8 nm for the azido functionalized nanoparticles and 17 nm for the initial alkyne-PEG polymer (Figure 3.11 bottom). Since the chain length of the all *trans* conformation of PEG is about 16 nm (from MM2 calculations), the observed hydrodynamic diameter in PEGylated silicon nanoparticles is very reasonable for a population of largely unaggregated nanoparticles (8nm (core) + 2 x 16 nm (shell) = 40 nm).

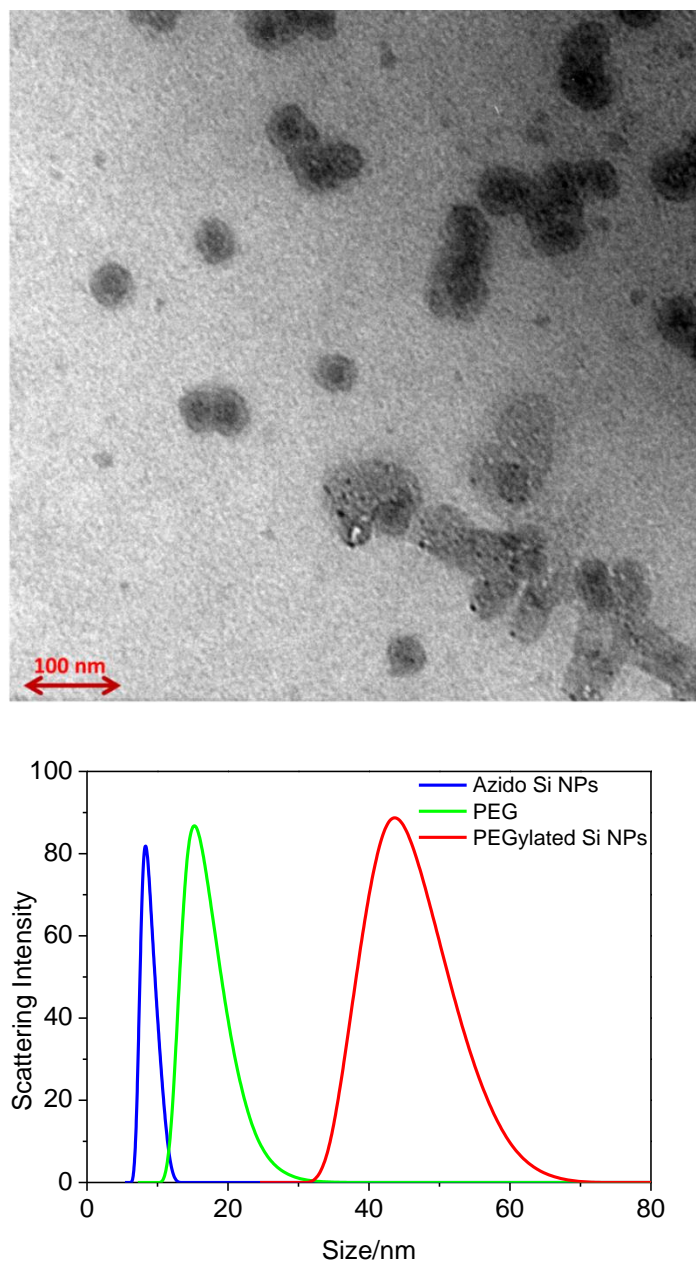


Figure 3.11 TEM image of PEGylated silicon nanoparticles (top) and multimodal particle size distributions from dynamic light scattering (DLS) of ω -azido-pentenyl (50%)-Si nanoparticles and PEGylated silicon nanoparticles (bottom)

The PEGylation of the nanoparticle surface improves its water solubility while maintaining the advantageous optoelectronic properties of the nanoparticle. Specifically,

the PEGylated nanoparticles demonstrate nearly identical UV-Vis absorption and PL emission spectra in aqueous solution (Figure 3.12) as the starting nanoparticles in CH_2Cl_2 . The PEG outer shell, however, imparts sufficient water solubility to form stable suspensions in cellular media. Cytotoxicity studies show that the PEGylated silicon nanoparticles exhibit essentially no cytotoxicity for both human colonic adenocarcinoma Caco-2 and rat alveolar macrophage NR8383 cells.⁸⁷

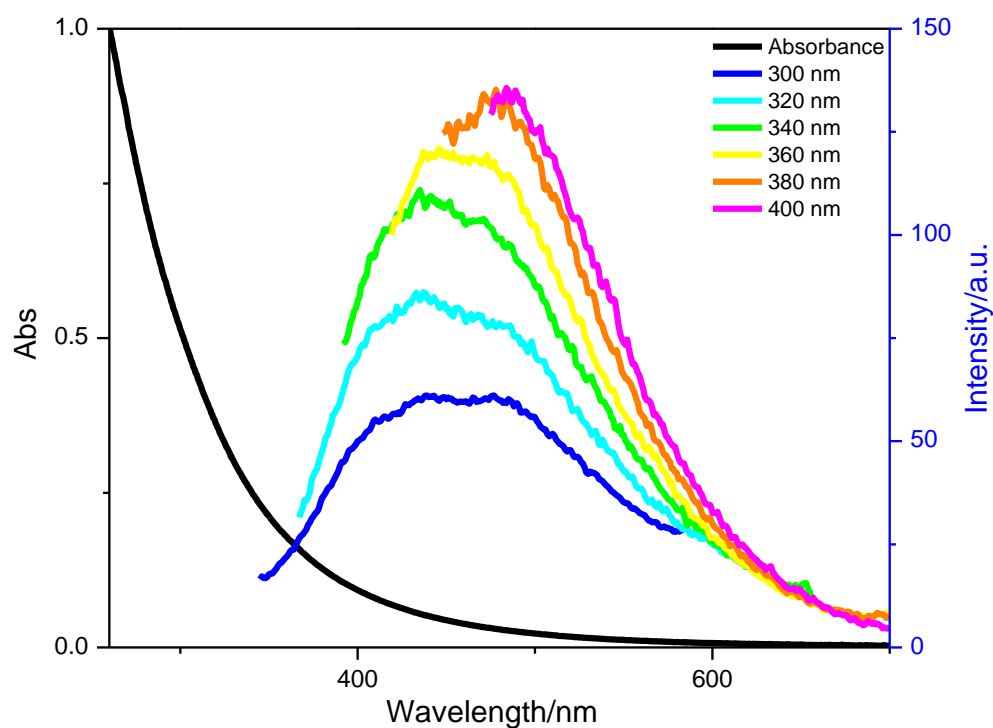


Figure 3.12 UV-Vis absorbance and PL emission of PEGylated silicon nanoparticles in distilled water

3.2.3 PEGylated silicon nanoparticle arrays

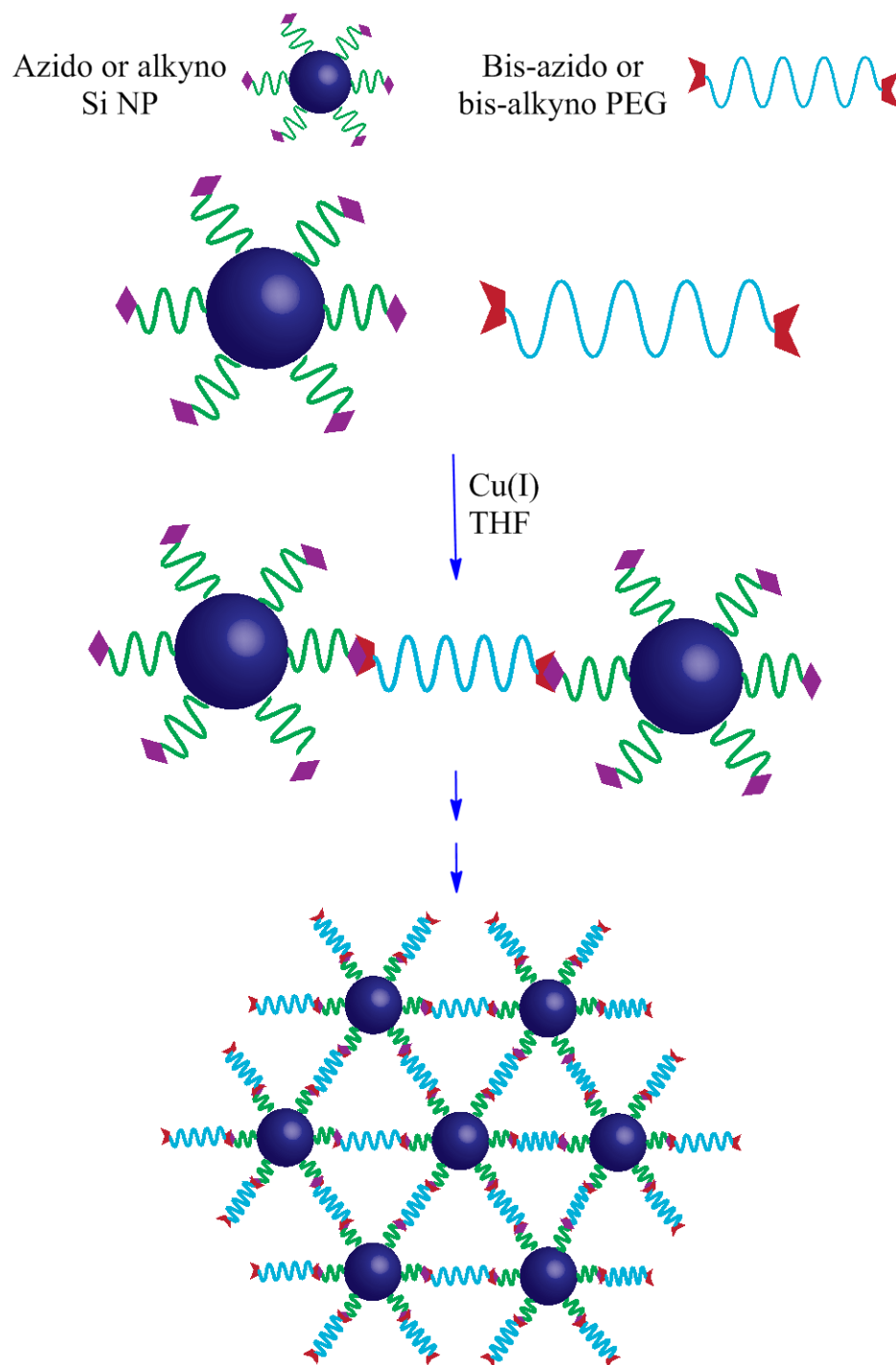


Figure 3.13 Illustration showing the preparation of a PEGylated silicon nanoparticle array

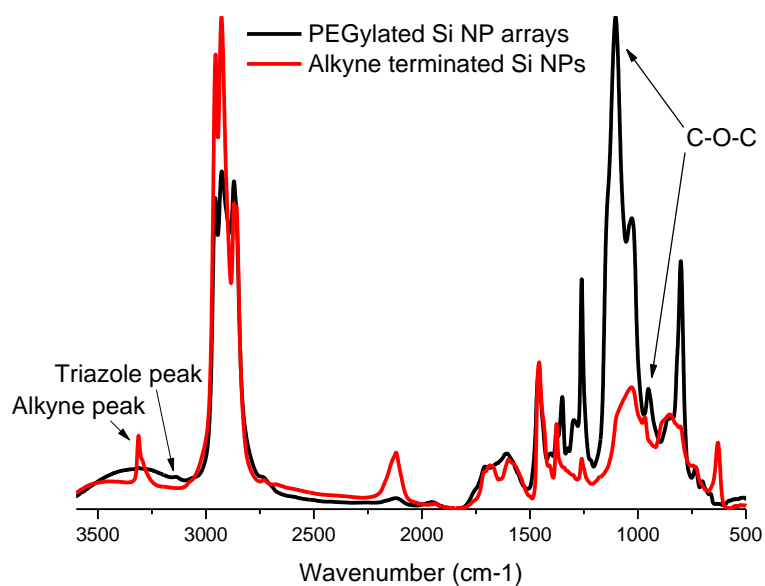
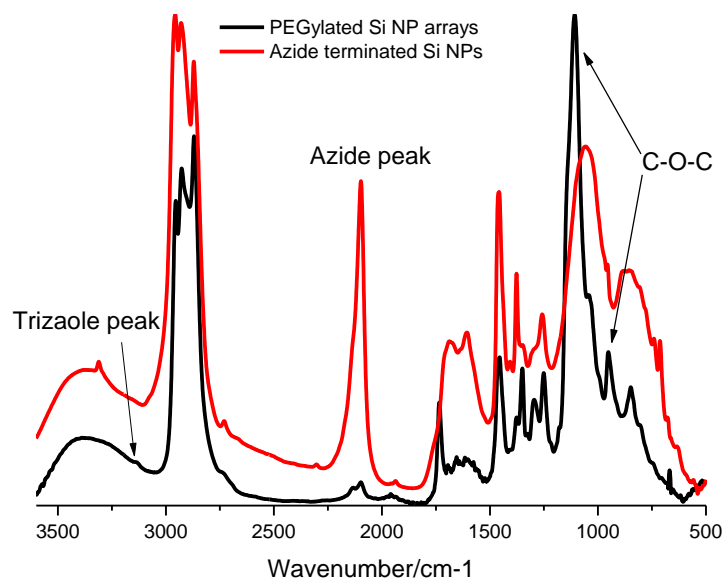


Figure 3.14 FTIR spectra of ω -azide-pentenyl (20%)-Si nanoparticles and PEGylated silicon nanoparticle arrays from azide terminated silicon nanoparticles and 2 KDa PEG (top), and FT-IR spectra of ω -alkynyl-octenyl (20%)-Si nanoparticles and PEGylated silicon nanoparticle arrays from alkyne terminated silicon nanoparticles and 2KDa PEG

Silicon nanoparticle arrays can be made within a fabric of PEG nano hydrogels (Figure 3.13) if difunctional PEGs are reacted with complementary multi-functional silicon nanoparticles. The cross-linking of the silicon nanoparticles is mediated via a CuAAC "click" reaction between either ω -azido-pentenyl (20%)-Si nanoparticles with α , ω -bis-alkynyl-PEG, or by reversing the placement of the functionalities with ω -alkynyl-octenyl (20%)-Si nanoparticles with α , ω -bis-azido-PEG. Si nanoparticles with 20% azide or alkyne surface coverage were used in order to reduce the cross-linking reaction between the nanoparticles and difunctional PEGs.

The FTIR spectra (Figure 3.14) show a peak from the azide group of the azide terminated silicon nanoparticles at 2100 cm^{-1} and a peak from the alkyne group of the alkyne terminated silicon nanoparticles at 3300 cm^{-1} both of which disappear after the "click" reaction, while the new peak for the triazole group from both of the PEGylated Si nanoparticles at 3140 cm^{-1} is observed.

Figures 3.15a and 3.15b clearly show that the nanoparticle arrays from azido-terminated silicon nanoparticles and 2 KDa bis-alkynyl-PEG are globular in shape and contain multiple 3 to 5 nm-sized silicon nanoparticles. The size distribution of the globular clusters ranges from 40 to 80 nm. The TEM images from Figure 3.15c and 3.15d show that the PEGylated nanoparticle arrays from alkyne-terminated silicon nanoparticles and 2 KDa bis-azido-PEG are globular but their boundaries are more irregularly shaped although they have a similar 40 to 80 nm size range. The cause of the differences in observed morphology, regular vs irregular edges, is uncertain but may be related to the mechanism of the CuAAC reaction by which the copper center undergoes prior coordination to an alkyne terminated silicon nanoparticle versus an alkyne

terminated PEG.¹²⁴ The hydrodynamic diameters of these two PEGylated silicon nanoparticle arrays are 100 nm and 120 nm, respectively, as measured by dynamic light scattering in CH₂Cl₂ (Figure 3.16). The diameters obtained from the TEM images are somewhat smaller than those found in solution by DLS and are likely due to the loss of associated solvent molecules in the sample preparation process.

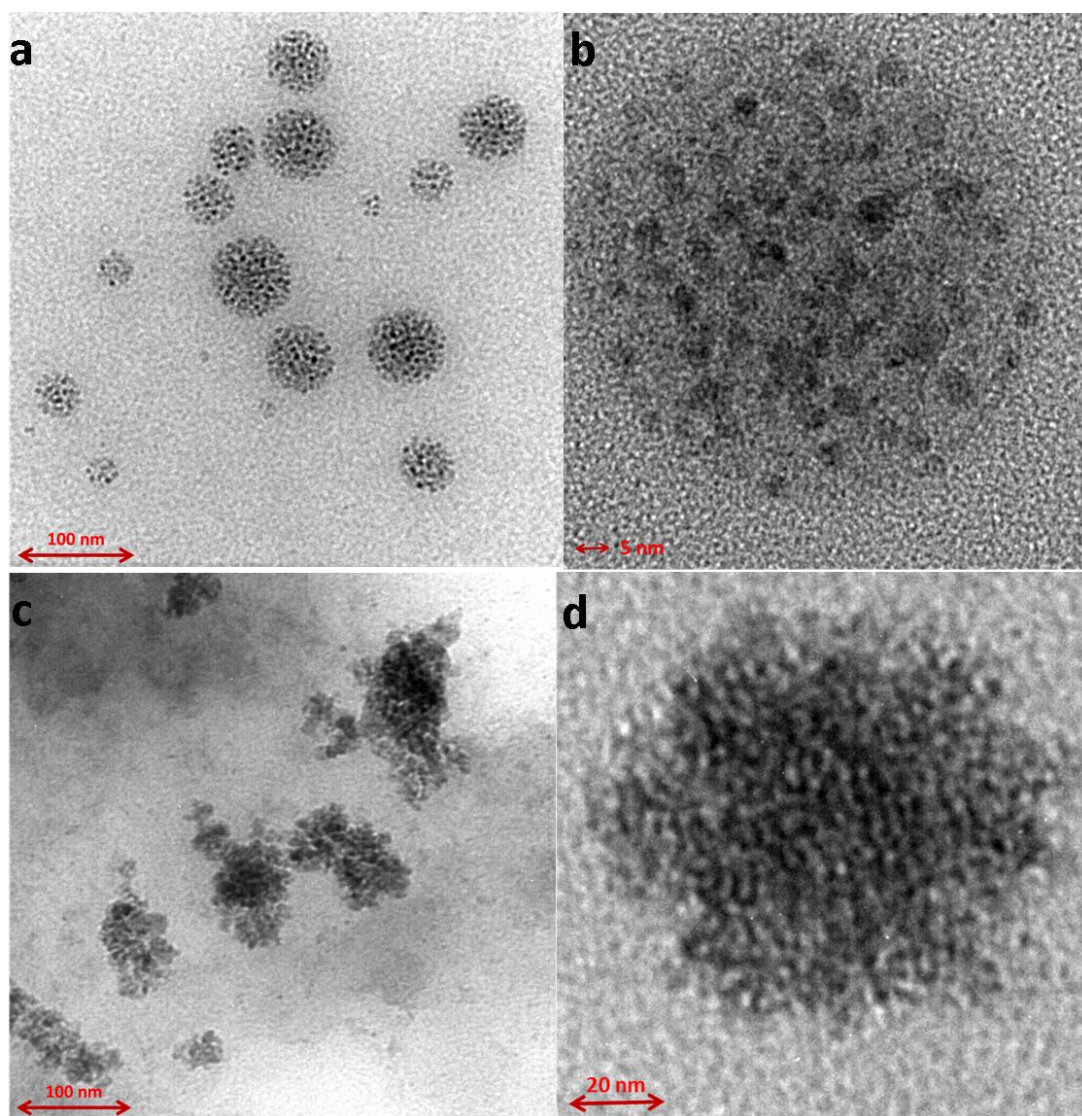


Figure 3.15 TEM and HRTEM image of PEGylated silicon nanoparticle arrays from azide terminated silicon nanoparticles with 2 KDa PEG linkers (a,b) and alkyne terminated silicon nanoparticles (c,d) with 2 KDa PEG linkers.

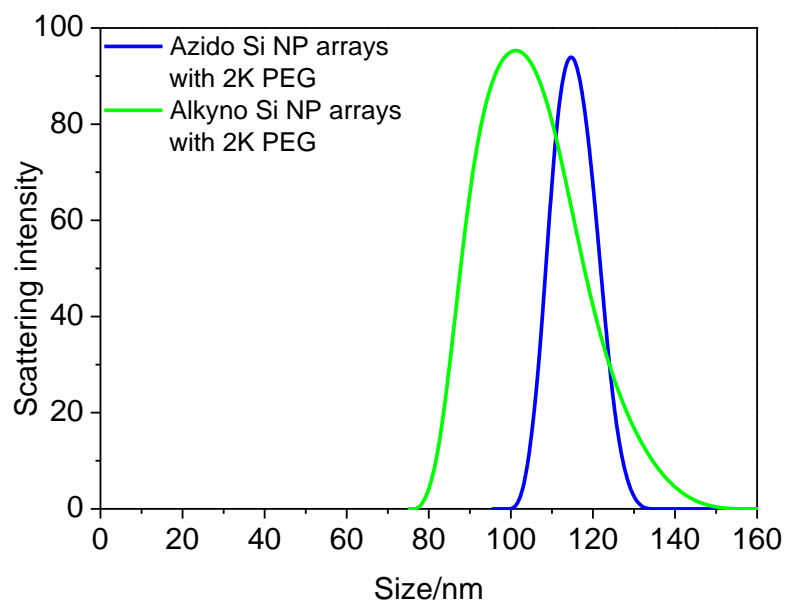


Figure 3.16 The size distribution of PEGylated silicon nanoparticle arrays from azide terminated silicon and alkyne terminated silicon nanoparticles from DLS in CH_2Cl_2 .

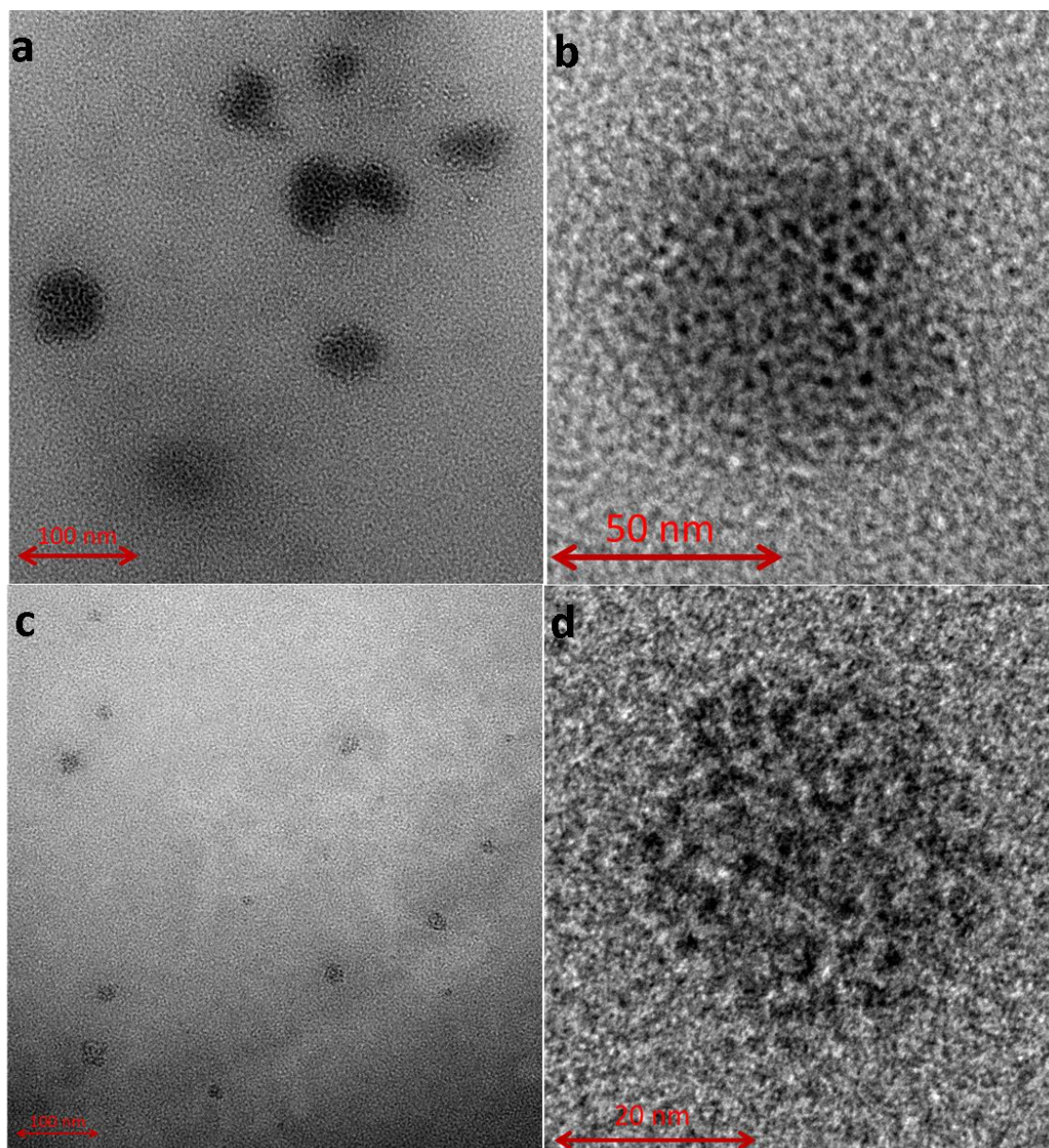


Figure 3.17 TEM and HRTEM image of PEGylated silicon nanoparticle arrays from azide terminated silicon nanoparticles with 1 KDa PEG (a,b) and 4.6 KDa PEG (c,d) linkers

Bis-alkynyl-PEGs of different lengths were used as linkers to probe if changing the linker length affected the inter-particle distance of the silicon nanoparticle arrays. Figures 3.17a-d clearly show that the nanoparticle arrays from the reaction of azido-terminated

silicon nanoparticles with 1 kDa and 4.6 kDa bis-alkynyl-PEGs are globular in shape and consist of 3 to 5 nm sized silicon nanoparticles. The size distribution of the globular clusters with 1kDa and 4.6 kDa PEG linkers are in the 40 to 80 nm range and 30 to 50 nm range, respectively. The TEM images show the PEGylated nanoparticle arrays with 1 kDa and 4.6 kDa PEG linkers have similar globular structures and inter-particle distances as the nanoparticle arrays with 2 kDa PEG linkers. However, these data are from TEM, which is expected to visualize the nano-arrays in their unswelled-state. The PEGylated nanoparticle arrays with 4.6 kDa PEG linkers tend to be smaller and contain less silicon nanoparticles than the other two arrays. This may be due to the reduced reactivity of the end groups of the larger molecular weight PEG with the nanoparticle shell. The overall globular form of the nanoparticle arrays may be due to the effects of surface tension on the lightly cross-linked web of nanoparticle spheres. Similar structures are found for silicon nanoparticles which are micelle-encapsulated with PEG polymers.¹¹⁹

The TGA (Figure 3.18) of three silicon nanoparticle arrays with different sizes of PEG linkers (1K, 2K, and 4.6K) show a dramatic weight loss at approximately 500°C due to the rupture of the Si-C bonds and loss of the PEG chains. The final weight losses of 74.2%, 86.8%, and 97.8% may be due to the increasing mass fraction of the PEG linkers in the nanoparticle arrays, or the unreacted PEG molecules inside the sample.

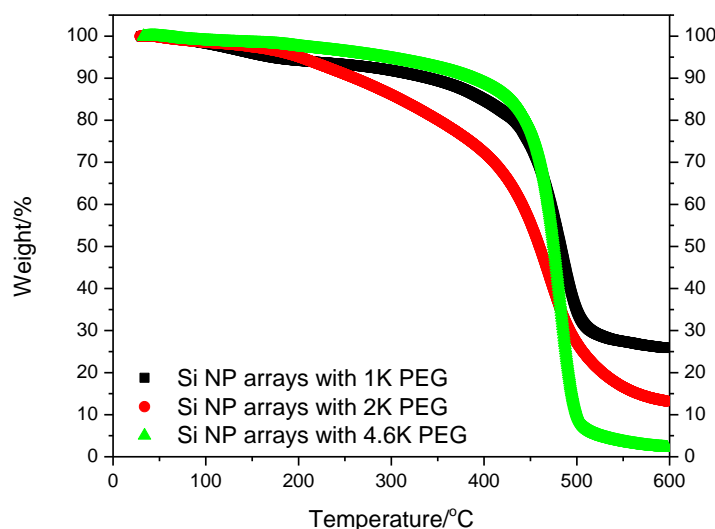
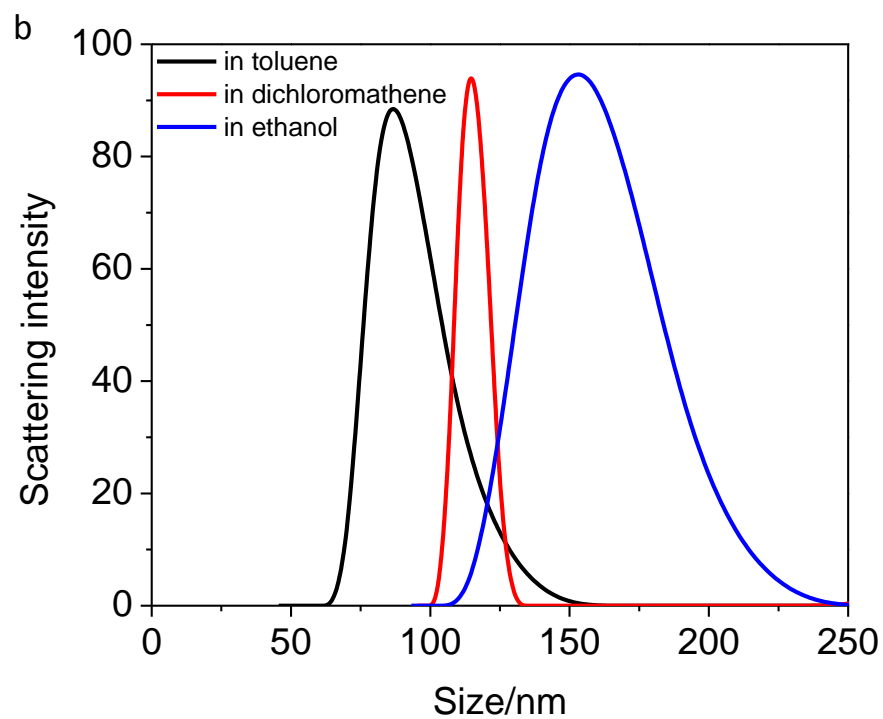
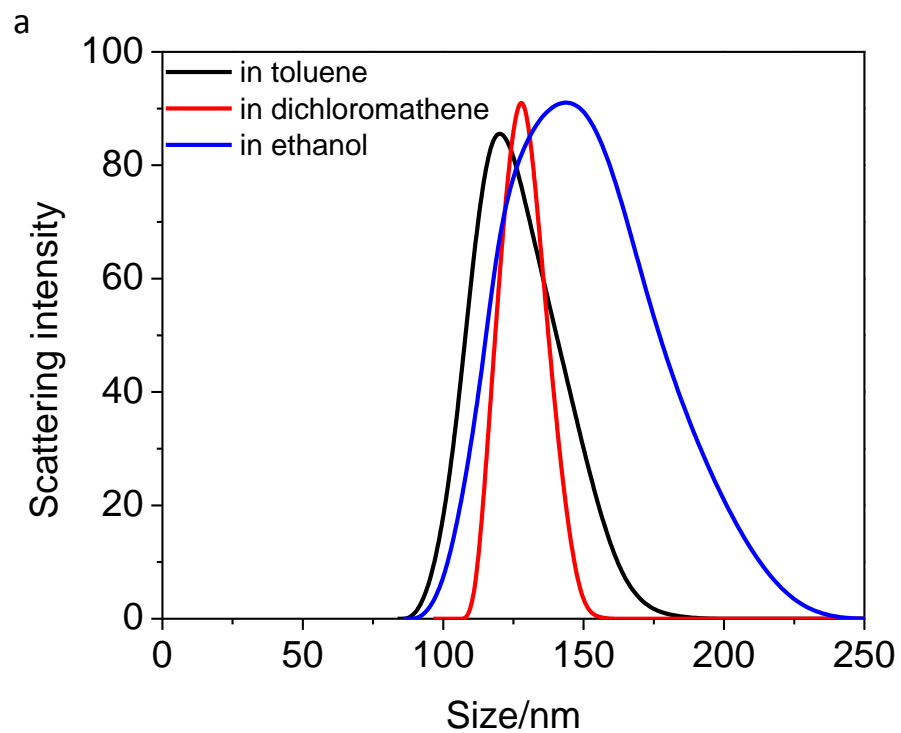


Figure 3.18 TGA of PEGylated Si nanoparticle arrays with PEG linkers of different sizes

The size distributions of the three PEGylated silicon nanoparticle arrays with 1 KDa, 2 KDa and 4.6 KDa PEG linkers, as measured by dynamic light scattering in toluene, dichloromethane and ethanol solvents are shown in Figure 3.19. The average hydrodynamic diameters of these three PEGylated silicon nanoparticle arrays in these different solvents are summarized in Table 3.1. The sizes of the arrays increase with the solvent polarity, which parallels the increasing compatibility of the PEG molecules in polar solvent.¹²⁵ The size of silicon nanoparticle arrays with 1 KDa, 2 KDa and 4.6 KDa PEG linkers increase by 28 nm, 64 nm and 76 nm, respectively, in going from toluene to ethanol as a solvent. The degree of swelling, similar to those of simple nano-hydrogels, reflects an increasing degree of internal solvent-polymer interactions which is constrained by the cross-linking. As predicted, increasing the length of the PEG spacers enables a greater degree of swelling in polar solvents, relative to the unswollen state in non-polar solvents.



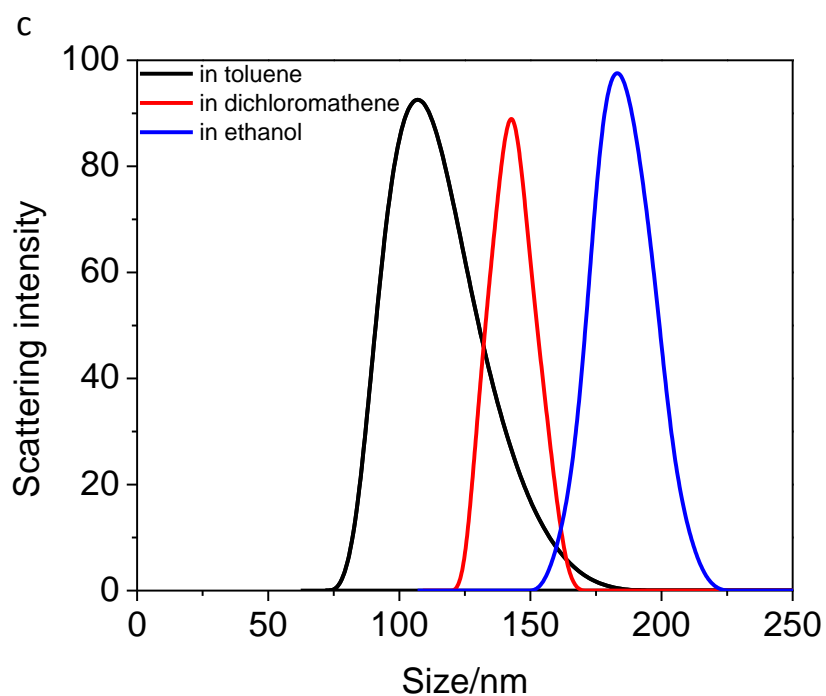
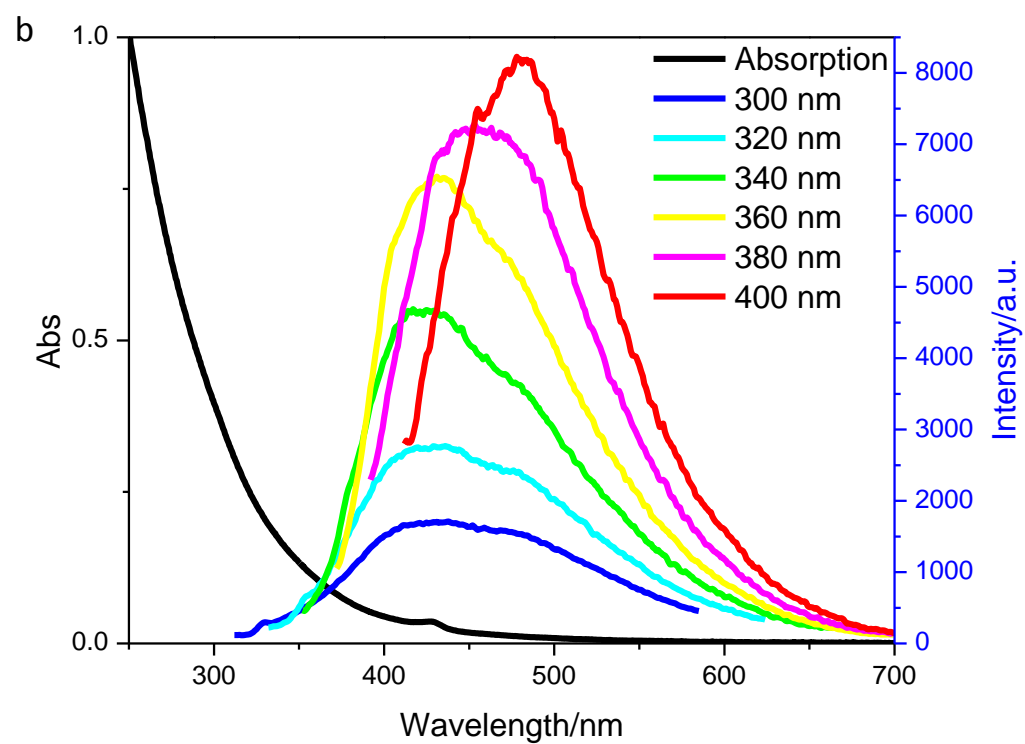
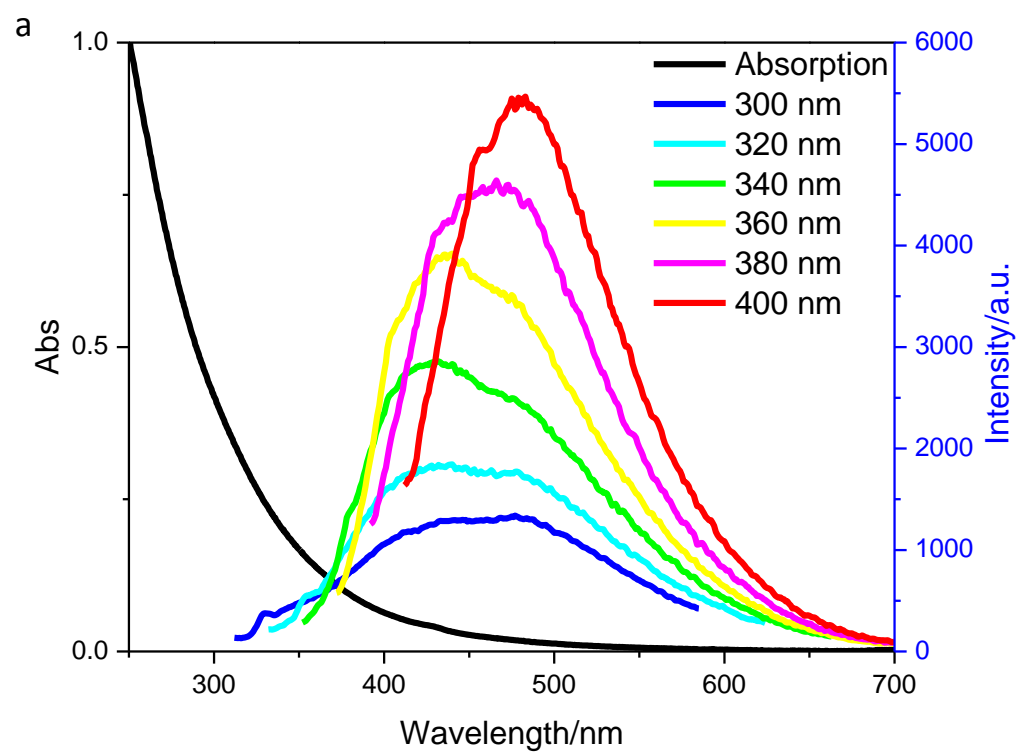


Figure 3.19 Multimodal size distribution of PEGylated silicon nanoparticle arrays from azide terminated silicon nanoparticles with 1 KDa PEG (a), 2 KDa PEG (b) and 4.6 KDa PEG (c) linkers in different solvents from DLS

Table 3.1 Sizes distribution of PEGylated silicon nanoparticle arrays from DLS

	Toluene	Dichloromethane	Ethanol
NP arrays with 1KDa PEG linkers	117 ± 23 nm	128 ± 12 nm	145 ± 34 nm
NP arrays with 2KDa PEG linkers	92 ± 19 nm	116 ± 9 nm	156 ± 32 nm
NP arrays with 4.6KDa PEG linkers	111 ± 23 nm	143 ± 10 nm	187 ± 15 nm



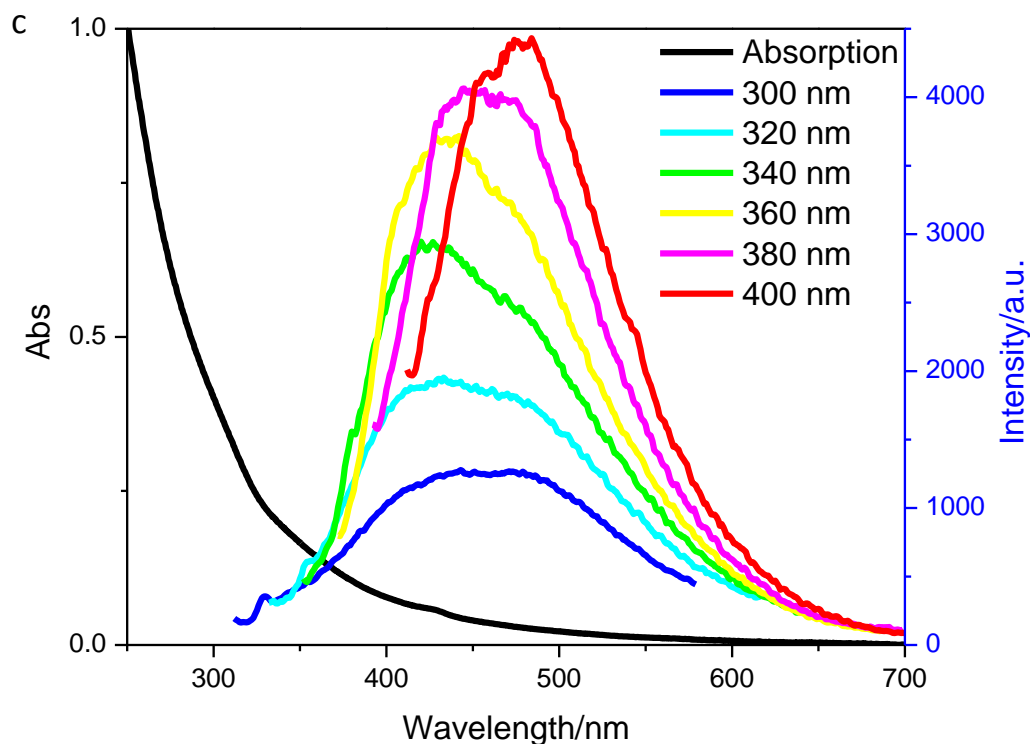


Figure 3.20 UV-Vis absorption and PL emission of PEGylated silicon nanoparticle arrays with 1 KDa PEG (a), 2 KDa PEG (b) and 4.6 KDa PEG (c) linkers in CH_2Cl_2 .

Finally, the PEGylated Si nanoparticle arrays also show similar UV-Vis absorption and PL emission as the ungrafted Si nanoparticles in CH_2Cl_2 (Figure 3.20), indicating little perturbation of the electronic structure of the individual silicon nanoparticles by the nanoarray environment.

3.3 Conclusion

Water soluble PEGylated silicon nanoparticles were successfully synthesized through the application of CuAAC “click” chemistry using azido functionalized nanoparticles and mono-alkynyl-PEG polymers. These nanoparticles exhibited vastly improved water solubility while maintaining the strong blue photoluminescence associated with the unmodified nanoparticles. In addition, a new class of PEGylated silicon nanoparticle arrays were prepared in a similar fashion, by crosslinking functionalized silicon nanoparticles with α,ω -bis-difunctional-PEG polymers. These colloidal photoluminescent nanoparticle arrays have flexible globular structures in which the swelling behavior may be readily tuned by controlling the length of the PEG linkers. The strong PL emission suggests these PEGylated silicon nanoparticle arrays may be used for bioimaging and labeling purposes. Additionally, the porous structure of these globular arrays portends the potential application in drug delivery, since the silicon nanoparticles are known to degrade *in vivo*.⁹¹ The ability to simultaneously incorporate both the imaging and therapeutic applications within one nanodevice, as well as tune the swelling behavior, suggests that these materials have relevance to the rapidly growing field of theranostics.

3.4 Experimental Section

3.4.1 Materials and methods

All chemicals were purchased from Sigma-Aldrich or Alfa Aesar, and employed without further purification unless specified. Tetrahydrofuran (THF) was distilled over sodium-benzophenone prior to use. Dichloromethane was distilled over CaH_2 before use. Silicon wafer (undoped, mirror finish, orientation [111]) was obtained from Silrec Corp. (Lexington, KY). Size exclusion chromatography (SEC) was used for the purification of nanoparticles. Bio-beads S-X1 were swollen overnight in dry THF and packed into a 40cm x 1.3cm glass column. Dichloromethane was used as an elution solvent. A concentrated nanoparticle solution (~50mg in 1 ml CH_2Cl_2) was added to the top of the column and eluted into 3x10ml fractions collected in separate vials. The first fraction was collected when the first colored band began to elute. This fraction contained nanoparticles and was used for the synthetic reactions. The second and third fractions, containing mostly impurities, were discarded.

3.4.2 Synthesis of ω -alkynyl-octenyl (20%)-Si nanoparticles

A silicon wafer (1.0 g, 36 mmol) was placed in a stainless steel milling vial along with two stainless steel milling balls (diameter of 1.2 cm, weighing approximately 8.1 g). The vial was filled in a Vacuum Atmospherics dry box under a nitrogen atmosphere with 4 mL (30 mmol) of 1,7-octadiyne and 16 mL (140 mmol) of 1-hexyne and then tightly sealed. The milling vial was placed in a SPEX 8000-D Dual Mixer/Mill, and high-energy ball milling was performed for 24 hours. After 24 hours of milling, the reaction mixture was centrifuged to remove larger particles. The solution contained alkyne-terminated silicon nanoparticles which were soluble in non-polar organic solvents. All of the

solvents were removed by vacuum distillation. The nanoparticles were redispersed in CH_2Cl_2 and purified by gel permeation chromatography (GPC) using Bio-beads S-X1 beads. Yield: 50-70 mg. $^1\text{H-NMR}$ (δ , 300 MHz, CD_2Cl_2): 2.5 (broad), 2.2 (broad), 2.0-0.5 (multiple broad peaks). FTIR (thin film on KBr plate): 3300 cm^{-1} (ν ($\equiv\text{C-H}$)), $2820\text{-}2990\text{ cm}^{-1}$ (ν (C-H)), 2100 cm^{-1} (ν (Si-H)), $1500\text{-}1750\text{ cm}^{-1}$ (ν (C=C)), $1465\text{-}1376\text{ cm}^{-1}$ (δ (C-H)), 1250 cm^{-1} (δ (Si-C)), $1190\text{-}850\text{ cm}^{-1}$ (ν (Si-O)), 830 cm^{-1} (ν (Si-CH_2)). UV-vis Absorption (in CH_2Cl_2): Single absorption with a tail up to 600 nm. PL emission (in CH_2Cl_2): 350-700 nm emission peaks by changing excitation wavelength from 300-400 nm.

3.4.3 Synthesis of ω -azido-pentenyl (20%)-Si nanoparticles and ω -azido-pentenyl (50%)-Si nanoparticles

A silicon wafer (1.0g, 36 mmol)) was ball milled for 24 h with a mixture of 4.0 mL (38 mmol) 5-chloro-1-pentyne and 16 mL 1-pentyne (160 mmol) for a 20% functionalized surface (or 10. mL (94 mmol) 5-chloro-1-pentyne and 10. mL (100 mmol) 1-pentyne for a 50% functionalized surface) to yield the chloro-terminated silicon nanoparticles. Sodium azide (0.30 g, 4.6 mmol) was added to a solution of 50 mg chloro-terminated silicon nanoparticles in 20 mL of dry dimethylformamide (DMF). The solution was stirred at 65°C overnight under nitrogen atmosphere. DMF was removed by vacuum distillation and dry THF was added. The mixture was centrifuged to remove NaCl and unreacted NaN_3 . The solution contained azide-terminated silicon nanoparticles which were soluble in THF. The solvent was removed by rotary evaporator. The nanoparticles were redispersed in CH_2Cl_2 and purified by GPC. Yield: 40-60 mg. $^1\text{HNMR}$ (δ , 300 MHz, CD_2Cl_2): 3.25 (s), 2.0-0.5 (m, broad). UV-vis Absorption (in

CH₂Cl₂): Single absorption with a tail up to 600 nm. PL emission (in CH₂Cl₂): 350-700 nm emission peaks by changing excitation wavelength from 300-400 nm. FTIR (thin film on KBr): 2820-2990 cm⁻¹ (ν (C-H)), 2100 cm⁻¹ (ν (N=N=N)), 1500-1750 cm⁻¹ (ν (C=C)), 1465-1376 cm⁻¹ (δ (C-H)), 1250 cm⁻¹ (δ (Si-CH₂)), 1190-850 cm⁻¹ (ν (Si-O)), 830 cm⁻¹ (ν (Si-C)). *Safety note: Large scale reactions of azide are prone to dangerous exothermic reactions. The use of chlorinated solvents in the presence of sodium azide must be avoided, as the byproducts may be highly explosive.*

3.4.4 Synthesis of functionalized PEG polymers

All the functionalized PEG polymers were synthesized and well characterized by Dr. Grayson's group.⁶⁹

3.4.5 Synthesis of PEGylated water soluble silicon nanoparticles

ω-Azido-pentenyl (50%)-Si nanoparticles (35 mg) and mono-alkynyl-PEG (20. mg, 10. μmol) were dissolved in 15 mL of THF. Cu(I) bromide (10. mg, 48 μmol) was added into the reaction mixture. The solution was stirred at room temperature overnight under nitrogen atmosphere. After removal of THF by vacuum distillation 20 mL of dichloromethane and 1 mL of ethylenediamine were added. The solution was subsequently washed three times with a saturated brine solution. The PEGylated silicon nanoparticles were purified by GPC to removed unreacted silicon nanoparticles and excess PEG. The yield was 47 mg. ¹HNMR (δ, 300 MHz, CD₂Cl₂): 7.6 (weak broad peak, triazole proton), 4.1-3.2 (multiple, all PEG methylene protons), 2.5-0.4 (multiple broad peaks, alkyl protons on the surface of silicon nanoparticle). FTIR (thin film on KBr): 3150 cm⁻¹ (ν (=C-H) on triazole ring), 2820-2990 cm⁻¹ (ν (C-H)), 1500-1750 cm⁻¹ (ν (C=C)), 1465-1376 cm⁻¹ (δ (C-H)), 1250 cm⁻¹ (δ (Si-C H₂)), 1100 cm⁻¹ (ν (C-O)), 1190-

850 cm^{-1} (ν (Si-O)), 830 cm^{-1} (ν (Si-C)). UV-vis Absorption (in water): Single absorption with a tail up to 600 nm. PL emission (in water): 350-700 nm emission peaks by changing excitation wavelength from 300-400 nm.

3.4.6 Synthesis of silicon nanoparticle arrays

Silicon nanoparticles (20% alkyne or azide terminated, 20. mg) and 7.5 μmol of the bifunctional PEG (with complementary azido or alkynyl groups) were added to 15 mL of THF. Cu(I) bromide (10 mg, 48 μmol) was added into the reaction mixture. The solution was stirred at room temperature overnight under a nitrogen atmosphere. The THF was removed by vacuum distillation and 20 mL dichloromethane and 1 mL ethylenediamine were added. The solution was washed three times with a saturated brine solution. The silicon nanoparticle arrays were purified by GPC to removed unreacted silicon nanoparticles and PEG. The yield of PEGylated silicon nanoparticle arrays from azide terminated silicon nanoparticles with 1 kDa PEG, 2 kDa PEG and 4.6 kDa PEG linkers were 22 mg, 28 mg and 19 mg, respectively; and the yield of PEGylated silicon nanoparticle arrays from alkyne terminated silicon nanoparticles with 2 kDa PEG linkers was 23 mg.

3.4.7 Analytical methods

3.4.7.1 NMR sample preparation and acquisition

NMR samples were prepared by vacuum drying ~1.5 mL of the silicon nanoparticle solution, adding 0.8 mL of the preferred deuterated solvent, and then transferring the solution to a 5 mm NMR tube. ^1H -NMR measurements were performed on a Bruker Avance 300 spectrometer equipped with a 5 mm BBO probe.

3.4.7.2 Infrared spectroscopy

FTIR spectra were recorded at 1 cm^{-1} resolution with 1000 scans on a Thermo Nicolet NEXUS 670 FTIR instrument. Samples were prepared as a thin film of passivated silicon nanoparticles prepared by depositing dichloromethane solution of silicon nanoparticles on a KBr plate. The FT-IR sample chamber was purged with dry nitrogen before collecting any data.

3.4.7.3 UV-vis absorption and photoluminescence spectroscopy

UV-Vis absorption spectra were recorded in a quartz cuvette (1cm), using a Cary 50 spectrophotometer and were corrected for the solvent absorption. The scan range was 200-800 nm with a 300 nm min^{-1} scan rate. Excitation-emission spectra were recorded in a quartz cuvette (1cm), using a Varian Cary Eclipse spectrofluorometer with a scan rate of 120 nm min^{-1} .

3.4.7.4 Transmission electron microscopy

High-resolution transmission electron microscopy (TEM) studies were performed with a JEOL 2011 TEM using an accelerating voltage of 200 kV or a Tecnai G2 TEM using an accelerating voltage of 300 kV. The EDX data were obtained in the TEM using an Oxford Inca or Bruker attachment, using a 3nm beam spot. TEM samples were prepared by dropping a sonicated diluted solution of silicon nanoparticles in toluene onto a carbon-coated 400 mesh carbon coated copper grid which placed on a filter paper. The filter paper soaked up the excess solution before inserting in grid in the TEM sample holder.

3.4.7.5 Dynamic light scattering

Dynamic light scattering (DLS) experiments were performed with a Brookhaven 90Plus particle size analyzer (90° , $\lambda = 660$ nm) at room temperature, using toluene, dichloromethane, and ethanol as solvents. The DLS measurements provided the intensity average based diameter of the particles (D_h), related, through Stokes Einstein equation, to the diffusion coefficient derived from intensity autocorrelation functions,¹²⁶ expanded in terms of cumulates.¹²⁷

3.4.7.6 Thermogravimetric Analysis

Thermogravimetric analysis (TGA) experiments were performed on a TA Instruments Hi-Res TGA2950 Thermogravimetric Analyzer. The samples (5-10 mg) were put in aluminum pans and then tested under flowing nitrogen atmosphere at a heating rate of $10^\circ\text{C}/\text{min}$ from room temperature to 600°C .

Chapter 4: Energy and electron transfer in silicon nanoparticle-based light-harvesting complexes

4.1 Introduction

The development of efficient, low-cost organic solar cells is one of the most attractive strategies for the conversion and storage of solar energy.¹²⁸ In the past several years, many studies have focused on artificial photosynthesis to construct efficient solar cells which mimic the natural photosynthesis system.¹²⁹ In natural systems, the light absorption and energy transfer to photosynthetic reaction centers are utilized by many photosynthetic light-harvesting complexes, which have stimulated people to design and build artificial photosynthetic antennas.¹³⁰ Porphyrins are one of the most popular chromophores for light-harvesting complexes due to their higher stability and ease of synthesis as compared to natural chlorophylls; their ability to strongly absorb in the visible region; and their ease of functionalization which allows for fine tuning of optical, physical, electrochemical and photovoltaic properties.¹³¹ Therefore, multiporphyrin arrays have been frequently synthesized via numerous approaches to study the light-harvesting and energy/electron transfer processes.¹³²

Imahori et al. have reported various nanoparticles including metal nanoparticles,¹³³ silica nanoparticles¹³⁴ and CdSe nanoparticles^{131a} as nanoscaffolds to organize porphyrins into multiporphyrin arrays. However, energy transfer quenching in metal nanoparticles by the metal surface limits the power conversion efficiency of the system,^{133a} while the silica nanoparticles exhibit no light-harvesting properties.^{131a} Moreover, the expense and toxicity of the CdSe nanoparticles limit their application as photosynthetic materials.

Silicon nanoparticles which have size dependent optical and electronic properties⁷⁵ and stability against photo-bleaching^{17, 22b, 27} have been considered as attractive alternatives for organic dyes and have shown great potential in photovoltaic applications. Additionally, several studies have been reported that the lifetime of the electronically excited-state of silicon nanoparticles can be on the order of nanoseconds which make them feasible for the energy transfer studies.^{17, 27} However, unlike CdSe nanoparticles, reports on energy transfer between silicon nanoparticles and energy acceptors are limited.^{17, 135}

In this study, silicon nanoparticles are used as nanoscaffolds for organizing the porphyrins to form light-harvesting complexes thereby enhancing the light absorption of the system. In particular, various multiple Zn-porphyrin functionalized silicon nanoparticles were synthesized via azide-alkyne “click” reactions between azide-terminated silicon nanoparticles and 5-(4-(prop-2-yn-1-yloxy))-phenyl-10,15,20-triphenyl-zincporphyrin. The energy transfer from silicon nanoparticles to porphyrin acceptors was investigated by both steady-state and time-resolved fluorescence spectroscopy. The energy transfer efficiency depended on the donor-acceptor ratio and the distance between the nanoparticle and the porphyrin ring. The addition of C₆₀ resulted in the formation of silicon nanoparticle-porphyrin-fullerene nanoclusters which led to charge separation upon irradiation of the porphyrin ring. The electron-transfer process between the porphyrin and fullerene was investigated by femto-second transient absorption spectroscopy.

4.2 Results and Discussion

4.2.1 Synthesis and characterization of initially functionalized silicon nanoparticles

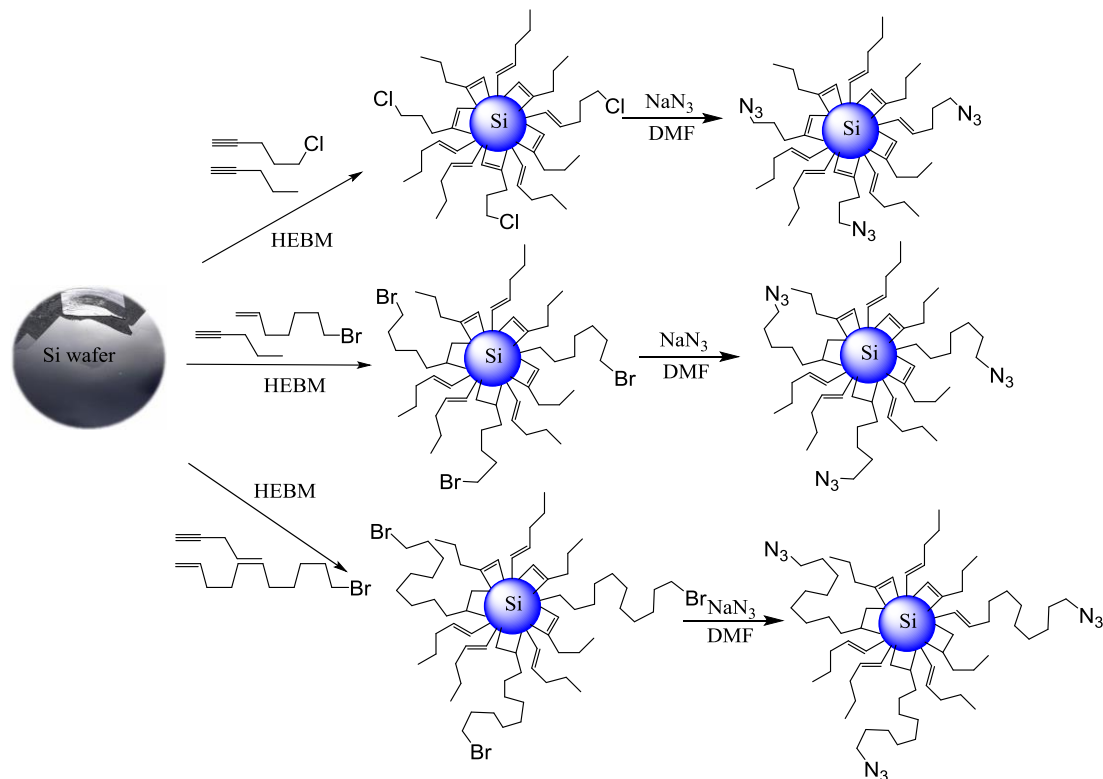


Figure 4.1 Synthesis of various azide-terminated silicon nanoparticles

Haloalkyl-terminated silicon nanoparticles with three different chain lengths were synthesized by reactive high energy ball milling (RHEBM) of a silicon wafer with a mixture of 1-pentyne with either 5-chloro-1-pentyne, 7-bromo-1-heptene or 11-bromo-1-undecene, respectively. The 1-pentyne can act as a diluent to the functional groups on the surface and roughly control the surface coverage of these functional groups. Azidoalkyl-terminated silicon nanoparticles were easily obtained through the reactions of haloalkyl-terminated silicon nanoparticles and NaN_3 in DMF (Figure 4.1).

4.2.1.1 Synthesis and characterization of ω -azidopentenyl Si nanoparticles

The synthesis and characterization of ω -azidopentenyl silicon nanoparticles (Si-C₅-N₃ NPs) have been discussed in Chapter 3.

4.2.1.2 Synthesis and characterization of ω -azidoheptyl Si nanoparticles

The ω -bromoheptyl silicon nanoparticles were directly obtained from reactive high-energy ball milling of a silicon wafer with a mixture of 7-bromo-1-heptene and 1-pentyne (1:2 v/v). The ω -azidoheptyl silicon nanoparticles (Si-C₇-N₃ NPs) were easily synthesized through the reactions of ω -bromoheptyl silicon nanoparticles with NaN₃ in DMF.

The ω -bromoheptyl silicon nanoparticles and ω -azidoheptyl silicon nanoparticles show similar FTIR and ¹H NMR spectra as the ω -chloropentenyl silicon nanoparticles and ω -azidopentenyl silicon nanoparticles. The FTIR (Figure 4.2, normalized to the C-H stretching peaks) and the ¹H NMR (Figure 4.3) spectra of both bromo-terminated and azide-terminated silicon nanoparticles are consistent with the presence of terminal bromo and azide groups in the ligand shell. The electronegative bromo and azide groups result in methylene resonances which are shifted downfield in the ¹H NMR spectra, at 3.4 for the bromo-functionalized nanoparticles and 3.2 ppm for the azido-functionalized nanoparticles. In addition, a strong absorbance at ~2100cm⁻¹ in the FTIR spectrum is assigned to $\nu(\text{N}=\text{N}=\text{N})$ on the azidoalkyl terminated silicon nanoparticles.

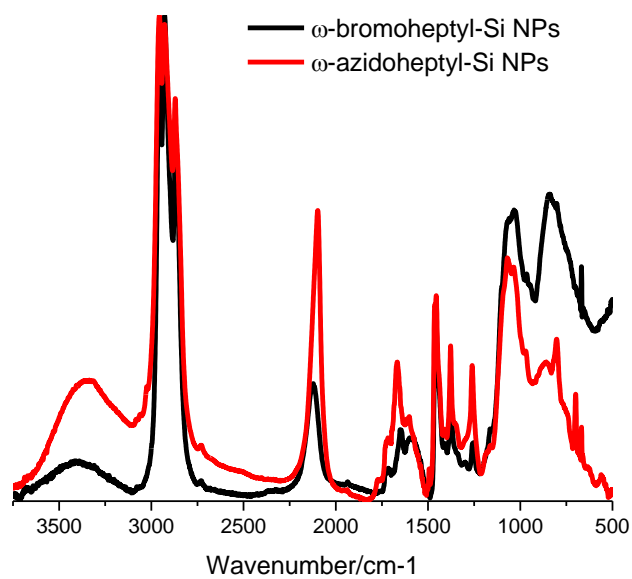


Figure 4.2 FTIR of ω -bromoheptyl Si nanoparticles and ω -azidoheptyl Si nanoparticles

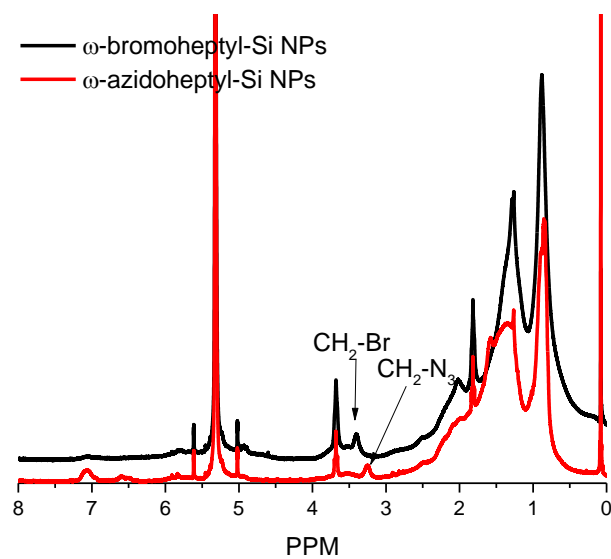


Figure 4.3 ¹H-NMR of ω -bromoheptyl Si nanoparticles and ω -azidoheptyl Si nanoparticles in CD₂Cl₂

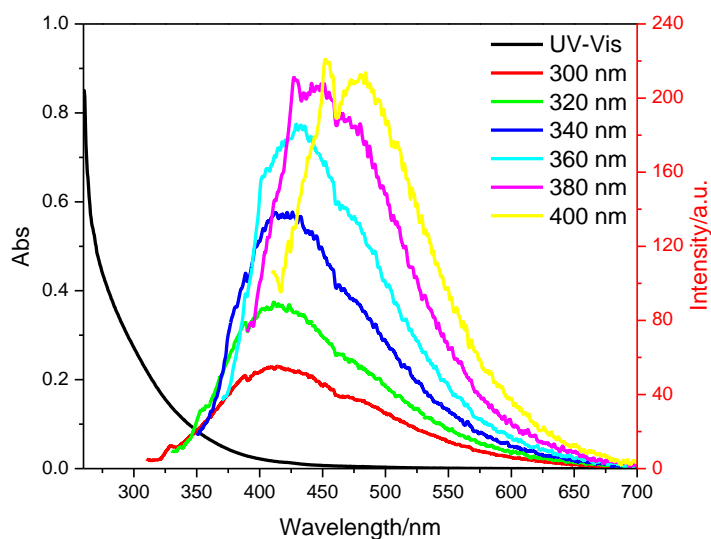
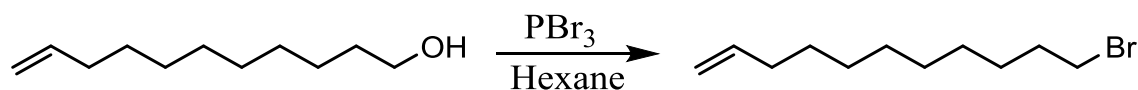


Figure 4.4 UV-Vis absorption and emission spectra of ω -azidoheptyl Si nanoparticles in CH_2Cl_2

Similarly, the ω -azidoheptyl silicon nanoparticles show a broad, continuous UV-Vis absorption tailing at around 550 nm (Figure 4.4). The emission spectra of azido terminated silicon nanoparticles were recorded with various excitation wavelengths, ranging from 300 to 400 nm in CH_2Cl_2 . The nanoparticles show a strong emission in the range of 300 to 700 nm similar to other functionalized silicon nanoparticles formed by RHEBM.

4.2.1.3 Synthesis of 11-bromo-1-undecene



Scheme 4.1 Synthesis of 11-bromo-1-undecene

11-bromo-1-undecene was synthesized using a substitution reaction between 10-undecen-1-ol and phosphorus tribromide in hexane. The resulting bromide was used as a ligand to obtain the ω -bromoundecyl silicon nanoparticles (Scheme 4.1).

Figure 4.5 shows the ^1H -NMR spectrum of the 11-bromo-1-undecene. The intense peak at 1.3 ppm is assigned to protons on the $-\text{CH}_2$ groups on the alkyl chain, while the peaks at 1.8 ppm and 3.5 ppm are assigned to the protons on the $-\text{CH}_2-\text{CH}_2-\text{Br}$ group. Resonances at 2.2 ppm, 4.9 ppm and 5.8 ppm are assigned to the $\text{CH}_2-\text{C}=\text{C}$, $\text{CH}_2=\text{C}-$ and $\text{C}=\text{CH}-$ respectively.

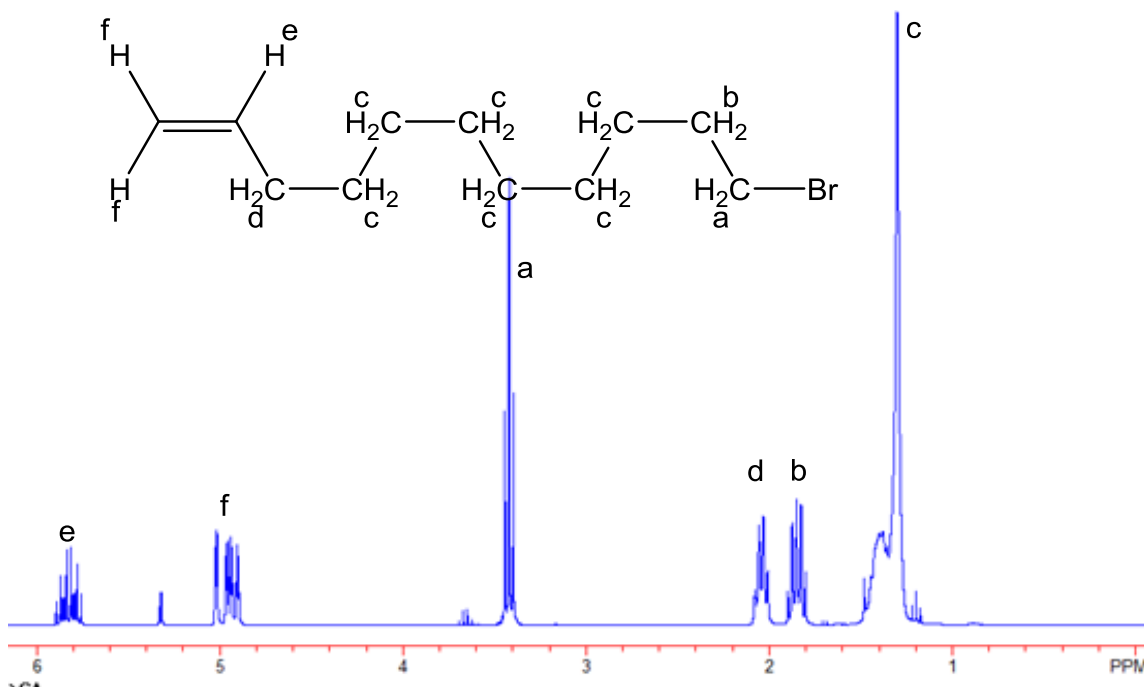


Figure 4.5 ^1H -NMR spectrum of 11-bromo-1-undecene in CD_2Cl_2

Furthermore, the GC-MS spectrum further confirms the formation and purity (95%) of the 11-bromo-1-undecene (Figure 4.5).

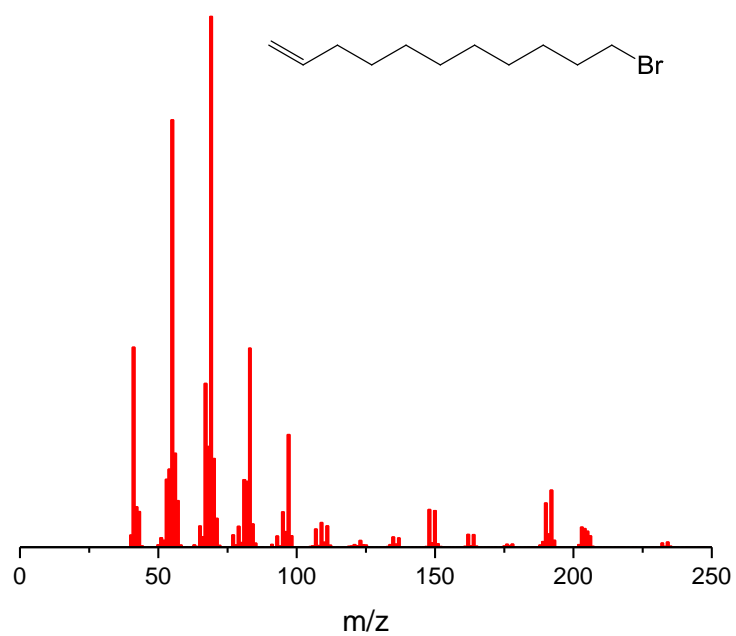
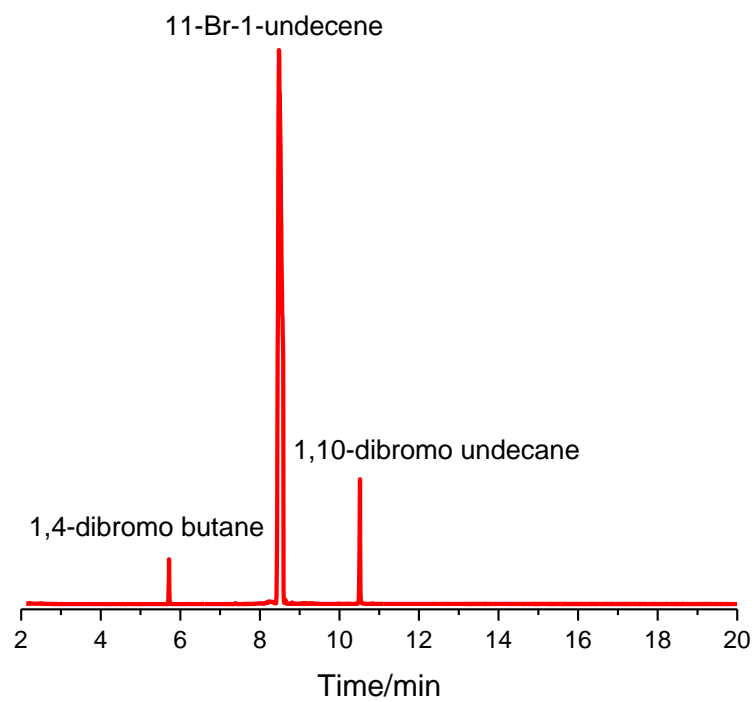


Figure 4.6 GC-MS spectrum of 11-bromo-1-undecene

4.2.1.4 Synthesis and characterization of ω -azidoundecyl Si nanoparticles

Similar to the ω -bromoheptyl silicon nanoparticles, the ω -bromoundecyl silicon nanoparticles were directly obtained from reactive high-energy ball milling of a silicon wafer with a mixture of 11-bromo-1-undecene and 1-pentyne (1:2 v/v). The ω -azidoundecyl silicon nanoparticles (Si-C₁₁-N₃ NPs) were also synthesized through the reactions of ω -bromoundecyl silicon nanoparticles with NaN₃ in DMF.

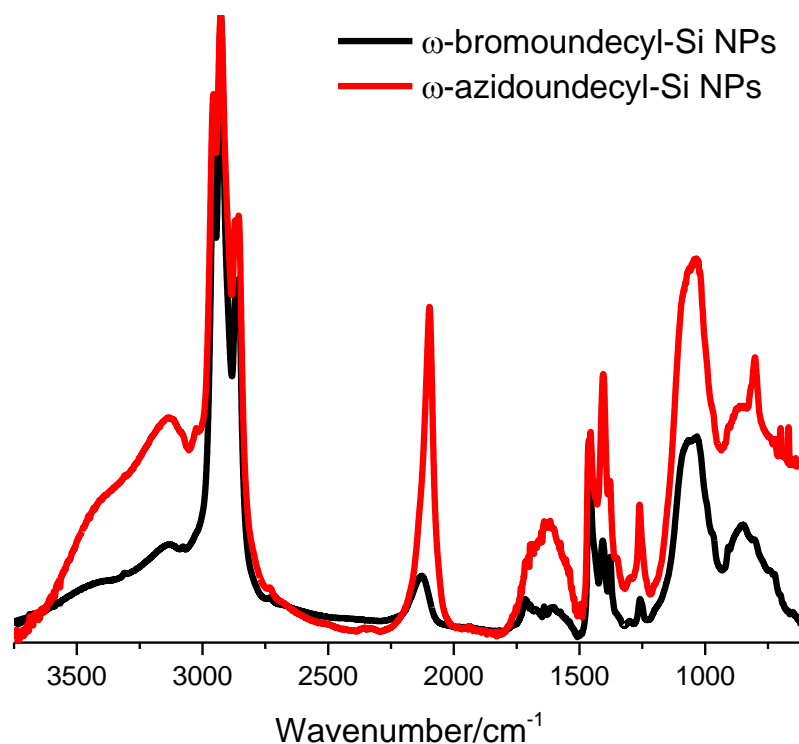


Figure 4.7 FTIR of ω -bromoundecyl Si nanoparticles and ω -azido-undecyl Si nanoparticles

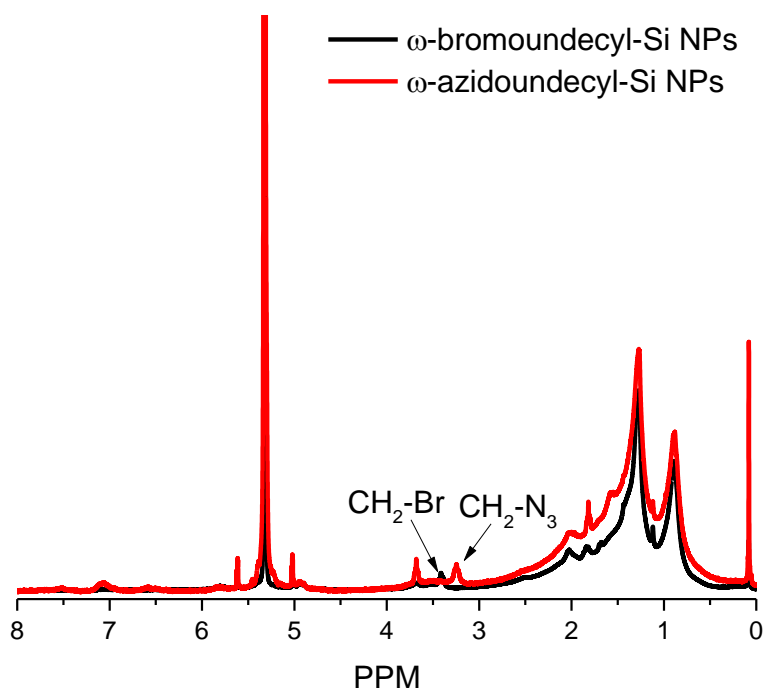


Figure 4.8 ^1H -NMR of ω -bromoundecyl Si nanoparticles and ω -azidoundecyl Si nanoparticles in CD_2Cl_2

The FTIR (Figure 4.7) and the ^1H NMR (Figure 4.8) spectra of both ω -bromoundecyl silicon nanoparticles and ω -azidoundecyl silicon nanoparticles support the presence of terminal bromo and azide groups on the nanoparticles. The resonance at 3.4 ppm is assigned to $\text{CH}_2\text{-Br}$ on bromo-functionalized nanoparticles, while the resonance at 3.2 ppm is assigned to $\text{CH}_2\text{-N}_3$ on azido-functionalized nanoparticles. Similarly, a strong absorbance at $\sim 2100\text{cm}^{-1}$ in the FTIR spectrum is due to $\nu(\text{N}=\text{N}=\text{N})$ on the ω -azidoundecyl silicon nanoparticles.

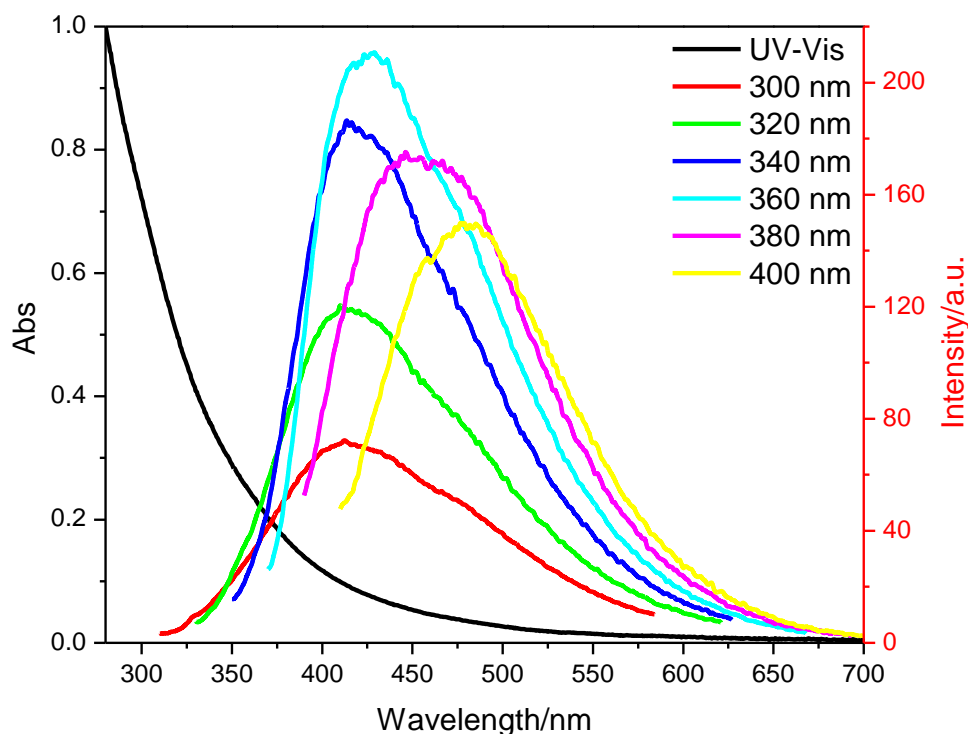


Figure 4.9 UV-Vis absorption and emission spectra of ω -azidoundecyl Si nanoparticles in CH_2Cl_2

The ω -azidoundecyl silicon nanoparticles show a broad, continuous UV-Vis absorption tailing at around 650 nm, and a strong emission in the range of 300 to 700 nm with various excitation wavelengths ranging from 300 to 400 nm in CH_2Cl_2 (Figure 4.9).

4.2.2 The donor-acceptor ratio dependence of energy transfer efficiency

The UV-Vis absorption and emission of the individual porphyrin and silicon nanoparticles were compared to study their possibility to be an energy donor-accepter pair. The UV-Vis absorption spectrum of Zn-porphyrin in CH_2Cl_2 is showed in Figure 4.10 (black line). The intense band at 420 nm is the Soret band which encompasses the ligand-centred $\pi \rightarrow \pi^*$ transition.¹³⁶ Two lower energy absorption bands between 530-600

nm are the Q band absorptions. All of these absorption bands of the Zn-porphyrin overlap with the fluorescent emission of azide-terminated silicon nanoparticles (Figure 4.10, blue line), indicating the possibility of energy transfer from silicon nanoparticles to the Zn-porphyrin. Furthermore, the emission spectrum of Zn-porphyrin (Figure 4.10, red line) displays two intense emission bands centered at 600 nm and 645 nm, and these emission peaks are largely separated from the blue emission of silicon nanoparticles.

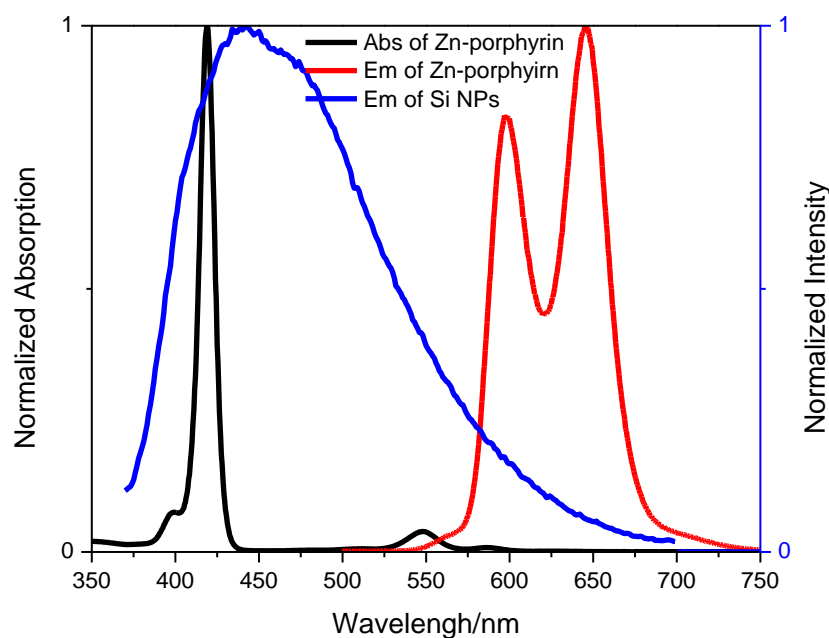


Figure 4.10 Emission of ω -azidopentynyl (20%) Si nanoparticles in CH_2Cl_2 ; absorption and emission of Zn-porphyrin ($\lambda_{\text{exc}}=355$ nm)

The Zn-porphyrin was attached to Si- $\text{C}_5\text{-N}_3$ NPs using a CuAAC “click” reaction to obtain the silicon-pentynyl-porphyrin system (Si- $\text{C}_5\text{-Por}$) (Figure 4.11).

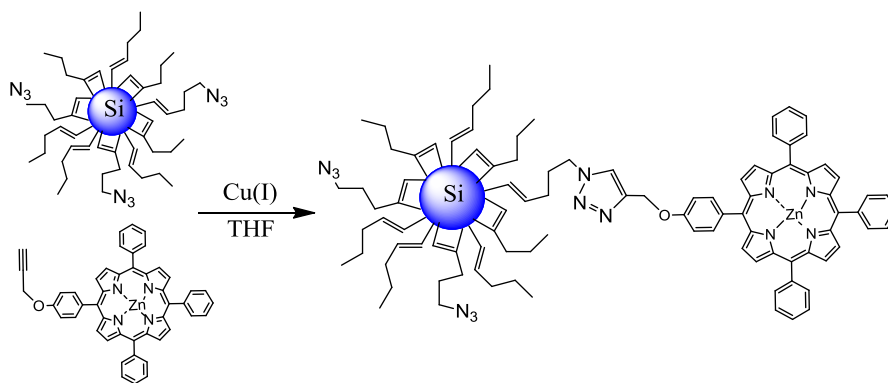


Figure 4.11 Synthesis of silicon nanoparticle-porphyrin system

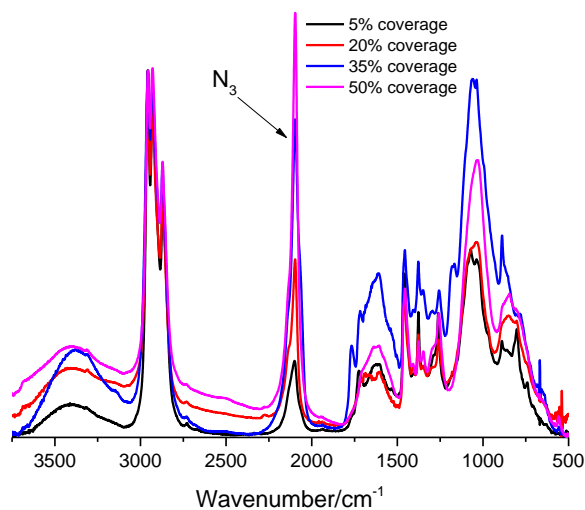


Figure 4.12 FTIR of ω -azidopentenyl Si nanoparticles with different azide group surface coverage

In order to tune the donor-acceptor ratio in the Si-C₅-Por system, Si-C₅-N₃ NPs with different azide group surface coverages were prepared. Figure 4.12 shows the FTIR spectra of the Si-C₅-N₃ NPs with nominal 5%, 20%, 35% and 50% azide group surface coverage. The relative increase of the $\nu(\text{N}=\text{N}=\text{N})$ stretching peaks at 2100 cm⁻¹ reflects

the increasing coverage of the terminal azide group on the silicon nanoparticles with increasing the ratio of the 5-chloro-1-pentyne in the starting ligand mixture.

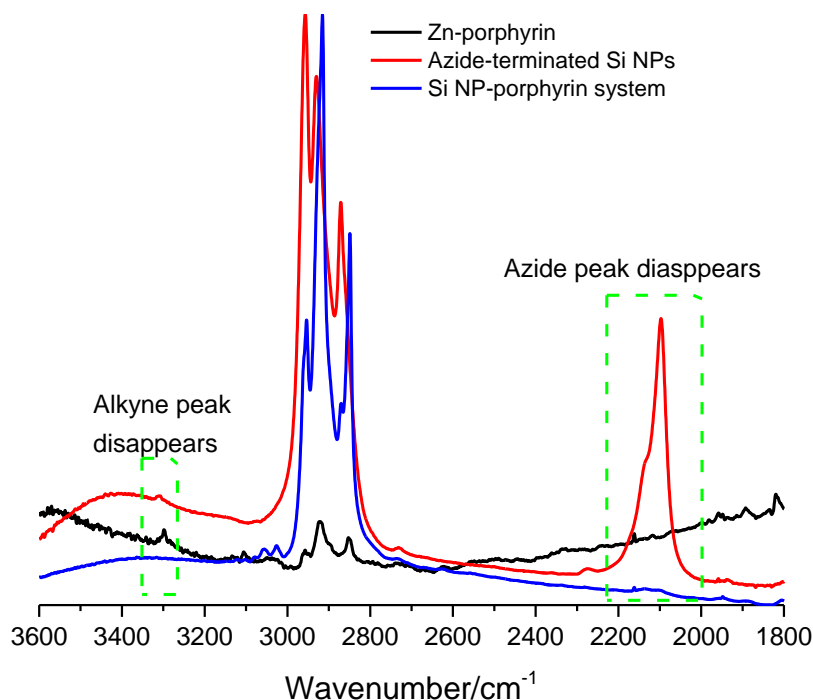


Figure 4.13 FTIR of Zn-porphyrin, azido-terminated Si nanoparticles and Zn-porphyrin functionalized Si nanoparticles.

The synthesis of the Si-C₅-Por is indicated by the FTIR spectra (Figure 4.13). Changes in the FTIR spectra show that both the $\nu(\text{N}=\text{N}=\text{N})$ from the azide group of the silicon nanoparticles at 2100 cm⁻¹ and the alkyne C-H stretching of the reacting Zn-porphyrin at 3250 cm⁻¹ disappear during the course of the reaction.

The grafting of the Zn-porphyrin to the silicon nanoparticles was further supported by the ¹H-NMR spectra (Figure 4.14). The Si-C₅-Por **a**, **b**, **c** and **d** correspond to nanoparticles with nominal 5%, 20%, 35% and 50% azide group surface coverage,

respectively. All of the ^1H -NMR spectra consist of the peaks from both the organic ligands on the silicon nanoparticles and the attached Zn-porphyrin. The actual surface coverage of porphyrin on the silicon nanoparticles for the four Si-C₅-Por systems can be obtained from ^1H -NMR spectra (Figure 4.14) by comparing the ratio of β -H on the porphyrin and the protons on the $-\text{CH}_3$ groups on the silicon nanoparticles, which is 1.2%, 2.7%, 3.4 % and 6.5%, respectively. The actual porphyrin surface coverage indicates that the reaction efficiency between the azide groups on the silicon nanoparticle and the porphyrin decreases with increasing the azide surface coverage, probably due to the steric hindrance on the nanoparticle surface. The number of porphyrins on each nanoparticle can also be estimated based on a model of silicon nanoparticles (see Section 4.5), which assumes the silicon nanoparticle has a spherical shape with diameter of 3.2 nm, and that the entire surface of the nanoparticle is covered by the organic ligands. Based on two bonding types between the silicon surface and organic ligands (one Si atom per ligand on Si (111) surface or two Si atoms per ligand on Si (100) surface), the number of porphyrin on each silicon nanoparticle for the four systems is 2.0, 4.6, 5.7, 10.9 for all cycloadditions (two Si atoms per ligand), and 4.0, 9.2, 11.4, 21.8 for all single point attachments (one Si atom per ligand).

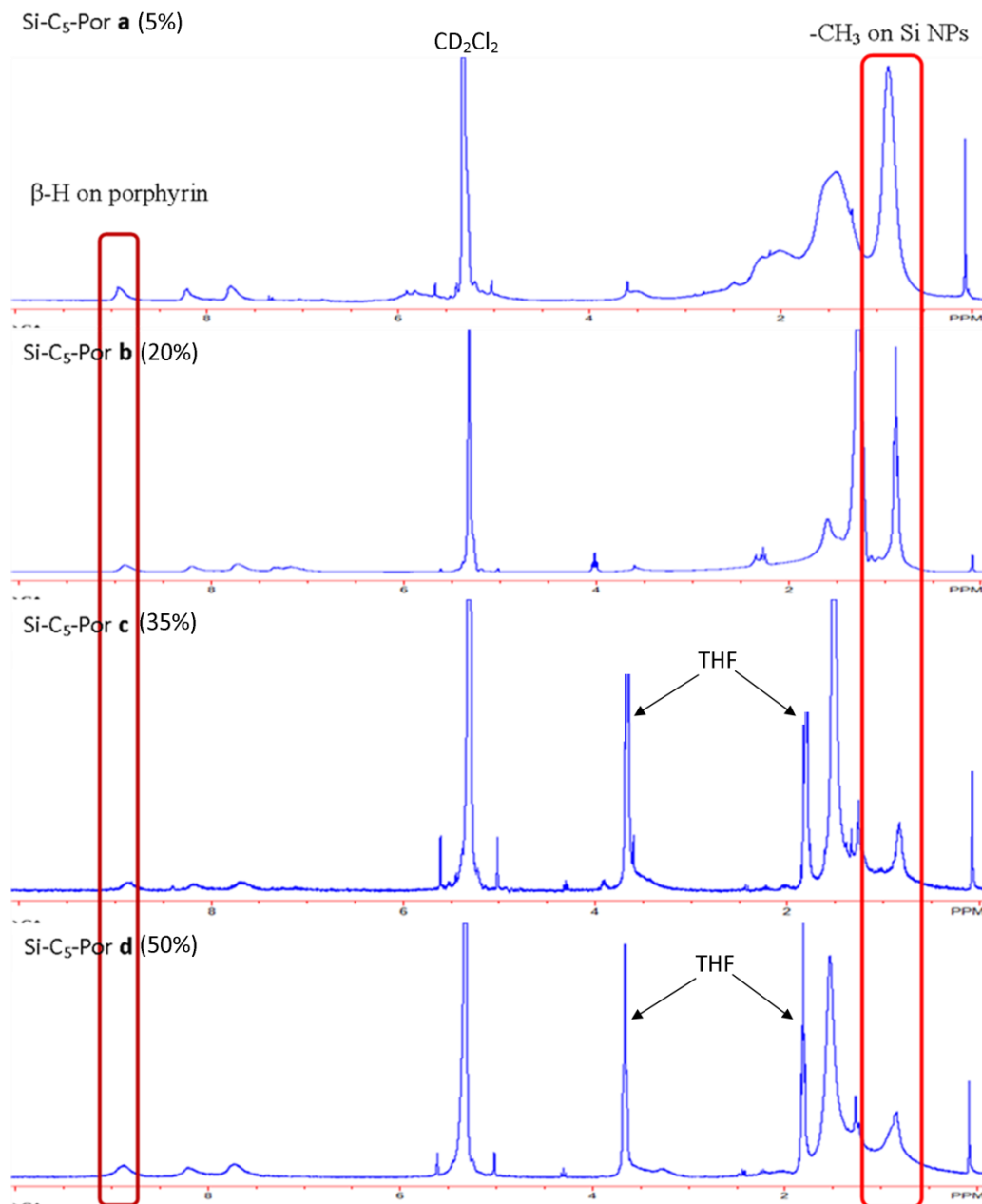


Figure 4.14 ^1H -NMR of Zn-porphyrin functionalized Si nanoparticles with different donor-acceptor ratios in CD_2Cl_2 .

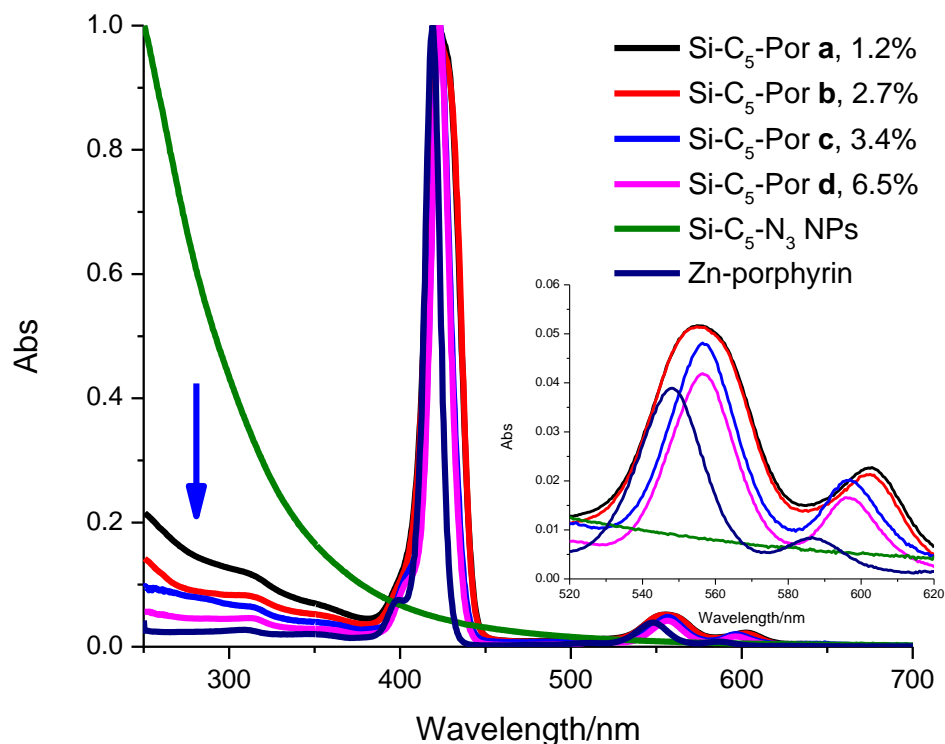


Figure 4.15 The absorption spectra of Zn-porphyrin and Si-C₅-N₃ NPs without and with different ratio of Zn-porphyrin attached in CH₂Cl₂ (Insert is the zooming range of 530-620 nm)

The absorption spectra of all of the Zn-porphyrin functionalized silicon nanoparticles exhibit an additive absorption of both silicon nanoparticles and the Zn-porphyrin (Figure 4.15). There is no additional absorption band formed, which indicates no strong ground-state interaction between silicon nanoparticle and the attached Zn-porphyrin. When the absorption maxima at 420 nm which is from Zn-porphyrin were normalized as 1, the absorptions below 380 nm due to the silicon nanoparticles decrease with increasing ratio of attached Zn-porphyrin.

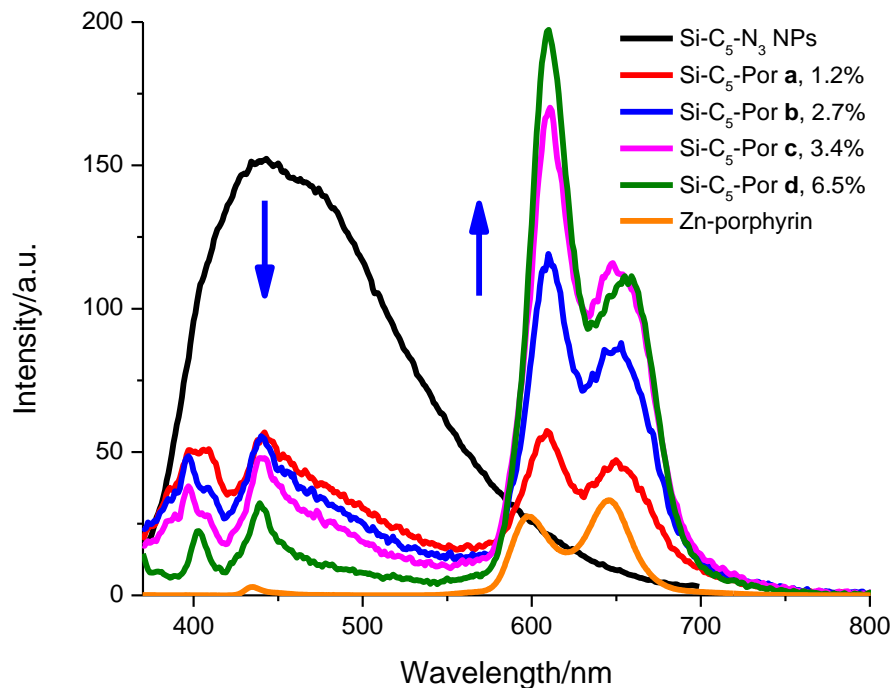


Figure 4.16 The emission spectrum of Zn-porphyrin, and the emission spectra of Si-C₅-N₃ NPs without and with different ratio of Zn-porphyrin attached in CH₂Cl₂ ($\lambda_{\text{exc}}=355$ nm). The emissions are normalized by absorption at 355 nm

The emission spectra ($\lambda_{\text{exc}}=355$ nm) of all the Zn-porphyrin functionalized silicon nanoparticles consist of two distinct regions: one in the blue (370 nm to 570 nm) and one in the red (570 nm to 750 nm) (Figure 4.16). Since the Zn-porphyrin has a negligible fluorescent emission when it is excited at 355 nm (Figure 4.16 orange line), the emission spectra of Zn-porphyrin attached silicon nanoparticles accurately represents both the emission from the directly excited silicon nanoparticles and the emission from the indirectly excited Zn-porphyrin. In addition, as shown in Figure 4.16, the relative fluorescent emission intensity in the blue region from the silicon nanoparticles is significantly decreased compared with the ungrafted silicon nanoparticles. Also, a dip

around 420 nm in the blue region emission was observed, which corresponds to the Soret absorption band of the Zn-porphyrin. Furthermore, the relative fluorescent emission intensity in the red region is from the Zn-porphyrin and increases when the ratio of acceptor-donor is higher. These behaviors provide the first indication that the energy transfers from the excited silicon nanoparticles to the attached Zn-porphyrin and also indicates that there is more energy transfer from the silicon nanoparticle to porphyrin acceptors when the number of the Zn-porphyrin on each nanoparticle increases.

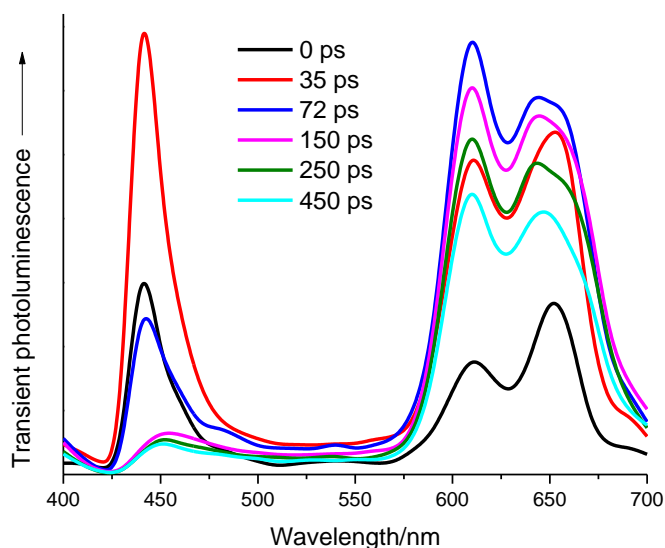


Figure 4.17 Time-resolved emission spectra of Si-C₅-Por **d** (6.5%) in CH₂Cl₂ at $\lambda_{\text{exc}}=355$ nm

Time-resolved emission spectra of Si-C₅-Por **d** (6.5%) were measured in CH₂Cl₂ at $\lambda_{\text{exc}}=355$ nm (Figure 4.17) in order to achieve further insight into photodynamics of the system. As the silicon nanoparticle emission at 450 nm decays quickly in about 100 ps, the Zn-porphyrin emission at 610 nm initially rises and then decays slowly, which clearly shows that energy transfer occurs within the system.

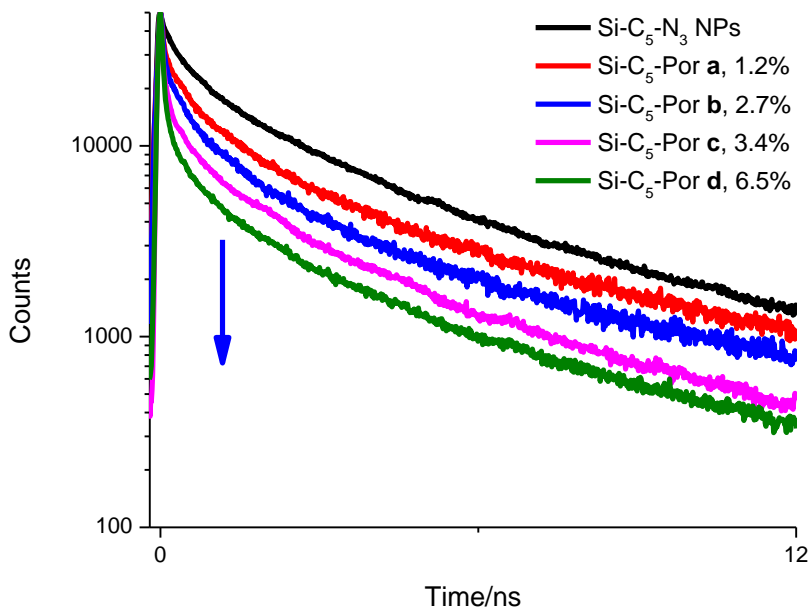


Figure 4.18 The fluorescence decay curves of Si-C₅-N₃ NPs without and with different ratio of Zn-porphyrin attached in CH₂Cl₂ (λ_{exc} =355 nm, λ_{em} =450 nm)

The excited state lifetime of the donor decreases in the presence of acceptor,¹³⁷ so the occurrence of the energy transfer processes in silicon nanoparticle-porphyrin systems have been further confirmed by comparing the excited state lifetimes of the azide-terminated silicon nanoparticles with and without Zn-porphyrin attached (Figure 4.18). All the fluorescence decays were fitted with a stretched exponential function, which is a useful model to fit the fluorescence decay of complex samples with a continuous distribution of fluorescence lifetimes.¹³⁸ The mean lifetimes and the mean lifetime-derived efficiency for four systems are shown in the Table 4.1. The mean lifetime of the Si-C₅-N₃ without the attached Zn-porphyrin is 1.72(3) ns. Upon the attachment of the Zn-porphyrin acceptor, the energy donor lifetimes become shorter, which proving again the occurrence of the energy transfer in this system. With 3.1% surface coverage of

porphyrin acceptors, the mean lifetime of the donor decreases to 1.37(3) ns in Si-C₅-Por **a**. Upon increasing the number of acceptor on the nanoparticle surface, the mean lifetime of the donor decrease, indicates that the energy transfers from the silicon nanoparticle to the Zn-porphyrin more efficiently.

Energy transfer efficiencies can be calculated using the following equation,¹³⁹ where τ_{DA} and τ_D are the emission lifetimes of silicon nanoparticles with and without the attached Zn-porphyrin.

$$E_T^{lifetime} = 1 - \frac{\tau_{DA}}{\tau_D} \quad (1)$$

For the four Zn-porphyrin functionalized silicon nanoparticle systems, the lifetime-derived energy transfer efficiencies are 0.20, 0.28, 0.33 and 0.52, respectively (Table 4.1), which corresponds with increasing the number of the attached Zn-porphyrin. The maximum energy transfer efficiency of the silicon nanoparticle-porphyrin system is higher than that of the multiporphyrin-modified CdSe nanoparticles (33%) developed by Imahori,^{131a} and similar as the energy transfer efficiency of the Ru-polypyridine modified silicon nanoparticles (55%) developed by Zuilhof.¹⁴⁰

Table 4.1: Summary data of Si-pentenyl-azide NPs without and with different ratio of attached Zn-porphyrin

Systems	Average surface coverage of porphyrin	Emission lifetime	$E_T^{lifetime}$
Si-pentenyl-azide NPs	--	1.72(3) ns	0
Si-C ₅ -Por a	1.2%	1.37(3) ns	0.20
Si-C ₅ -Por b	2.7%	1.24(3) ns	0.28
Si-C ₅ -Por c	3.4%	1.15(1) ns	0.33
Si-C ₅ -Por d	6.5%	0.83(2) ns	0.52

4.2.3 The distance dependence of energy transfer efficiency

The distance dependence of the energy transfer efficiency in the silicon nanoparticle-porphyrin system was investigated using three different linkers to modulate the distance between the Zn-porphyrin dye and the silicon core (Figure 4.1). The three silicon-porphyrin composites examined include silicon-pentenyl-porphyrin (Si-C₅-Por), silicon-heptyl-porphyrin (Si-C₇-Por) and silicon-undecyl-porphyrin (Si-C₁₁-Por). The ratio of donor to acceptor was held to a comparable value to exclude the possibility of changing energy transfer efficiency due to the different donor-acceptor ratios. The actual surface coverage of the porphyrin on the silicon nanoparticles for these three different systems (Table 4.2) was also determined by ¹H-NMR spectra (Figure 4.19), which is

4.0%, 4.3% and 3.4%, respectively. The number of porphyrin on each nanoparticle for the three systems was also estimated based on a model of silicon nanoparticles (see section 4.5), which is 6.7, 7.2, 5.7 for all cycloadditions (two Si atoms per ligand), and 13.4, 14.4, 11.4 for all single point attachments (one Si atom per ligand).

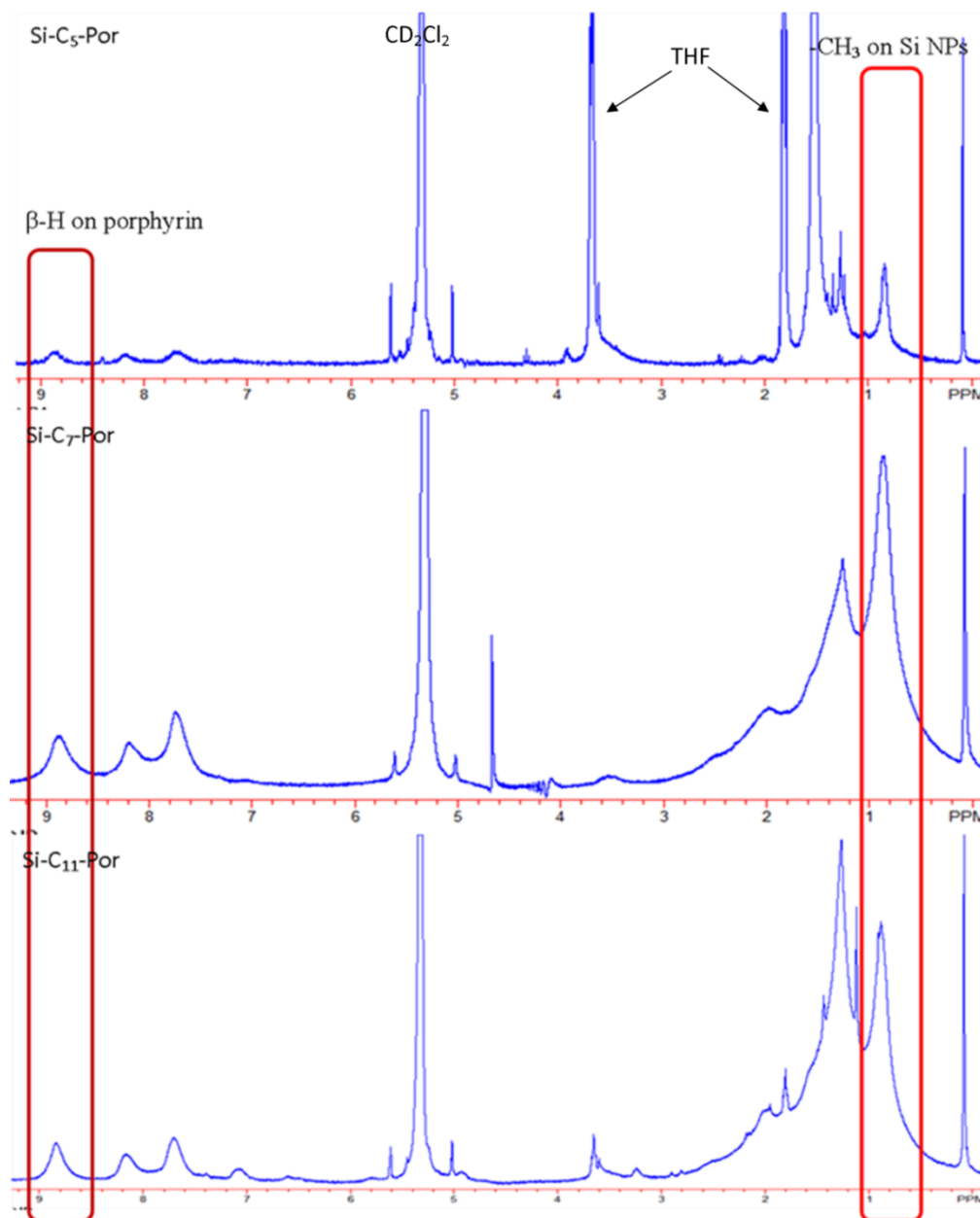


Figure 4.19. ^1H -NMR of Zn-porphyrin functionalized Si nanoparticles with different donor-acceptor distance in CD_2Cl_2 .

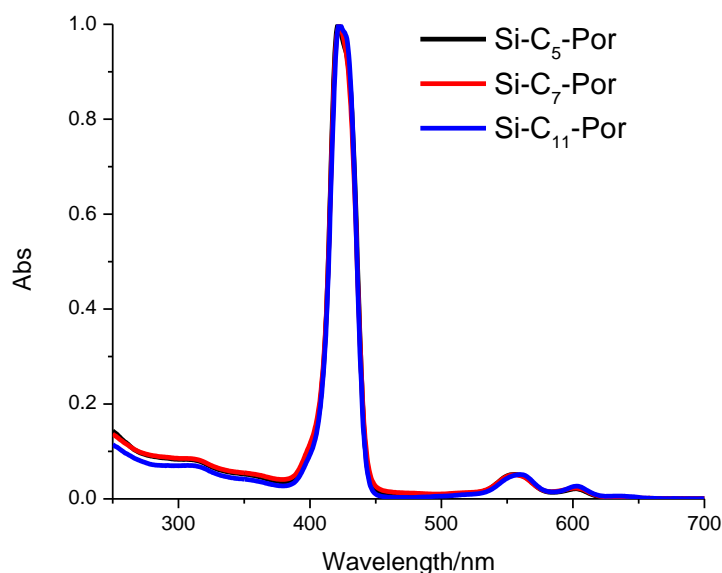


Figure 4.20 The absorption spectra of Si-C₅-N₃ NPs, Si-C₇-N₃ NPs and Si-C₁₁-N₃ NPs with attached Zn-porphyrin in CH₂Cl₂

Si-C₇-Por and Si-C₁₁-Por show similar UV-Vis absorption as the Si-C₅-Por, displaying the absorption of the silicon nanoparticle and the attached Zn-porphyrin (Figure 4.20). When the absorptions from Zn-porphyrin at 420 nm are normalized as 1, the absorptions from silicon nanoparticles of three systems are almost the same, due to the similar donor-acceptor ratio in these systems.

The emission spectra of three silicon nanoparticle-porphyrin systems all consist of blue (370 nm to 570 nm) and red regions (570 nm to 750 nm), representing the sum of both silicon nanoparticles and Zn-porphyrin emissions (Figure 4.21). As shown clearly in Figure 4.22, the emissions of the azide-terminated silicon nanoparticles around 450 nm are quenched when the Zn-porphyrin was attached to the silicon nanoparticle. This provides the indication that the energy transfer occurs in all three systems.

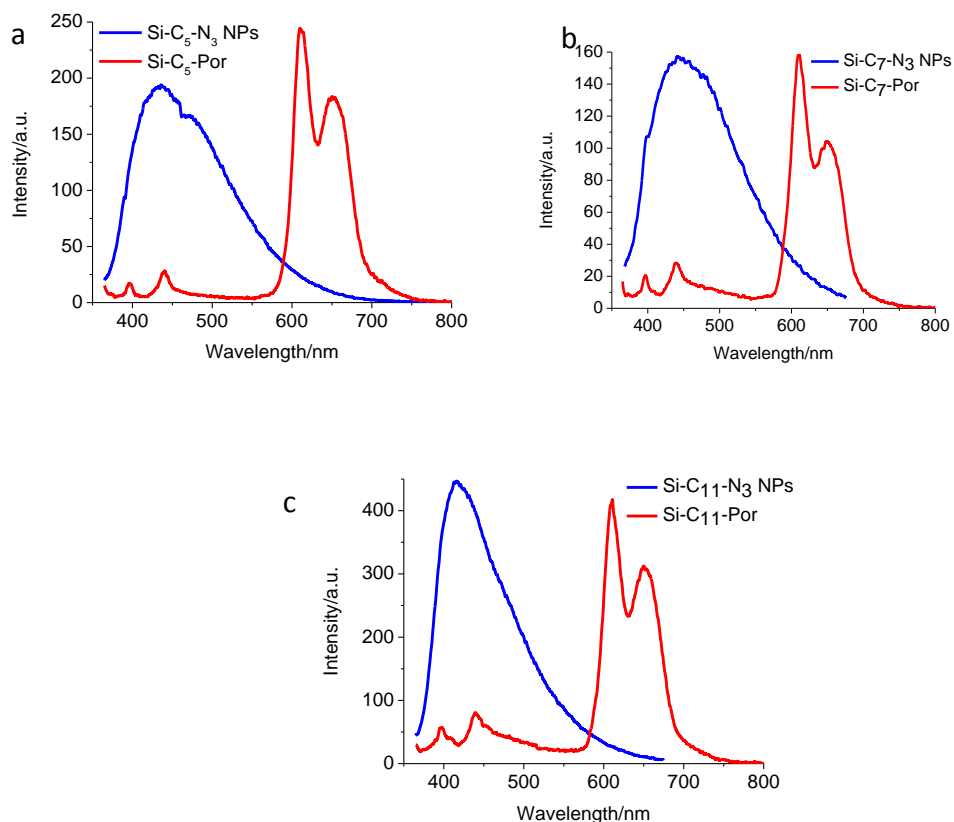


Figure 4.21 The emission spectra of (a) Si-C₅-N₃ NPs, (b) Si-C₇-N₃ NPs and (c) Si-C₁₁-N₃ NPs with attached Zn-porphyrin in CH₂Cl₂ (λ_{exc} =355 nm). The emissions are normalized by absorption at 355 nm

The excited state lifetimes of the azide-terminated silicon nanoparticles with and without the Zn-porphyrin attached have been compared (Figure 4.22). After fitting the fluorescence decays with stretched exponential function, the mean lifetimes of distribution are shown in Table 4.2, as well as the mean lifetime-derived efficiency and energy transfer rate. The mean lifetime of all azide terminated silicon nanoparticles are in the range of 1.72~1.78 ns. The energy donor (silicon nanoparticle) lifetimes become shorter when the Zn-porphyrin acceptor is attached. In Si-C₁₁-Por, with the longest linker, the mean lifetime of the donor decreased to 1.45(4) ns. Upon decreasing the distance

between the silicon core and the Zn-porphyrin, the mean lifetime of the donor increases, indicating an increase of energy transfer efficiency. In addition, the experimental energy transfer rate of these three silicon nanoparticle-porphyrin systems can be calculated from the following equation:¹⁴¹

$$k_{ET} = \frac{1}{\tau_{DA}} - \frac{1}{\tau_D} \quad (2)$$

where τ_D = the lifetime of the donor in the absence of the acceptor, and τ_{DA} = the lifetime of the donor in the presence of the acceptor. The experimental energy transfer rates for Si-C₅-Por, Si-C₇-Por and Si-C₁₁-Por are 5.7×10^8 , 3.8×10^8 and 1.3×10^8 s⁻¹, respectively.

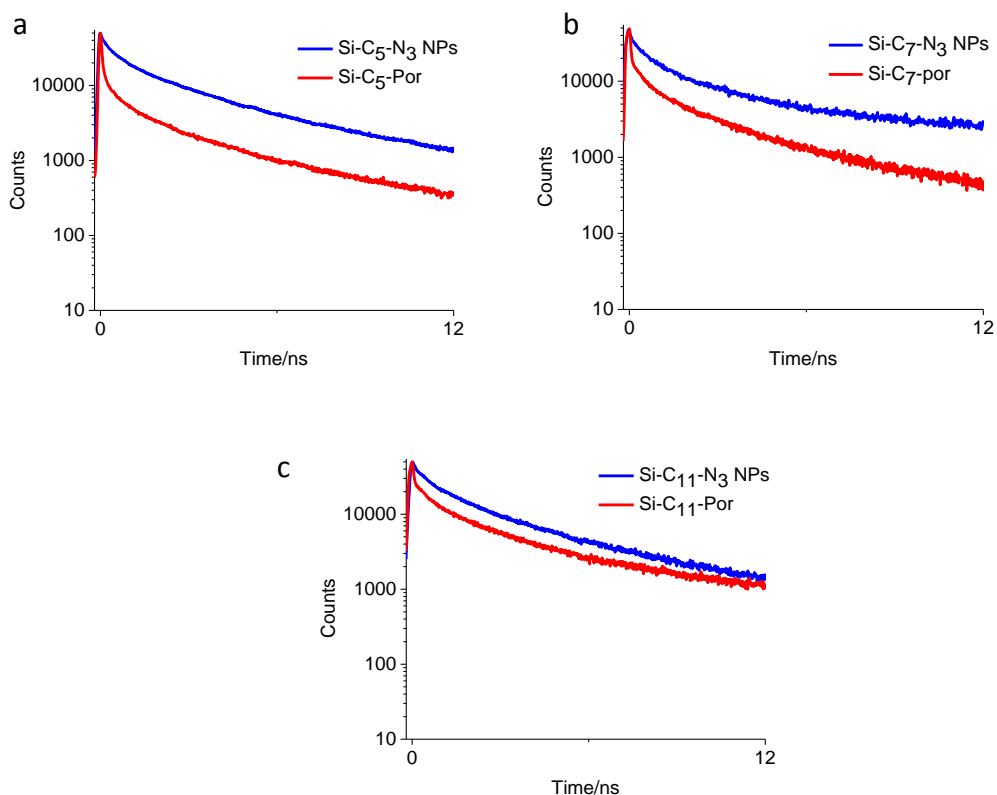


Figure 4.22 The fluorescence decay curves of (a) Si-C₅-N₃ NPs, (b) Si-C₇-N₃ NPs and (c) Si-C₁₁-N₃ NPs with attached Zn-porphyrin in CH₂Cl₂ (λ_{exc} =355 nm, λ_{em} =450 nm)

Table 4.2: Summary data of Si nanoparticle-porphyrin systems without and with attached Zn-porphyrin

Systems	Average surface coverage of porphyrin	τ_D	τ_{DA}	$E_T^{lifetime}$	κ_{ET} (exp.)	κ_{ET} (theo.)
Si-C ₅ -Por	4.0%	1.72(3) ns	0.87(4) ns	0.49	$5.7 \times 10^8 \text{ s}^{-1}$	$3.9 \times 10^8 \text{ s}^{-1}$
Si-C ₇ -Por	4.3%	1.73(2) ns	1.04(5) ns	0.40	$3.8 \times 10^8 \text{ s}^{-1}$	$2.7 \times 10^8 \text{ s}^{-1}$
Si-C ₁₁ -Por	3.4%	1.78(4) ns	1.45(4) ns	0.19	$1.3 \times 10^8 \text{ s}^{-1}$	$1.4 \times 10^8 \text{ s}^{-1}$

There are two typical mechanisms that can describe energy transfer between two chromophores, the Forster resonance energy transfer (FRET)¹⁴² and the Dexter energy transfer.¹⁴³ The FRET describes a model that the energy released from an excited donor could simultaneously excite the ground-state acceptor based on the nonradiative dipole-dipole coupling between these two chemical groups, while the Dexter energy transfer describes another mechanism that an excited donor group and an acceptor group might indeed exchange electrons to accomplish the nonradiative process. The efficiency of the Forster resonance energy transfers is inversely proportional to the sixth power of the distance between donor and acceptor, while the efficiency of the Dexter energy transfer has an exponential distance dependence, making them extremely sensitive to small changes in distance.¹⁴⁴ Moreover, the exchange mechanism of the Dexter energy transfer typically occurs within 1 nm, while the distance between the donor and the acceptor in a

FRET system is typically in the range of 1-10 nm.¹⁴⁵ Considering the distance of donor-acceptor in the silicon nanoparticle-porphyrin system is in the range of 1-10 nm, the energy transfer process in the silicon nanoparticle-porphyrin system should follow the Forster-type mechanism. The distances between the silicon nanoparticle core and the Zn-porphyrin center is fixed based on the mean size of the silicon nanoparticles (3.2±1.3 nm), and the chain length of the linker, then the Forster energy transfer rate can be calculated from the standard Forster equations:

$$k_{ET} = \frac{1}{\tau_D} \left(\frac{R_0}{R} \right)^6 \text{ and}$$

$$R_0^6 = \frac{9000\kappa^2 \ln 10}{128\pi^5 n^4 N_{AV}} \Phi_D \int_0^\infty F_D(\lambda) \epsilon_A(\lambda) \lambda^4 d\lambda \quad (3)$$

where τ_D = the lifetime of the donor in the absence of the acceptor, R = the separation distance between the donor and acceptor, R_0 = the Forster critical distance, κ^2 = the orientation factor which is 2/3, N_{AV} = Avogadro's number, n = refractive index of the solvent, Φ_D = the quantum yield of the donor, $F_D(\lambda)$ = the normalized donor emission spectrum, and $\epsilon_A(\lambda)$ = the molar extinction coefficient of the acceptor.

$\int_0^\infty F_D(\lambda) \epsilon_A(\lambda) \lambda^4 d\lambda$ = the degree of spectral overlap between the donor emission and the acceptor absorption.¹³⁹ The overlap integral is calculated from the absorption and emission in Figure 4.10 and 4.21. Since some of the quantities in equation 3 have uncertainties, the calculated value of R_0 is a rough estimate based on the distance from the center of silicon nanoparticle to the center of Zn-porphyrin, which is around 30Å. So, considering the silicon nanoparticle as a single chromophore, the donor-acceptor distance R can be estimated based on the distance between the center of the silicon nanoparticle

and the Zn atom in Zn-porphyrin (the diameter of silicon core is 32 Å, the length of each carbon carbon bond is around 1 Å). The Forster energy transfer rates for Si-C₅-Por, Si-C₇-Por and Si-C₁₁-Por are estimated to be 3.9×10^8 , 2.7×10^8 and 1.4×10^8 s⁻¹, respectively. The results are comparable with the experimental energy transfer rates, which supported that the energy transfer process inside the silicon nanoparticle-porphyrin systems followed the Forster-type mechanism.

4.2.4 Photoinduced electron transfer in Si nanoparticle-porphyrin-fullerene nanocluster

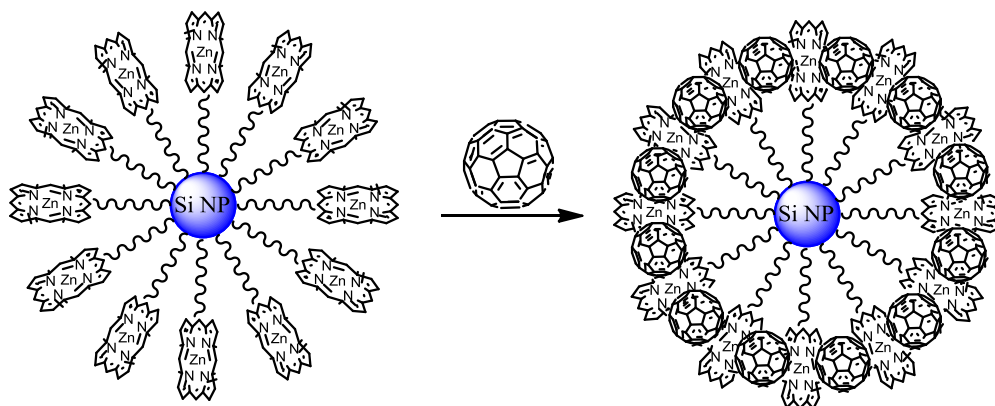


Figure 4.23 Illustration of the organization of Si nanoparticle-porphyrin-fullerene nanocluster

Transforming light energy into charge separation is an essential step for solar energy conversion.¹⁴⁶ An electron acceptor can be introduced into the porphyrin-silicon nanoparticle hybrid system in order to obtain an electron donor-acceptor complex to effect charge separation. Jayawickramarajah reported that bis(porphyrin) tweezers can bind with fullerenes to form a sandwich structure via a π - π interaction.¹⁴⁷ The prototypical fullerene, C₆₀ was therefore added to Zn-porphyrin-silicon nanoparticles as

an electron acceptor to obtain the silicon nanoparticle-porphyrin-fullerene nanocluster (Si NP-Por-C₆₀).

Si NP-Por-C₆₀ was obtained by titrating the toluene solution of C₆₀ into the Zn-porphyrin-Si nanoparticle hybrid system with a toluene/acetonitrile (1:1) solvent mixture which can significantly increase the magnitude of host-fullerene interactions due to the strong lyophobic interaction between the porphyrin and C₆₀ molecules in the mixed solvent.^{134a, 147} Figure 4.23 illustrates the possible organization of Si NP-Por-C₆₀ nanocluster.

Figure 4.24 shows the UV-Vis absorption spectra of the Zn-porphyrin functionalized silicon nanoparticles and pure C₆₀. The absorption band of C₆₀ at 328 nm is well separated from the Soret band of Zn-porphyrin at 420 nm.

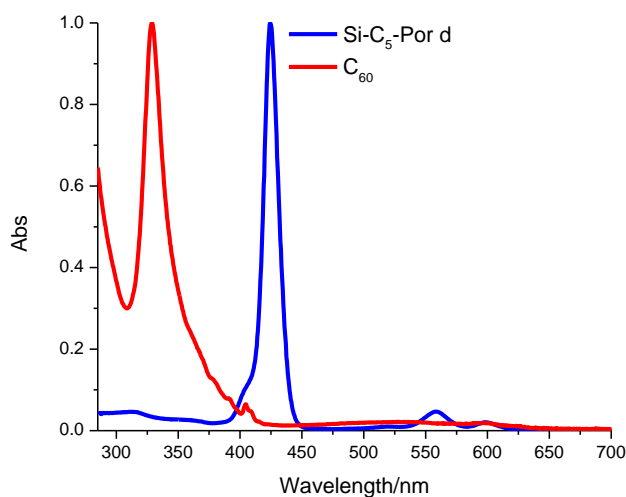


Figure 4.24 UV-Vis absorption spectra of the Si-C₅-Por **d** (blue line) and C₆₀ (red line) in toluene/acetonitrile (1:1)

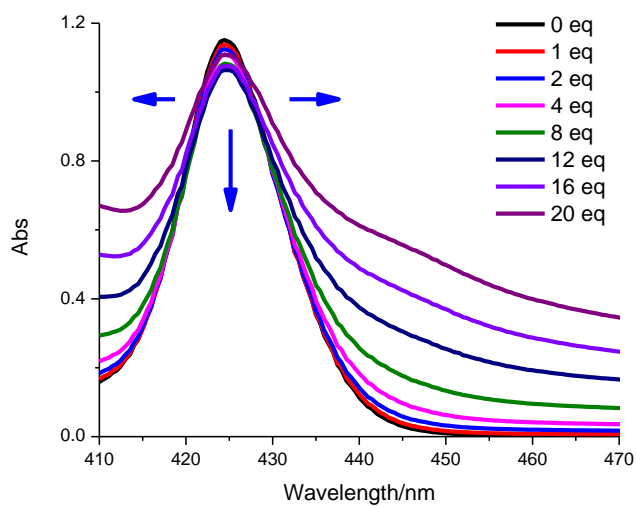


Figure 4.25 UV-Vis absorption spectra of the Zn-porphyrin functionalized silicon nanoparticles upon addition of C₆₀ (0-20 equiv.) in toluene/acetonitrile (1:1)

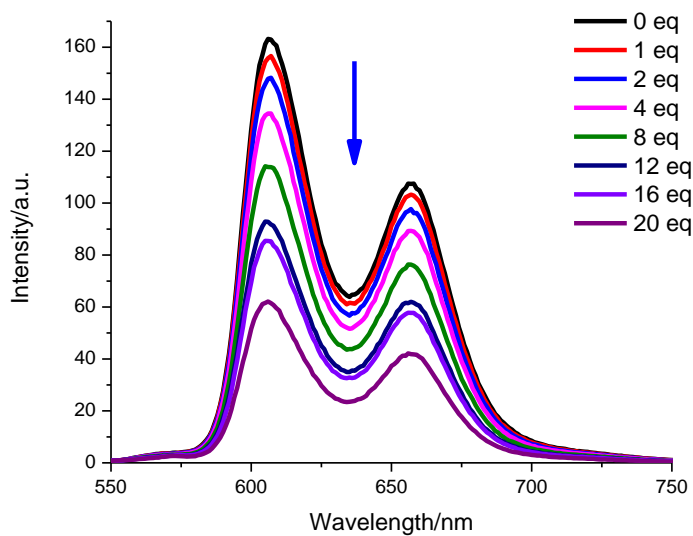


Figure 4.26 Fluorescence spectra of Zn-porphyrin functionalized silicon nanoparticles upon addition of C₆₀ (0-20 equiv., 1 equiv. = 8.80 $\mu\text{mol/L}$) in toluene/acetonitrile (1:1). (λ_{exc} =420 nm)

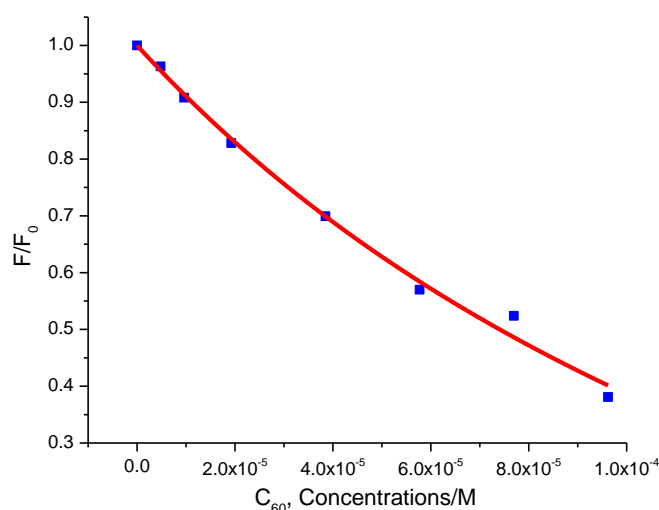


Figure 4.27 A plot of the change in fluorescence intensity of Zn-porphyrin functionalized silicon nanoparticles as a ratio of F/F_0 versus concentration of C_{60} in toluene/acetonitrile (1:1). [$K_a=5.4 \pm 1.6 \times 10^3 M^{-1}$; $R^2=0.99$]

Evidence for a strong interaction of the Zn-porphyrin functionalized silicon nanoparticles with C_{60} was gathered from UV-Vis titrations (Figure 4.25).¹⁴⁸ Titration of C_{60} into a solution containing the Zn-porphyrin functionalized silicon nanoparticles resulted in the broadening of the Soret band due to the π - π interactions between the Zn-porphyrin and C_{60} .^{134a}

Fluorescence titration was performed to further confirm the interaction and determine quantitative association constants (K_a) between the Zn-porphyrin functionalized silicon nanoparticles and C_{60} . Aliquots of C_{60} in toluene (stock concentration: $4.03 \times 10^{-3} M$) were added into a solution of Zn-porphyrin functionalized silicon nanoparticles in toluene/acetonitrile (1:1). In Figure 4.26, the quenching of the porphyrin fluorescence by the C_{60} is observed, which may be the first evidence of photoinduced electron transfer inside the Si NP-Por- C_{60} system.¹⁴⁹ In addition, the

fluorescence maximum at 606 nm decreases with increasing aliquots of C₆₀ confirming the complexation of C₆₀ by the Zn-porphyrin functionalized silicon nanoparticles. The binding constant (K_a) was determined by plotting fluorescence emission (F/F_0) versus the concentration of fullerenes followed by non-linear curve fitting to a 1:1 binding mode:¹⁵⁰

$$\frac{F}{F_0} = \frac{1 + \frac{k_{11}}{k_s} K_a [L]}{1 + K_a [L]} \quad (4)$$

where k_{11} and k_s are proportionality constants and $[L]$ is the fullerene concentration. As shown in Figure 4.27, the binding constant between C₆₀ and Zn-porphyrin functionalized silicon nanoparticles is $K_a = 5.4 \pm 1.6 \times 10^3 \text{ M}^{-1}$. The binding constant of this system is lower than binding constants of most of other porphyrin-C₆₀ constructs developed by other groups (Table 4.3). This may be due to less organization of porphyrins on the silicon nanoparticle.

Many studies have reported that there is no noticeable interaction between porphyrin monomer and C₆₀.^{147, 151} However, a parallel experiment with just the Zn-porphyrin and the same C₆₀ increments still showed the quenching of the porphyrin emission by C₆₀ (Figure 4.28). The quenching coefficient (k_q) was determined by plotting fluorescence emission (F_0/F) versus the concentration of fullerenes ($[L]$) followed by the Stern-Volmer relationship:

$$F_0/F = 1 + k_q \tau_0 [L] = 1 + K_D [L] \quad (5)$$

where τ_0 is the lifetime of the emission excited state of porphyrin, k_q is the bimolecular quenching constant, and K_D is the Stern-Volmer quenching constant. As shown in Figure

4.29, the quenching constant is $2.0 \pm 0.1 \times 10^3 \text{M}^{-1}$, which is about three times smaller than the bonding constant of C_{60} and Zn-porphyrin functionalized silicon nanoparticles. These results indicate that the assembly of the Zn-porphyrin moieties by silicon nanoparticles indeed facilitates embedding the C_{60} and helps to mediate a fast intramolecular quenching.

Table 4.3: Binding Constants (M^{-1}) of a Variety of Porphyrin- C_{60} Constructs

Host	Binding constant	Ref
Pd bisporphyrin(Zn) cleft	3.7×10^4	152
Zn(por)[RuPor] ₄ box	9.65×10^3	151
Calixarene bisporphyrin(Zn)	8.60×10^3	153
Thiacalixarene bisporphyrin(Zn)	2.71×10^3	153
Stilbene-linked bisporphyrin(Zn)	2.9×10^4	147
Au NP- C_{12} -porphyrin(H_2)	3.4×10^4	134a
Au NP- C_{24} -porphyrin(H_2)	7.7×10^4	134a
This study	5.4×10^3	

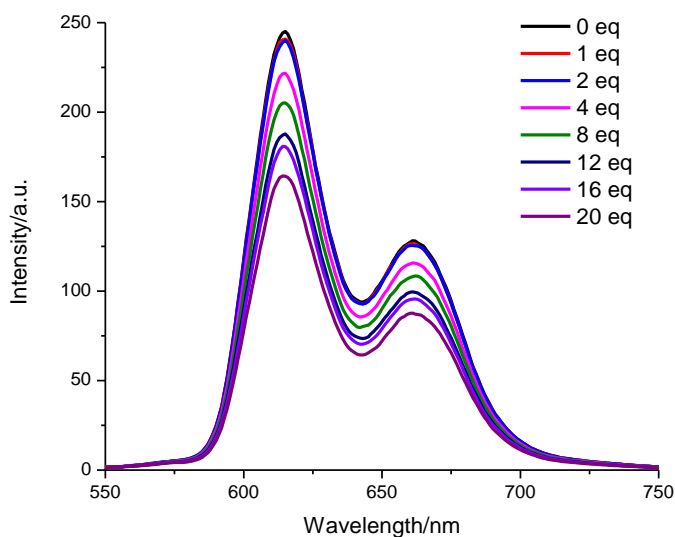


Figure 4.28 Fluorescence spectra of the Zn-porphyrin upon addition of C_{60} (0-20 equiv., 1 equiv. = $11.7 \mu\text{mol/L}$) in toluene/acetonitrile (1:1). ($\lambda_{\text{exc}}=420 \text{ nm}$)

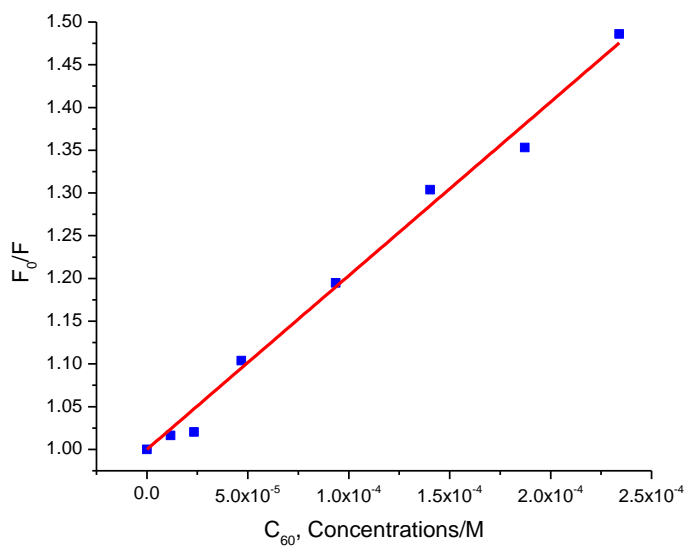


Figure 4.29 A plot of the change in fluorescence intensity of Zn-porphyrin as a ratio of F_0/F versus concentration of C_{60} in toluene/acetonitrile (1:1). [$K_D=2.0 \pm 0.1 \times 10^3 \text{ M}^{-1}$; $R^2=0.99$]

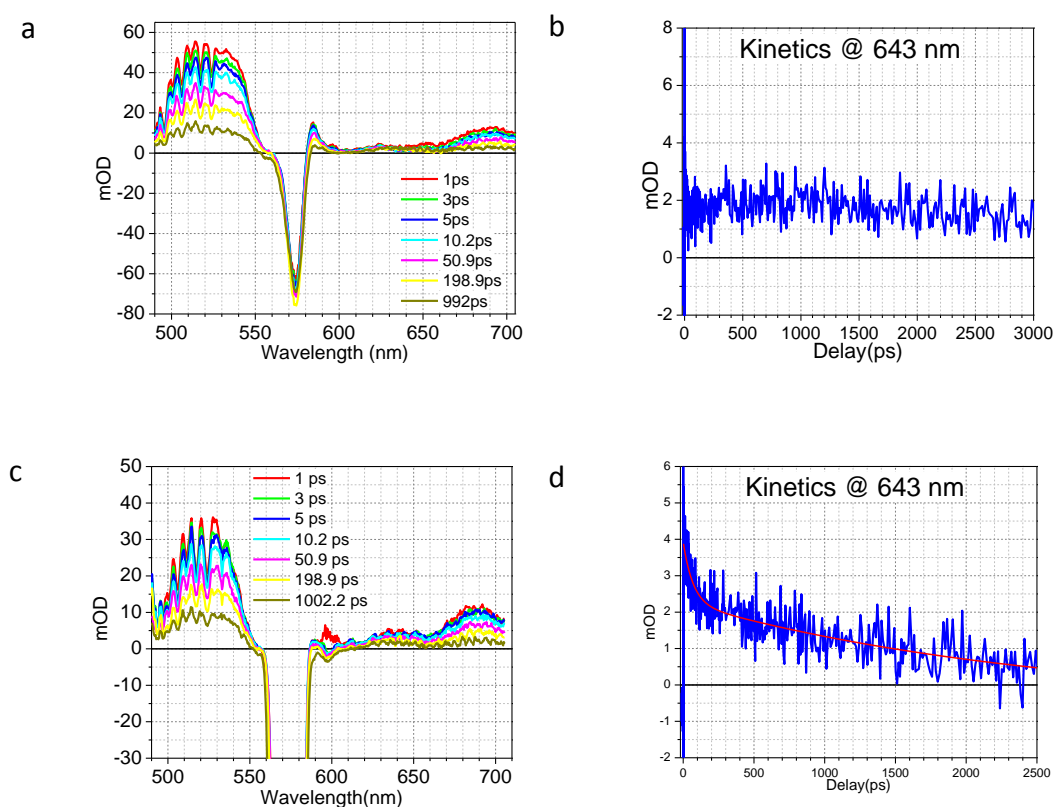


Figure 4.30 a) Femtosecond transient absorption spectra of Si-C₅-Por **d** in argon-saturated toluene/acetonitrile (1:1) at 298 K after laser excitation at 575 nm. b) Time profiles of absorption at 643 nm of Si-C₅-Por **d** in argon-saturated toluene/acetonitrile (1:1) at 298 K. c) Femtosecond transient absorption spectra of Si NP-Por-C₆₀ ([C₆₀] = 2.01 × 10³ μmol/L) in argon-saturated toluene/acetonitrile (1:1) at 298 K after laser excitation at 575 nm. d) Time profiles of absorption at 643 nm of Si NP-Por-C₆₀ in argon-saturated toluene/acetonitrile (1:1) at 298 K.

Transient absorption studies were carried out by the femto-second scale transient absorption spectroscopy in order to investigate the electron transfer in the Si NP-Por-C₆₀ system. The results for the Si-C₅-Por **d** and the Si NP-Por-C₆₀ are shown in Figure 4.30. The broad absorption band around 640 nm due to the ZnP⁺⁺ moiety¹⁵⁴ is observed in the

spectra of the Si NP-Por- C_{60} system (Figure 4.30c), which doesn't show in the spectra of the Si- C_5 -Por **d** without adding C_{60} (Figure 4.30a). The formation of ZnP^{*+} may due to the porphyrin excited singlet state quenching by C_{60} to yield the charge-separated state.^{133b} The changing of absorption is further confirmed by comparing the absorption decay of ZnP^{*+} at 643 nm before and after adding C_{60} (Figure 4.30b, d). The absorption decay of ZnP^{*+} is only shown after adding C_{60} . Since absorption bands of $C_{60}^{\bullet-}$ are expected to appear at 1000-1080 nm,¹⁵⁴ $C_{60}^{\bullet-}$ was not confirmed by the transient absorption study due to the limitation of the detector. All the spectra changing indicated the formation of the ZnP^{*+} when the electron acceptor was added into the system, which proving the ability of the porphyrin-Si nanoparticle hybrid system to effect the charge separation. In addition, the yield of ZnP^{*+} can be calculated based on the ratio of the concentration of the excited Zn-porphyrin and the ZnP^{*+} , which can be obtained based on the Beer-Lambert law. As shown on Figure 4.30c, the absorption of excited Zn-porphyrin at 520 nm is 36 and the absorption of ZnP^{*+} at 643 nm is 5.4. Since the molar extinction of Zn-porphyrin at 520 nm is $4.5 \times 10^3 \text{ cm}^{-1}\text{M}^{-1}$ and the molar extinction of ZnP^{*+} at 643 nm is $3.0 \times 10^4 \text{ cm}^{-1}\text{M}^{-1}$, the yield of the ZnP^{*+} is calculated to be 2.2%.

4.3 Conclusion

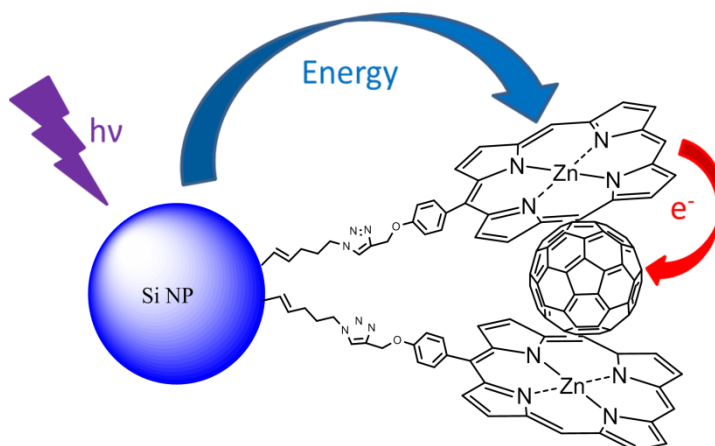


Figure 4.31 Illustration of the energy/electron transfer inside the Si NP-Por-C₆₀ system

Zn-porphyrin functionalized silicon nanoparticles were successfully synthesized. The energy transfer process inside the silicon nanoparticle-porphyrin system was proved by steady-state and time-resolved fluorescence measurement, which also indicated that the azide-terminated silicon nanoparticles are excellent energy donors with Zn-porphyrin acceptor molecules. A simple tuning of the ratio and distance between the donor and acceptor can give the desirable energy transfer efficiency up to 52% in the case of a short linker and higher acceptor-donor ratio. The energy transfer rates were calculated, which are very high for all examined systems and follow the distance dependence based on Forster energy transfer theory. The photoinduced electron transfer process inside the silicon nanoparticle-porphyrin-fullerene nanocluster was supported by the femto-second transient absorption spectroscopy, showing the ability of the porphyrin-silicon nanoparticle hybrid system to effect charge separation (Figure 4.31). Thus, the Zn-porphyrin functionalized silicon nanoparticles represent novel artificial photosynthetic materials. Also, it was hoped that this study would provide basic and valued information

on the design of chromophore-modified silicon nanoparticles for constructing efficient solar cells.

4.4 Experimental Section

4.4.1 Materials and methods

All chemicals were purchased from Sigma-Aldrich or Alfa Aesar, and employed without further purification unless specified. Tetrahydrofuran (THF) was distilled over sodium-benzophenone prior to use. Dichloromethane was distilled over CaH_2 before use. Hexane, toluene and acetonitrile were distilled over sodium prior to use. Gel permeation chromatography (GPC) was used for the purification of nanoparticles. Bio-beads S-X1 were swelled overnight in dry THF and packed into a 40cm x 1.3cm glass column. Dichloromethane was used as an elution solvent. A concentrated nanoparticle solution (50mg in 1 ml CH_2Cl_2) was added to column and eluted into 3 fractions collected in 10ml increments in separate vials. The first fraction was collected when the first colored band began to elute. This fraction contained nanoparticles and was used in the synthetic reactions. The second and third fractions, containing mostly impurities, were discarded.

4.4.2 Synthesis of 11-bromo-1-undecene

10-undecen-1-ol (8.5g, 50 mmol) was dissolved in 300 mL dry hexane in a 500 mL three-necked reaction flask. PBr_3 (28.5g, 105 mmol) was added dropwise through an additional funnel into a flask containing the 10-undecen-1-ol solution at 0 °C. The solution was stirred at room temperature overnight under nitrogen atmosphere. The solution was then poured into 300mL of ice water to quench the reaction and NaHCO_3 (50.4g, 600 mmol) was added to neutralize the HBr and H_3PO_4 . The organic layer was washed three times by saturated NaCl solution (300 mL each time) and dried by anhydrous MgSO_4 . The solid was removed by filtration and the solvent was removed by rotary evaporation. The product was purified by vacuum distillation (0.3 mmHg, ≥ 60 °C).

The yield is 6.4g, 55%. $^1\text{H-NMR}$ (δ , 300 MHz, CD_2Cl_2): 5.8 (m, 1H), 4.9 (m, 1H), 3.4 (m, 2H), 2.1 (m, 2H), 1.9 (m, 2H), 1.3 (broad, s, 12H). GC: 8.5 min, 94.6%. MS: 232.1 (100% intensity), 234.1 (97.3% intensity), 233.1 (12.1% intensity).

4.4.3 Synthesis of ω -azidopentenyl (5%, 20%, 35%, 50%)-Si nanoparticles

1.0g (36 mmol) silicon wafer (as obtained from Silrec, undoped, mirror finish, orientation [111]) was placed in a stainless steel milling vial along with two stainless steel milling balls (diameter of 1.2 cm, weighing approximately 8.1g). The vial was filled in a Vacuum Atmospherics dry box under a nitrogen atmosphere with a mixture of 5-chloro-1-pentyne and 1-pentyne and then tightly sealed. The following quantities of 5-chloro-pentyne and 1-pentyne were used for the specified surface compositions: 1.0 mL (9.4 mmol) 5-chloro-1-pentyne and 19 mL (192 mmol) 1-pentyne for a 5% functionalized surface; 4.0 mL (38 mmol) 5-chloro-1-pentyne and 16 mL (162 mmol) 1-pentyne for a 20% functionalized surface; 7.0 mL (66 mmol) 5-chloro-1-pentyne and 13 mL (132 mmol) 1-pentyne for a 35% functionalized surface; 10mL (94 mmol) 5-chloro-1-pentyne and 10 mL (101 mmol) 1-pentyne for a 50% functionalized surface. The milling vial was placed in a SPEX 8000-D Dual Mixer/Mill, and high energy ball-milling were performed for 24 hours. After 24 hours of milling, the reaction mixture was centrifuged to remove larger particles. The solution contains chloro-terminated silicon nanoparticles which are soluble in non-polar organic solvents. All of the solvents were removed by vacuum distillation and the nanoparticles were redispersed in CH_2Cl_2 . Sodium azide (0.30 g, 4.6 mmol) was added to a solution of 50 mg chloro-terminated silicon nanoparticles in 20 mL of dry dimethylformamide (DMF). The solution was stirred at 65°C overnight under nitrogen atmosphere. DMF was removed by vacuum distillation and dry THF was added. The

mixture was centrifuged to remove NaCl and unreacted NaN₃. The solution contains azide-terminated silicon nanoparticles which are soluble in THF. The solvent was removed by rotary evaporator and the nanoparticles were redispersed in CH₂Cl₂ and purified by GPC. Yield: 40-60 mg. FTIR (thin film on KBr): 2820-2990 cm⁻¹ (ν (C-H)), 2100 cm⁻¹ (ν (N=N=N)), 1500-1750 cm⁻¹ (ν (C=C)), 1465-1376 cm⁻¹ (δ (C-H)), 1250 cm⁻¹ (δ (Si-C)), 1190-850 cm⁻¹ (ν (Si-O)), 830 cm⁻¹ (ν (Si-C)). *Safety note: Large scale reactions of azide are prone to dangerous exothermic reactions. The use of chlorinated solvents in the presence of sodium azide must be avoided, as the byproducts may be highly explosive.*

4.4.4 Synthesis of ω-azidoheptyl (35%)-Si nanoparticles

Silicon wafer (1.0g, 36 mmol) was ball milled with a mixture of 7.0 mL (46 mmol) 7-bromo-1-heptene and 13 mL (132 mmol) 1-pentyne for 24 hours to synthesize the bromo-terminated silicon nanoparticles. Sodium azide (0.30 g, 4.6 mmol) was added to a solution of 50 mg bromo-terminated silicon nanoparticles in 20 mL of dry dimethylformamide (DMF). The solution was stirred at 65°C overnight under nitrogen atmosphere. DMF was removed by vacuum distillation and dry THF was added. The mixture was centrifuged to remove NaBr and unreacted NaN₃. The solution contains azide-terminated silicon nanoparticles which are soluble in THF. The solvent was removed by rotary evaporator and the nanoparticles were redispersed in CH₂Cl₂ and purified by GPC. Yield: 40-60 mg. ¹HNMR (δ, 300 MHz, CD₂Cl₂): 3.25 (s), 2.5-0.5 (m, broad). UV-vis Absorption (in CH₂Cl₂): Single absorption with a tail up to 550 nm. PL emission (in CH₂Cl₂): 350-700 nm emission peaks by changing excitation wavelength from 300-400 nm. FTIR (thin film on KBr): 2820-2990 cm⁻¹ (ν (C-H)), 2100 cm⁻¹ (ν

(N=N=N)), 1500-1750 cm^{-1} (ν (C=C)), 1465-1376 cm^{-1} (δ (C-H)), 1250 cm^{-1} (δ (Si-C)), 1190-850 cm^{-1} (ν (Si-O)), 830 cm^{-1} (ν (Si-C)). *Safety note: Large scale reactions of azide are prone to dangerous exothermic reactions. The use of chlorinated solvents in the presence of sodium azide must be avoided, as the byproducts may be highly explosive.*

4.4.5 Synthesis of ω -azidoundecyl (35%)-Si nanoparticles

Silicon wafer (1.0g, 36 mmol) was ball milled with a mixture of 7.0 mL (32 mmol) 11-bromo-1-undecene and 13 mL (132 mmol) 1-pentyne for 24 hours to synthesize the bromo-terminated silicon nanoparticles. Sodium azide (0.30 g, 4.6 mmol) was added to a solution of 50 mg bromo-terminated silicon nanoparticles in 20 mL of dry dimethylformamide (DMF). The solution was stirred at 65°C overnight under nitrogen atmosphere. DMF was removed by vacuum distillation and dry THF was added. The mixture was centrifuged to remove NaBr and unreacted NaN_3 . The solution contains azide-terminated silicon nanoparticles which are soluble in THF. The solvent was removed by rotary evaporator and the nanoparticles were redispersed in CH_2Cl_2 and purified by GPC. Yield: 40-60 mg. ^1H NMR (δ , 300 MHz, CD_2Cl_2): 3.25 (s), 2.5-0.5 (m, broad). UV-vis Absorption (in CH_2Cl_2): Single absorption with a tail up to 650 nm. PL emission (in CH_2Cl_2): 350-700 nm emission peaks by changing excitation wavelength from 300-400 nm. FTIR (thin film on KBr): 2820-2990 cm^{-1} (ν (C-H)), 2100 cm^{-1} (ν (N=N=N)), 1500-1750 cm^{-1} (ν (C=C)), 1465-1376 cm^{-1} (δ (C-H)), 1250 cm^{-1} (δ (Si-C)), 1190-850 cm^{-1} (ν (Si-O)), 830 cm^{-1} (ν (Si-C)). *Safety note: Large scale reactions of azide are prone to dangerous exothermic reactions. The use of chlorinated solvents in the presence of sodium azide must be avoided, as the byproducts may be highly explosive.*

4.4.6 Synthesis of 5-(4-(prop-2-yn-1-yloxy))phenyl-10,15,20-triphenyl-Zincporphyrin

5-(4-(prop-2-yn-1-yloxy))phenyl-10,15,20-triphenyl-Zincporphyrin was synthesized and well characterized by Dr. Jayawickramarajah's group.¹⁵⁵

4.4.7 Functionalization of Azide-terminated Si NPs with Zn-porphyrin

Azide-terminated Si nanoparticles (20 mg) and 5-(4-(prop-2-yn-1-yloxy))phenyl - 10,15,20-triphenyl-Zincporphyrin (10 mg, 1.4×10^{-2} mmol) were dissolved in 15 mL of THF. Cu(I) bromide (10 mg, 4.8×10^{-2} mmol) was added into the reaction mixture. The solution was stirred at room temperature overnight under nitrogen atmosphere. THF was removed by vacuum distillation and 20 mL dichloromethane and 1 mL ethylenediamine was added. The solution was subsequently washed three times with saturated brine solution. The Zn-porphyrin functionalized silicon nanoparticles were purified by GPC to removed unreacted silicon nanoparticles and Zn-porphyrin. Yield: 15-25 mg. ¹HNMR (δ , 300 MHz, CD₂Cl₂): 9.1-7.8 (multiple broad peaks, aromatic protons), 2.3-0.5 (multiple broad peaks, alkyl protons on the surface of silicon nanoparticle). UV-vis Absorption (in water): broad absorption in 250-380 nm, Soret band absorption at 425 nm, Q band absorption at 560 nm and 600 nm.

4.4.8 Analytical methods

4.4.8.1 NMR sample preparation and acquisition

NMR samples were prepared by vacuum drying ~1.5 mL of the silicon nanoparticle solution, adding 0.8 mL of the preferred deuterated solvent, and then transferring the

solution to a 5 mm NMR tube. ^1H -NMR measurements were performed on a Bruker Avance 300 spectrometer equipped with a 5 mm BBO probe.

4.4.8.2 Infrared spectroscopy

FTIR spectra were recorded at 1 cm^{-1} resolution with 1000 scans on a Thermo Nicolet NEXUS 670 FTIR instrument. Samples were prepared as a thin film of passivated silicon nanoparticles prepared by depositing dichloromethane solution of silicon nanoparticles on a KBr plate. The FT-IR sample chamber was purged with dry nitrogen before collecting any data.

4.4.8.3 UV-vis absorption and photoluminescence spectroscopy

UV-Vis absorption spectra were recorded in a quartz cuvette (1cm), using a Cary 50 spectrophotometer and were corrected for the solvent absorption. The scan range was 200-800 nm with a 300 nm min^{-1} scan rate. Excitation-emission spectra were recorded in a quartz cuvette (1cm), using a Varian Cary Eclipse spectrofluorometer with a scan rate of 120 nm min^{-1} .

4.4.8.4 GC-MS

GC-MS analysis was performed by GC-MS (Varian 450 GC, Varian 300 MS) with VF5-MS capillary column. 2 μL diluted solution in methylene chloride was injected into the GC-MS system.

4.4.8.5 Time-resolved emission spectroscopy

Time-resolved decay measurements were made using a home built system employing time-correlating single photon counting (TCSPC) with CH_2Cl_2 as a solvent. A Vanguard laser ($\lambda_{\text{exc}} = 355\text{nm}$) was used as an excitation source, and photons were

collected until a maximum of 5×10^4 counts. All sample cuvettes were held at an angle 45° to preclude any back reflections of excitation pulses back into the sample. Lifetimes decay analysis was carried out using custom written routines within Excel worksheets. Fitting was done with a stretched exponential function and expressed as a mean lifetime of distribution, according to the method of French et al.¹⁵⁶

4.4.8.6 Femtosecond transient absorption spectroscopy

The femtosecond transient absorption measurements were made using toluene/acetonitrile (1:1) as a solvent. A laser beam at 804 nm and 44 fs in duration produced by a Ti: sapphire oscillator (Vitesse, Coherent Inc) and regenerative amplifier (Spitfire pro, Spectra-Physics) was split in to two parts. One part was used to pump an in-house built optical parametric amplifier (OPA), which produces signal-idler pulse pairs. The signal beam (ca. 2 μ J/pulse) was delayed by a translation stage (Parker) and focused by a 100 mm lens into the sample. The other part of the fundamental beam was used to generate white light continuum, ranging from 460 nm to 750 nm. After passing a translation stage (NRT150, Thorlabs Inc), the white light continuum was then focused into the sample with a 40 nm schromatic lens and detected by a CCD array detector (TCE-1209-U), Mightex). By chopping the excitation beam at half the laser repetition rate, difference spectra were recorded with excitation pulses on and off.

4.5 Model of Si nanoparticles ¹⁵⁷

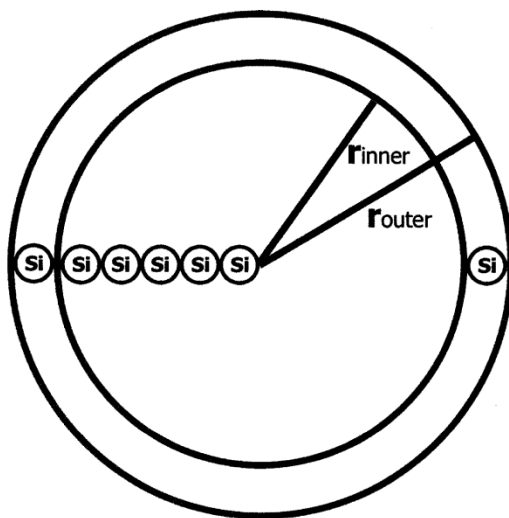


Figure 4.32 Model of a Si nanoparticle

In order to estimate the number of Zn-porphyrin on each nanoparticle, a model of the silicon nanoparticle was developed. Assuming the silicon nanoparticle is spherical in shape and the density of the silicon nanoparticle equal to the density of the bulk silicon, the total number of silicon atoms in a nanoparticle equal to the volume, $V = \frac{4}{3}\pi r^3$ (cm³), multiplying by the density of silicon (2.33 g/cm³), and then dividing by the molecular weight (28.02 g/mol), followed by multiplying by Avogadro's number (6.02×10^{23} molecules/mol), which showed in the following equation:

$$N(\text{total}) = \frac{4}{3} \pi r_{\text{outer}}^3 * 2.33 * \frac{1}{28.02} * 6.02 * 10^{23}$$

The number of surface sites is determined by the difference in the number of silicon atoms between two spheres that differ in radius by the width of one silicon atom, which is 2.34 Å. The equations are shown below:

$$N(surface) = N(total) - N(inner)$$

$$N(inner) = \frac{4}{3} \pi r_{inner}^3 * 2.33 * \frac{1}{28.02} * 6.02 * 10^{23}$$

Base on the TEM image, the average size of silicon core of azide terminated silicon nanoparticles is around 3.2 nm. So,

$$N(total) = \frac{4}{3} * 3.14 * \left(\frac{3.2}{2} * 10^{-7} \right)^3 * 2.33 * \frac{1}{28.02} * 6.02 * 10^{23}$$

$$= 905$$

$$N(inner) = \frac{4}{3} * 3.14 * \left(\left(\frac{3.2}{2} - 0.234 \right) * 10^{-7} \right)^3 * 2.33 * \frac{1}{28.02} * 6.02 * 10^{23}$$

$$= 568$$

$$N(surface) = N(total) - N(inner)$$

$$= 905 - 568$$

$$= 337$$

When the surface of the silicon nanoparticle is passivated by covalently bound organic ligands, there are two different bonding types between the silicon surface and the organic ligands. On the Si (111) surface, the bonding type is one Si atom per ligand, while it is two Si atoms per ligand on the Si (100) surface. Assuming the entire surface of the nanoparticle is covered by the organic ligands, the number of organic ligands on the surface is in the range of 168~337.

From the ¹H-NMR of the four silicon nanoparticle-porphyrin systems with different donor-acceptor ratio (Figure 4.14), the ratio of β-proton peak which is from the Zn-porphyrin and the methyl group which is from the pentenyl group on the surface of the silicon nanoparticle can be calculated based on the integrated area of these two peaks. To

avoid the overlap between the $-\text{CH}_3$ peak and $-\text{CH}_2$ peak, the integrated area of the $-\text{CH}_3$ is estimated by double the integrated area of the half peak at 0.5-0.8 ppm. So the ratio of β -proton and methyl group in the four silicon nanoparticle-porphyrin systems are 1:31.0, 1:13.4, 1:10.7 and 1:5.4, respectively. Then the number of Zn-porphyrin on each nanoparticle in the four different silicon nanoparticle-porphyrin systems can be calculated, which giving the range are 2.0~4.0, 4.6~9.2, 5.7~11.4 and 10.9~21.8, respectively.

Similar calculations have been done with the silicon-pentenyl-porphyrin system, silicon-heptyl-porphyrin system and silicon-undecyl-porphyrin system which have different donor-acceptor distance. The ratios of β -proton and methyl group in these three silicon nanoparticle-porphyrin systems are 1:9.0, 1:8.4 and 1:10.7, respectively. The number of Zn-porphyrin on each nanoparticle in the three different silicon nanoparticle-porphyrin systems are in the range of 6.7~13.4, 7.2~14.4 and 5.7~11.4, respectively.

Chapter 5: Silicon Nanoparticle-based Nanocarriers for Porphyrin

Delivery in Photodynamic Therapy

5.1 Introduction

Photodynamic therapy (PDT) is a promising, relatively new method for cancer treatment, where tumor cells are damaged by light-induced reactive oxygen species, such as singlet oxygen ($^1\text{O}_2$) or superoxide (O_2^-).¹⁵⁸ As shown in Figure 5.1, the singlet oxygen is generated by a photosensitizer when excited at a specific wavelength. After absorbing light energy, the excited-state triplet photosensitizer transfers energy to the ground-state triplet oxygen and produces reactive singlet oxygen which can directly kill tumor cells by the induction of necrosis and/or apoptosis.^{158a} The major advantages of PDT compared to the traditional cancer treatments are that it is relatively inexpensive and non-invasive, has low cumulative toxicity and can be applied locally.¹⁵⁹

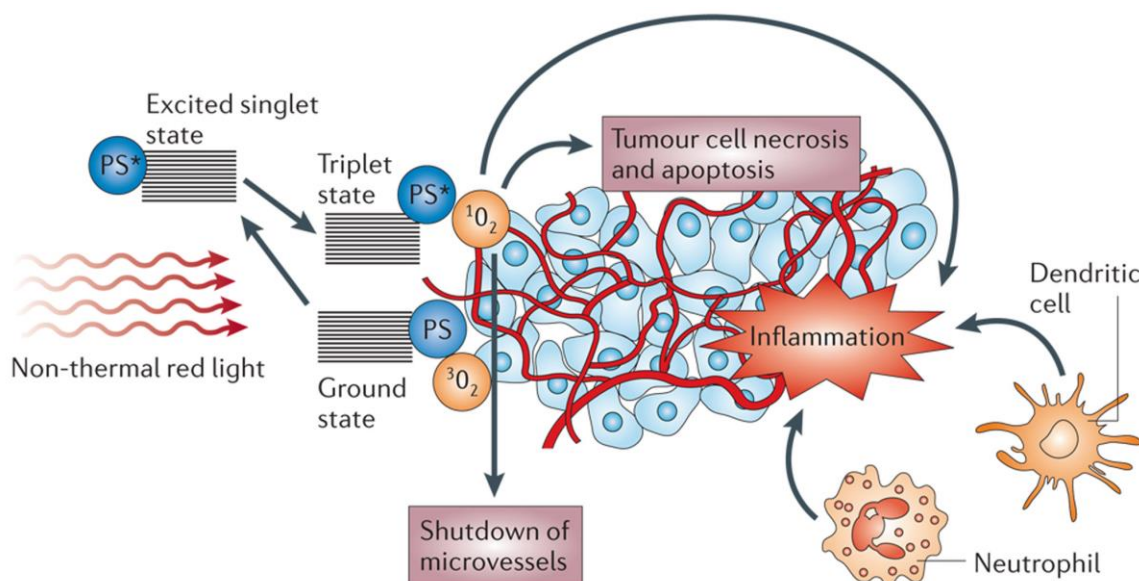


Figure 5.1 The mechanism of action on tumors in photodynamic therapy^{158a}

The photosensitizers in use today are mostly organic dye molecules, such as porphyrins. Porphyrins and their derivatives are efficient photosensitizers for PDT because of their unique properties which meet several photophysical and photochemical requisites: they have relatively long excited state lifetimes in order to transfer their energy to oxygen molecules; they have low dark cytotoxicity to the human body; they have adjustable absorption properties in the red light range; and they are easy to synthesize and modify.¹⁵⁹⁻¹⁶⁰ However, similar to other molecular photosensitizers, there are several limitations of porphyrins used in PDT, including low selectivity for malignant tissues, low solubility and low photophysical/chemical activity in aqueous media due to the aggregation.^{159, 161}

To overcome these limitations, nanoparticles have been employed as nanocarriers of photosensitizing molecules to improve the PDT due to their critical properties. The nanoparticle surface can be modified with various functional molecules, such as photosensitizers and targeting molecules, and prevent the aggregation of photosensitizers.¹⁶² Nanoparticles with photoluminescence also can act as light antennas for photosensitizing molecules to enhance the PDT efficiency.¹⁶³ Furthermore, nanoparticles with certain size can selectively accumulate in tumor tissue based on the enhanced permeability and retention (EPR) effects.¹⁶⁴

Silicon nanoparticles have been established as excellent candidates as drug delivery materials useful for cancer therapies because of their excellent biocompatibility, biodegradability, low cytotoxicity and multiple possibilities for surface functionalization.^{87, 93} Cunin and coworkers have used porous silicon nanoparticles (35 nm-245 nm) as nanocarriers for delivering porphyrin drugs into breast cancer cells for

PDT applications.^{161a} The water soluble porphyrin was covalently immobilized onto the surface of a porous silicon nanoparticle via an allyl isocyanate reaction. The porphyrin-grafted porous silicon nanoparticles were shown to be a more efficient PDT *in vitro* compared to the plain photosensitizer. However, the mass loading of the porphyrin drug in this porphyrin-grafted porous silicon nanoparticles system is only 13.3 µg per mg of nanoparticles, and the pathway of the cell death induced by this system is still unknown. Furthermore, no study has been reported on the immobilization of porphyrin photosensitizers on small size (<10 nm) silicon nanoparticles for PDT so far. Hence, here we present a new approach to synthesize water soluble PEGylated porphyrin functionalized silicon nanoparticles for PDT, in which the silicon nanoparticles act as nanocarriers to deliver porphyrins into human embryonic kidney 293T (HEK293T) cells. The successful internalization of the PEGylated porphyrin grafted silicon nanoparticles in the HEK293T cell was observed, which formulated a demonstrated efficient PDT after the cells were irradiated by red light.

Small size azide-terminated silicon nanoparticles, obtained from reactive high energy ball milling, were functionalized with PEGylated alkyno Zn-porphyrins via an azide-alkyne “click” reaction (Figure 5.2). The three PEG chains on the porphyrin increase the water solubility of the porphyrin-silicon nanoparticle system. PEG was chosen in this system because it is an ideal water soluble polymer for the modification of nanostructured materials due to its biocompatibility and low-toxicity. Furthermore, PEG grafting has also been proved to reduce hemolytic toxicity and increase the blood circulation times in drug delivery systems.¹²¹ Finally, the large amounts of PEG

substituents create steric hindrance between the porphyrin units to prevent porphyrin aggregation.

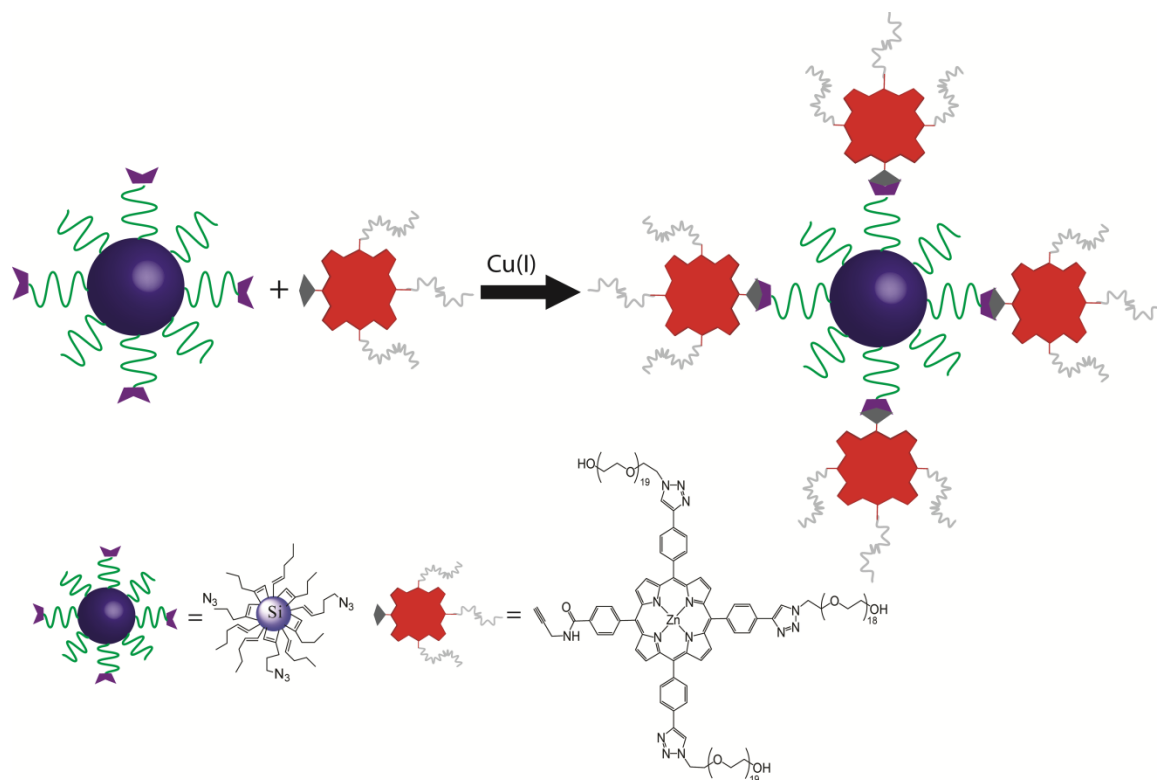


Figure 5.2 Illustration showing the synthesis of PEGylated porphyrin grafted silicon nanoparticles

5.2 Results and Discussion

5.2.1 Synthesis and characterization of PEGylated porphyrin grafted silicon nanoparticles

The ω -azido-pentenyl silicon nanoparticles were obtained through the reaction of NaN₃ and the ω -chloro-pentenyl silicon nanoparticles, which were prepared by reactive high energy ball milling. The systematic characterization of azido-terminated silicon nanoparticles has been discussed in Chapter 3. The PEGylated porphyrin grafted silicon

nanoparticles were prepared by the Huisgen [3+2] cycloaddition of the PEGylated alkyno-porphyrin and the azido-terminated silicon nanoparticles.

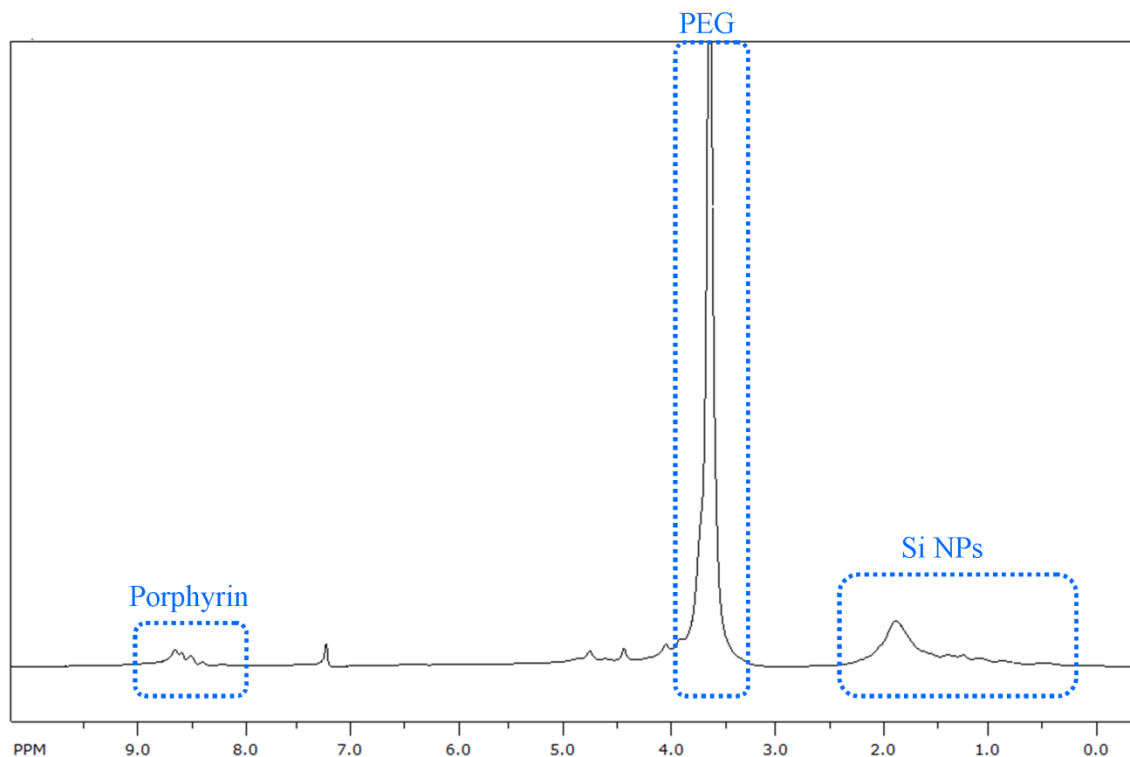


Figure 5.3 ¹H-NMR spectrum of PEGylated porphyrin grafted silicon nanoparticles in CDCl₃

The successful attachment of the PEGylated porphyrin onto the silicon nanoparticles is supported by the ¹H-NMR spectrum (Figure 5.3). The ¹H-NMR spectrum of the PEGylated porphyrin grafted silicon nanoparticles exhibit the peaks from the organic surface ligands, the porphyrin units and the PEG substituents. The characteristic peaks around 8.5 ppm are assigned to the aromatic protons of the porphyrin units, while the strong peak around 3.6 ppm is assigned to the –CH₂ groups on the PEG chain. The peaks from 0.5 ppm – 2.0 ppm are assigned to the alkyl protons on the silicon nanoparticles. The surface coverage of the porphyrin on the silicon nanoparticles can be estimated based

on the ^1H -NMR spectrum. First, the ratio of the porphyrin units and the pentenyl groups on the surface of the silicon nanoparticle can be calculated by comparing the integrated area of the aromatic proton peaks (around 8.6 ppm) and the high field alkyl proton peaks (from 0.5-2.0 ppm). Since the theoretical ratio of ω -azido-pentenyl group which has 4 high field alkyl protons and the pentenyl group which has 7 high field alkyl protons on the starting ω -azido-pentenyl (50%) silicon nanoparticles is 1:1, the average number of protons on each pentenyl chain on the silicon nanoparticles can be estimated to be 5.5. In addition, the total number of the aromatic protons on each porphyrin unit is 28 (including β -pyrrole protons, phenyl protons and triazole protons). Therefore, the ratio of the porphyrin units to the pentenyl groups was estimated to be 1:27.8, which means the surface coverage of porphyrin units on the silicon nanoparticle is about 7.2% and indicates the incomplete conversion of the azide groups. The inefficiency of the reaction may be due to the steric hindrance caused by the bulky structure of the PEGylated porphyrin. Changes in the FTIR spectra shown in Figure 5.4, which include the decrease of the azide vibration peak at 2100 cm^{-1} , further support the incomplete attachment of the PEGylated porphyrins.

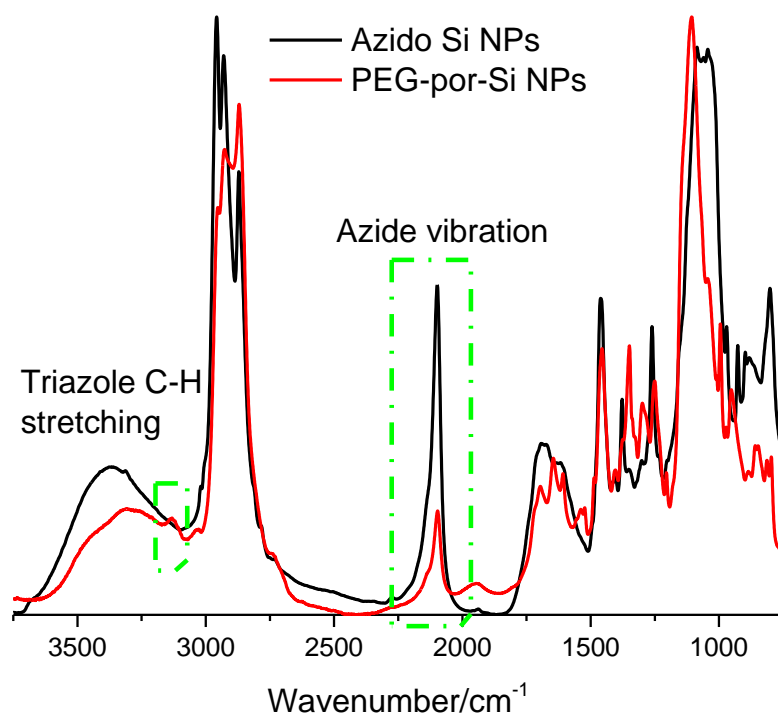


Figure 5.4 FTIR spectra of azido-terminated silicon nanoparticles and PEGylated porphyrin grafted silicon nanoparticles

The images of PEGylated porphyrin grafted silicon nanoparticles were first obtained by tapping mode AFM using a freshly cleaved mica substrate. The AFM image of the starting azido-terminated silicon nanoparticles (Figure 5.5a) clearly shows the spherical particles with an apparent height around 3.4 ± 1.4 nm (Figure 5.5b). The observed heights of the nanoparticles are consistent with the results from TEM images discussed previously which shows the average size of the azido-terminated silicon nanoparticles is around 3.3 ± 1.3 nm (Chapter 3). In addition, the AFM image of the PEGylated porphyrin grafted silicon nanoparticles (Figure 5.5c) show amorphous structures with a bright core in the center. The apparent height of the bright core around 3.9 ± 0.6 nm (Figure 5.5d) is

in accord with the height of the starting azido-terminated silicon nanoparticles. The amorphous structure around the bright core may correspond to the PEGylated porphyrins attached on the silicon nanoparticles. The width of the object in the AFM image is significant larger than the actual width, which is the image artifact. This is because the observed width including the actual width of the object and the diameter of the tip.

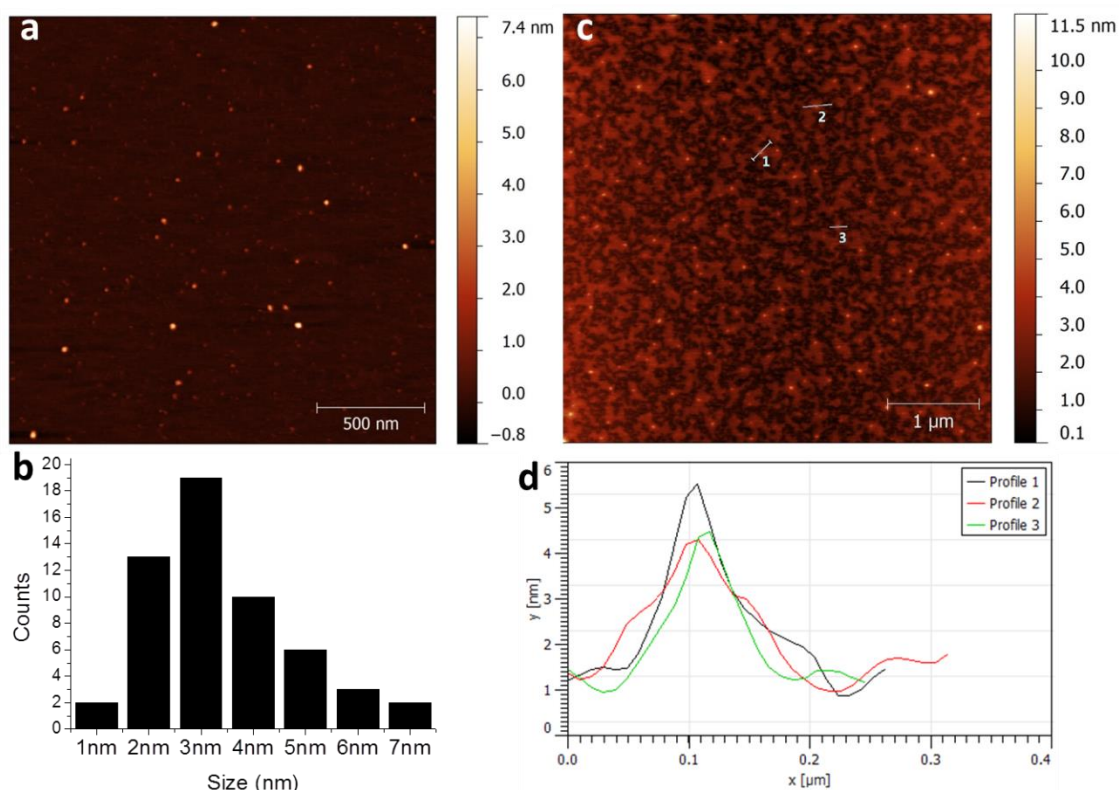


Figure 5.5 AFM image (a) and histogram height distribution (b) of the azido-terminated silicon nanoparticles; AFM image of the PEGylated porphyrin grafted silicon nanoparticles (c) and the height profiles collected at the indicated white lines (labeled 1,2,3 respectively) (d).

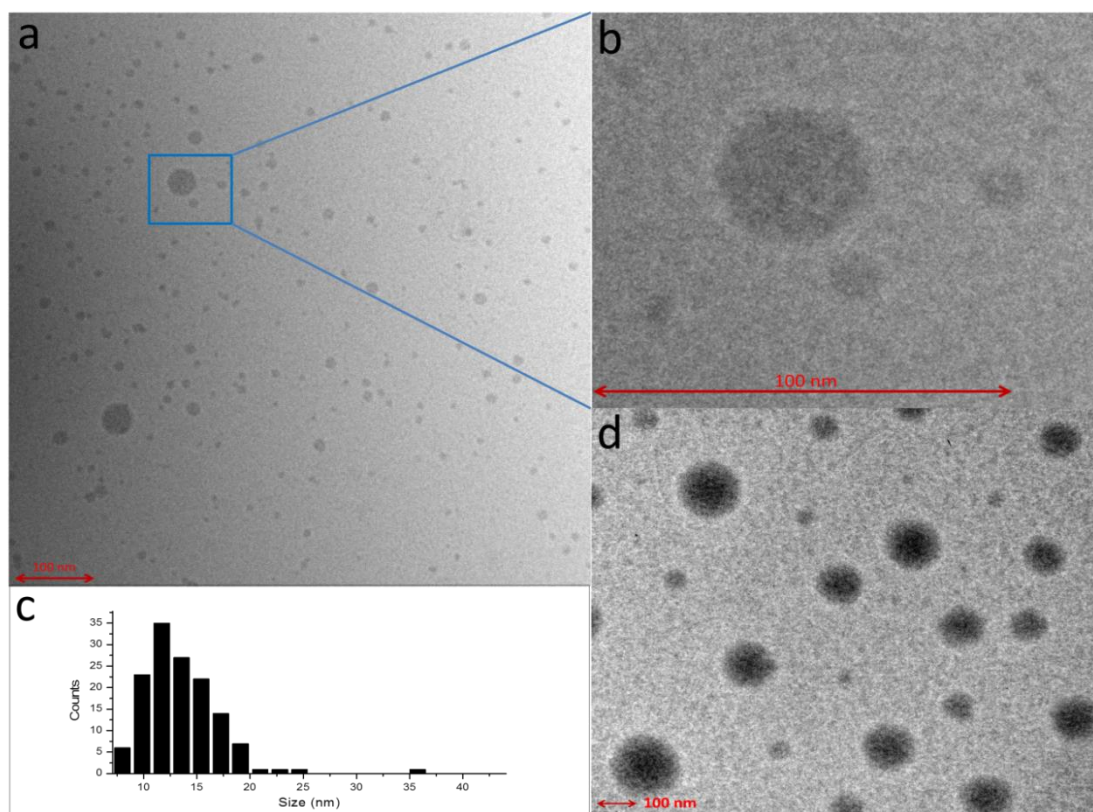


Figure 5.6 Cryo-TEM image (a), a zoom in image (b) and the histogram size distribution of the PEGylated porphyrin grafted silicon nanoparticles in water (0.10 mg/mL, 20 μ M of porphyrin); (d) Conventional TEM image of PEGylated porphyrin grafted silicon nanoparticles in water.

Cryo-TEM was utilized to probe the structure of the PEGylated porphyrin grafted silicon nanoparticles in aqueous media. Cryo-TEM, where the sample is studied at cryogenic temperatures, allows the observation of nanoparticles that have not been stained or fixed in any way, showing them in their native environment. As shown in Figure 5.6a, the Cryo-TEM image of the PEGylated porphyrin grafted silicon nanoparticles in water shows spherical structures with a diameter around 13.5 ± 3.8 nm corresponding to individual nanoparticles. A few larger micelle-like nanostructures with diameters around 35 nm are also observed, which are due to the aggregation of the

PEGylated porphyrin grafted silicon nanoparticles. Figure 5.6b shows a micelle-like nanostructure with darker spots inside the structure indicating that the micelles consist of the smaller silicon nanoparticles. The formation of the micelle-like nanostructure may be due to the hydrophilic/hydrophilic interactions between the PEG chains or the hydrophobic/hydrophobic interactions between the alkyl chains since the PEGylated porphyrin grafted silicon nanoparticles have amphiphilic structure. In order to prove the formation of the micelle-like nanostructure, conventional TEM was performed on the identical nanoparticle sample that used for cryo-TEM characterization. TEM sample were prepared by evaporation of the nanoparticle solutions on a copper grid. During the drying process, the concentration of the PEGylated porphyrin grafted silicon nanoparticles increases resulting in the aggregation of the nanoparticles and formation of micelle-like nanostructures. In contrast to cryo-TEM, the conventional TEM image of this sample shows much larger spherical micelle-like nanostructures with diameters in the range of 50-150 nm. Dynamic light scattering (DLS) was performed to measure the hydrodynamic diameter of the micelle-like structure. However, the DLS analysis didn't show a reasonable result, which might be due to the laser frequency of the DLS ($\lambda = 660$ nm) being absorbed by the porphyrin.⁷⁰

One weakness of organic photosensitizers such as porphyrins is their aggregation, including J-aggregates and H-aggregates, in aqueous media which reduces their photophysical/chemical activity. J-aggregates are formed with the porphyrin molecules arranged side-by-side such that the transition moment of the porphyrins are parallel and the angle between the transition moment and the line joining the molecular centers is nearly zero.¹⁶⁵ The strong coupling of the porphyrins in J-aggregates results in the

absorption band shifts to a longer wavelength.¹⁶⁶ In contrast to the J-aggregates, H-aggregates are face-to-face arrangement, in which the transition moments of the porphyrins are perpendicular to the line of centers.¹⁶⁵ The H-aggregates are known to lead to a blue shift of the absorption band.¹⁶⁷

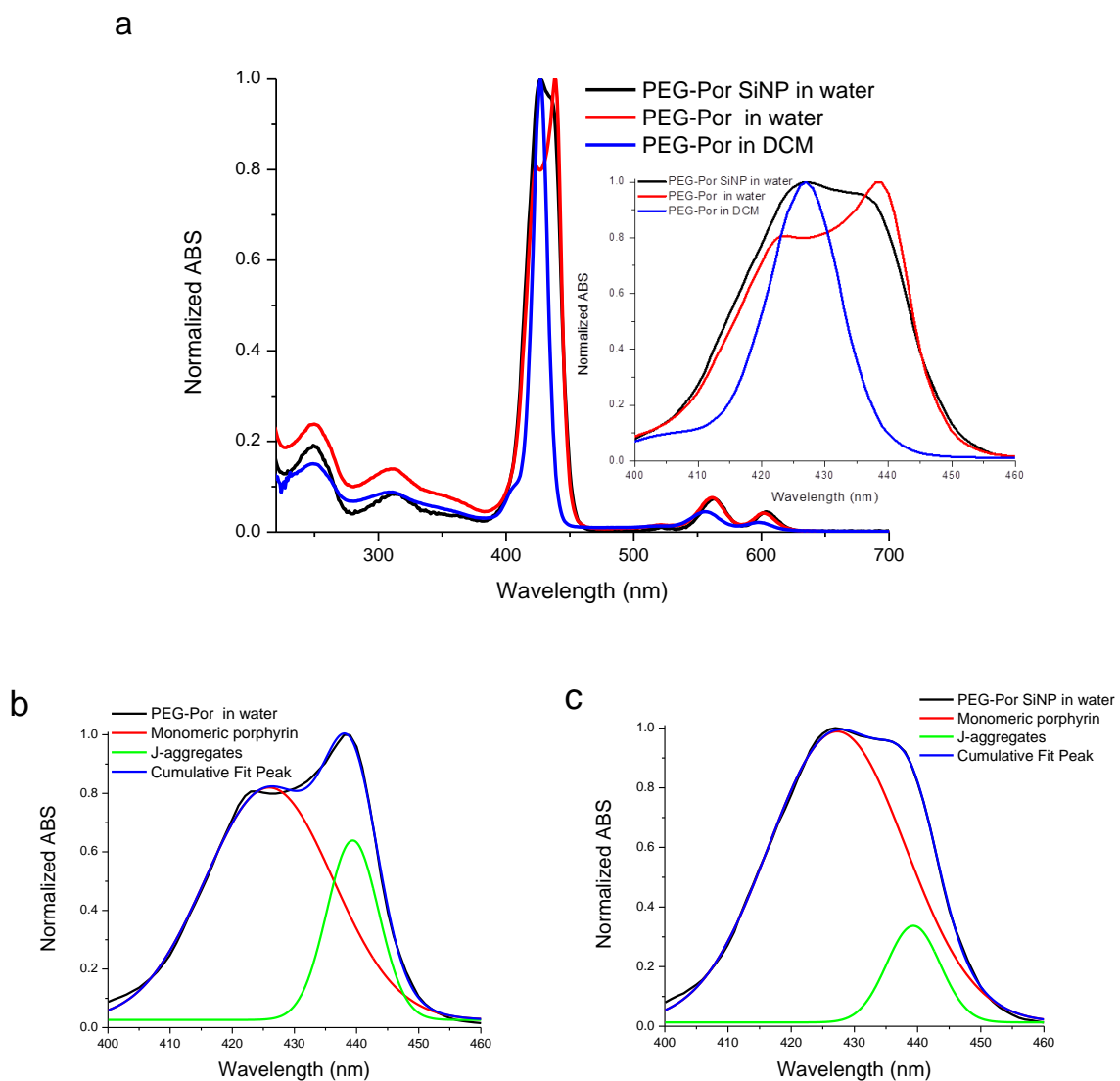


Figure 5.7 (a) UV-Vis absorption spectra of PEGylated porphyrin in water and CH_2Cl_2 and PEGylated porphyrin grafted Si nanoparticles in water (insert is the absorption in 400-460 nm range); Reconstructed Soret peaks of PEGylated porphyrin (b) and PEGylated porphyrin grafted Si nanoparticles (c)

One of the advantages of using silicon nanoparticles as nanocarriers in this system is to prevent the aggregation of the porphyrin in aqueous media. As shown in Figure 5.7a, the PEGylated porphyrin in methylene chloride displays the identical sharp Soret band and Q bands which are ascribed to the monomeric porphyrin molecules. Additionally, the PEGylated porphyrin in water shows a broadened Soret band which consists of the Soret band of monomeric porphyrin at 427 nm and a red shifted absorption peak at 438 nm due to the J-aggregates of the porphyrin molecules. Similarly, the PEGylated porphyrin grafted silicon nanoparticles in water also show a broadened Soret band indicating that the porphyrin units in both the PEGylated porphyrin and PEGylated porphyrin grafted silicon nanoparticles undergo some self-aggregation via π -stacking interactions in aqueous media. However, the fact that the red shifted absorption peak of the PEGylated porphyrin grafted silicon nanoparticles is weaker than that of the pure PEGylated porphyrin shows that the aggregation of the porphyrin is minimized by silicon nanoparticles. Gaussian multi-peak fitting function in Origin Pro 8.6 was applied to reconstruct the Soret absorption peaks of these two samples (Figure 5.7b, c). Quantification of porphyrin aggregation by silicon nanoparticles was obtained by calculating the ratio of the integrated area between monomeric porphyrin absorption peak and porphyrin J-aggregate peak in these two samples. The ratio is 1:0.36 for the PEGylated porphyrin and 1:0.16 for the PEGylated porphyrin grafted silicon nanoparticles, respectively. The minimization of the porphyrin aggregation may be due to the bulky PEG substituents on the porphyrin units, the unfavorable orientations of the porphyrin units, as well as the hydrophobic environment created by the alkyl chains on the surface of the silicon nanoparticles.

In addition, the mass loading of the porphyrin in the PEGylated porphyrin grafted silicon nanoparticles system also can be determined by the UV-Vis absorption spectra. The mass loading is defined as the mass of the drug component in nanoparticles per mg of nanoparticles. It determines the performance of the drug delivery system since it influences the rate and extent of drug release from the system.¹⁶⁸ The extinction coefficient of the PEGylated porphyrin monomer in methanol was first determined to be $3.11(1) \times 10^5 \text{ dm}^3 \text{ mol}^{-1} \text{ cm}^{-1}$ at 430 nm. Then the absorption of a 4.0 mg/L solution of the PEGylated porphyrin grafted silicon nanoparticles in methanol was measured, which was 0.2732(1) at 430 nm. Therefore, the concentration of the PEGylated porphyrin substituents in the nanoparticle solution was determined to be 0.88 $\mu\text{mole/L}$ or 3.16 mg/L. Since the weight percentage of porphyrin unit in the PEGylated porphyrin is 23.1% (the molecular weight of porphyrin unit over the molecular weight of the PEGylated porphyrin), the concentration of the porphyrin unit in the nanoparticle solution was 0.73 mg/L ($3.16 \times 23.1\%$), which means that the mass loading of the porphyrin in the PEGylated porphyrin grafted silicon nanoparticles system was 0.18 mg per mg of nanoparticles. It is 13 times higher than that of the porphyrin-porous silicon nanoparticles system developed by Cunin and coworkers for photodynamic therapy.^{161a}

5.2.2 Cellular uptake and subcellular localization of the PEGylated porphyrin grafted silicon nanoparticles

Since the photosensitizer causes cell damage by generating singlet oxygen, near-IR millisecond phosphorescence emission spectroscopy was performed in order to detect any singlet oxygen produced. The 577 nm irradiation of the air-saturated PEGylated porphyrin grafted silicon nanoparticles (0.05 mg/mL) in deuterated acetone results in the

absorption of a photon into the first Q-band of the porphyrin. A phosphorescence emission spectrum showed an emission peak at ~1278 nm which corresponds to the singlet oxygen emission (Figure 5.7).¹⁶⁹

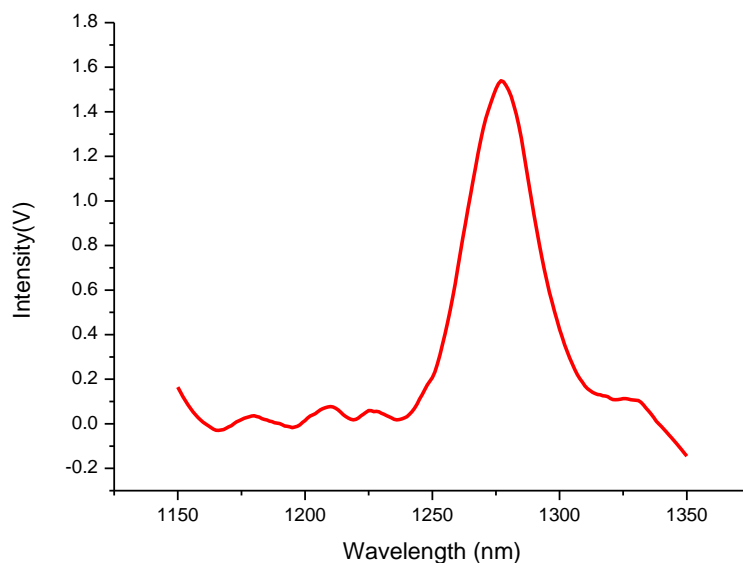


Figure 5.8 Near-IR Emission spectra of singlet oxygen phosphorescence in air-saturated solution of PEGylated porphyrin grafted silicon nanoparticles in deuterated acetone at room temperature. Absorbance of the PEGylated porphyrin grafted silicon nanoparticles was ~0.5 at $\lambda = 430$ nm.

HEK293T cells were used to determine cellular uptake of the PEGylated porphyrin grafted silicon nanoparticles, because these cells are very easy to grow and work with, and can be used in experiments in which the behavior of the cell itself is not of interest.¹⁷⁰ In each of the two independent experiments, the five HEK293T cell samples ($\sim 10^5$ cells/ μ L) were cultured in the incubating media which contained Dulbecco's Modified Eagle's Medium (DMEM), 10% fetal bovine serum and 1000 units/mL

penicillin/Streptomycin. An aqueous solution of the PEGylated porphyrin grafted silicon nanoparticles was added into the five cell samples at the time point of 0, 12, 18, 21 and 23 hours to achieve a concentration of 0.05 mg/mL (10 μ M in porphyrin) in the incubating media, and the cells were harvested at the end of 24 hours. This process meant these cell samples were incubated in the media with the same concentration of the PEGylated porphyrin grafted silicon nanoparticles for 1, 3, 6, 12, and 24 hours respectively. A control experiment, in which the cells were incubated for 24 hours in a media without PEGylated porphyrin grafted silicon nanoparticles, was also performed. After the incubation, all the growth media were removed and the cells were washed with 1X phosphate buffered saline (PBS buffer) twice. All the cell lysates were analyzed using UV-Vis spectroscopy to determine the uptake concentration of the PEGylated porphyrin grafted silicon nanoparticles by HEK293T cells.

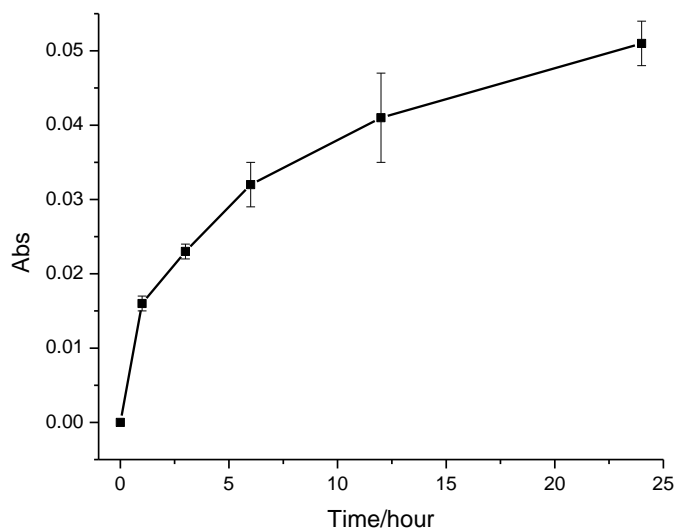


Figure 5.9 Cellular uptake curve of PEGylated porphyrin grafted silicon nanoparticles monitored by UV absorption at $\lambda = 430$ nm (average of two independent experiments).

The time-dependent uptake curve of the PEGylated porphyrin grafted silicon nanoparticles (Figure 5.9) was obtained by monitoring the UV-Vis absorption of the cell lysates at $\lambda = 430$ nm. The graph clearly indicates the uptake of the nanoparticles by the HEK293T cells with increasing the incubation time.

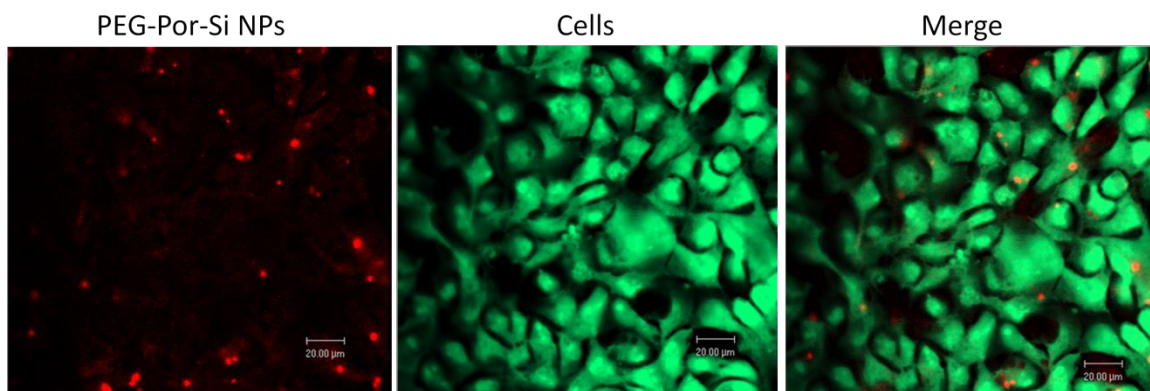


Figure 5.10 Confocal microscope images of fixed HEK293T cells. The cells were incubated with PEGylated porphyrin grafted silicon nanoparticles (0.05 mg/mL, 10 μ M in porphyrin) for 24 hours and co-stained with a whole cell stain (Cell Mask green). The stained cells were fixed with 4% PFA (4g paraformaldehyde and 2g sucrose in 100 mL PBS buffer) and then rinsed briefly with PBS buffer. The fixed cells were visualized by 488 nm laser excitation and a 515nm long pass (emission) filter was applied. PEGylated porphyrin grafted silicon nanoparticles were visualized by 633 nm laser excitation, and a 650-715 band pass (emission) filter was applied.

Confocal microscopy was utilized to investigate the cellular internalization of PEGylated porphyrin grafted silicon nanoparticles. Confocal microscopy is used to increase optical resolution and contrast of a micrograph by using point illumination and a spatial pinhole to eliminate out-of-focus light in specimens that are thicker than the focal plane, which enables the reconstruction of three-dimensional structures from the obtained

images.¹⁷¹ A very strong luminescent emission from PEGylated porphyrin grafted silicon nanoparticles was observed when the fixed cells, which were incubated with the nanoparticles for 24 hours, were selectively excited by a 633 nm excitation laser (Figure 5.10). When this image was merged with the image of the whole cells visualized by the Cell Mask Green which could stain the cytoplasm and the nucleus, the merged image clearly shows that the bright red luminescent dots were located inside the cells. Additionally, the confocal microscopy studies indicated that the luminescent dots and the cells were on the same plane, which further supported that the nanoparticles were internalized in the cells.

The time-dependent cellular uptake experiment and the confocal microscopy indicated that the PEGylated porphyrin grafted silicon nanoparticles were efficiently internalized in HEK293T cells, and that the internalization process can be detected by the red fluorescence emission from the porphyrin units on the nanoparticles.

Many studies have been reported and suggest that the reactive oxygen species generated by photosensitizers in different organelles induced cell death by different pathways.¹⁷² For example, Lam et al. claimed that the reactive oxygen species generation in mitochondria led to cell death in a mitochondrial apoptosis pathway such as cytochrome *c* release.^{172d} The subcellular localization of the PEGylated porphyrin grafted silicon nanoparticles was therefore investigated in order to elucidate the possible mechanism of these nanoparticles causing the cell death.

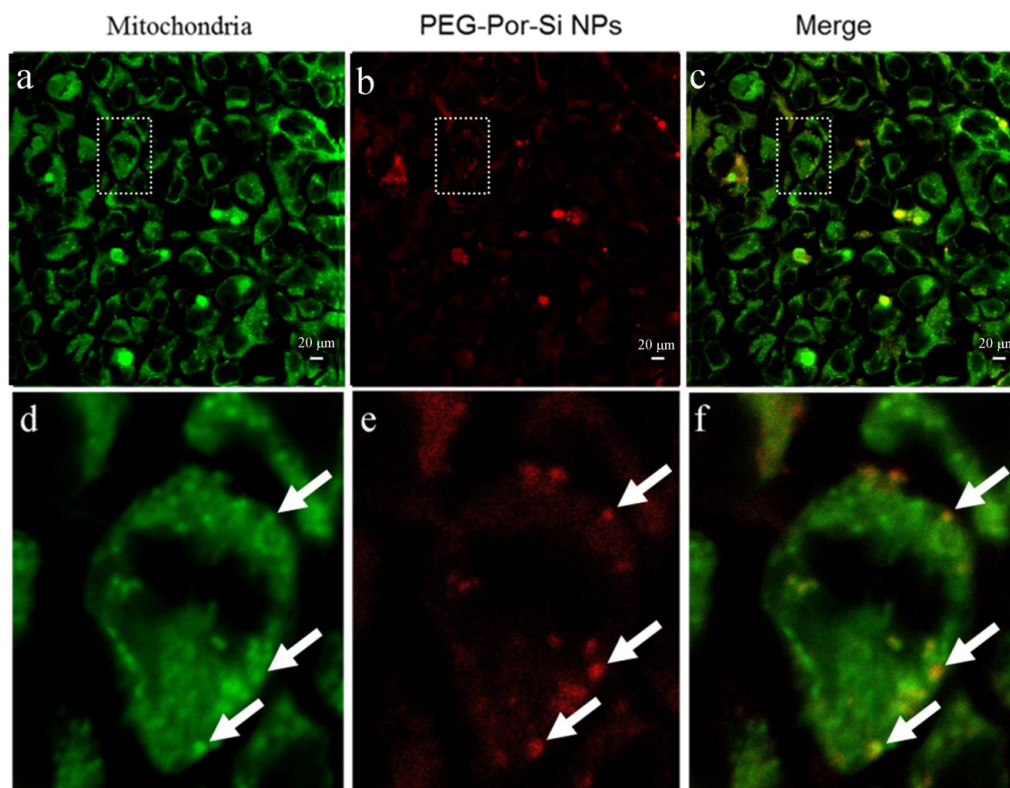


Figure 5.11 Confocal microscope images of fixed HEK293T cells to determine the subcellular localization of the nanoparticles. The cells were incubated with PEGylated porphyrin grafted Si nanoparticles (0.05 mg/mL, 10 μ M in porphyrin) for 24 hours and stained with a mitochondrial stain (MitoTracker Deep Red). Mitochondria were visualized by 633 nm laser excitation and a 650-715 nm band pass (emission) filter was applied. PEGylated porphyrin grafted Si nanoparticles were visualized by 554 nm laser excitation, and a 650-715 nm band pass (emission) filter was applied. The scale bar is 20 μ m.

A mitochondrial tracker (MitoTracker Deep Red) was used to stain the mitochondria in HEK293T cells to localize the mitochondria.^{172d} Upon excitation by laser irradiation, the fluorescence of the PEGylated porphyrin grafted silicon nanoparticles was observed and overlapped with the fluorescence of the mitochondrial tracker (Figure 5.11 a-c), indicating the PEGylated porphyrin grafted silicon nanoparticles accumulated in the

mitochondria. Figure 5.11 d-f showing zoom-in images of an individual cell further demonstrating that the nanoparticles locate in the mitochondria. Therefore, it is likely that the PEGylated porphyrin grafted silicon nanoparticles cause the cell death by generating singlet oxygen in mitochondria by a mitochondrial apoptosis pathway.

5.2.3 *In vitro* photodynamic therapy

The photodynamic therapy potential of the PEGylated porphyrin grafted silicon nanoparticles was examined by performing an *in vitro* photodynamic study with HEK293T cells. For this study, four HEK293T cell samples ($\sim 10^5$ cells/ μL) were incubated for 24 hours (two controls were incubated in the absence of PEGylated porphyrin grafted silicon nanoparticles, and two samples were treated with PEGylated porphyrin grafted silicon nanoparticles (0.01 mg/mL)). After the incubation, the medium was replaced with fresh growth medium and the cells were separated into two groups with one control and one sample in each group. One group was kept in the dark, while the other group was irradiated by a filtered high intensity Xenon arc (200 W) light with a 530 nm cut off long pass filter and a water IR filter (filters light from 1000 to 3000 nm). The irradiation process was performed for 30 minutes followed by a 30 minutes recovery period in an incubator to allow re-oxygenation of the media. The process was repeated 6 times to achieve 3 hours of light dose with the total light fluence of 39 J/cm^2 . After the irradiation, fluorescence microscopy was performed on all the samples stained with 4',6-diamidino-2-phenylindole (DAPI), which can stain the nucleus of the cells, to evaluate the phototoxicity. As shown in Figure 5.12d, the nucleus of the cells treated with both the PEGylated porphyrin grafted silicon nanoparticles and light show a dense, spherical morphology indicating the death of the cells.¹⁷³ In contrast, the nucleus of the cells in all

the controls (cells with and without light irradiation in the absence of the PEGylated porphyrin grafted silicon nanoparticles, and cells without irradiation in the presence of PEGylated porphyrin grafted silicon nanoparticles) show a larger, amorphous morphology indicating living cells, and no significant cell death was observed. These data indicate that the HEK293T cells can only be killed by applying both the PEGylated porphyrin grafted silicon nanoparticles and excitation light. This indicates that PEGylated porphyrin grafted silicon nanoparticles have excellent phototoxicity as well as low dark cytotoxicity.

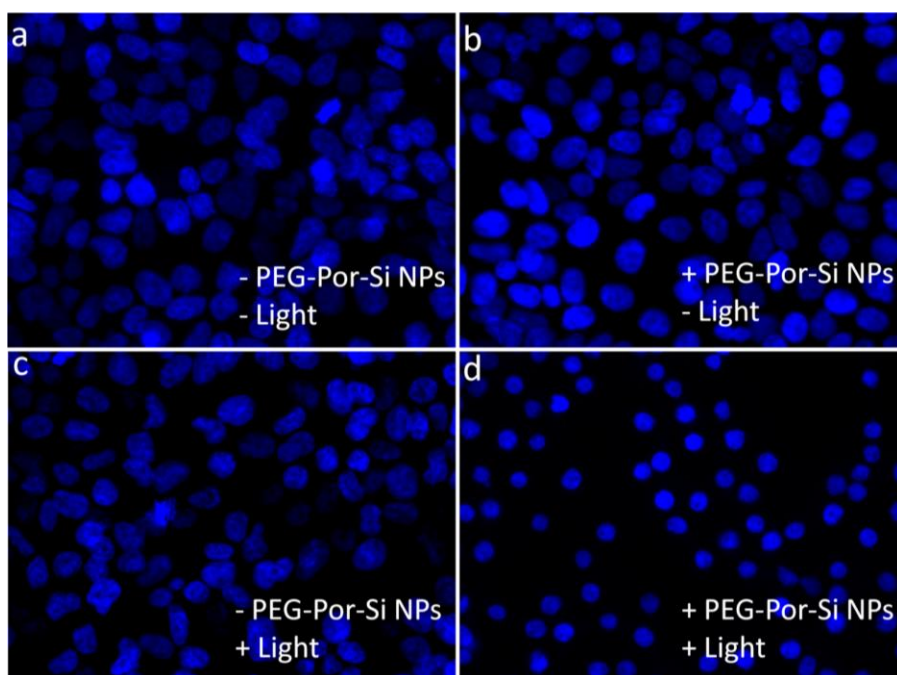


Figure 5.12 Fluorescence microscopy image of DAPI stained nucleus. (a) HEK293T cells without PEG-Por-Si NPs and irradiation, (b) HEK293T cells incubated with 0.01 mg/mL PEG-Por-Si NPs for 24 hours without irradiation, (c) HEK293T cell without PEG-Por-Si NPs and irradiated for 3 hours, (d) HEK293T cells incubated with 0.01 mg/mL PEG-Por-Si NPs for 24 hours and irradiated for 3 hours.

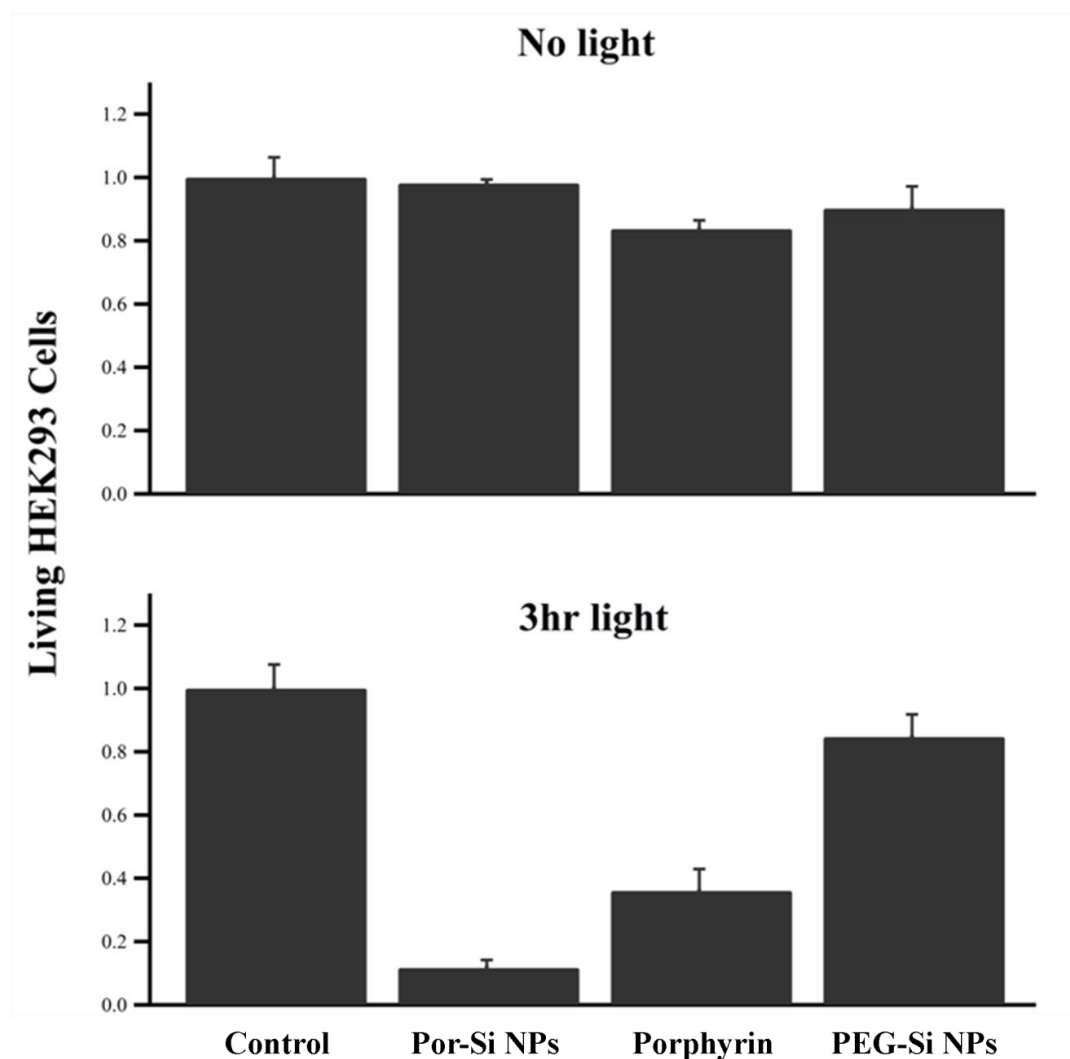


Figure 5.13 Efficacy of PEGylated porphyrin grafted silicon nanoparticles in inducing cellular death by a photodynamic process. HEK293T cells were incubated for 24 hours with PEG-Por-Si NPs (10 μ M in porphyrin), PEGylated porphyrin (10 μ M in porphyrin), or PEGylated silicon nanoparticles (no porphyrin, 0.01 mg/mL). Cells were washed and irradiated for 3 hours. Further 12 hours incubation after irradiation, cell death was measured.

The photodynamic response of the PEGylated porphyrin grafted silicon nanoparticles was further analyzed and compared with the free PEGylated porphyrin by

performing a MTT assay. The MTT assay is a simple and accurate method to measure the activity of living cells via mitochondrial dehydrogenases.¹⁷⁴ The key component is 3-[4,5-dimethylthiazol-2-yl]-2,5-diphenyl tetrazolium bromide (MTT). Solutions of MTT, which dissolved in medium or balanced salt solutions without phenol red, are yellowish in color. Mitochondrial dehydrogenases of viable cells cleave the tetrazolium ring, yielding purple formazan crystals which are insoluble in aqueous solutions. The crystals are dissolved in acidified isopropanol. The resulting purple solution is spectrophotometrically measured. An increase or decrease in cell number results in a concomitant change in the amount of formazan formed, indicating the degree of cytotoxicity caused by the test material.¹⁷⁴⁻¹⁷⁵

For this study, HEK293T cells were treated with PEG-Por-Si NPs (10 μ M in porphyrin), PEGylated porphyrin (10 μ M in porphyrin), or PEGylated silicon nanoparticles (no porphyrin, 0.01 mg/mL). After 24 hours incubation, the medium was replaced with fresh growth medium and the cells were subjected to irradiation for 3 hours as described previously. Further 12 hours incubation after irradiation was carried out to ensure there was enough time for the apoptosis of cell damaged by PDT. Then a MTT assay was performed to evaluate the photodynamic response.^{161a} As shown in the Figure 5.13, the irradiation of HEK293T cells alone did not induce any toxicity. Furthermore, the cytotoxicity assays clearly show that the PEGylated silicon nanoparticles (no porphyrin) were almost non-toxic to the cells. In the presence of the PEGylated silicon nanoparticles (no porphyrin), around 90% of the HEK293T cells remain alive after 24 hours of incubation either with or without irradiation. In addition, free PEGylated porphyrin incubated with the HEK293T cells under the same conditions and without

irradiation induced only about 17% cytotoxicity. However, a higher level of the cell death (60%) was observed in cells treated with free PEGylated porphyrin and subjected to irradiation indicating the PEGylated porphyrin itself is a good photosensitizer for PDT. In the control experiment, cells treated with PEGylated porphyrin grafted silicon nanoparticles without irradiation caused almost no cell death, which further support the excellent low-dark cytotoxicity of this system. Finally, the PEGylated porphyrin grafted silicon nanoparticles induced about 90% cell death after irradiation for 3 hours. The phototoxicity of the PEGylated porphyrin grafted silicon nanoparticles was significantly increased while their dark cytotoxicity was decreased compared to the free PEGylated porphyrin. The increased phototoxicity observed with the PEGylated porphyrin grafted silicon nanoparticles may be attributed to the higher cellular uptake of the porphyrin and the reduced porphyrin aggregation achieved by the silicon nanoparticles. The decreased cytotoxicity of the system may be because the silicon nanoparticles can “holding” the porphyrin and prevent the degradation of porphyrins.

5.3 Conclusion

The water soluble PEGylated porphyrin grafted silicon nanoparticle system, in which the silicon nanoparticles were used as nanocarriers, were synthesized by conjugating the PEGylated porphyrins onto the azido-terminated silicon nanoparticles. The obtained PEGylated porphyrin grafted silicon nanoparticles have diameters around 13.5 ± 3.8 nm. The cryo-TEM and conventional TEM analysis showed that the PEGylated porphyrin grafted silicon nanoparticle also can form micelle-like structures at higher concentration in water via self-assembly. The UV-Vis absorption analysis demonstrated that the silicon nanoparticle can reduce the porphyrin aggregation in water, which can prevent the reduction of the photophysical activity of porphyrin. The cell studies demonstrated that the silicon nanoparticle can deliver the porphyrin drugs into HEK293T cells and accumulate in the mitochondrial, where the porphyrin can serve as an efficient photosensitizer to generate singlet oxygen and kill these cells via mitochondrial apoptotic pathway. The functionalized silicon nanoparticles exhibited lower dark cytotoxicity compared to the free PEGylated porphyrin, and a more efficient photodynamic therapy was observed *in vitro*.

5.4 Experimental Section

5.4.1 Materials and methods

All chemicals were purchased from Sigma-Aldrich or Alfa Aesar, and employed without further purification unless specified. Tetrahydrofuran (THF) was distilled over sodium-benzophenone prior to use. Dichloromethane was distilled over CaH_2 before use. Hexane, toluene and acetonitrile were distilled over sodium prior to use. Gel permeation chromatography (GPC) was used for the purification of nanoparticles. Bio-beads S-X1 were swelled overnight in dry THF and packed into a 40cm x 1.3cm glass column. Dichloromethane was used as an elution solvent. A concentrated nanoparticle solution (50mg in 1 ml CH_2Cl_2) was added to column and eluted into 3 fractions collected in 10ml increments in separate vials. The first fraction was collected when the first colored band began to elute. This fraction contained nanoparticles and was used in the synthetic reactions. The second and third fractions, containing mostly impurities, were discarded.

5.4.2 Synthesis of ω -azido-pentenyl (50%)-Si nanoparticles

1.0g (36 mmol) silicon wafer (as obtained from Silrec, undoped, mirror finish, orientation [111]) was placed in a stainless steel milling vial along with two stainless steel milling balls (diameter of 1.2 cm, weighing approximately 8.1g). The vial was filled in a Vacuum Atmospherics dry box under a nitrogen atmosphere with a mixture of 10mL (94 mmol) 5-chloro-1-pentyne and 10 mL (101 mmol) 1-pentyne, and then tightly sealed. The milling vial was placed in a SPEX 8000-D Dual Mixer/Mill, and high energy ball-milling were performed for 24 hours. After 24 hours of milling, the reaction mixture was centrifuged to remove larger particles. The solution contains chloro-terminated silicon nanoparticles which are soluble in non-polar organic solvents. All of the solvents were

removed by vacuum distillation and the nanoparticles were redispersed in CH₂Cl₂. Sodium azide (0.30 g, 4.6 mmol) was added to a solution of 50 mg chloro-terminated silicon nanoparticles in 20 mL of dry dimethylformamide (DMF). The solution was stirred at 65°C overnight under nitrogen atmosphere. DMF was removed by vacuum distillation and dry THF was added. The mixture was centrifuged to remove NaCl and unreacted NaN₃. The solution contains azide-terminated silicon nanoparticles which are soluble in THF. The solvent was removed by rotary evaporator and the nanoparticles were redispersed in CH₂Cl₂ and purified by GPC. Yield: 40 mg. ¹HNMR (δ, 300 MHz, CD₂Cl₂): 3.25 (s), 2.0-0.5 (m, broad). UV-vis Absorption (in CH₂Cl₂): Single absorption with a tail up to 600 nm. PL emission (in CH₂Cl₂): 350-700 nm emission peaks by changing excitation wavelength from 300-400 nm. FTIR (thin film on KBr): 2820-2990 cm⁻¹ (ν (C-H)), 2100 cm⁻¹ (ν (N=N=N)), 1500-1750 cm⁻¹ (ν (C=C)), 1465-1376 cm⁻¹ (δ (C-H)), 1250 cm⁻¹ (δ (Si-C)), 1190-850 cm⁻¹ (ν (Si-O)), 830 cm⁻¹ (ν (Si-C)).

Safety note: Large scale reactions of azide are prone to dangerous exothermic reactions. The use of chlorinated solvents in the presence of sodium azide must be avoided, as the byproducts may be highly explosive.

5.4.3 Synthesis of PEGylated alkyno-zinc(II)porphyrin

The PEGylated alkyno-Zincporphyrin was synthesized and well characterized by Dr. Jayawickramarajah's group. See the thesis of Dr. Nan Zhang for further details.

5.4.4 Synthesis of PEGylated porphyrin grafted silicon nanoparticles

Azide-terminated Si nanoparticles (20 mg) and alkyno-zinc(II)porphyrin (20 mg, 5.8×10⁻³ mmol) were dissolved in 15 mL of THF. Cu(I) bromide (10 mg, 4.8×10⁻² mmol)

was added into the reaction mixture. The solution was stirred at room temperature overnight under nitrogen atmosphere. THF was removed by vacuum distillation and 20 mL dichloromethane and 1 mL ethylenediamine was added. The solution was subsequently washed three times with saturated brine solution. The Zn-porphyrin functionalized silicon nanoparticles were purified by GPC to removed unreacted silicon nanoparticles and Zn-porphyrin. The purified nanoparticles were dissolved in a minimum amount of chloroform and precipitated from 10 mL anhydrous diethyl ether, collected by centrifugation, and then dried under high vacuum. Yield: 28 mg. ^1H NMR (δ , 400 MHz, CD_2Cl_2): 8.8-8.1 (multiple broad peaks, aromatic protons), 4.88 (broad), 4.75 (broad), 4.62 (broad), 4.43 (broad), 4.04 (broad), 3.91 (broad), 3.7-3.4 (multiple, all PEG methylene protons), 2.3-0.3 (multiple broad peaks, alkyl protons on the surface of silicon nanoparticle). FTIR (thin film on KBr): 3150 cm^{-1} (ν (C-H) on triazole ring), $2820\text{-}2990\text{ cm}^{-1}$ (ν (C-H)), 2100 cm^{-1} (ν (N=N=N)), $1500\text{-}1750\text{ cm}^{-1}$ (ν (C=C)), $1465\text{-}1376\text{ cm}^{-1}$ (δ (C-H)), 1250 cm^{-1} (δ (Si-C)), 1100 cm^{-1} (ν (C-O)), $1190\text{-}850\text{ cm}^{-1}$ (ν (Si-O)), 830 cm^{-1} (ν (Si-C)). UV-vis Absorption (in water): broad absorption in 230-380 nm, Soret band absorption at 425 nm and 437 nm, Q band absorption at 560 nm and 600 nm.

5.4.5 Cell culture

Human Embryonic Kidney 293T (HEK293T) cells were cultured in Dulbecco's Modified Eagle's Medium (DMEM) (Life Technologies) supplemented with 10% fetal bovine serum and 1000 U/mL penicillin/Streptomycin. Cells were allowed to grow in a humidified atmosphere at $37\text{ }^\circ\text{C}$ under 5% CO_2 .

5.4.6 Quantification of cell internalization

1X phosphate buffered saline (PBS buffer) was prepared using the following procedure. 8g NaCl, 0.2 g KCl, 1.44 g Na₂HPO₄ and 0.24 g of KH₂PO₄ were dissolved in 800 mL distilled H₂O. The pH of the solution was adjusted to 7.4 by adding HCl, and then the volume of the solution was adjusted to 1 L with additional distilled H₂O. Finally, the obtained PBS buffer was sterilized by autoclaving.

Confluent cells (100% confluency) were incubated with medium containing 10 µg/mL PEGylated porphyrin grafted silicon nanoparticles for 1, 3, 6, 12 and 24 hours. Then cells were washed twice with PBS buffer and lysed in buffer containing 25 mM tris-HCl pH 7.6, 150 mM NaCl, 1% NP-40 (nonyl phenoxypolyethoxylethanol), 1% sodium deoxycholate and 0.1% SDS (sodium dodecyl sulfate). After the cell extracts were centrifuged at 13,000 rpm for 10 min, the supernatant was taken for UV-Vis evaluation.

5.4.7 Cell imaging

HEK293T cells were incubated in medium containing 10 µg/mL PEGylated porphyrin grafted silicon nanoparticles for 24 hours. At the end of the incubation, the cells were incubated with PBS containing 2 µg/mL Cell Mask green (Invitrogen) for 15 min for the whole cell-staining for 15 min for the cell membrane staining, or the incubated with 250 nM MitoTracker Deep Red FM (Life Technologies) for 30 min for the mitochondrial staining. And then the cells were fixed with 4% paraformaldehyde solution for 15 min at room temperature. Images were taken with a Zeiss LSM 510 confocal microscope.

5.4.8 Photodynamic therapy experiment

A Thermo Oriel 200 W Xenon arc light system was used as a light source for this experiment. In order to filter off the short wave length UV and long wave length IR irradiation that can directly cause cell death, a 530 long pass filter and a water IR filter (filter off light from 1000 nm to 3000 nm) was fitted in front of the light source (Figure 5.14).

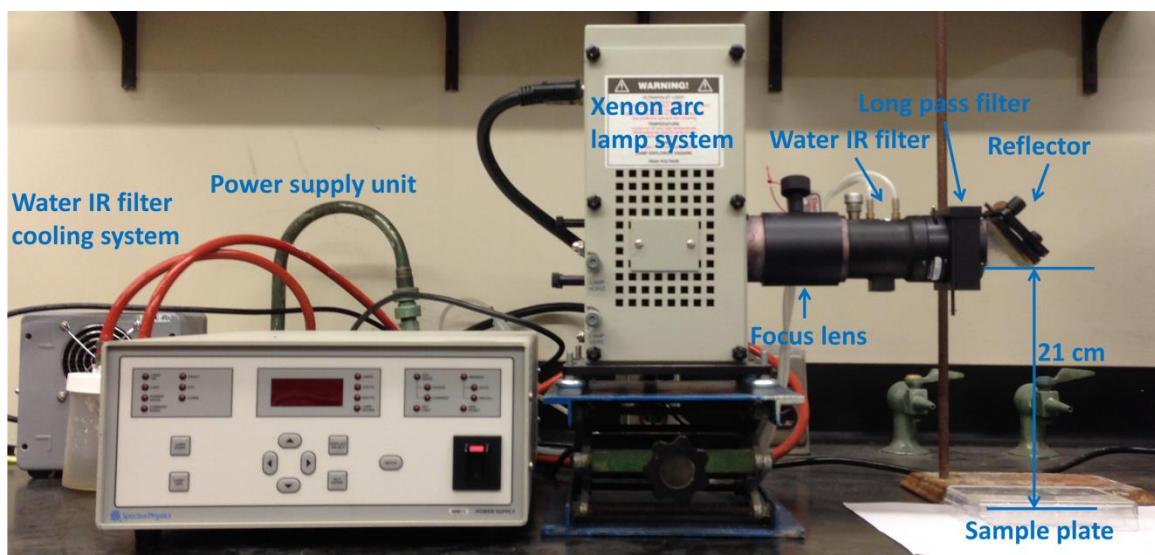


Figure 5.14 Thermo Oriel 200W Xenon arc light system

HEK293T cells incubated with or without 10 $\mu\text{g/mL}$ PEGylated porphyrin grafted silicon nanoparticles for 24 hours were subjected to light irradiation for 30 minutes followed by 30 minutes recovery period and repeated 6 times to achieve a total of 3 hours light dose. The distance from the sample to the light source is 21 cm, and the total light fluence of 39 J/cm^2 (The irradiation intensity was measured by a photo power meter, and the probe was put on the same place as the sample holder. The obtained intensity was 6~7 mW). Dark controls were incubated with 10 $\mu\text{g/mL}$ or without PEGylated porphyrin grafted silicon nanoparticles, then were maintained in the dark for 3 hours. To visualize

cell death, cells were stained with DAPI (a nucleus stain) for 5 min. Images of the nucleus were collected by an Olympus fluorescence microscope.

5.4.9 MTT assay

HEK-293T cells were seeded onto 96-well plates with 100 μ L culture medium and allowed to grow until cells reach half confluency (confluency is the term commonly used as an estimate of the number of adherent cells in a culture dish or a flask, referring to the proportion of the surface which is covered by cells). The cells were then incubated with PEG-Por-Si NPs (10 μ M in porphyrin), PEGylated porphyrin (10 μ M in porphyrin), or PEGylated silicon nanoparticles (no porphyrin, 0.01 mg/mL) for 24 hours. After incubation, the medium was removed and cells were washed with PBS and maintained in 100 μ L fresh culture medium. Finally, the cells were subjected to laser irradiation for 3 hours (650 nm, 5-6 mW cm⁻², 39 J cm⁻²). For the control (no laser) experiments, the cells were maintained in the dark for 3 hours. A MTT assay was performed to evaluate the phototoxicity after overnight incubation. Briefly, cells were incubated for 2 hours with 10 μ L of MTT (3-(4,5-dimethylthiazol-2-yl)-2,5-diphenyltetrazolium bromide; Sigma) in media. The MTT/media solution was then removed and the precipitated crystals were dissolved in 100 μ L of MTT Solubilization Solution. The solution absorbance was read at 570 nm.

5.4.10 Analytical methods

5.4.10.1 NMR sample preparation and acquisition

NMR samples were prepared by vacuum drying of ~1.5 mL of the silicon nanoparticle solution, adding 0.8 mL of the preferred deuterated solvent, and then

transferring the solution to a 5 mm NMR tube. ^1H -NMR measurements were performed on a Bruker Avance 300 spectrometer equipped with a 5 mm BBO probe.

5.4.10.2 Infrared spectroscopy

FTIR spectra were recorded at 1 cm^{-1} resolution with 1000 scans on a Thermo Nicolet NEXUS 670 FTIR instrument. Samples were prepared as a thin film of passivated silicon nanoparticles prepared by depositing dichloromethane solution of silicon nanoparticles on a KBr plate. The FT-IR sample chamber was purged with dry nitrogen before collecting any data.

5.4.10.3 UV-vis absorption spectroscopy

UV-Vis absorption spectra were recorded in a quartz cuvette (1cm), using a Cary 50 spectrophotometer and were corrected for the solvent absorption. The scan range was 200-800 nm with a 300 nm min^{-1} scan rate. Excitation-emission spectra were recorded in a quartz cuvette (1cm), using a Varian Cary Eclipse spectrofluorometer with a scan rate of 120 nm min^{-1} .

5.4.10.4 Transmission electron microscopy and Cryo-TEM

High-resolution TEM and Cryo-TEM studies were performed with a JEOL 2011 TEM using an accelerating voltage of 200 kV or a Tecnai G2 TEM using an accelerating voltage of 300 kV, respectively. TEM samples were prepared by dropping a sonicated diluted solution of silicon nanoparticles in toluene onto a carbon-coated 400 mesh carbon coated copper grid which was placed on a filter paper. The filter paper soaked up the excess solution before inserting in grid in the TEM sample holder.

Cryo-TEM samples were prepared by dropping a sonicated diluted solution of PEGylated porphyrin grafted silicon nanoparticles in water onto a 200 mesh copper grid with lacey carbon film (purchased from Electron Microscopy Science). The grid was blotted with filter paper to remove excess fluid, and then rapidly plunged into liquid ethane that has been cooled to liquid nitrogen temperature (Freezing rate of 1,000,000 K/sec) to prevent the formation of ice crystals. Finally, the grid was transferred to a cryo workstation and then into a cryo holder.

5.4.10.5 AFM experiments

AFM studies were carried out on a Veeco Bioscope AFM (Digital Instruments) under tapping mode in air. Bruker OTESPA AFM probes with nominal frequency, tip diameter, and spring constants of 300 KHz, 7 nm, and 42 N/m, respectively were used. Mica (highest grade V1 Mica disc, 10 mm diameter, was purchased from TED PELLA, Inc.) was used as the substrate and the mica plate was freshly cleaved via scotch tape to achieve a flat surface before use. The sample was prepared by applying 20 μ L solution of nanoparticles in dichloromethane ($\sim 1\mu\text{g/mL}$) on the mica surface. After drying with nitrogen gas flow, the sample was imaged.

alkynyl-octenyl (50%)-silicon nanoparticles and α,ω -azido-amino-bifunctional PEG (500 Da) (Figure 6.1). The attachment of the amino-PEG is supported by the comparison of the FTIR spectrum of the amino-PEGylated silicon nanoparticles with the FTIR spectra of the two starting materials. As shown in Figure 6.2, both the $\nu(\text{N}=\text{N}=\text{N})$ from the azide group of the amino-azido-PEG at 2100 cm^{-1} and the alkyne C-H stretching vibration of the silicon nanoparticle at 3250 cm^{-1} disappear during the course of the reaction, while new peaks for the aromatic C-H stretches on the triazole group and the N-H stretching and bending vibrations of the amino PEGylated silicon nanoparticles appear at 3200 cm^{-1} , 3100 cm^{-1} , 1600 cm^{-1} , 950 cm^{-1} , and 840 cm^{-1} , respectively.

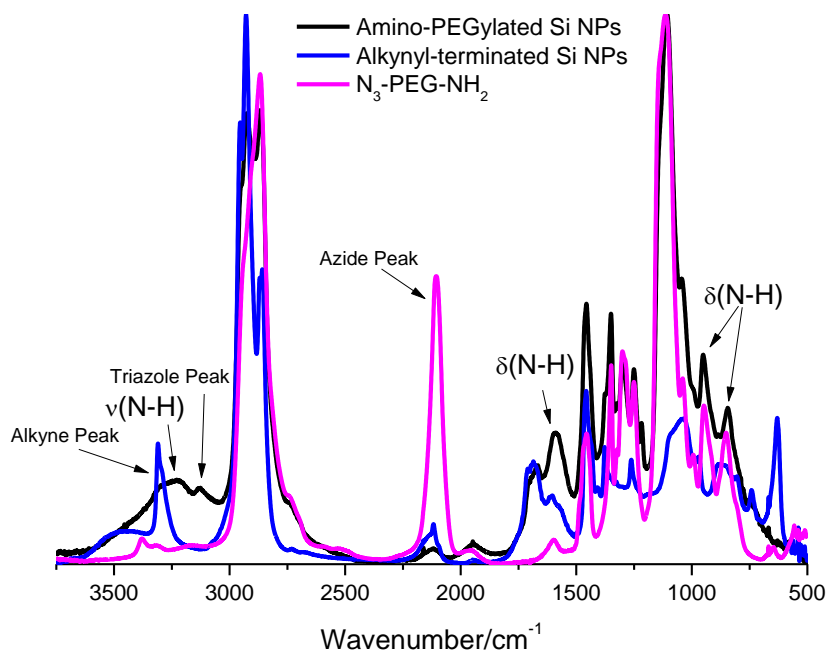


Figure 6.2 FTIR of spectra of ω -alkynyl-octenyl (50%)-Si nanoparticles, amino-azido-bifunctional-PEG and amino-PEGylated silicon nanoparticles.

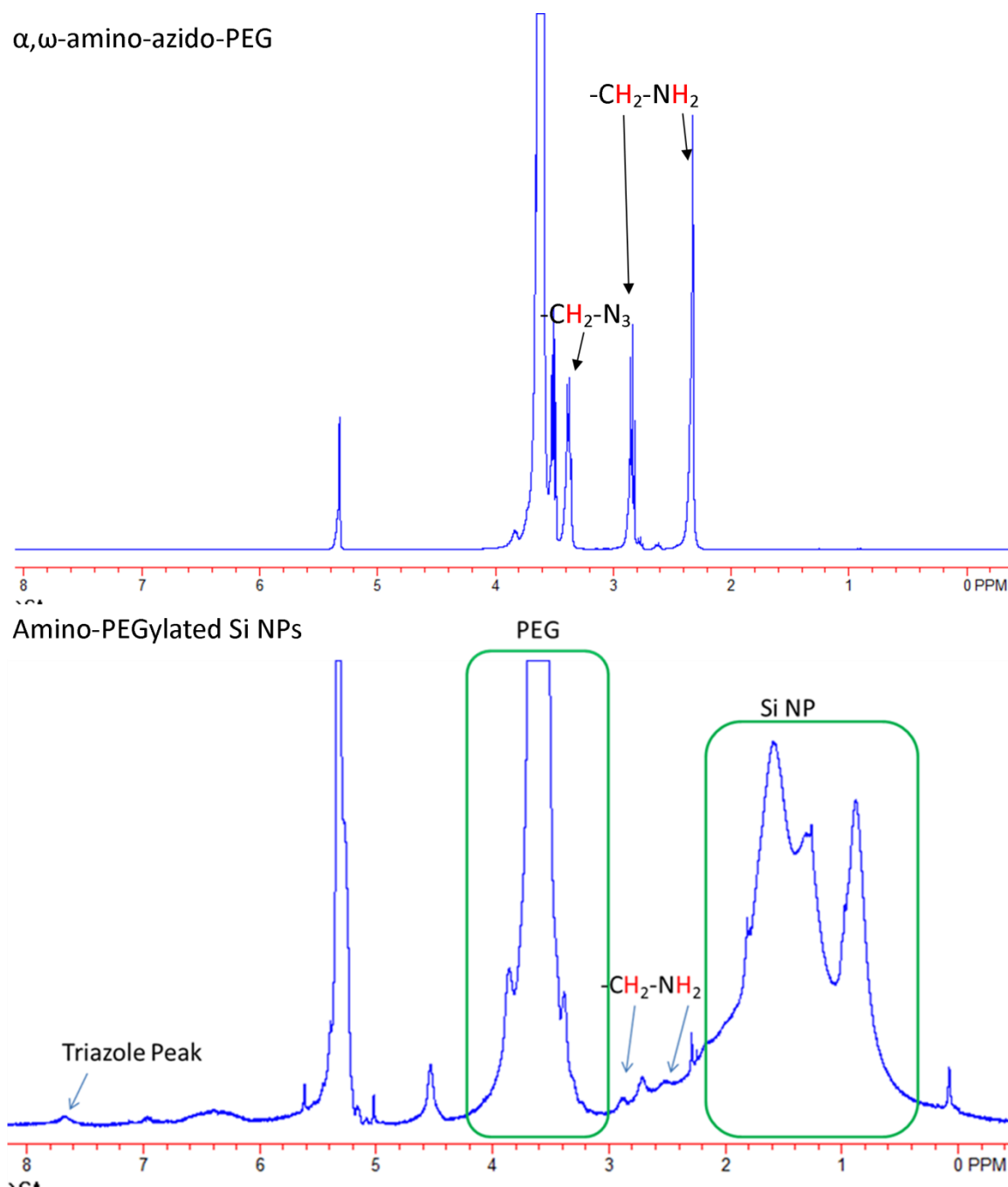


Figure 6.3 ^1H NMR spectrum of α,ω -amino-azido-PEG and amino-PEGylated silicon nanoparticles in CD_2Cl_2

^1H -NMR was performed to further access the success of the reaction. As shown in Figure 6.2, the ^1H -NMR spectrum of amino-PEGylated silicon nanoparticles shows the

peaks from both components, the silicon nanoparticles and the reacting PEG including the resonances for the $-\text{CH}_2-\text{NH}_2$ group appear at 2.9 ppm and 2.5 ppm respectively. Furthermore, a new resonance for the triazole group was observed at 7.7 ppm, which clearly indicates the grafting of the amino-PEG.

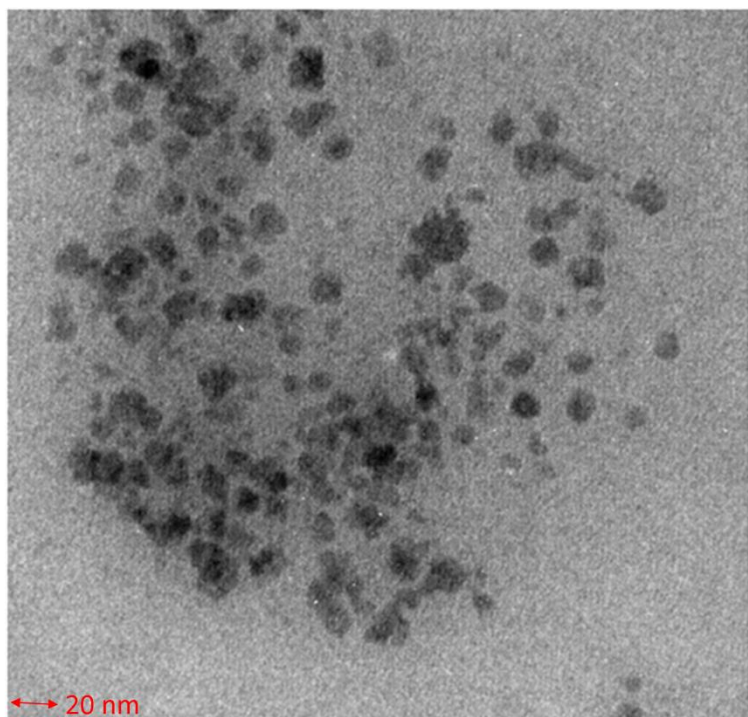


Figure 6.4 the TEM image of amino-PEGylated silicon nanoparticles in water

A typical TEM image of the amino-PEGylated silicon nanoparticles from a dispersion of the nanoparticles in water shows the isolated nanoparticles with the diameter of 10 to 15 nm. There may be some aggregation of the silicon nanoparticles due to the interaction of the PEG side chains or the N-H hydrogen bonding.

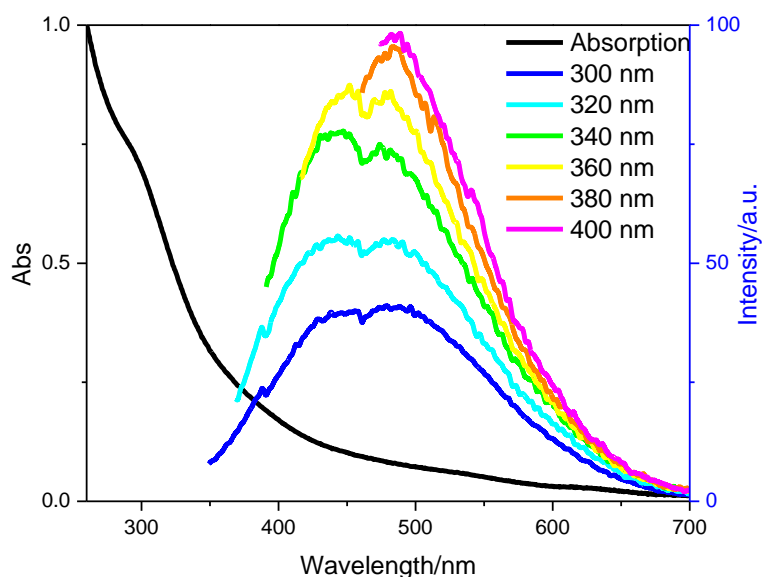


Figure 6.5 UV-Vis absorbance and PL emission of amino-PEGylated silicon nanoparticles in distilled water

The amino-PEGylated nanoparticles demonstrate nearly identical UV-Vis absorption and PL emission spectra in aqueous solution (Figure 6.5) as the starting nanoparticles in CH_2Cl_2 (see Chapter 3), including a broad continuous UV-Vis absorption tailing at 700 nm and a strong emission in the range of 350 to 700 nm. The small dip at 450 nm in the emission spectra may due to the internal filter used to filter out the scattering light.

In summary, the PEGylation of the nanoparticle surface improves its water solubility while maintaining the advantageous optoelectronic properties of the nanoparticle. And the distal amino groups provide the possibility of further modifying the silicon nanoparticles for biological application. Unfortunately, some of the nanoparticles precipitated out during the reaction and could not redisperse in any solvent, which caused

the low yield of this reaction. The precipitation may be due to the distal amino group which can form N-H hydrogen bonding. The mechanism of the precipitation is still unclear.

6.1.2 Synthesis of the amino-terminated silicon nanoparticles via “click” reaction

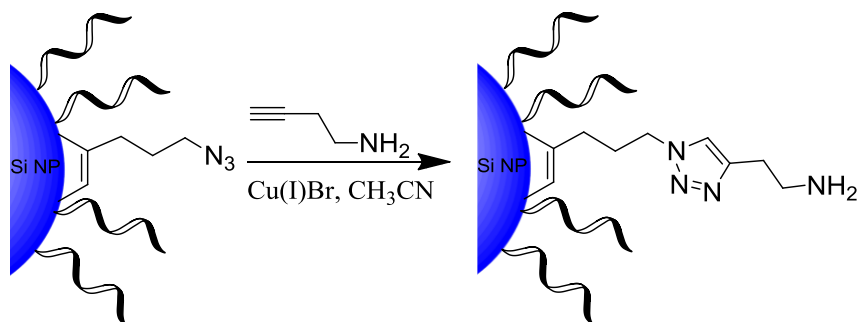


Figure 6.6 Synthesis of amino-terminated silicon nanoparticles via “click” reaction

The water soluble amino-terminated silicon nanoparticles were obtained via a CuAAC “click” reaction between the azido-terminated silicon nanoparticles and propargylamine (Figure 6.6). The ω -azido-pentenyl (50%) silicon nanoparticles were easily synthesized through the reactions of ω -chloro-pentenyl silicon nanoparticles, directly obtained from RHEBM of a silicon wafer with a mixture of 5-chloro-1-pentyne and 1-pentyne (1:1 v/v). The ω -chloro-pentenyl silicon nanoparticles were then reacted with NaN_3 in DMF. Changes in the FTIR spectra (Figure 6.7) of silicon nanoparticles before and after the “click” reaction first supported the grafting of the propargylamine. The azide group vibration peak from the azido-terminated silicon nanoparticles at 2100 cm^{-1} disappear after the “click” reaction, while the aromatic C-H stretching vibration on the triazole group and N-H bending vibration of the amino silicon nanoparticles show at 3100 cm^{-1} , 1600 cm^{-1} , and 840 cm^{-1} , respectively. In addition, a new resonance for the triazole group was observed at 7.1 ppm in the ^1H -NMR spectrum (Figure 6.8).

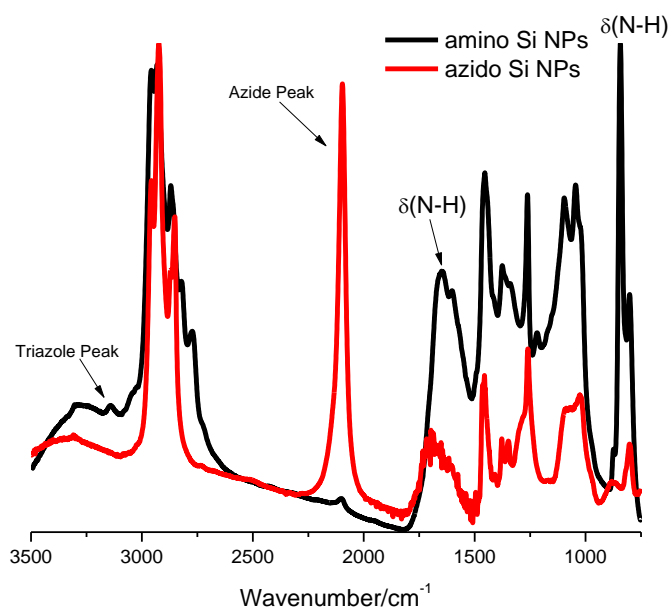


Figure 6.7 FTIR spectra of ω-azido-pentenyl (50%)-silicon nanoparticles and amino terminated silicon nanoparticles

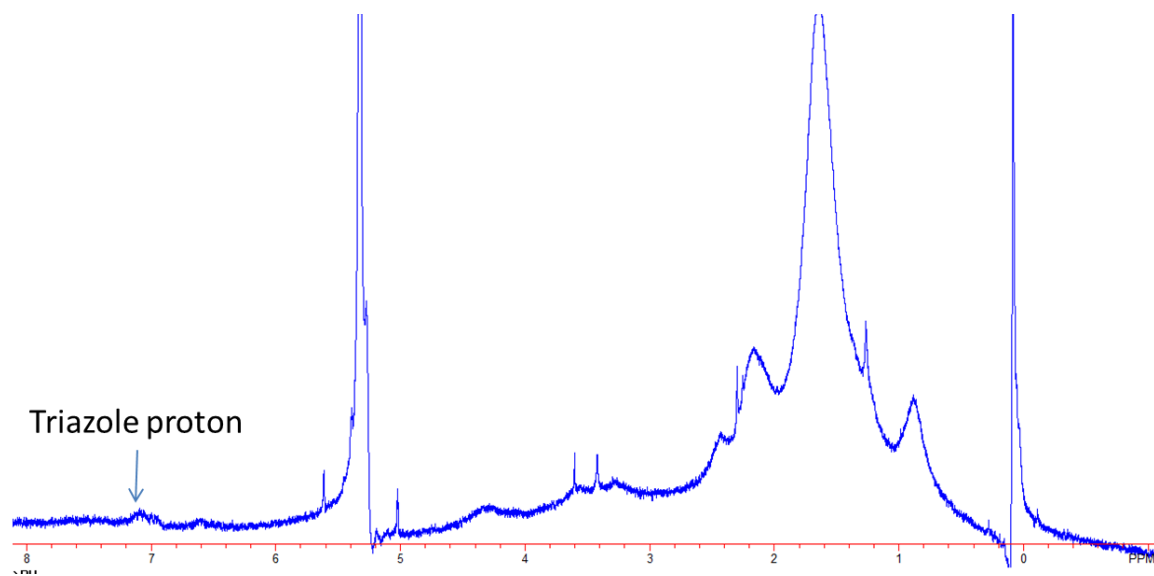


Figure 6.8 ¹H NMR spectrum of amino-terminated silicon nanoparticles in CD₂Cl₂

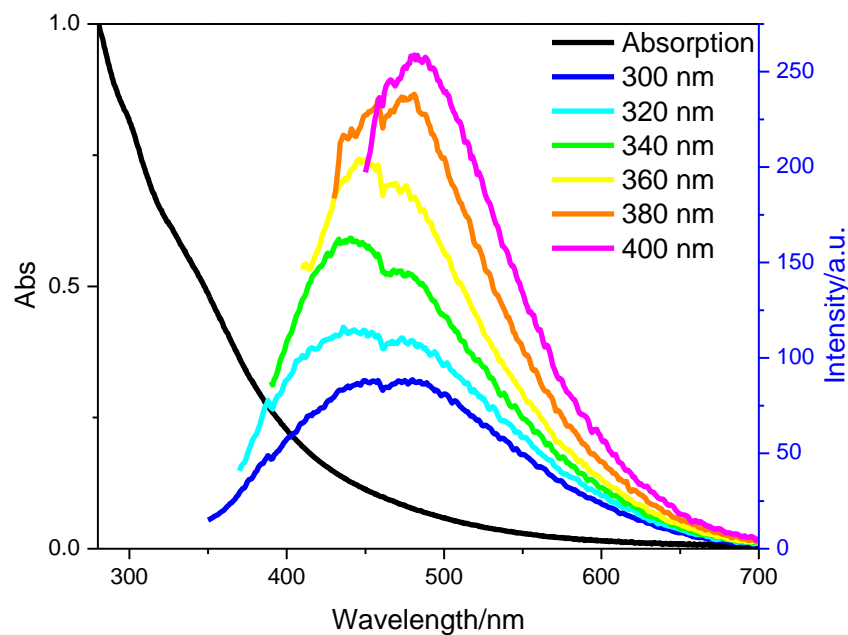
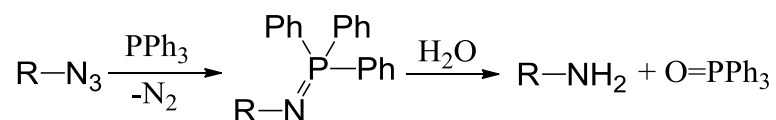


Figure 6.9 UV-Vis absorbance and PL emission of amino-terminated silicon nanoparticles in distilled water

As expected, the amino-terminated nanoparticles also display a broad continuous UV-Vis absorption and strong PL emission spectra in aqueous solution (Figure 6.9) similar to the starting nanoparticles in CH_2Cl_2 . The distal amino groups not only improve the water solubility of silicon nanoparticles, but also provide the possibility of further modifying the silicon nanoparticles for biological application. Unfortunately, the products are obtained in relative low yield due to the precipitation of nanoparticles during the reaction.

6.1.3 Synthesis of the amino-terminated silicon nanoparticles via Staudinger Reduction

Another approach to amino substituted nanoparticles is the Staudinger Reduction, in which the triphenylphosphine reacts with the azide to form an iminophosphorane and then produce the amine and phosphine oxide by aqueous work up (Scheme 6.1).¹⁷⁶ Therefore, the amino-terminated silicon nanoparticles were synthesized by reducing the azide groups on the ω -azido-pentenyl (50%)-silicon nanoparticles to amino groups using triphenylphosphine (Figure 6.10). The conversion of the azide groups was supported by FTIR spectra (Figure 6.11) including the disappearance of the $\nu(\text{N}=\text{N}=\text{N})$ from the azide group of the starting nanoparticles and appearance of a new peak for the amino group of the newly formed silicon nanoparticles.



Scheme 6.1 Schematic of Staudinger Reduction

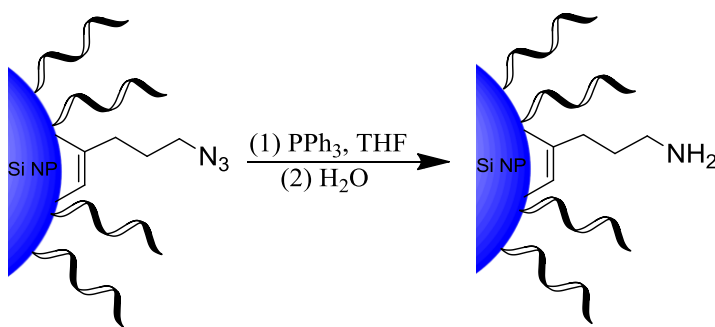


Figure 6.10 Synthesis of amino-terminated silicon nanoparticles via reduction reaction

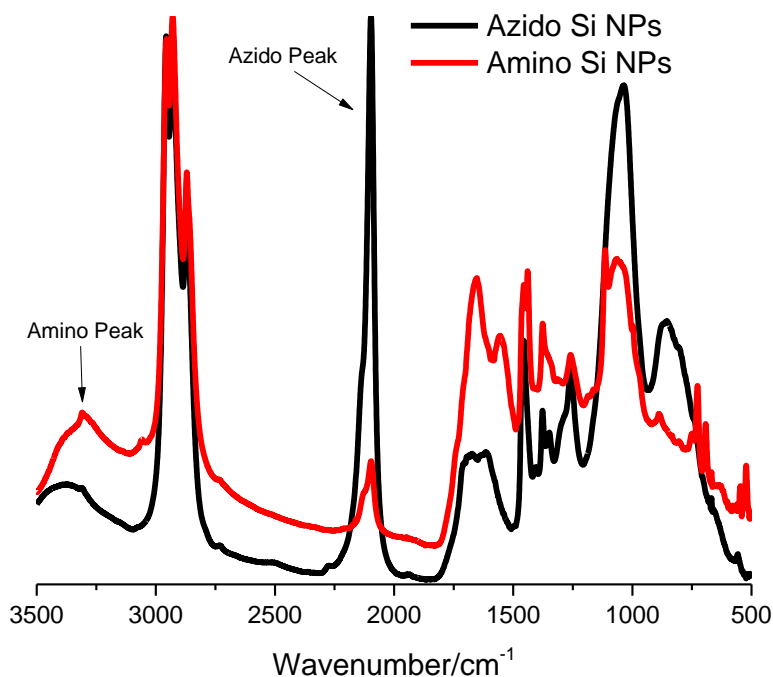


Figure 6.11 FTIR spectra of ω -azido-pentenyl (50%)-silicon nanoparticles and amino terminated silicon nanoparticles

Unfortunately, this approach to amino-terminated silicon nanoparticles resulted in extensive precipitation during the reaction, yielding insoluble solids. Therefore, FTIR spectroscopy was the only characterization method performed to analyze the product.

6.1.4 Synthesis of carboxylic acid-functionalized silicon nanoparticles

Carboxylic acid-functionalized silicon nanoparticles were obtained via a CuAAC “click” reaction between the ω -azido-pentenyl (50%)-silicon nanoparticles and propiolic acid (Figure 6.12).

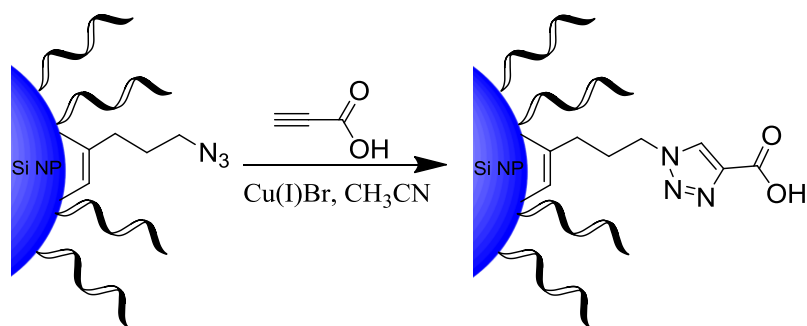


Figure 6.12 Synthesis of carboxylic acid-functionalized silicon nanoparticles via “click” reaction

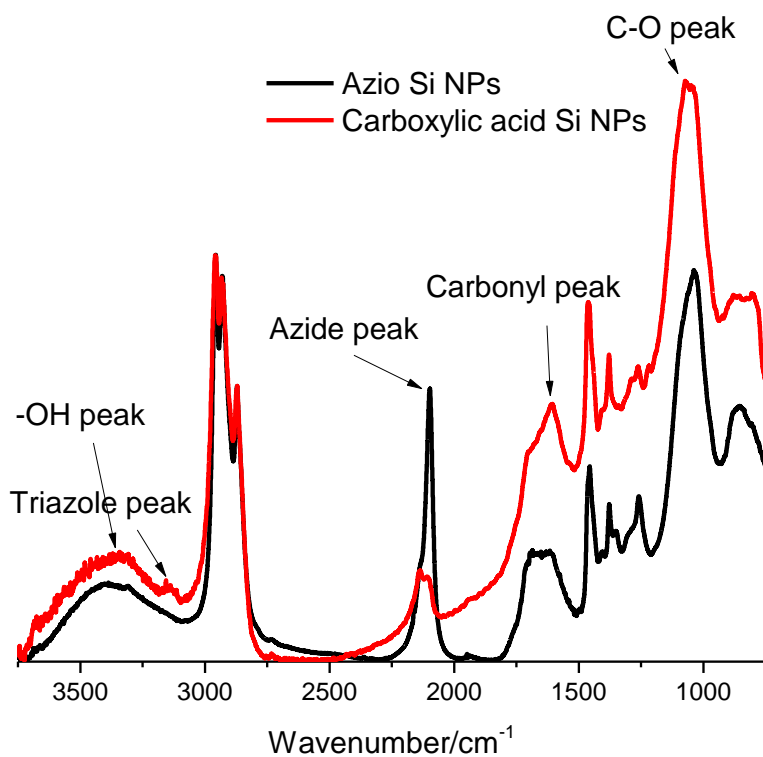


Figure 6.13 FTIR spectra of ω -azido-pentenyl (50%)-silicon nanoparticles and carboxylic acid-functionalized silicon nanoparticles

The occurrence of the “click” reaction was supported by FTIR spectra and ^1H -NMR spectra. As shown in Figure 6.13, new vibration peaks of the $-\text{OH}$ stretch, aromatic C-H

stretch, C=O stretch and C-O stretch on the carboxylic acid-functionalized silicon nanoparticles appears at 3300 cm^{-1} , 3100 cm^{-1} , 1600 cm^{-1} and 1100 cm^{-1} respectively in the FTIR spectrum, while the azido stretching vibration on the starting silicon nanoparticles at 2100 cm^{-1} disappear. Furthermore, a new resonance for the triazole proton was also observed at 7.6 ppm in the ^1H -NMR spectrum (Figure 6.14). However, the resonance of the carboxylic acid proton wasn't shown on the spectra, which might due to the broadness of the peak.

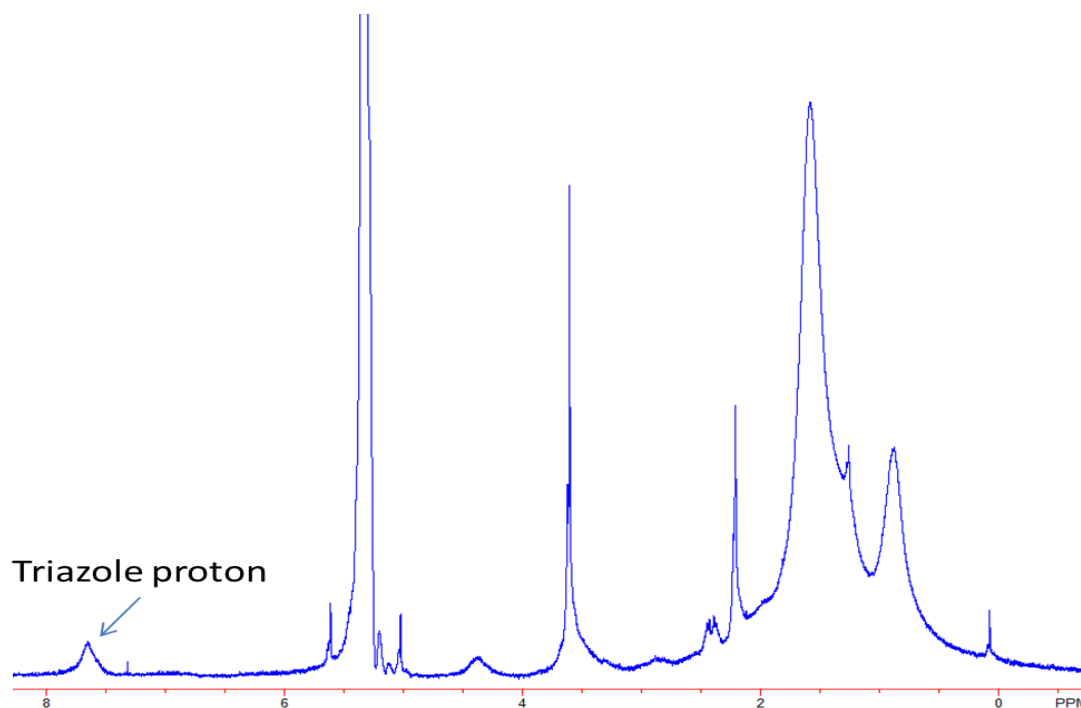


Figure 6.14 ^1H NMR spectrum of carboxylic acid-functionalized silicon nanoparticles in CD_2Cl_2

6.1.5 Synthesis of methyl viologen-functionalized silicon nanoparticles via “click” reactions

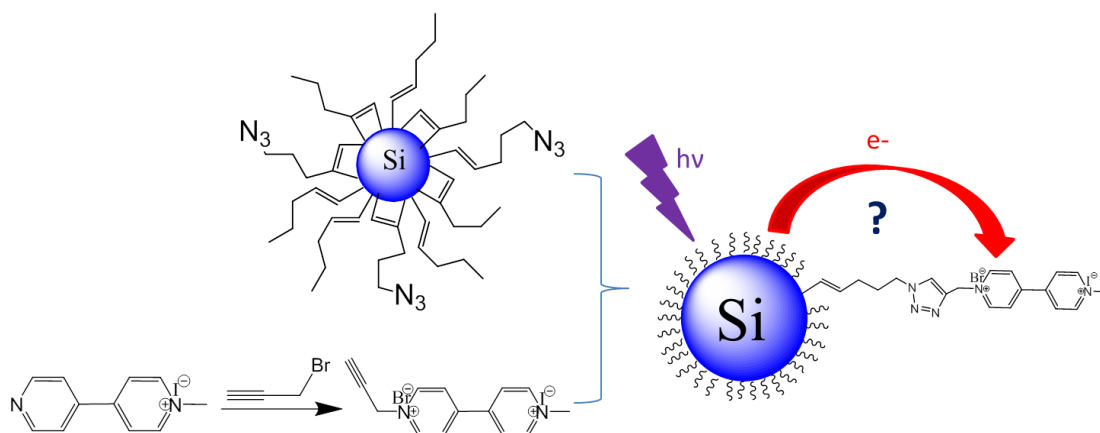


Figure 6.15 Schematic of the synthesis of methyl viologen-functionalized silicon nanoparticles via “click” reaction and the possible electron transfer process inside the system

Methyl viologen was used both as a water soluble ligand and an electron acceptor for functionalizing silicon nanoparticles. As shown in Figure 6.15, methyl viologen-functionalized silicon nanoparticles can be prepared via a CuAAC “click” reaction between the ω -azido-pentenyl (50%)-silicon nanoparticles and alkynyl-methyl-viologen.

First, alkynyl-methyl viologen was synthesized via a nucleophilic displacement reaction between the mono-methyl viologen and propargyl bromide as the precursor of the “click” reaction (Figure 6.19). In Figure 6.16, the new resonances for the $\text{CH}\equiv\text{C}-\text{CH}_2-$ group on the alkynyl-methyl viologen, which were identified by comparing the integrate area of all the resonances, appears at 6.4 ppm and 6.2 ppm respectively. The new resonances clearly indicate the attachment of a propargyl group.

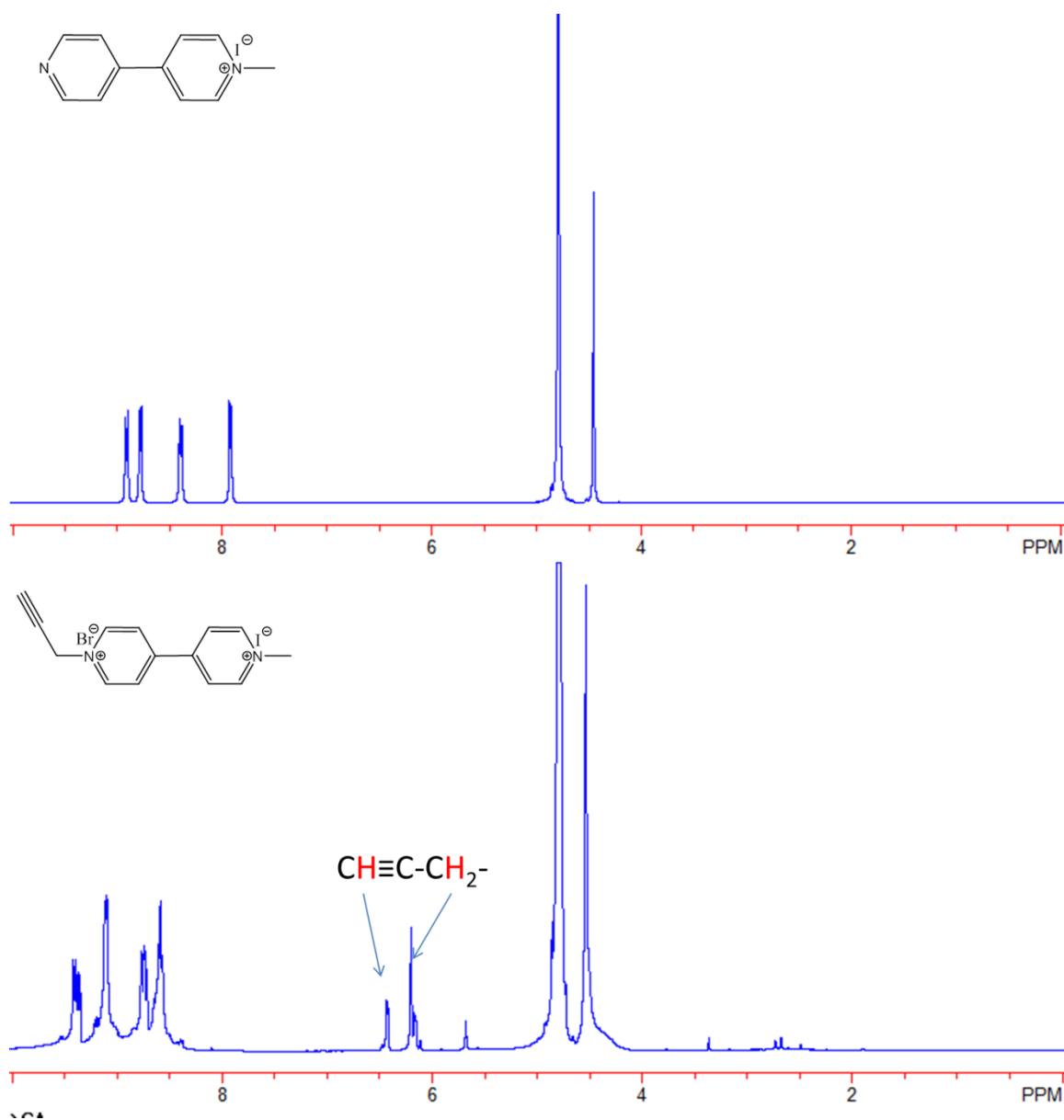


Figure 6.16 ^1H -NMR spectra of mono-methyl viologen and alkynyl-methyl viologen in D_2O

The alkynyl-methyl viologen was conjugated onto azide-terminated silicon nanoparticles via the “click” reaction. Unfortunately, the methyl viologen functionalized silicon nanoparticles were precipitated out during the reaction, and could not redisperse

in any solvent. Therefore, FTIR spectroscopy is the only method to characterize the resultant nanoparticles. The FTIR spectrum of the methyl viologen functionalized silicon nanoparticles (Figure 6.30) does not show the $\nu(\text{N}=\text{N}=\text{N})$ of the azide group at 2100 cm^{-1} , while the new aromatic C-H stretching vibration of the triazole group appears at 3100 cm^{-1} , which indicates the occurrence of the “click” reaction. However, more evidence was required to completely prove the attachment of the methyl viologen.

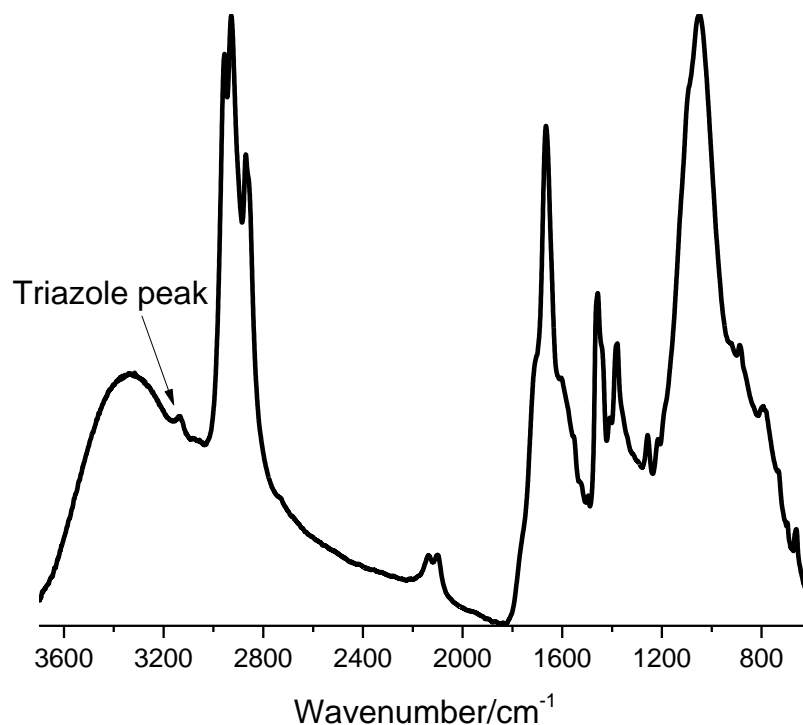


Figure 6.17 FTIR spectrum of the methyl viologen functionalized silicon nanoparticles

6.1.6 Synthesis of methyl viologen-functionalized silicon nanoparticles via nucleophilic displacement reaction

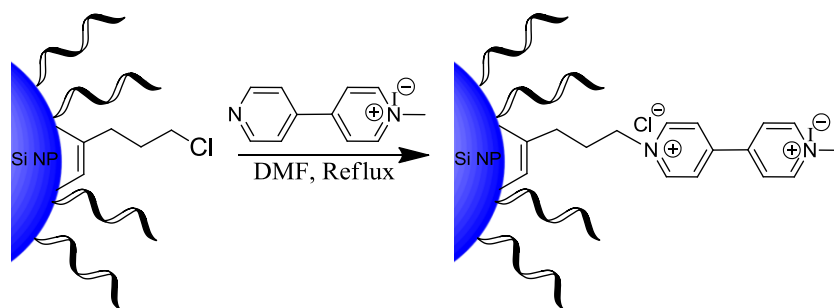


Figure 6.18 Synthesis of methyl viologen-functionalized silicon nanoparticles via nucleophilic displacement reaction

Methyl viologen functionalized silicon nanoparticles were also synthesized via a nucleophilic displacement reaction between the ω -chloro-pentenyl (50%)-silicon nanoparticles and the mono-methyl viologen in DMF (Figure 6.18). The grafting of the methyl viologen onto the nanoparticle surface was supported by comparing the ¹H-NMR spectra of the methyl viologen functionalized silicon nanoparticles and the starting chloro-terminated silicon nanoparticles. The resonance for the $-\text{CH}_2\text{-Cl}$ group of the starting chloro-terminated silicon nanoparticles at 3.5 ppm disappears after the grafting of methyl viologen, while the new resonances for the aromatic protons of the methyl viologen appears in the range of 7.0 to 9.2 ppm after the reaction (Figure 6.19). Since the obtained methyl viologen functionalized silicon nanoparticles can only disperse in DMSO, no other characterization has been performed.

6.2 Synthesis of silicon nanoparticle arrays via “host-guest” self-assembly

The assembly of semiconductor nanomaterials into three-dimensional structures is of interest for biological and microelectronic applications due to their special optical and electrical properties.¹⁷⁷ Particularly, silicon nanoparticle arrays have attracted wide interest due to their great potential applications in nanotechnology and nanoparticle-base devices.¹⁷⁸ Lee and Fan have reported water-dispersed silicon-based nanospheres with carboxylic acid terminal group for cellular probes application.¹¹⁸ Prasad and Swihart also reported PEGylated micelles encapsulated silicon quantum dots with non-covalent interactions for bioimaging application.¹¹⁹

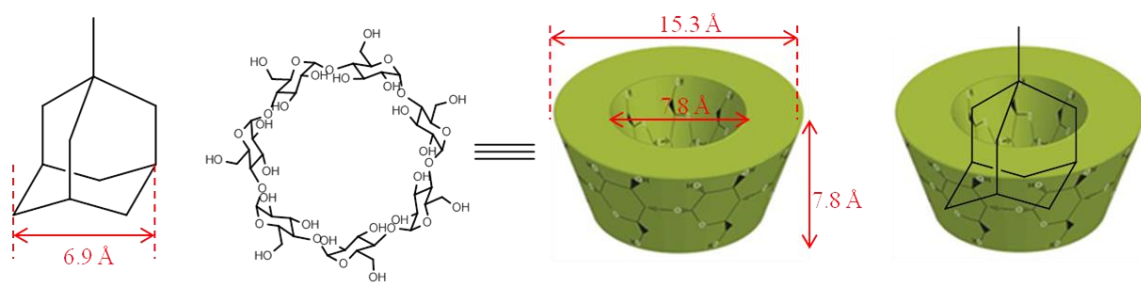


Figure 6.20 Structure of adamantane, β -cyclodextrin and their inclusion complexes

“Host-guest” self-assembly which rely on non-covalent interactions (hydrogen bonds, ionic bonds, van der Waals forces, and hydrophobic interactions), play an important role in the assembly of nanomaterials.¹⁷⁹ In “host-guest” self-assembly, macrocyclic host molecules are usually used as a cavity to trap the guest molecule in the interior of the cavity.^{179b} β -cyclodextrin is one of the macrocyclic molecules used extensively as a host in “host-guest” chemistry for biological application.^{179b, 180} On the other hand, adamantane, which is widely used as a guest molecule in “host-guest” chemistry, can form a strong inclusion complex (1:1) with β -cyclodextrin (Figure 6.20).

6.2.1 Synthesis of adamantane grafted silicon nanoparticles

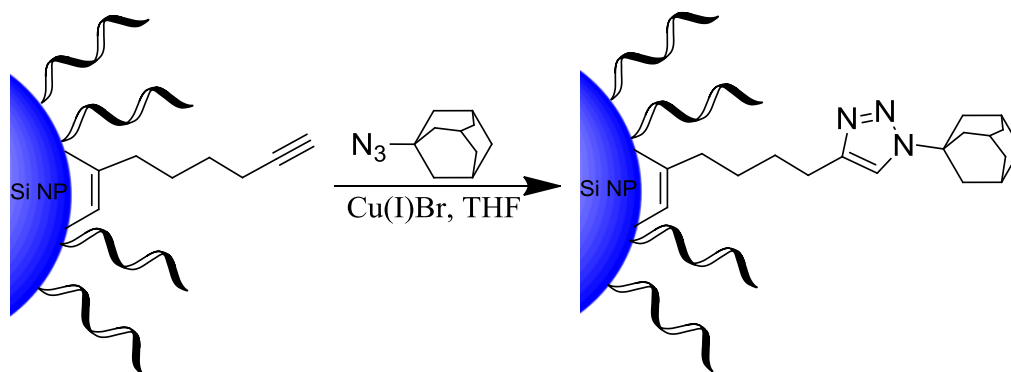


Figure 6.21 Synthesis of adamantane grafted silicon nanoparticles

In order to obtain the silicon nanoparticle arrays via “host-guest” self-assembly, adamantane grafted silicon nanoparticles were synthesized as one of the precursors via a CuAAC “click” reaction between the ω -alkyno-octenyl (20%)-silicon nanoparticles and azido-adamantane (Figure 6.21).

FTIR and $^1\text{H-NMR}$ spectra support the grafting of the adamantane to the nanoparticles. In Figure 6.22, the alkyne C-H stretching vibration of the silicon nanoparticle at 3250 cm^{-1} disappears and the aromatic C-H stretching vibration of the triazole group on the adamantane grafted silicon nanoparticles appears at 3100 cm^{-1} after the “click” reaction.

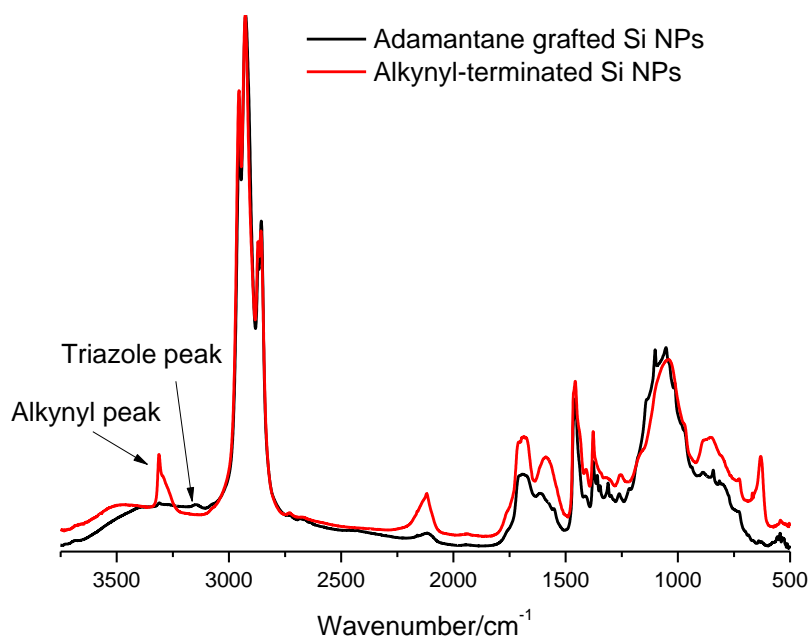


Figure 6.22 FTIR of spectra of ω -alkynyl-octenyl (50%)-Si nanoparticles and adamantane grafted silicon nanoparticles.

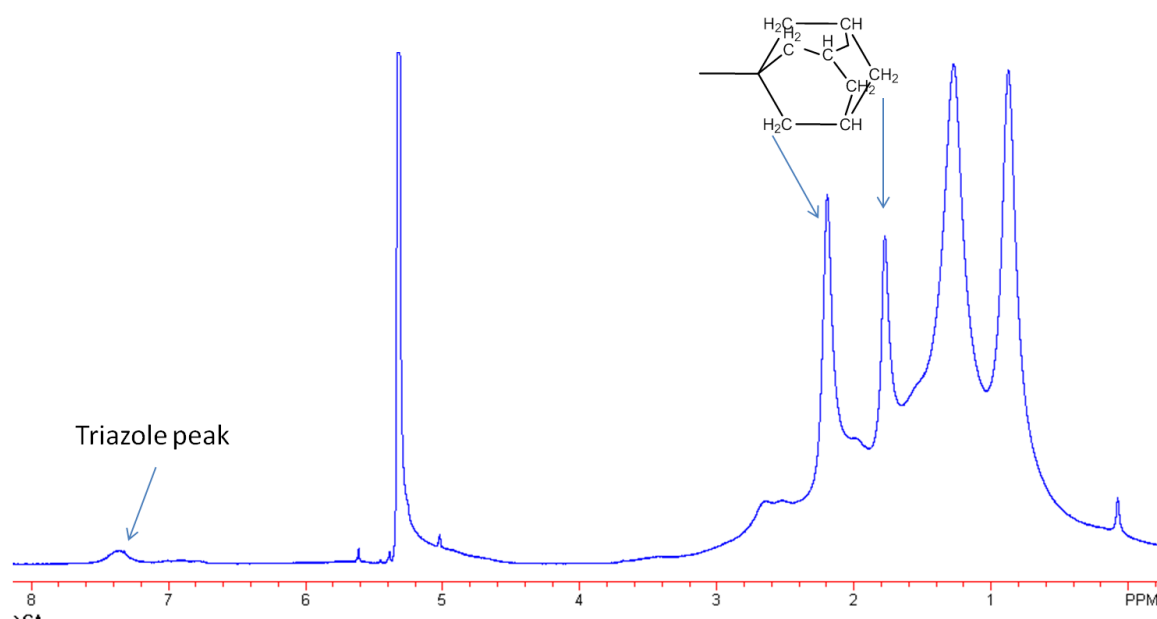


Figure 6.23 ¹H NMR spectrum of adamantane grafted silicon nanoparticles in CD₂Cl₂

In Figure 6.23, the ^1H -NMR spectrum of adamantane grafted silicon nanoparticles shows the peaks from both components, the silicon nanoparticles and the reacting adamantane including the resonances for the adamantane protons appear at 1.8 ppm and 2.2 ppm respectively. Furthermore, a new resonance for the triazole proton was observed at 7.4 ppm.

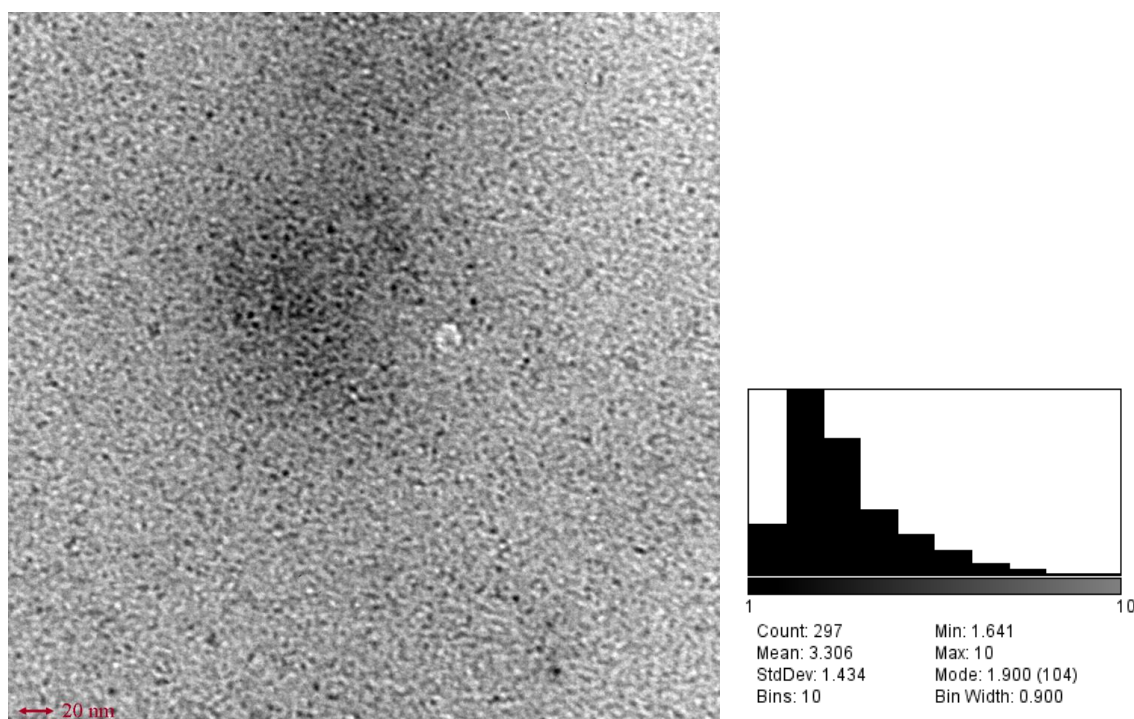


Figure 6.24 the TEM image of adamantane grafted silicon nanoparticles in toluene the corresponding particle size distribution histogram

A typical TEM image of the adamantane grafted silicon nanoparticles from a dispersion of the nanoparticles in toluene shows the isolated nanoparticles with the diameter of 3.3 ± 1.4 nm, which is consistent with the size of the starting alkynyl-terminated silicon nanoparticles (Chapter 3). This is because only the silicon core is observed by the TEM image since the short alkyl chains are either indiscernible by TEM due to insufficient contrast, or have been burned off due from the electron beam.

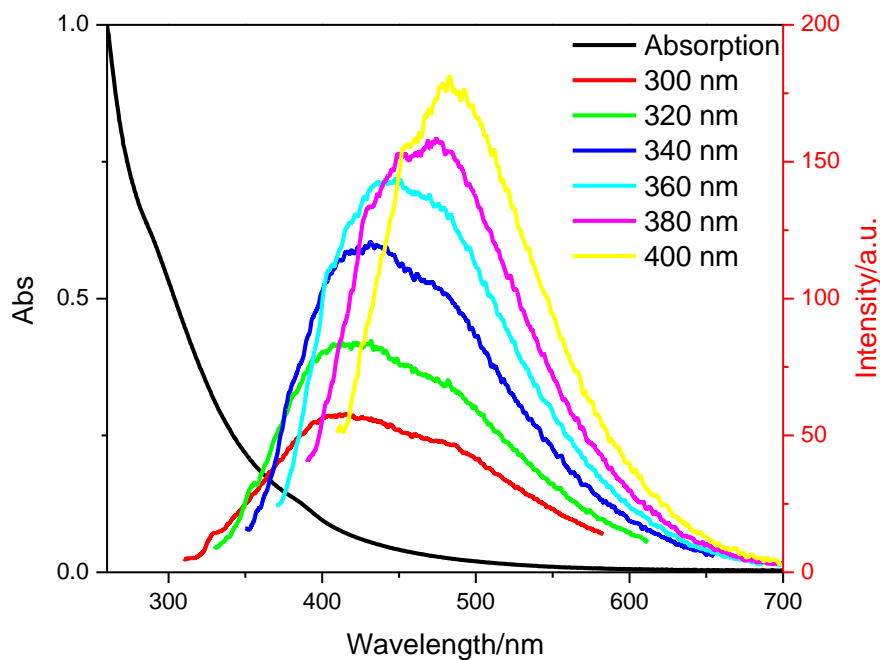


Figure 6.25 UV-Vis absorbance and PL emission of adamantane grafted silicon nanoparticles in CH_2Cl_2

The adamantane grafted silicon nanoparticles demonstrate nearly identical UV-Vis absorption and PL emission spectra (Figure 6.25) as the starting nanoparticles, which indicates that the grafting of the adamantane doesn't affect the optoelectronic properties of the silicon nanoparticles.

6.2.2 Synthesis of β -cyclodextrin grafted silicon nanoparticles

β -Cyclodextrin grafted silicon nanoparticles were synthesized as the complementary precursor for the silicon nanoparticle arrays. Azido- β -cyclodextrin was grafted onto the ω -alkyno-octenyl (20%)-silicon nanoparticles via a CuAAC “click” reaction (Figure 6.26).

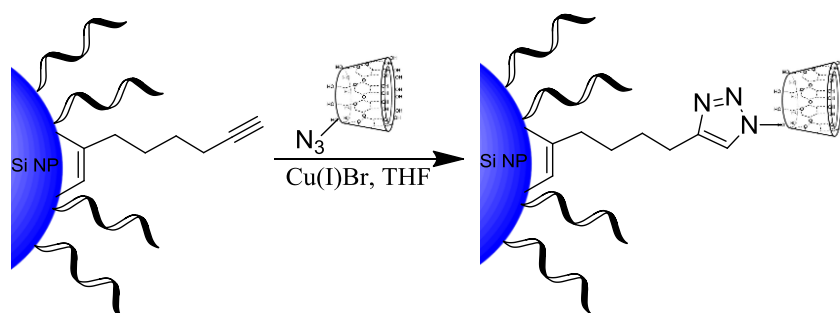


Figure 6.26 Synthesis of β -cyclodextrin grafted silicon nanoparticles

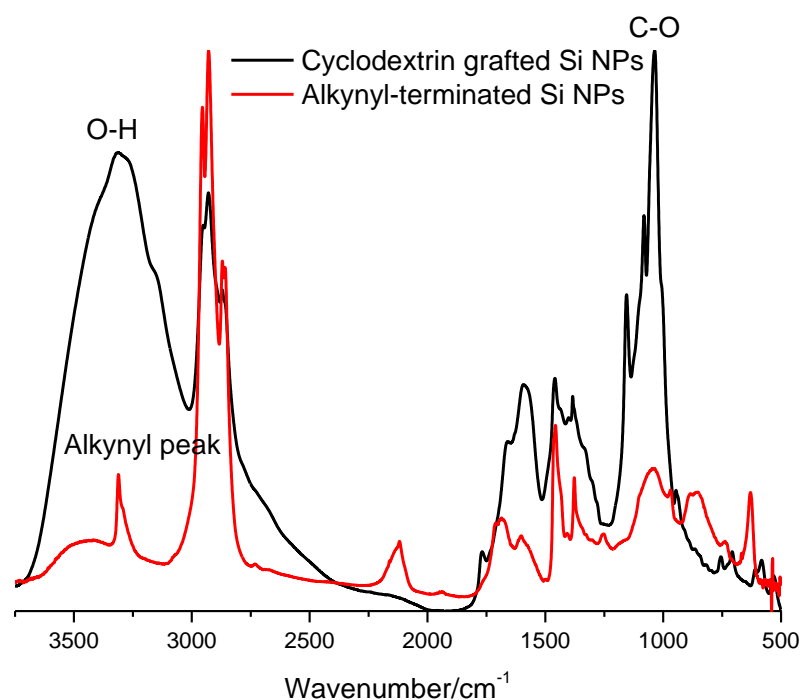


Figure 6.27 FTIR of spectra of ω -alkynyl-octenyl (50%)-Si nanoparticles and β -cyclodextrin grafted silicon nanoparticles.

The FTIR spectra of the silicon nanoparticles before and after the “click” reaction clearly support the conjugation of the β -cyclodextrin. In Figure 6.27, the FTIR spectrum of β -cyclodextrin grafted silicon nanoparticles shows the --OH and C--O stretching vibration at 3300 cm^{-1} and 1100 cm^{-1} respectively, while the alkyne C--H stretching

vibration of the alkyno-terminated silicon nanoparticle at 3250 cm^{-1} disappears after the grafting of β -cyclodextrin. The peak of the aromatic C-H vibration of the triazole group which should appear at 3100 cm^{-1} is overlap with the strong -OH stretching peaks. The shoulder of the -OH peak at 3100 cm^{-1} may be consider as the signal of the aromatic C-H vibration of the triazole group.

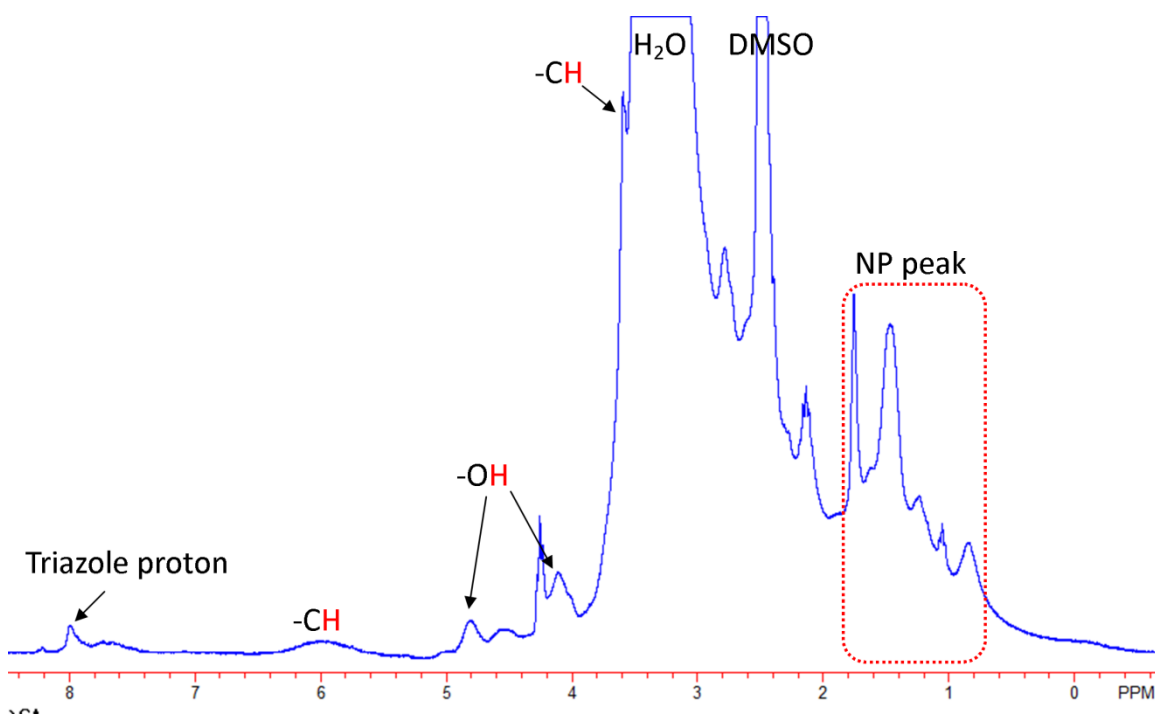


Figure 6.28 ^1H NMR spectrum of β -cyclodextrin grafted silicon nanoparticles in $\text{DMSO-}D_6$

Due to the low solubility of β -cyclodextrin grafted silicon nanoparticles in deuterated DMSO, all the peaks from β -cyclodextrin grafted silicon nanoparticles are relative weak, while the strong peaks from the deuterated DMSO and water are showing on the ^1H -NMR spectrum (Figure 6.28). However, the triazole proton peak at 7.9 ppm, as well as peaks from β -cyclodextrin and alkyl protons from the nanoparticle surface supports the grafting of β -cyclodextrin onto silicon nanoparticle surface. A broad peak at

6.0 ppm is assigned to the $-\text{CH}$ protons on the β -cyclodextrin. Resonances for the $-\text{OH}$ group on the β -cyclodextrin appears at 4.1 ppm and 4.8 ppm respectively. The resonance of the $-\text{CH}_2$ group on the β -cyclodextrin which should appear at 3.2 ppm was overlap with the strong water peak. Furthermore, methyl protons and methylene protons from nanoparticle surface appeared at 0.9-1.8 ppm.

6.2.3 Synthesis of silicon nanoparticle arrays via “host-guest” self-assembly

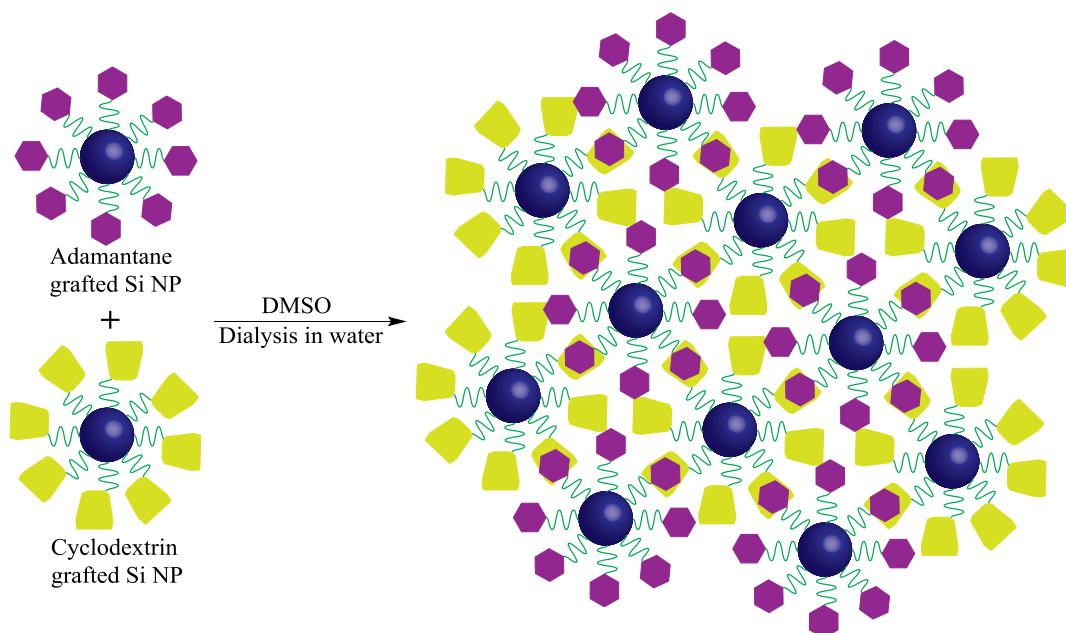


Figure 6.29 Synthesis of silicon nanoparticle arrays via “host-guest” self-assembly

After obtaining the adamantane grafted silicon nanoparticles and β -cyclodextrin grafted silicon nanoparticles, silicon nanoparticle arrays were produced via self-assembly based on the “host-guest” interaction between the attached adamantane and β -cyclodextrin (Figure 6.29).

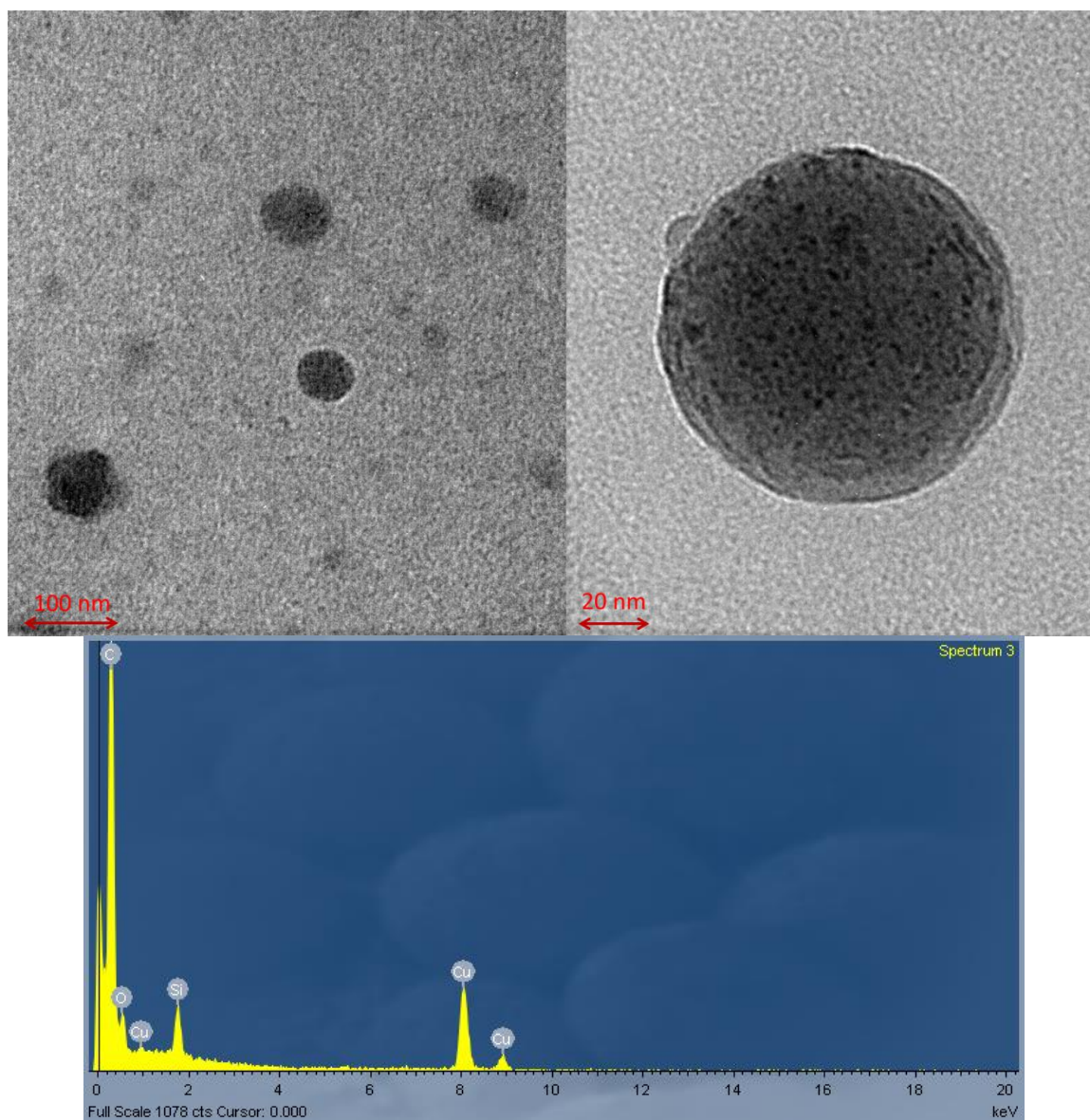


Figure 6.30 TEM images and EDS spectrum of silicon nanoparticles arrays via “host-guest” self-assembly

TEM was performed to support the formation of the silicon nanoparticle arrays after the sample was collected from the dialysis tube. The TEM images (Figure 6.30) clearly show that the silicon nanoparticle arrays are globular sphere with size in the ranges from 60-100 nm, and contain multiple 3 to 5 nm-sized silicon nanoparticles. The EDS spectrum indicates the silicon inside the nanoparticle arrays.

Unfortunately, the obtained silicon nanoparticle arrays cannot redisperse in any solvent after drying out from the aqueous solution, so no other characterization was performed.

6.2.4 Synthesis of water soluble silicon nanoparticle-porphyrin arrays via “host-guest” self-assembly

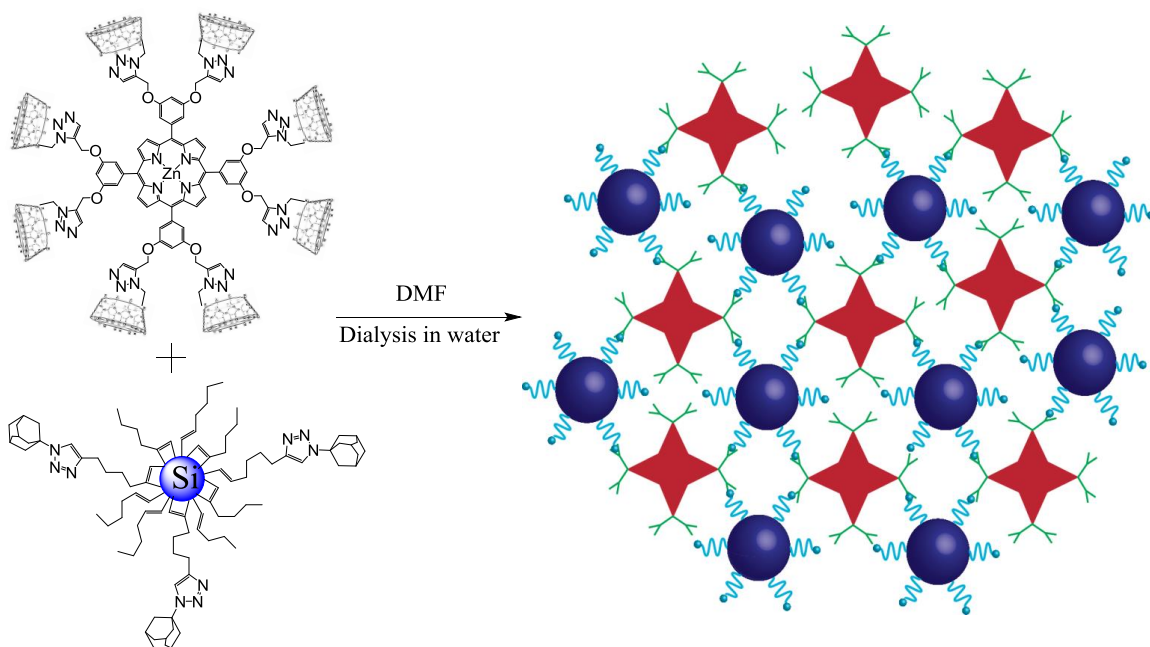


Figure 6.31 Synthesis of water soluble silicon nanoparticle-porphyrin arrays via “host-guest” self-assembly

Nanoparticles with certain size can be selectively accumulated into the tumor cells based on the enhanced permeability and retention (EPR) effect.¹⁶⁴ A new approach of synthesizing water soluble silicon nanoparticle-porphyrin arrays via “host-guest” self-assembly was examined in order to synthesize water soluble silicon nanoparticle-porphyrin arrays with controllable size, which have great potential application in photodynamic therapy. In Figure 6.31, adamantane grafted silicon nanoparticles and oct-

β -cyclodextrin functionalized porphyrin were mixed with 1:1 ratio in DMF. The solution was then dialyzed in water to produce the water soluble silicon nanoparticle-porphyrin arrays based on the “host-guest” interaction between the adamantane and β -cyclodextrin.

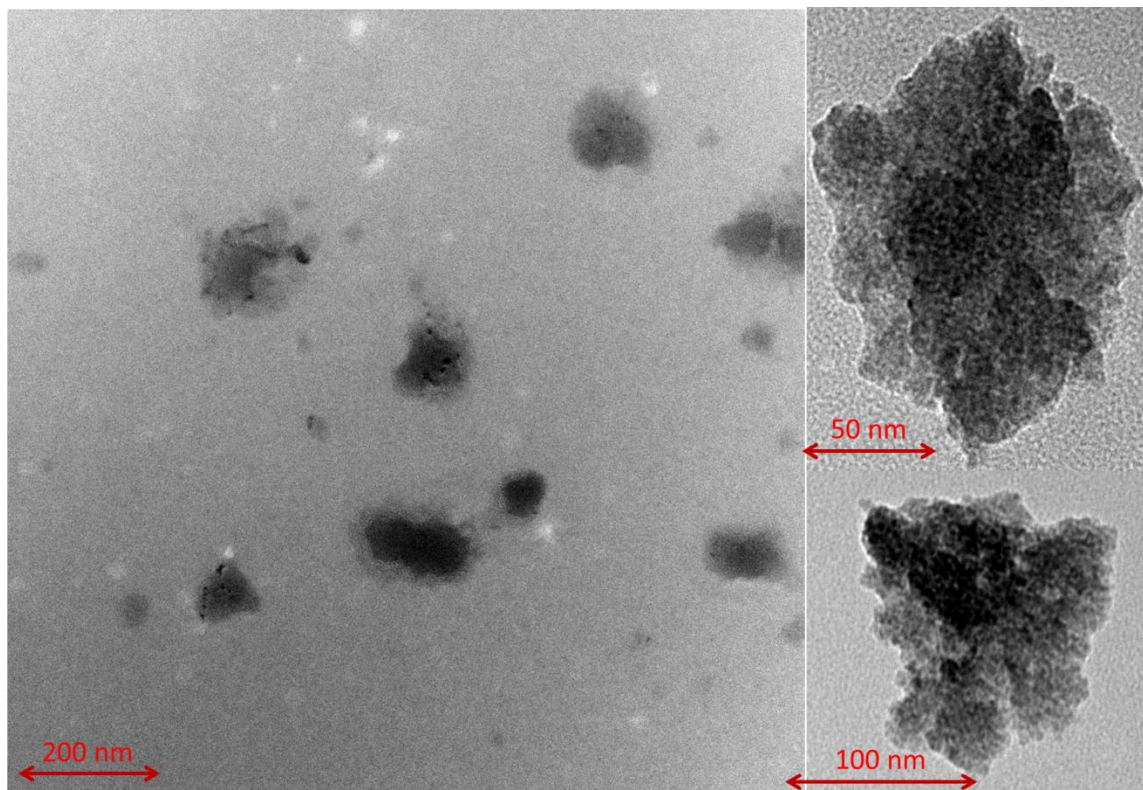


Figure 6.32 TEM images of silicon nanoparticle-porphyrin arrays in water

The TEM images of the silicon nanoparticle-porphyrin arrays in water (Figure 6.32) show the clusters are globular with irregular boundaries and contain multiple smaller size silicon nanoparticles. The size distribution of the clusters ranges from 80 to 120 nm. The cause of the irregular edges may due to the rigid structure of both two precursors and the short interparticle distance so that they are not flexible to form the regular boundaries.

The UV-Vis spectrum (Figure 6.33) of the silicon nanoparticle-porphyrin arrays in water shows an additive absorption from both components, the silicon nanoparticle and

the porphyrin, which further supports the formation of nanoparticle arrays because the adamantane grafted silicon nanoparticle itself is not water soluble.

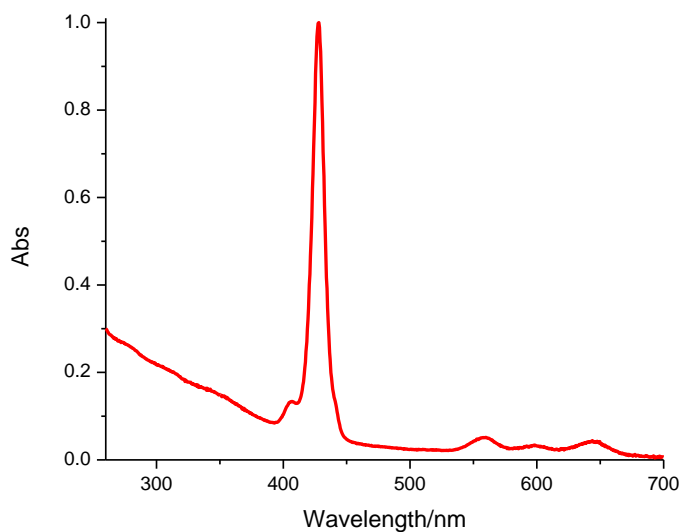


Figure 6.33 UV-Vis spectrum of silicon nanoparticle-porphyrin arrays in water

Moreover, the silicon nanoparticle-porphyrin arrays shows strong emission in water, which contains the blue emission from the silicon nanoparticles and the red emission from the porphyrin (Figure 6.34). Those sharp peaks around 330 to 450 nm are due to the Raman scattering from water. The silicon nanoparticle-porphyrin arrays demonstrated the excellent water solubility while maintaining the advantageous optoelectronic properties of the silicon nanoparticle and porphyrin, which suggests that these nanoparticle arrays can be attractive candidates for photodynamic therapy.

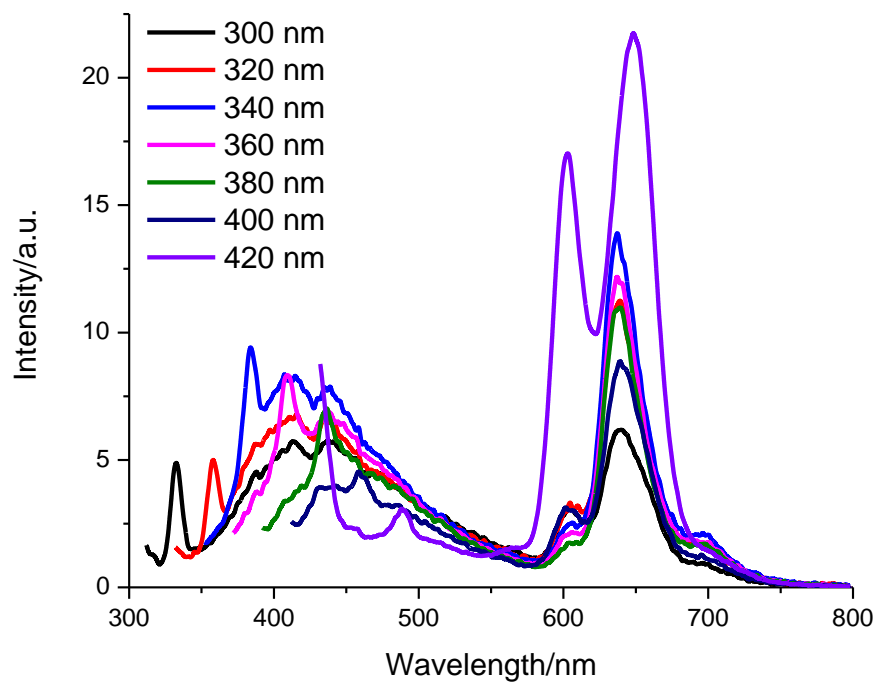


Figure 6.34 PL Emission spectra of silicon nanoparticle-porphyrin arrays in water

Unfortunately, the obtained silicon nanoparticle arrays cannot redisperse in any solvent after drying out from the aqueous solution, so no other characterization was performed.

6.3 Experimental Section

6.3.1 Materials and methods

All chemicals were purchased from Sigma-Aldrich or Alfa Aesar, and employed without further purification unless specified. Tetrahydrofuran (THF) was distilled over sodium-benzophenone prior to use. Dichloromethane was distilled over CaH_2 before use. Silicon wafer (undoped, mirror finish, orientation [111]) was obtained from Silrec Corp. (Lexington, KY). Size exclusion chromatography (SEC) was used for the purification of nanoparticles. Bio-beads S-X1 were swollen overnight in dry THF and packed into a 40cm x 1.3cm glass column. Dichloromethane was used as an elution solvent. A concentrated nanoparticle solution (~50mg in 1 ml CH_2Cl_2) was added to the top of the column and eluted into 3x10ml fractions collected in separate vials. The first fraction was collected when the first colored band began to elute. This fraction contained nanoparticles and was used for the synthetic reactions. The second and third fractions, containing mostly impurities, were discarded.

6.3.2 Synthesis of amino-PEGylated silicon nanoparticles

ω -Alkynyl-octenyl (50%)-silicon nanoparticles (30 mg, obtained from RHEBM) and amino-azido-bifunctional PEG (500 Da, 10 mg, 20 μmol) were dissolved in 15 mL of THF. Cu(I) bromide (10 mg, 48 μmol) was added into the reaction mixture. The solution was stirred at room temperature overnight under nitrogen atmosphere. After removal of THF by vacuum distillation 20 mL of dichloromethane and 1 mL of ethylenediamine were added. The solution was subsequently washed three times with a saturated brine solution. The amino-PEGylated silicon nanoparticles were purified by GPC to removed unreacted silicon nanoparticles and excess PEG. Yield: 10-15 mg. ^1H -NMR (δ , 300 MHz,

CD₂Cl₂): 7.7 (weak broad peak, triazole proton), 4.1-3.2 (multiple, all PEG methylene protons), 2.9 (broad, CH₂-N), 2.5 (broad, amino protons), 2.2-0.4 (multiple broad peaks, alkyl protons on the surface of silicon nanoparticle). FTIR (thin film on KBr): 3150 cm⁻¹ (ν (=C-H) on triazole ring), 2820-2990 cm⁻¹ (ν (C-H)), 1500-1750 cm⁻¹ (ν (C=C)), 1600 cm⁻¹ (δ (N-H)), 1465-1376 cm⁻¹ (δ (C-H)), 1250 cm⁻¹ (δ (Si-CH)), 1100 cm⁻¹ (ν (C-O)), 1000 cm⁻¹ (ν (Si-O)), 950 cm⁻¹ and 840 cm⁻¹ (δ (N-H)). UV-vis Absorption (in water): Single absorption with a tail up to 700 nm. PL emission (in water): 350-700 nm emission peaks by changing excitation wavelength from 300-400 nm.

6.3.3 Synthesis of the amino-terminated silicon nanoparticles via “click” reaction

ω-Azido-pentenyl (50%)-silicon nanoparticles (30 mg, obtained from RHEBM) and propylglycylamine (20 mg, 360 μmol) were dissolved in 15 mL of acetonitrile. Cu(I) bromide (10. mg, 48 μmol) was added into the reaction mixture. The solution was stirred at room temperature overnight under nitrogen atmosphere. After removal of THF by vacuum distillation 20 mL of dichloromethane and 1 mL of ethylenediamine were added. The solution was subsequently washed three times with a saturated brine solution. The amino-terminated silicon nanoparticles were purified by GPC. Yield: 5-10 mg. ¹H-NMR (δ, 300 MHz, CD₂Cl₂): 7.7 (weak broad peak, triazole proton), 4.3 (broad, 2H), 2.5-0.4 (multiple broad peaks, alkyl protons on the surface of silicon nanoparticle). FTIR (thin film on KBr): 3150 cm⁻¹ (ν (=C-H) on triazole ring), 2820-2990 cm⁻¹ (ν (C-H)), 1500-1750 cm⁻¹ (ν (C=C)), 1600 cm⁻¹ (δ (N-H)), 1465-1376 cm⁻¹ (δ (C-H)), 1250 cm⁻¹ (δ (Si-CH)), 1000 cm⁻¹ (ν (Si-O)), 840 cm⁻¹ (δ (N-H)). UV-vis (in water): Single absorption with a tail up to 700 nm. PL emission (in water): 350-700 nm emission peaks by changing excitation wavelength from 300-400 nm.

6.3.4 Synthesis of the amino-terminated silicon nanoparticles via Staudinger Reduction

ω -Azido-pentenyl (50%)-silicon nanoparticles (30 mg, obtained from RHEBM) and triphenylphosphine (20 mg, 76 μmol) were dissolved in 15 mL of acetonitrile. The solution was stirred at room temperature overnight under nitrogen atmosphere. After that, the solution was poured into 20 mL ice water to quench the reaction, and the THF in the mix solution was removed by vacuum distillation, and the product was extracted by 20 mL of dichloromethane twice. The obtained nanoparticle solution in dichloromethane was subsequently washed three times with a saturated brine solution. The crude amino-terminated silicon nanoparticles were purified by GPC. Yield: 15-20 mg. FTIR (solid IR): 3300 cm^{-1} (ν (N-H)), 2820-2990 cm^{-1} (ν (C-H)), 1500-1750 cm^{-1} (ν (C=C)), 1600 cm^{-1} (δ (N-H)), 1465-1376 cm^{-1} (δ (C-H)), 1250 cm^{-1} (δ (Si-CH)), 1000 cm^{-1} (ν (Si-O)), 950 cm^{-1} (δ (N-H)).

6.3.5 Synthesis of carboxylic acid-functionalized silicon nanoparticles

ω -Azido-pentenyl (50%)-silicon nanoparticles (30 mg, obtained from RHEBM) and propiolic acid (20 mg, 286 μmol) were dissolved in 15 mL of acetonitrile. Cu(I) bromide (10. mg, 48 μmol) was added into the reaction mixture. The solution was stirred at room temperature overnight under nitrogen atmosphere. After removal of THF by vacuum distillation 20 mL of dichloromethane was added. The solution was subsequently washed three times with a saturated brine solution. The carboxylic acid functionalized silicon nanoparticles were purified by GPC. Yield: 20-25 mg. ^1H NMR (δ , 300 MHz, CD_2Cl_2): 7.7 (weak broad peak, triazole proton), 4.3 (broad, 2H), 2.2-0.4 (multiple broad peaks, alkyl protons on the surface of silicon nanoparticle). FTIR (thin film on KBr): 3300 cm^{-1}

(ν (O-H)), 3150 cm^{-1} (ν (=C-H) on triazole ring), $2820\text{-}2990\text{ cm}^{-1}$ (ν (C-H)), $1500\text{-}1750\text{ cm}^{-1}$ (ν (C=C)), $1465\text{-}1376\text{ cm}^{-1}$ (δ (C-H)), 1250 cm^{-1} (δ (Si-CH)), 1000 cm^{-1} (ν (Si-O)).

6.3.6 Synthesis of alkynyl-methyl viologen

Mono-methyl viologen (30 mg, $100\text{ }\mu\text{mol}$) and propargyl bromide (15 mg, $126\text{ }\mu\text{mol}$) were dissolved in 5 mL of acetonitrile. The solution was stirred at room temperature overnight under nitrogen atmosphere. After that, the product was collected by vacuum filtration followed by vacuum dry overnight. The yield is 37 mg, 82%. $^1\text{H-NMR}$ (δ , 300 MHz, D_2O): 9.5-8.6 (m, aromatic protons, 4H), 6.5 (s, 1H), 6.2 (m, 2H), 4.5 (s, 3H).

6.3.7 Synthesis of methyl viologen-functionalized silicon nanoparticles via “click” reaction

ω -Azido-pentenyl (50%)-silicon nanoparticles (30 mg, obtained from RHEBM) and alkynyl-methyl viologen (10 mg, $24\text{ }\mu\text{mol}$) were dissolved in 15 mL of acetonitrile. Cu(I) bromide (10. mg, $48\text{ }\mu\text{mol}$) was added into the reaction mixture. The solution was stirred at room temperature overnight under nitrogen atmosphere. After that the product was precipitated out by adding 20 mL water. Then the product was collected by vacuum filtration followed by vacuum dry overnight. Yield: 25-30 mg. FTIR (solid IR): 3300 cm^{-1} (ν (N-H)), 3150 cm^{-1} (ν (=C-H) on triazole ring), $2820\text{-}2990\text{ cm}^{-1}$ (ν (C-H)), $1500\text{-}1750\text{ cm}^{-1}$ (ν (C=C)), 1600 cm^{-1} (δ (N-H)), $1465\text{-}1376\text{ cm}^{-1}$ (δ (C-H)), 1250 cm^{-1} (δ (Si-CH)), 1000 cm^{-1} (ν (Si-O)), 950 cm^{-1} (δ (N-H)).

6.3.8 Synthesis of methyl viologen-functionalized silicon nanoparticles via a nucleophilic displacement reaction

ω -Chloro-pentenyl (50%)-silicon nanoparticles (30 mg, obtained from RHEBM) and mono-methyl viologen (10 mg, 33 μ mol) were dissolved in 15 mL of DMF. The solution was reflux overnight under nitrogen atmosphere. After that the product was precipitated out by adding 20 mL water. Then the product was collected by vacuum filtration followed by vacuum dry overnight. The yield is 26 mg, 65%. $^1\text{H-NMR}$ (δ , 300 MHz, DMSO- D_6): 9.0-1.0 (m, aromatic protons), 4.0-0.4 (multiple broad peaks, alkyl protons on the surface of silicon nanoparticle).

6.3.9 Synthesis of adamantane grafted silicon nanoparticles

ω -Alkynyl-octenyl (20%)-silicon nanoparticles (30 mg, obtained from RHEBM) and azido-adamantane (10 mg, 56 μ mol) were dissolved in 15 mL of THF. Cu(I) bromide (10. mg, 48 μ mol) was added into the reaction mixture. The solution was stirred at room temperature overnight under nitrogen atmosphere. After removal of THF by vacuum distillation 20 mL of dichloromethane and 1 mL of ethylenediamine were added. The solution was subsequently washed three times with a saturated brine solution. The adamantane grafted silicon nanoparticles were purified by GPC to removed unreacted silicon nanoparticles and excess adamantane. Yield: 25-30 mg. $^1\text{H-NMR}$ (δ , 300 MHz, CD_2Cl_2): 7.5 (weak broad peak, triazole proton), 2.2 (broad, adamantane protons), 1.9 (broad, adamantane protons), 1.8-0.4 (multiple broad peaks, alkyl protons on the surface of silicon nanoparticle). FTIR (thin film on KBr): 3150 cm^{-1} (ν ($=\text{C-H}$) on triazole ring), 2820-2990 cm^{-1} (ν (C-H)), 1500-1750 cm^{-1} (ν ($\text{C}=\text{C}$)), 1465-1376 cm^{-1} (δ (C-H)), 1250 cm^{-1} (δ (Si-CH)), 1000 cm^{-1} (ν (Si-O)), 850 cm^{-1} (ν (Si-C)). UV-vis Absorption (in DCM):

Single absorption with a tail up to 600 nm. PL emission (in water): 350-700 nm emission peaks by changing excitation wavelength from 300-400 nm.

6.3.10 Synthesis of β -cyclodextrin grafted silicon nanoparticles

ω -Alkynyl-octenyl (50%)-silicon nanoparticles (30 mg, obtained from RHEBM) and azido- β -cyclodextrin (20 mg, 18 μ mol) were dissolved in 15 mL of THF. Cu(I) bromide (10. mg, 48 μ mol) was added into the reaction mixture. The solution was stirred at room temperature overnight under nitrogen atmosphere. After removal of THF by vacuum distillation 20 mL of dichloromethane and 1 mL of ethylenediamine were added. The solution was subsequently washed three times with a saturated brine solution. The β -cyclodextrin grafted silicon nanoparticles were purified by SEC to removed unreacted silicon nanoparticles and excess β -cyclodextrin. Yield: 25-30 mg. $^1\text{H-NMR}$ (δ , 300 MHz, DMSO- D_6): 7.9 (weak broad peak, triazole proton), 6.0 (broad, -CH), 5.8 (broad, -OH), 4.1 (broad, -OH), 3.9 (broad, -CH), 2.0-0.4 (multiple broad peaks, alkyl protons on the surface of silicon nanoparticle). FTIR (solid IR): 3300 cm^{-1} (ν (O-H)), 2820-2990 cm^{-1} (ν (C-H)), 1500-1750 cm^{-1} (ν (C=C)), 1465-1376 cm^{-1} (δ (C-H)), 1250 cm^{-1} (δ (Si-CH)), 1100 cm^{-1} (ν (C-O)), 1000 cm^{-1} (ν (Si-O)), 850 cm^{-1} (ν (Si-C)).

6.3.11 Synthesis of silicon nanoparticle arrays via “host-guest” self-assembly

Adamantane grafted silicon nanoparticles (10 mg) and β -cyclodextrin grafted silicon nanoparticles (10 mg) were dissolved in 5 mL of DMSO. The solution was dialyzed in water overnight. After that, the solution inside the dialysis tube was collected and sonicated for 1 hour, and the obtained solution was characterized by TEM. Yield: 16 mg.

6.3.12 Synthesis of silicon nanoparticle-porphyrin arrays via “host-guest” self-assembly

Adamantane grafted silicon nanoparticles (10 mg) and oct-cyclodextrin functionalized porphyrin (10 mg, obtained from Dr. Jayawickramarajah’s group) were dissolved in 5 mL of DMF. The solution was dialyzed in water overnight. After that, the solution inside the dialysis tube was collected and sonicated for 1 hour, and the obtained solution was characterized by TEM, UV-Vis spectroscopy and photoluminescence spectroscopy. Yield: 15 mg. UV-vis Absorption (in water): broad absorption in 250-380 nm, Soret band absorption at 425 nm, Q band absorption at 560 nm, 600 nm and 650 nm. PL emission (in water): Blue region (350-550 nm) and red region (550-750 nm) emission peaks by changing excitation wavelength from 300-420 nm.

6.3.13 Analytical methods

6.3.13.1 NMR sample preparation and acquisition

NMR samples were prepared by vacuum drying ~1.5 mL of the silicon nanoparticle solution, adding 0.8 mL of the preferred deuterated solvent, and then transferring the solution to a 5 mm NMR tube. ¹H-NMR measurements were performed on a Bruker Avance 300 spectrometer equipped with a 5 mm BBO probe.

6.3.13.2 Infrared spectroscopy

FTIR spectra were recorded at 1 cm⁻¹ resolution with 1000 scans on a Thermo Nicolet NEXUS 670 FTIR instrument. Samples were prepared as a thin film of passivated silicon nanoparticles prepared by depositing dichloromethane solution of

silicon nanoparticles on a KBr plate. The FT-IR sample chamber was purged with dry nitrogen before collecting any data.

6.3.13.3 UV-vis absorption and photoluminescence spectroscopy

UV-Vis absorption spectra were recorded in a quartz cuvette (1cm), using a Cary 50 spectrophotometer and were corrected for the solvent absorption. The scan range was 200-800 nm with a 300 nm min^{-1} scan rate. Excitation-emission spectra were recorded in a quartz cuvette (1cm), using a Varian Cary Eclipse spectrofluorometer with a scan rate of 120 nm min^{-1} .

6.3.13.4 Transmission electron microscopy

High-resolution transmission electron microscopy (TEM) studies were performed with a JEOL 2011 TEM using an accelerating voltage of 200 kV or a Tecnai G2 TEM using an accelerating voltage of 300 kV. The EDX data were obtained in the TEM using an Oxford Inca or Bruker attachment, using a 3nm beam spot. TEM samples were prepared by dropping a sonicated diluted solution of silicon nanoparticles in toluene or water onto a carbon-coated 400 mesh carbon coated copper grid which placed on a filter paper. The filter paper soaked up the excess solution before inserting in grid in the TEM sample holder.

Chapter 7: Conclusion and Future Direction

7.1 Conclusion

Mechanochemical synthesis via reactive high energy ball milling (RHEBM) is an efficient and facile way to produce passivated silicon nanoparticles with various terminal functional groups. These functionalized silicon nanoparticles can be used as precursors for solar energy materials and biocompatible materials via further modification.

The surface structure and optical properties of the passivated silicon nanoparticles have been systematically characterized to confirm the successful production of the nanoparticles via RHEBM. Due to the polydispersity of the silicon nanoparticles, and the tendency of alkynes to undergo cyclotrimerization reactions to form trisubstituted benzene during the ball milling, a fast approach for purifying and size separating the silicon nanoparticles using a gravity GPC column has been developed. The hydrodynamic diameters and size distribution of the separated silicon nanoparticles have been characterized using GPC and DOSY NMR analysis due to the limitation of TEM for characterizing ultra-small size silicon nanoparticles. The results show the excellent effectiveness of GPC and DOSY NMR as reliable approaches for determining the nanoparticle sizes. These two methods are faster and more cost-effective compared to TEM alone.

“Click” chemistry is an attractive tool for functionalizing silicon nanoparticles because of its high yields, modular approach, and broad functional group tolerance compared to hydrosilylation or other organometallic methods. The copper (I) catalyzed azide-alkyne cycloaddition (CuAAC) in particular is one of the most efficient “click”

reactions due to its high selectivity and mild reaction conditions. CuAAC “click” reaction has been used to functionalize or assemble the passivated silicon nanoparticles with certain organic dye molecules and polymers. The resultant silicon nanoparticles and silicon nanoparticle arrays can be used for further photovoltaic and biological application.

Water soluble PEGylated silicon nanoparticles were synthesized through the application of CuAAC “click” chemistry using azido functionalized nanoparticles and mono-alkynyl-PEG polymers. PEG is an ideal polymer for the modification of nanostructured materials based on its intrinsic biocompatibility and water solubility. The PEGylated silicon nanoparticles exhibited vastly improved water solubility while maintaining the strong blue photoluminescence associated with the unmodified nanoparticles. Cytotoxicity studies of these water soluble silicon nanoparticles were performed *in vitro* and had demonstrated the low cytotoxicity of the PEGylated silicon nanoparticles.

In addition, a new class of PEGylated silicon nanoparticle arrays were prepared by crosslinking functionalized silicon nanoparticles with α,ω -bis-difunctional-PEG polymers. These colloidal photoluminescent nanoparticle arrays have flexible globular structures in which the swelling behavior may be readily tuned by controlling the length of the PEG linkers. The strong PL emission suggests these PEGylated Si nanoparticle arrays may be used for bioimaging and labeling purposes. Additionally, the porous structure of these globular arrays portends the potential application in drug delivery, since the silicon nanoparticles are known to degrade *in vivo*. The ability to simultaneously incorporate both the imaging and therapeutic applications within one nanomaterial, as well as tune

the swelling behavior, suggests that these materials have relevance to the rapidly growing field of theranostics.

Zn-porphyrin functionalized silicon nanoparticles also have been synthesized via the CuAAC “click” reaction using the azide-terminated silicon nanoparticles and mono-alkynyl-zincporphyrin. The energy transfer process within the silicon nanoparticle-porphyrin systems has been shown by steady-state and time-resolved fluorescence measurements. The azide-terminated silicon nanoparticles are excellent energy donors with Zn-porphyrin acceptor molecules. A simple tuning of the ratio and distance between the donor and acceptor can give desirable energy transfer efficiency up to 52% in the case of a short linker and higher acceptor-donor ratio. The energy transfer rate were calculated, which are very high for all examined systems and follow the distance dependence based on Forster energy transfer theory.

Furthermore, C₆₀ has been added into the silicon nanoparticle-porphyrin system to form the silicon nanoparticle-porphyrin-fullerene nanocluster based on the π - π interaction between the Zn-porphyrin and fullerene. The photoinduced electron transfer process inside the nanocluster has been confirmed by femto-second transient absorption spectroscopy, which proving the ability of porphyrin-Si nanoparticle hybrid system to effect the charge separation. Thus, the Zn-porphyrin functionalized silicon nanoparticles are highly promising as novel artificial photosynthetic materials. This study should provide basic and valued information for the design of chromophore-modified silicon nanoparticles necessary for the constructing of efficient solar cells.

A water soluble PEGylated porphyrin grafted silicon nanoparticle system, in which the silicon nanoparticles were used as nanocarriers, has been synthesized for photodynamic therapeutic application. The PEGylated porphyrin functionalized silicon nanoparticles were obtained by conjugating the PEGylated alkynyl-porphyrins onto the azido-terminated silicon nanoparticles via a CuAAC “click” reaction. The resultant PEGylated porphyrin grafted silicon nanoparticles have diameters around 13.5 ± 3.8 nm. The cryo-TEM and conventional TEM analysis proved that the PEGylated porphyrin grafted silicon nanoparticle could form the micelle-like structures at higher concentration in water via self-assembly. The UV-Vis absorption analysis demonstrated that the silicon nanoparticle could reduce the porphyrin aggregation in water. The cell studies have demonstrated that the silicon nanoparticle could deliver the porphyrin drugs into HEK293T cells while the porphyrin could serve as an efficient photosensitizer to kill these cells via mitochondrial apoptotic pathway. The functionalized silicon nanoparticles exhibited lower dark cytotoxicity compared to the free PEGylated porphyrin, and a more efficient photodynamic therapy was observed *in vitro*.

7.2 Future direction

7.2.1 Synthesis of mono-functionalized silicon nanoparticles

Unlike small molecules or polymers, chemical reactions on nanoparticles are difficult to control due to the uncertain number of the functional groups on the nanoparticle surface. Usually, it is possible to tune the percentage surface coverage of the functional group, but impossible to accurately control with certainty the number of functional groups on the nanoparticle surface. Therefore, an approach to prepare silicon nanoparticles with a discrete number of functional groups is desirable in order to accurately control the surface modification and assembly of the silicon nanoparticles.

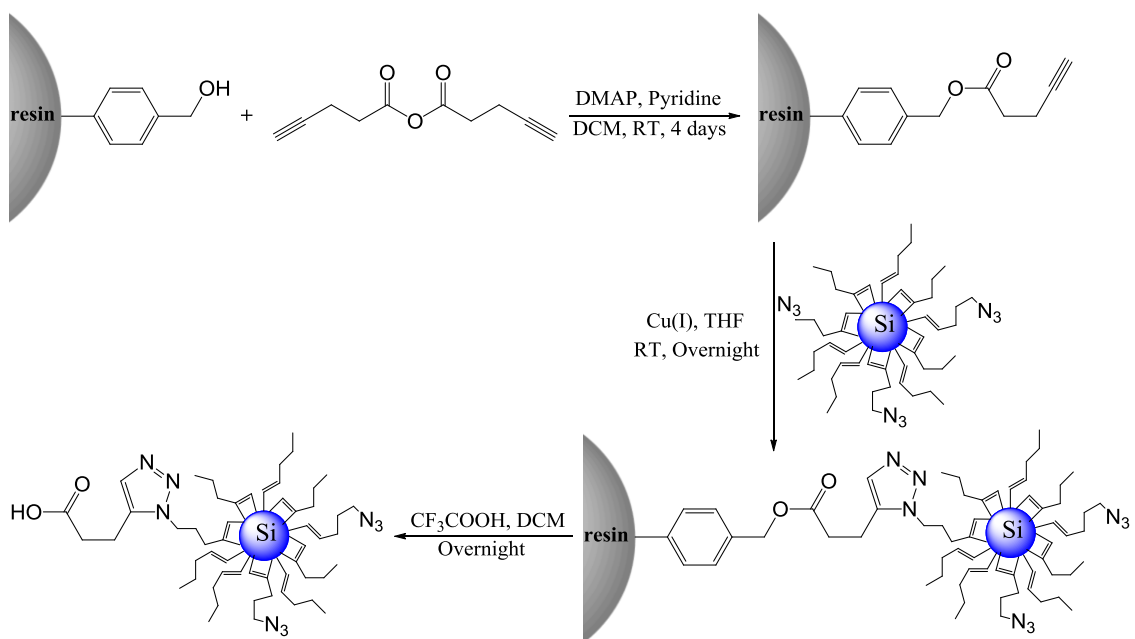


Figure 7.1 The proposed synthesis approach of mono-functionalized silicon nanoparticles

Polystyrene Wang resin is the most widely used resin in solid phase organic synthesis.¹⁸¹ It also has been used as solid-supports to synthesize monofunctional gold nanoparticles via a noncovalent interaction based solid-phase modification approach.¹⁸² Hence, we propose an approach to synthesize the mono-functionalized silicon nanoparticles via a heterogeneous CuAAC “click” reactions (Figure 7.1). Attachment of a carboxylic acid can be achieved with N,N'-dicyclohexylcarbodiimide (DCC)/4-dimethylaminopyridine (DMAP).¹⁰² Cleavage of esters to provide the corresponding carboxylic acids can be obtained using concentrated trifluoroacetic acid (TFA) or TFA-dichloromethane (DCM). In our proposal, the anhydride of 4-pentynoic acid will be reacted with polystyrene Wang resin to obtain an alkyne functionalized resin which can react with azide terminated silicon nanoparticles via a heterogeneous "click" reaction. If the alkyne functional group density of Wang resin is low enough, the neighboring alkyne groups on the surface of Wang resin are sufficiently far apart, which ruling out the possibility that more than one alkyne groups react with the same azide terminated silicon nanoparticle. When the alkyne functionalized Wang resin are allowed to react with azide terminated silicon nanoparticles, only one Wang resin will be attached to the nanoparticle. After cleavage from the resin, silicon nanoparticle with monocarboxylic acid functional group will be obtained. Those mono-functionalized silicon nanoparticles can be applied to a series of reactions with various molecules to obtain systems with well-designed structure.

7.2.2 Fabrication of solar cell based on silicon nanoparticle-porphyrin system

7.2.2.1 Fabrication of solar cell based on silicon nanoparticle-porphyrin-fullerene nanocluster

Since the silicon nanoparticle-porphyrin system based light harvesting material has been successfully synthesized and its ability of affecting the charge separation after capturing light energy have been demonstrated, the next step would be fabricating a hybrid solar cell based on the silicon nanoparticle-porphyrin system and determining the power conversion efficiency that it can achieve.

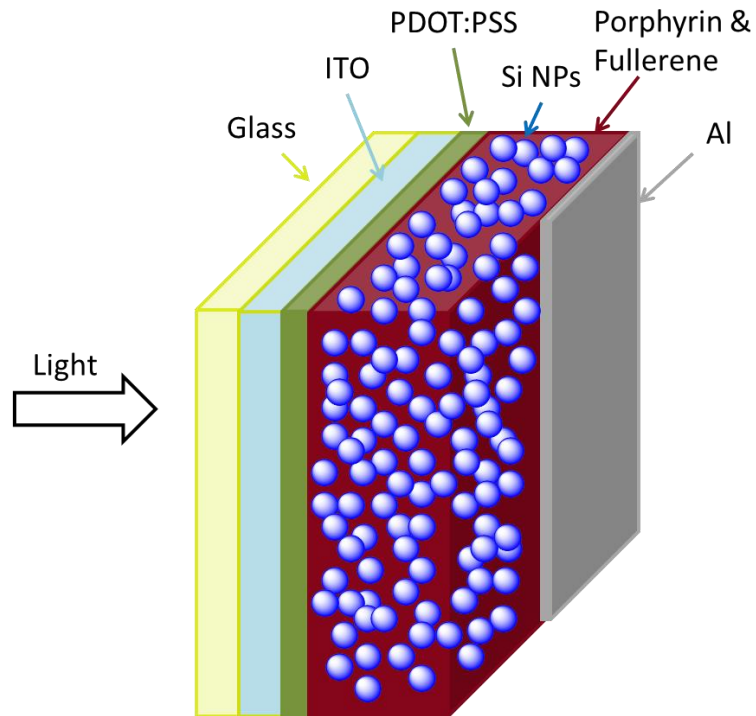


Figure 7.2 Schematic of a silicon nanoparticles-porphyrin-fullerene hybrid solar cell

Based on the method that developed by Kortshagen and coworkers,^{78, 82} we propose to fabricate the silicon nanoparticles-porphyrin-fullerene hybrid solar cell (Figure 7.2). The solar cells can be fabricated by spin-coating silicon nanoparticle-porphyrin-fullerene

Figure 7.3 shows the charge separation process inside the solar cells. After silicon nanoparticle capturing the light energy, the energy will transfer from the silicon nanoparticle to the porphyrin unit and induce the charge separation between the porphyrin and fullerene. The electron will finally transfer to the Al electrode while the positive charge will move the ITO layer.

7.2.2.2 Layer-by-layer surface modification of TiO₂ thin films with a silicon nanoparticles-porphyrin system

Another potential application of the silicon nanoparticle-porphyrin light harvesting complex in solar cell will be applied in the surface modification of titania. Titania is one of the leading candidates for photo-electrodes in photoelectrochemical cells¹⁸⁴. However, titania has very low energy conversion efficiency of less than 1%.¹⁸⁵ In order to increase the energy conversion efficiency, the titania surface has been modified with organic dyes.¹⁸⁶

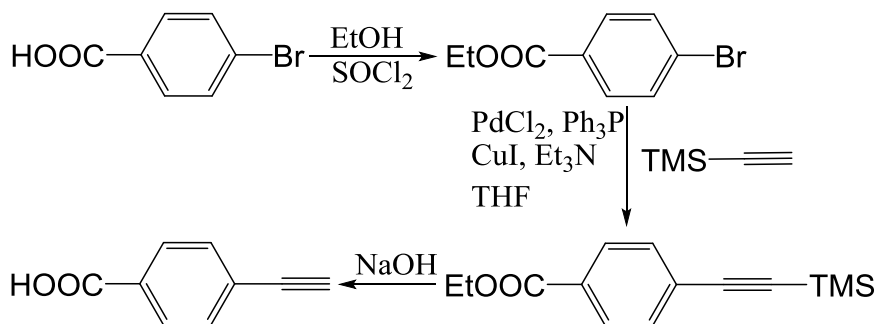


Figure 7.4 Proposed synthesis of 4-ethynylphenylacetic acid

We propose to modify the titania with silicon nanoparticle-porphyrin complex via a series of reactions. First, 4-ethynylphenylacetic acid will be synthesized from 4-bromophenylacetic acid (Figure 7.4) and immobilized on the surface of titania plate to achieve alkyne group capped titania plate. Alkyne capped titania plates can be modified

by a mono-layer of Si nanoparticles via a "click" reaction with azide terminated Si nanoparticles. To achieve further modification of titania plate with multiple Si nanoparticle layers, the alkyne capped titania plate will react with different sizes Si nanoparticles (from larger size to smaller size) and bis-alkynyl-porphyrin, layer by layer (Figure 7.5). The tendency of the size decreasing of silicon nanoparticles in each layer will result in the increasing of the band gap, which can enhance the electron transfer from the silicon nanoparticle layers to the TiO₂ thin film.

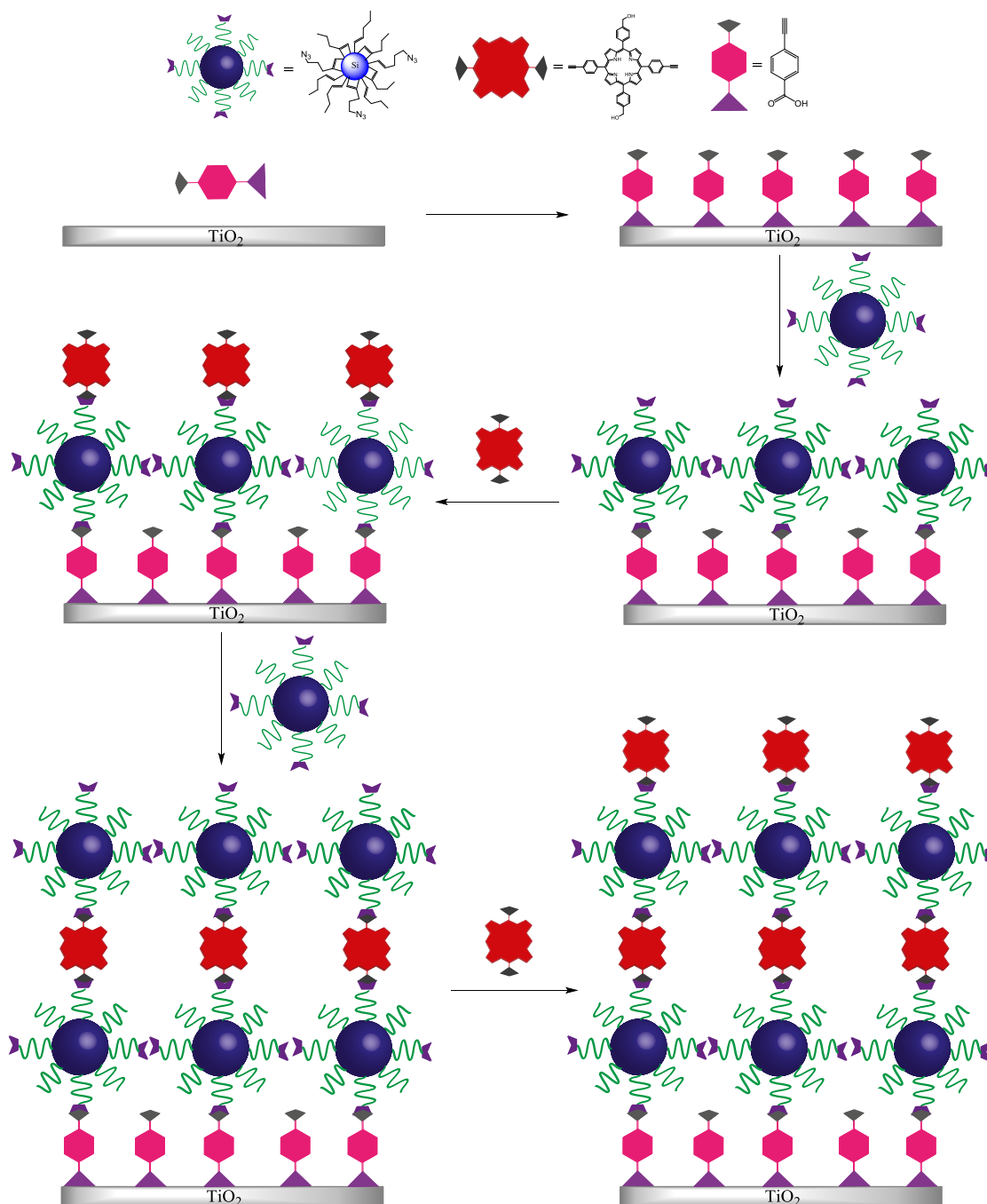


Figure 7.5 Schematic of layer by layer surface modification of TiO_2 plate with silicon nanoparticle-porphyrin complex

Due to the light harvesting ability of the silicon nanoparticle-porphyrin complex, we expect the energy conversion efficiency of the titania will be increased.

7.2.3 Further modification of PEGylated porphyrin-silicon nanoparticle system to enhance their selectivity for photodynamic therapy

7.2.3.1 Synthesis of PEGylated porphyrin-silicon nanoparticle micelles with controllable size

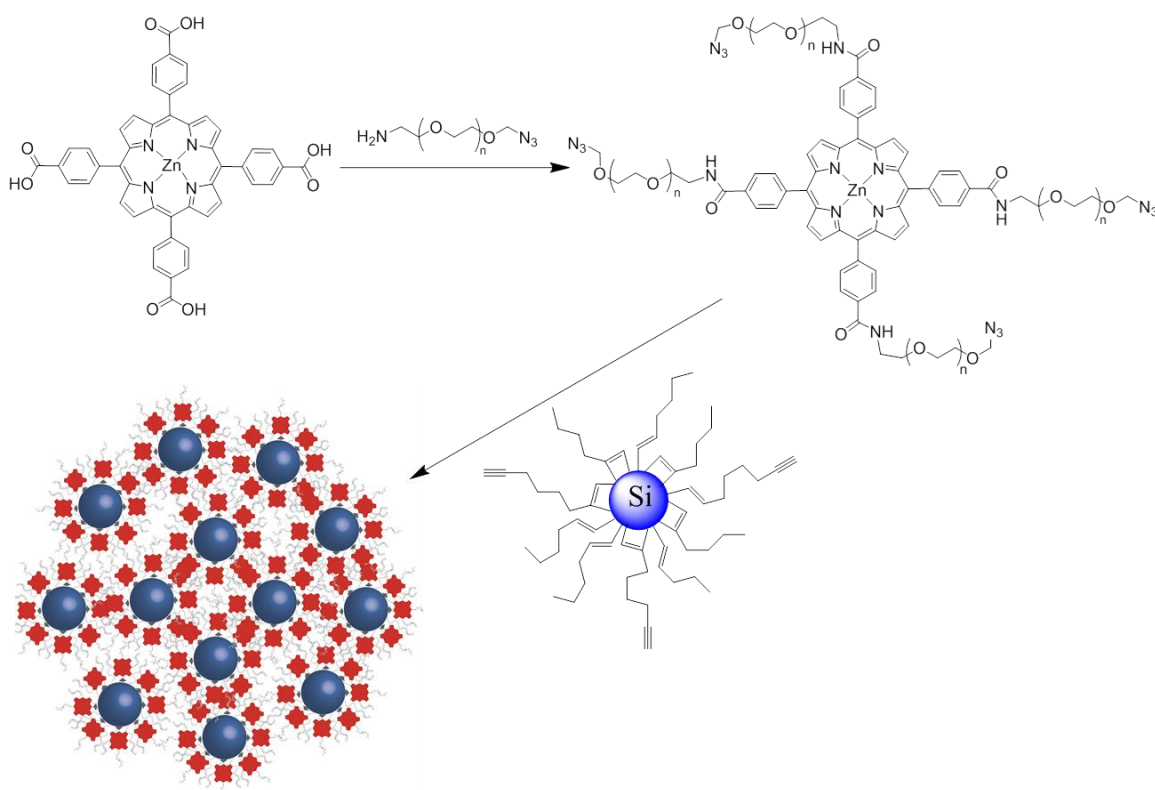


Figure 7.6 Schematic of synthesis PEGylated porphyrin functionalized silicon nanoparticle array

One well-known strategy to enhance the selectivity of the nanoparticles accumulating into the cancer cells is based on the enhanced permeability and retention (EPR) effect that certain sizes of nanoparticles tend to accumulate in tumor tissue much more than they do in normal tissues. As discussed previously in Chapter 5, the PEGylated porphyrin grafted silicon nanoparticles can form the micelle-like nanostructures via self-assembly in aqueous media. However, the size of these micelle structures is

uncontrollable. Hence, we propose to synthesize the PEGylated porphyrin functionalized silicon nanoparticle arrays with tunable size.

Figure 7.6 shows the potential synthetic route to the new PEGylated porphyrin functionalized silicon nanoparticle arrays. First, the ω -azido-PEGylated-porphyrin will be obtained from an esterification reaction between the tetra-carboxylicacid-porphyrin and the amino-azido-bifunctional-PEG. Then the PEGylated porphyrin functionalized silicon nanoparticle arrays can be prepared by crosslinking functionalized silicon nanoparticles with the ω -azido-PEGylated-porphyrin. Similar as discussed in Chapter 3, the size of these arrays can be tuned by changing the surface coverage of the alkyne groups on the silicon nanoparticles, or the chain length of the PEG polymers.

7.2.3.2 Conjugation of PEGylated porphyrin-silicon nanoparticle system with cellular targeting ligands

Another strategy to enhance the selectivity of nanoparticles is to conjugate the cellular targeting ligands, which can be recognized by the cancer cells, onto the surface of the nanoparticles. Many studies have been done on the conjugation of various cellular targeting ligands, such as folic acid¹⁸⁷, natural¹⁸⁸ and artificial¹⁸⁹ bioactive peptides and large T antigen proteins¹⁹⁰, onto the gold nanoparticles to enhance the internalization and cellular uptake of the nanoparticles by cancer cells. According to the method developed by Nam and coworkers¹⁹¹, we propose a new cyclic RGD (arginine-glycine-aspartic acid) PEGylated porphyrin grafted silicon nanoparticle system as a multifunctional photosensitizer for photodynamic therapy, in which the cyclic RGD small peptides act as the targeting ligand to the $\alpha_v\beta_3$ integrin on the tumor cell membranes.

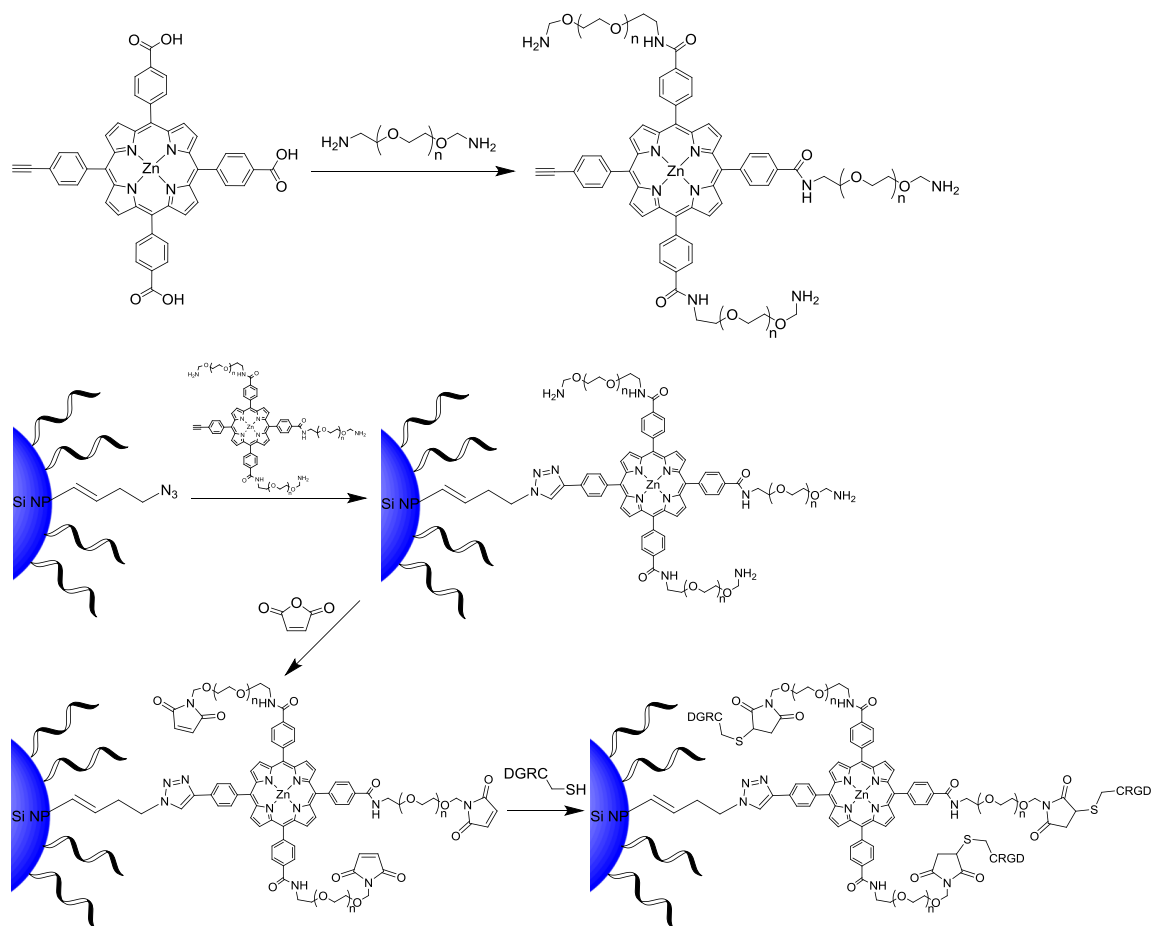


Figure 7.7 Schematic of synthesis of amino-PEGylated porphyrin and RGD-PEGylated porphyrin grafted silicon nanoparticles.

Figure 7.7 shows the potential synthetic route to the new CRGD (cysteine-arginine-glycine-aspartic acid) PEGylated porphyrin functionalized silicon nanoparticle. First, the ω -triamino-alkynyl-PEGylated-porphyrin will be obtained from an esterification reaction between the tricarboxylic acid-alkynyl-porphyrin and the bis-amino-PEG. Then the amino-PEGylated-porphyrin can be conjugated to the azido-terminated silicon nanoparticles via azide-alkyne “click” reaction. Finally, after treating the obtained amino-PEGylated porphyrin grafted silicon nanoparticles with malic anhydride, the CRGD can be conjugated onto the nanoparticles via the maleimide-thiol reaction.

Chapter 8: Reference

1. Brady, G. S.; Clauser, H. R.; Vaccari, J. A., *Materials handbook: an encyclopedia for managers, technical professionals, purchasing and production managers, technicians, and supervisors*. McGraw-Hill: 1997.
2. Alivisatos, A. P., Semiconductor Clusters, Nanocrystals, and Quantum Dots. *Science* **1996**, 271 (5251), 933-937.
3. Fan, J.; Chu, P. K., Group IV Nanoparticles: Synthesis, Properties, and Biological Applications. *Small* **2010**, 6 (19), 2080-2098.
4. Swihart, M. T., Silicon Nanoparticles for Biophotonics. In *Nanotechnology in biology and Medicine: Methods, Devices, and Applications*, Vo-Dinh, T., Ed. CRC Press: Boca Raton, 2007; Vol. 4.
5. Canham, L. T., Silicon quantum wire array fabrication by electrochemical and chemical dissolution of wafers. *Applied Physics Letters* **1990**, 57 (10), 1046-1048.
6. Vo-Dinh, T., *Nanotechnology in Biology and Medicine: Methods, Devices, and Applications*. Taylor & Francis: 2007.
7. (a) Pavesi, L.; Dal Negro, L.; Mazzoleni, C.; Franzo, G.; Priolo, F., Optical gain in silicon nanocrystals. *Nature* **2000**, 408 (6811), 440-444; (b) Walters, R. J.; Bourianoff, G. I.; Atwater, H. A., Field-effect electroluminescence in silicon nanocrystals. *Nat Mater* **2005**, 4 (2), 143-146.
8. (a) Rama Krishna, M. V.; Friesner, R. A., Quantum confinement effects in semiconductor clusters. *The Journal of Chemical Physics* **1991**, 95 (11), 8309-8322; (b) Zorman, B.; Ramakrishna, M. V.; Friesner, R. A., Quantum Confinement Effects in CdSe Quantum Dots. *The Journal of Physical Chemistry* **1995**, 99 (19), 7649-7653; (c) Nirmal, M.; Brus, L., Luminescence Photophysics in Semiconductor Nanocrystals. *Accounts of Chemical Research* **1998**, 32 (5), 407-414.
9. Brus, L. E., Electron-electron and electron-hole interactions in small semiconductor crystallites: The size dependence of the lowest excited electronic state. *The Journal of Chemical Physics* **1984**, 80 (9), 4403-4409.

10. (a) Delerue, C.; Allan, G.; Lannoo, M., Electron-phonon coupling and optical transitions for indirect-gap semiconductor nanocrystals. *Physical Review B* **2001**, *64* (19), 193402; (b) Kovalev, D.; Diener, J.; Heckler, H.; Polisski, G.; Künzner, N.; Koch, F., Optical absorption cross sections of Si nanocrystals. *Physical Review B* **2000**, *61* (7), 4485-4487; (c) Kovalev, D.; Heckler, H.; Polisski, G.; Diener, J.; Koch, F., Optical properties of silicon nanocrystals. *Optical Materials* **2001**, *17* (1–2), 35-40.
11. Hybertsen, M. S., Absorption and emission of light in nanoscale silicon structures. *Physical Review Letters* **1994**, *72* (10), 1514-1517.
12. (a) Meier, C.; Lüttjohann, S.; Offer, M.; Wiggers, H.; Orke, A., Silicon Nanoparticles: Excitonic Fine Structure and Oscillator Strength. In *Advances in Solid State Physics*, Haug, R., Ed. Springer Berlin Heidelberg: 2009; Vol. 48, pp 79-90; (b) Nayfeh, M. H.; Rigakis, N.; Yamani, Z., Photoexcitation of Si-Si surface states in nanocrystallites. *Physical Review B* **1997**, *56* (4), 2079-2084; (c) Takagahara, T.; Takeda, K., Theory of the quantum confinement effect on excitons in quantum dots of indirect-gap materials. *Physical Review B* **1992**, *46* (23), 15578-15581.
13. (a) Allan, G.; Delerue, C.; Lannoo, M., Nature of Luminescent Surface States of Semiconductor Nanocrystallites. *Physical Review Letters* **1996**, *76* (16), 2961-2964; (b) Wolkin, M. V.; Jorne, J.; Fauchet, P. M.; Allan, G.; Delerue, C., Electronic States and Luminescence in Porous Silicon Quantum Dots: The Role of Oxygen. *Physical Review Letters* **1999**, *82* (1), 197-200.
14. Stesmans, A.; Afanas'ev, V. V., Electron spin resonance features of interface defects in thermal (100)Si/SiO₂. *Journal of Applied Physics* **1998**, *83* (5), 2449-2457.
15. Godefroo, S.; Hayne, M.; Jivanescu, M.; Stesmans, A.; Zacharias, M.; Lebedev, O. I.; Van Tendeloo, G.; Moshchalkov, V. V., Classification and control of the origin of photoluminescence from Si nanocrystals. *Nat Nano* **2008**, *3* (3), 174-178.
16. Zhao, Y.; Li, D.; Sang, W.; Yang, D.; Jiang, M., The influence of microstructure on optical properties of porous silicon. *Solid-State Electronics* **2007**, *51* (5), 678-682.
17. Rosso-Vasic, M.; Spruijt, E.; van Lagen, B.; De Cola, L.; Zuilhof, H., Alkyl-Functionalized Oxide-Free Silicon Nanoparticles: Synthesis and Optical Properties. *Small* **2008**, *4* (10), 1835-1841.

18. Li, X. G.; He, Y. Q.; Swihart, M. T., Surface functionalization of silicon nanoparticles produced by laser-driven pyrolysis of silane followed by HF-HNO₃ etching. *Langmuir* **2004**, *20* (11), 4720-4727.
19. (a) Hua, F.; Swihart, M. T.; Ruckenstein, E., Efficient Surface Grafting of Luminescent Silicon Quantum Dots by Photoinitiated Hydrosilylation. *Langmuir* **2005**, *21* (13), 6054-6062; (b) Wilson, W. L.; Szajowski, P. F.; Brus, L. E., Quantum Confinement in Size-Selected, Surface-Oxidized Silicon Nanocrystals. *Science* **1993**, *262* (5137), 1242-1244.
20. Jurbergs, D.; Rogojina, E.; Mangolini, L.; Kortshagen, U., Silicon nanocrystals with ensemble quantum yields exceeding 60%. *Applied Physics Letters* **2006**, *88* (23), -.
21. Li, Z. F.; Ruckenstein, E., Water-Soluble Poly(acrylic acid) Grafted Luminescent Silicon Nanoparticles and Their Use as Fluorescent Biological Staining Labels. *Nano Letters* **2004**, *4* (8), 1463-1467.
22. (a) Maurice, D. R.; Courtney, T. H., The physics of mechanical alloying: A first report. *Metall and Mat Trans A* **1990**, *21* (1), 289-303; (b) Zou, J.; Baldwin, R. K.; Pettigrew, K. A.; Kauzlarich, S. M., Solution synthesis of ultrastable luminescent siloxane-coated silicon nanoparticles. *Nano Letters* **2004**, *4* (7), 1181-1186.
23. Bley, R. A.; Kauzlarich, S. M., A Low-Temperature Solution Phase Route for the Synthesis of Silicon Nanoclusters. *Journal of the American Chemical Society* **1996**, *118* (49), 12461-12462.
24. (a) Royea, W. J.; Juang, A.; Lewis, N. S., Preparation of air-stable, low recombination velocity Si(111) surfaces through alkyl termination. *Applied Physics Letters* **2000**, *77* (13), 1988-1990; (b) Yu, H.; Webb, L. J.; Ries, R. S.; Solares, S. D.; Goddard, W. A.; Heath, J. R.; Lewis, N. S., Low-Temperature STM Images of Methyl-Terminated Si(111) Surfaces. *The Journal of Physical Chemistry B* **2004**, *109* (2), 671-674.
25. Wilcoxon, J. P.; Samara, G. A.; Provencio, P. N., Optical and electronic properties of Si nanoclusters synthesized in inverse micelles. *Physical Review B* **1999**, *60* (4), 2704-2714.

26. Tilley, R. D.; Warner, J. H.; Yamamoto, K.; Matsui, I.; Fujimori, H., Micro-emulsion synthesis of monodisperse surface stabilized silicon nanocrystals. *Chemical Communications* **2005**, (14), 1833-1835.
27. Warner, J. H.; Hoshino, A.; Yamamoto, K.; Tilley, R. D., Water-Soluble Photoluminescent Silicon Quantum Dots. *Angewandte Chemie International Edition* **2005**, 44 (29), 4550-4554.
28. Pettigrew, K. A.; Liu, Q.; Power, P. P.; Kauzlarich, S. M., Solution synthesis of alkyl- and alkyl/alkoxy-capped silicon nanoparticles via oxidation of Mg(2)Si. *Chemistry of Materials* **2003**, 15 (21), 4005-4011.
29. Neiner, D.; Chiu, H. W.; Kauzlarich, S. M., Low-Temperature Solution Route to Macroscopic Amounts of Hydrogen Terminated Silicon Nanoparticles. *Journal of the American Chemical Society* **2006**, 128 (34), 11016-11017.
30. Holmes, J. D.; Ziegler, K. J.; Doty, R. C.; Pell, L. E.; Johnston, K. P.; Korgel, B. A., Highly Luminescent Silicon Nanocrystals with Discrete Optical Transitions. *Journal of the American Chemical Society* **2001**, 123 (16), 3743-3748.
31. English, D. S.; Pell, L. E.; Yu, Z. H.; Barbara, P. F.; Korgel, B. A., Size tunable visible luminescence from individual organic monolayer stabilized silicon nanocrystal quantum dots. *Nano Letters* **2002**, 2 (7), 681-685.
32. Li, X.; He, Y.; Talukdar, S. S.; Swihart, M. T., Process for Preparing Macroscopic Quantities of Brightly Photoluminescent Silicon Nanoparticles with Emission Spanning the Visible Spectrum. *Langmuir* **2003**, 19 (20), 8490-8496.
33. Hessel, C. M.; Henderson, E. J.; Veinot, J. G. C., Hydrogen Silsesquioxane: A Molecular Precursor for Nanocrystalline Si-SiO₂ Composites and Freestanding Hydride-Surface-Terminated Silicon Nanoparticles. *Chemistry of Materials* **2006**, 18 (26), 6139-6146.
34. Mangolini, L.; Thimsen, E.; Kortshagen, U., High-Yield Plasma Synthesis of Luminescent Silicon Nanocrystals. *Nano Letters* **2005**, 5 (4), 655-659.
35. Bhandarkar, U. V.; Swihart, M. T.; Girshick, S. L.; Kortshagen, U. R., Modelling of silicon hydride clustering in a low-pressure silane plasma. *Journal of Physics D: Applied Physics* **2000**, 33 (21), 2731.

36. Arul Dhas, N.; Raj, C. P.; Gedanken, A., Preparation of Luminescent Silicon Nanoparticles: A Novel Sonochemical Approach. *Chemistry of Materials* **1998**, *10* (11), 3278-3281.
37. (a) Nayfeh, M. H.; Barry, N.; Therrien, J.; Akcikir, O.; Gratton, E.; Belomoin, G., Stimulated blue emission in reconstituted films of ultrasmall silicon nanoparticles. *Applied Physics Letters* **2001**, *78* (8), 1131-1133; (b) Sweryda-Krawiec, B.; Cassagneau, T.; Fendler, J. H., Surface modification of silicon nanocrystallites by alcohols. *Journal of Physical Chemistry B* **1999**, *103* (44), 9524-9529.
38. (a) Carter, R. S.; Harley, S. J.; Power, P. P.; Augustine, M. P., Use of NMR spectroscopy in the synthesis and characterization of air- and water-stable silicon nanoparticles from porous silicon. *Chemistry of Materials* **2005**, *17* (11), 2932-2939; (b) Lie, L. H.; Duerdin, M.; Tuite, E. M.; Houlton, A.; Horrocks, B. R., Preparation and characterisation of luminescent alkylated-silicon quantum dots. *Journal of Electroanalytical Chemistry* **2002**, *538*, 183-190.
39. (a) Amoroso, S.; Bruzzese, R.; Spinelli, N.; Velotta, R.; Vitiello, M.; Wang, X.; Ausanio, G.; Iannotti, V.; Lanotte, L., Generation of silicon nanoparticles via femtosecond laser ablation in vacuum. *Applied Physics Letters* **2004**, *84* (22), 4502-4504; (b) Chiu, L. A.; Seraphin, A. A.; Kolenbrander, K. D., Gas phase synthesis and processing of silicon nanocrystallites: Characterization by photoluminescence emission spectroscopy. *JEM* **1994**, *23* (3), 347-354; (c) Geohegan, D. B.; Puretzky, A. A.; Duscher, G.; Pennycook, S. J., Photoluminescence from gas-suspended SiO_x nanoparticles synthesized by laser ablation. *Applied Physics Letters* **1998**, *73* (4), 438-440; (d) Li, S.; Silvers, S. J.; El-Shall, M. S., Surface Oxidation and Luminescence Properties of Weblike Agglomeration of Silicon Nanocrystals Produced by a Laser Vaporization–Controlled Condensation Technique. *The Journal of Physical Chemistry B* **1997**, *101* (10), 1794-1802; (e) Makimura, T.; Mizuta, T.; Murakami, K., Formation dynamics of silicon nanoparticles after laser ablation studied using plasma emission caused by second-laser decomposition. *Applied Physics Letters* **2000**, *76* (11), 1401-1403; (f) Makimura, T.; Mizuta, T.; Murakami, K., Laser Ablation Synthesis of Hydrogenated Silicon Nanoparticles with Green Photoluminescence in the Gas Phase. *Japanese Journal of Applied Physics* **2002**, *41* (Part 2, No. 2A), L144-L146; (g) Mizuta, T.; Takeuchi, D.; Makimura, T.; Murakami, K., Chemical Reaction of Si Nanoparticles during Formation in Gas Phase Observed by a Time-Resolved Photoluminescence Method. *Japanese Journal of Applied Physics* **2002**, *41* (Part 1, No. 9), 5739-5744.

40. Brian S. Mitchell, H. W., Zejing Xu, Mark J. Fink, and Dmitry Shchukin, Functionalized Photoluminescent Silicon Nanoparticles from Reactive Cavitation Erosion of Silicon Wafers. **In preparation.**
41. (a) Hallmann, S.; Fink, M. J.; Mitchell, B. S., Mechanochemical synthesis of functionalized silicon nanoparticles with terminal chlorine groups. *Journal of Materials Research* **2011**, 26 (08), 1052-1060; (b) Heintz, A. S.; Fink, M. J.; Mitchell, B. S., Mechanochemical Synthesis of Blue Luminescent Alkyl/Alkenyl-Passivated Silicon Nanoparticles. *Advanced Materials* **2007**, 19 (22), 3984-3988; (c) Heintz, A. S.; Fink, M. J.; Mitchell, B. S., Silicon nanoparticles with chemically tailored surfaces. *Applied Organometallic Chemistry* **2010**, 24 (3), 236-240.
42. Veinot, J., Surface Passivation and Functionalization of Si Nanocrystals. In *Silicon Nanocrystals*, Wiley-VCH Verlag GmbH & Co. KGaA: 2010; pp 155-172.
43. Buriak, J. M.; Allen, M. J., Lewis Acid Mediated Functionalization of Porous Silicon with Substituted Alkenes and Alkynes. *Journal of the American Chemical Society* **1998**, 120 (6), 1339-1340.
44. (a) Linford, M. R.; Chidsey, C. E. D., Alkyl monolayers covalently bonded to silicon surfaces. *Journal of the American Chemical Society* **1993**, 115 (26), 12631-12632; (b) Linford, M. R.; Fenter, P.; Eisenberger, P. M.; Chidsey, C. E. D., Alkyl Monolayers on Silicon Prepared from 1-Alkenes and Hydrogen-Terminated Silicon. *Journal of the American Chemical Society* **1995**, 117 (11), 3145-3155.
45. Buriak, J. M., Illuminating Silicon Surface Hydrosilylation: An Unexpected Plurality of Mechanisms. *Chemistry of Materials* **2013**, 26 (1), 763-772.
46. Sato, S.; Swihart, M. T., Propionic-Acid-Terminated Silicon Nanoparticles: Synthesis and Optical Characterization. *Chemistry of Materials* **2006**, 18 (17), 4083-4088.
47. Rogozhina, E. V.; Eckhoff, D. A.; Gratton, E.; Braun, P. V., Carboxyl functionalization of ultrasmall luminescent silicon nanoparticles through thermal hydrosilylation. *Journal of Materials Chemistry* **2006**, 16 (15), 1421-1430.
48. Choi, J.; Wang, N. S.; Reipa, V., Conjugation of the Photoluminescent Silicon Nanoparticles to Streptavidin. *Bioconjugate Chemistry* **2008**, 19 (3), 680-685.

49. (a) Rosso-Vasic, M.; Spruijt, E.; Popovic, Z.; Overgaag, K.; van Lagen, B.; Grandidier, B.; Vanmaekelbergh, D.; Dominguez-Gutierrez, D.; De Cola, L.; Zuilhof, H., Amine-terminated silicon nanoparticles: synthesis, optical properties and their use in bioimaging. *Journal of Materials Chemistry* **2009**, *19* (33), 5926-5933; (b) Sudeep, P. K.; Page, Z.; Emrick, T., PEGylated siliconnanoparticles: synthesis and characterization. *Chemical Communications* **2008**, (46), 6126-6127.
50. Sudeep, P. K.; Emrick, T., Functional Si and CdSe Quantum Dots: Synthesis, Conjugate Formation, and Photoluminescence Quenching by Surface Interactions. *Acs Nano* **2009**, *3* (12), 4105-4109.
51. Zhao, W.; Pacard, E.; Chaix-Bauvais, C.; Pichot, C.; Brook, M. A., Covalent assembly of silica nanoparticle aggregates for oligonucleotide synthesis. *Colloids and Surfaces A: Physicochemical and Engineering Aspects* **2009**, *339* (1–3), 26-34.
52. Nelles, J.; Sendor, D.; Petrat, F.-M.; Simon, U., Electrical properties of surface functionalized silicon nanoparticles. *J Nanopart Res* **2010**, *12* (4), 1367-1375.
53. Li, Z. F.; Swihart, M. T.; Ruckenstein, E., Luminescent Silicon Nanoparticles Capped by Conductive Polyaniline through the Self-Assembly Method. *Langmuir* **2004**, *20* (5), 1963-1971.
54. (a) Liu, Q.; Kauzlarich, S. M., A new synthetic route for the synthesis of hydrogen terminated silicon nanoparticles. *Materials Science and Engineering: B* **2002**, *96* (2), 72-75; (b) Mayeri, D.; Phillips, B. L.; Augustine, M. P.; Kauzlarich, S. M., NMR Study of the Synthesis of Alkyl-Terminated Silicon Nanoparticles from the Reaction of SiCl₄ with the Zintl Salt, NaSi. *Chemistry of Materials* **2001**, *13* (3), 765-770; (c) Yang, C.-S.; Bley, R. A.; Kauzlarich, S. M.; Lee, H. W. H.; Delgado, G. R., Synthesis of Alkyl-Terminated Silicon Nanoclusters by a Solution Route. *Journal of the American Chemical Society* **1999**, *121* (22), 5191-5195.
55. Rogozhina, E.; Belomoin, G.; Smith, A.; Abuhassan, L.; Barry, N.; Akcakir, O.; Braun, P. V.; Nayfeh, M. H., Si-N linkage in ultrabright, ultrasmall Si nanoparticles. *Applied Physics Letters* **2001**, *78* (23), 3711-3713.
56. Becer, C. R.; Hoogenboom, R.; Schubert, U. S., Click Chemistry beyond Metal-Catalyzed Cycloaddition. *Angewandte Chemie-International Edition* **2009**, *48* (27), 4900-4908.

57. (a) Tornøe, C. W.; Christensen, C.; Meldal, M., Peptidotriazoles on Solid Phase: [1,2,3]-Triazoles by Regiospecific Copper(I)-Catalyzed 1,3-Dipolar Cycloadditions of Terminal Alkynes to Azides. *The Journal of Organic Chemistry* **2002**, 67 (9), 3057-3064; (b) Rostovtsev, V. V.; Green, L. G.; Fokin, V. V.; Sharpless, K. B., A Stepwise Huisgen Cycloaddition Process: Copper(I)-Catalyzed Regioselective “Ligation” of Azides and Terminal Alkynes. *Angewandte Chemie* **2002**, 114 (14), 2708-2711.
58. Posner, T., Beiträge zur Kenntniss der ungesättigten Verbindungen. II. Ueber die Addition von Mercaptanen an ungesättigte Kohlenwasserstoffe. *Berichte der deutschen chemischen Gesellschaft* **1905**, 38 (1), 646-657.
59. Kolb, H. C.; Finn, M. G.; Sharpless, K. B., Click chemistry: Diverse chemical function from a few good reactions. *Angewandte Chemie-International Edition* **2001**, 40 (11), 2004-+.
60. Chan, T. R.; Hilgraf, R.; Sharpless, K. B.; Fokin, V. V., Polytriazoles as Copper(I)-Stabilizing Ligands in Catalysis. *Organic Letters* **2004**, 6 (17), 2853-2855.
61. (a) Zhang, T.; Zheng, Z.; Ding, X.; Peng, Y., Smart Surface of Gold Nanoparticles Fabricated by Combination of RAFT and Click Chemistry. *Macromolecular Rapid Communications* **2008**, 29 (21), 1716-1720; (b) Voliani, V.; Ricci, F.; Signore, G.; Nifosi, R.; Luin, S.; Beltram, F., Multiphoton Molecular Photorelease in Click-Chemistry-Functionalized Gold Nanoparticles. *Small* **2011**, 7 (23), 3271-3275.
62. (a) Cardiel, A. C.; Benson, M. C.; Bishop, L. M.; Louis, K. M.; Yeager, J. C.; Tan, Y.; Hamers, R. J., Chemically Directed Assembly of Photoactive Metal Oxide Nanoparticle Heterojunctions via the Copper-Catalyzed Azide–Alkyne Cycloaddition “Click” Reaction. *Acs Nano* **2011**, 6 (1), 310-318; (b) Hu, J.; Qian, Y.; Wang, X.; Liu, T.; Liu, S., Drug-Loaded and Superparamagnetic Iron Oxide Nanoparticle Surface-Embedded Amphiphilic Block Copolymer Micelles for Integrated Chemotherapeutic Drug Delivery and MR Imaging. *Langmuir* **2011**, 28 (4), 2073-2082.
63. Moitra, N.; Trens, P.; Raehm, L.; Durand, J.-O.; Cattoen, X.; Chi Man, M. W., Facile route to functionalized mesoporous silica nanoparticles by click chemistry. *Journal of Materials Chemistry* **2011**, 21 (35), 13476-13482.
64. (a) Huang, K.; Duclairoir, F.; Pro, T.; Buckley, J.; Marchand, G.; Martinez, E.; Marchon, J.-C.; De Salvo, B.; Delapierre, G.; Vinet, F., Ferrocene and Porphyrin Monolayers on Si(100) Surfaces: Preparation and Effect of Linker Length on Electron

Transfer. *ChemPhysChem* **2009**, *10* (6), 963-971; (b) Devaraj, N. K.; Collman, J. P., Copper Catalyzed Azide-Alkyne Cycloadditions on Solid Surfaces: Applications and Future Directions. *QSAR & Combinatorial Science* **2007**, *26* (11-12), 1253-1260.

65. Belomoin, G.; Therrien, J.; Smith, A.; Rao, S.; Twesten, R.; Chaieb, S.; Nayfeh, M. H.; Wagner, L.; Mitas, L., Observation of a magic discrete family of ultrabright Si nanoparticles. *Applied Physics Letters* **2002**, *80* (5), 841-843.

66. Yerci, S.; Doğan, I.; Seyhan, A.; Gencer, A.; Turan, R., Characterization of Si Nanocrystals. In *Silicon Nanocrystals*, Wiley-VCH Verlag GmbH & Co. KGaA: 2010; pp 583-611.

67. Geisse, N. A., AFM and combined optical techniques. *Materials Today* **2009**, *12* (7-8), 40-45.

68. Mayandi, J.; Finstad, T. G.; Foss, S.; Thøgersen, A.; Serincan, U.; Turan, R., Luminescence from silicon nanoparticles in SiO₂: atomic force microscopy and transmission electron microscopy studies. *Physica Scripta* **2006**, *T126*, 77-80.

69. Zejing Xu, Y. L., Boyu Zhang, Tapas Purkait, Alina Alb,2; Brian S. Mitchell, S. M. G., Mark J. Fink, Water Soluble PEGylated Silicon Nanoparticles and Their Assembly into Swellable Nanoparticle Arrays. **In Preparation**.

70. Berne, B. J.; Pecora, R., *Dynamic Light Scattering: With Applications to Chemistry, Biology, and Physics*. Dover Publications: 2000.

71. Lu, F.; Doane, T. L.; Zhu, J.-J.; Burda, C., A method for separating PEGylated Au nanoparticle ensembles as a function of grafting density and core size. *Chemical Communications* **2014**, *50* (6), 642-644.

72. Tang, Z.; Xu, B.; Wu, B.; Germann, M. W.; Wang, G., Synthesis and Structural Determination of Multidentate 2,3-Dithiol-Stabilized Au Clusters. *Journal of the American Chemical Society* **2010**, *132* (10), 3367-3374.

73. Canzi, G.; Mrse, A. A.; Kubiak, C. P., Diffusion-Ordered NMR Spectroscopy as a Reliable Alternative to TEM for Determining the Size of Gold Nanoparticles in Organic Solutions. *The Journal of Physical Chemistry C* **2011**, *115* (16), 7972-7978.

74. Salorinne, K.; Lahtinen, T.; Koivisto, J.; Kalenius, E.; Nissinen, M.; Pettersson, M.; Häkkinen, H., Nondestructive Size Determination of Thiol-Stabilized Gold Nanoclusters in Solution by Diffusion Ordered NMR Spectroscopy. *Analytical Chemistry* **2013**, 85 (7), 3489-3492.
75. Nayfeh, M.; E. Rogozhina; Mitas, L., Silicon Nanoparticles: Next Generation of Ultrasensitive Fluorescent Markers. In *Synthesis, Functionalization and Surface Treatment of Nanoparticles*, Baraton, M.-I., Ed. American Scientific Publishers: Stevenson Ranch, 2003; Vol. 10.
76. Schuppler, S.; Friedman, S. L.; Marcus, M. A.; Adler, D. L.; Xie, Y. H.; Ross, F. M.; Chabal, Y. J.; Harris, T. D.; Brus, L. E.; Brown, W. L.; Chaban, E. E.; Szajowski, P. F.; Christman, S. B.; Citrin, P. H., Size, shape, and composition of luminescent species in oxidized Si nanocrystals and H-passivated porous Si. *Physical Review B* **1995**, 52 (7), 4910-4925.
77. (a) Kirchner, C.; Liedl, T.; Kudera, S.; Pellegrino, T.; Muñoz Javier, A.; Gaub, H. E.; Stölzle, S.; Fertig, N.; Parak, W. J., Cytotoxicity of Colloidal CdSe and CdSe/ZnS Nanoparticles. *Nano Letters* **2004**, 5 (2), 331-338; (b) Mayne, A. H.; Bayliss, S. C.; Barr, P.; Tobin, M.; Buckberry, L. D., Biologically Interfaced Porous Silicon Devices. *physica status solidi (a)* **2000**, 182 (1), 505-513; (c) Nilsson, J. R., How cytotoxic is zinc? A study on effects of zinc on cell proliferation, endocytosis, and fine structure of the ciliate Tetrahymena. *Acta Protozoologica* **2003**, 42 (1), 19-29; (d) Zhang, Y.; Chen, W.; Zhang, J.; Liu, J.; Chen, G.; Pope, C., In Vitro and In Vivo Toxicity of CdTe Nanoparticles. *Journal of Nanoscience and Nanotechnology* **2007**, 7 (2), 497-503.
78. Liu, C.-Y.; Holman, Z. C.; Kortshagen, U. R., Hybrid Solar Cells from P3HT and Silicon Nanocrystals. *Nano Letters* **2008**, 9 (1), 449-452.
79. van Buuren, T.; Dinh, L. N.; Chase, L. L.; Siekhaus, W. J.; Terminello, L. J., Changes in the Electronic Properties of Si Nanocrystals as a Function of Particle Size. *Physical Review Letters* **1998**, 80 (17), 3803-3806.
80. Gowrishankar, V.; Scully, S. R.; McGehee, M. D.; Wang, Q.; Branz, H. M., Exciton splitting and carrier transport across the amorphous-silicon/polymer solar cell interface. *Applied Physics Letters* **2006**, 89 (25), 252102.

81. Adikaari, A. A. D. T.; Dissanayake, D. M. N. M.; Hatton, R. A.; Silva, S. R. P., Efficient laser textured nanocrystalline silicon-polymer bilayer solar cells. *Applied Physics Letters* **2007**, *90* (20), 203514.
82. Liu, C.-Y.; Holman, Z. C.; Kortshagen, U. R., Optimization of Si NC/P3HT Hybrid Solar Cells. *Advanced Functional Materials* **2010**, *20* (13), 2157-2164.
83. (a) Boyraz, O.; Jalali, B., Demonstration of directly modulated silicon Raman laser. *Opt. Express* **2005**, *13* (3), 796-800; (b) Kortshagen, U.; Anthony, R.; Gresback, R.; Holman, Z.; Ligman, R.; Liu, C. Y.; Mangolini, L.; Campbell, S. A., Plasma synthesis of group IV quantum dots for luminescence and photovoltaic applications. *Pure and Applied Chemistry* **2008**, *80* (9), 1901-1908; (c) Larson, D. R.; Zipfel, W. R.; Williams, R. M.; Clark, S. W.; Bruchez, M. P.; Wise, F. W.; Webb, W. W., Water-Soluble Quantum Dots for Multiphoton Fluorescence Imaging in Vivo. *Science* **2003**, *300* (5624), 1434-1436; (d) Pillai, S.; Catchpole, K. R.; Trupke, T.; Zhang, G.; Zhao, J.; Green, M. A., Enhanced emission from Si-based light-emitting diodes using surface plasmons. *Applied Physics Letters* **2006**, *88* (16); (e) Raniero, L.; Zhang, S.; Águas, H.; Ferreira, I.; Igreja, R.; Fortunato, E.; Martins, R., Role of buffer layer on the performances of amorphous silicon solar cells with incorporated nanoparticles produced by plasma enhanced chemical vapor deposition at 27.12 MHz. *Thin Solid Films* **2005**, *487* (1-2), 170-173; (f) Wang, L.; Reipa, V.; Blasic, J., Silicon Nanoparticles as a Luminescent Label to DNA. *Bioconjugate Chemistry* **2004**, *15* (2), 409-412.
84. Fujioka, K.; Hiruoka, M.; Sato, K.; Manabe, N.; Miyasaka, R.; Hanada, S.; Hoshino, A.; Tilley, R. D.; Manome, Y.; Hirakuri, K.; Yamamoto, K., Luminescent passive-oxidized silicon quantum dots as biological staining labels and their cytotoxicity effects at high concentration. *Nanotechnology* **2008**, *19* (41), 415102.
85. Alsharif, N. H.; Berger, C. E. M.; Varanasi, S. S.; Chao, Y.; Horrocks, B. R.; Datta, H. K., Alkyl-Capped Silicon Nanocrystals Lack Cytotoxicity and have Enhanced Intracellular Accumulation in Malignant Cells via Cholesterol-Dependent Endocytosis. *Small* **2009**, *5* (2), 221-228.
86. Tedrick, K.; Trischuk, T.; Lehner, R.; Eitzen, G., Enhanced Membrane Fusion in Sterol-enriched Vacuoles Bypasses the Vrp1p Requirement. *Molecular Biology of the Cell* **2004**, *15* (10), 4609-4621.

87. Bhattacharjee, S.; Rietjens, I. M. C. M.; Singh, M. P.; Atkins, T. M.; Purkait, T. K.; Xu, Z.; Regli, S.; Shukaliak, A.; Clark, R. J.; Mitchell, B. S.; Alink, G. M.; Marcelis, A. T. M.; Fink, M. J.; Veinot, J. G. C.; Kauzlarich, S. M.; Zuilhof, H., Cytotoxicity of surface-functionalized silicon and germanium nanoparticles: the dominant role of surface charges. *Nanoscale* **2013**, *5* (11), 4870-4883.
88. (a) Fernandez-Rosas, E.; Gomez, R.; Ibanez, E.; Barrios, L.; Duch, M.; Esteve, J.; Nogues, C.; Plaza, J. A., Intracellular polysilicon barcodes for cell tracking. *Small* **2009**, *5* (21), 2433-9; (b) Gómez-Martínez, R.; Vázquez, P.; Duch, M.; Muriano, A.; Pinacho, D.; Sanvicens, N.; Sánchez-Baeza, F.; Boya, P.; de la Rosa, E. J.; Esteve, J.; Suárez, T.; Plaza, J. A., Intracellular Silicon Chips in Living Cells. *Small* **2010**, *6* (4), 499-502; (c) Kim, D.-H.; Kim, Y.-S.; Amsden, J.; Panilaitis, B.; Kaplan, D. L.; Omenetto, F. G.; Zakin, M. R.; Rogers, J. A., Erratum: "Silicon electronics on silk as a path to bioresorbable, implantable devices" [Appl. Phys. Lett. 95, 133701 (2009)]. *Applied Physics Letters* **2009**, *95* (26), -.
89. Erogbogbo, F.; Yong, K.-T.; Roy, I.; Xu, G.; Prasad, P. N.; Swihart, M. T., Biocompatible Luminescent Silicon Quantum Dots for Imaging of Cancer Cells. *Acc Nano* **2008**, *2* (5), 873-878.
90. He, Y.; Su, Y.; Yang, X.; Kang, Z.; Xu, T.; Zhang, R.; Fan, C.; Lee, S.-T., Photo and pH Stable, Highly-Luminescent Silicon Nanospheres and Their Bioconjugates for Immunofluorescent Cell Imaging. *Journal of the American Chemical Society* **2009**, *131* (12), 4434-4438.
91. Park, J.-H.; Gu, L.; von Maltzahn, G.; Ruoslahti, E.; Bhatia, S. N.; Sailor, M. J., Biodegradable luminescent porous silicon nanoparticles for in vivo applications. *Nat Mater* **2009**, *8* (4), 331-336.
92. (a) Gao, X.; Cui, Y.; Levenson, R. M.; Chung, L. W. K.; Nie, S., In vivo cancer targeting and imaging with semiconductor quantum dots. *Nat Biotech* **2004**, *22* (8), 969-976; (b) Lee, J.-H.; Huh, Y.-M.; Jun, Y.-w.; Seo, J.-w.; Jang, J.-t.; Song, H.-T.; Kim, S.; Cho, E.-J.; Yoon, H.-G.; Suh, J.-S.; Cheon, J., Artificially engineered magnetic nanoparticles for ultra-sensitive molecular imaging. *Nat Med* **2007**, *13* (1), 95-99; (c) Liu, Z.; Davis, C.; Cai, W.; He, L.; Chen, X.; Dai, H., Circulation and long-term fate of functionalized, biocompatible single-walled carbon nanotubes in mice probed by Raman spectroscopy. *Proceedings of the National Academy of Sciences* **2008**, *105* (5), 1410-

1415; (d) Torchilin, V. P., Recent advances with liposomes as pharmaceutical carriers. *Nat Rev Drug Discov* **2005**, *4* (2), 145-160.

93. (a) Föll, H.; Christophersen, M.; Carstensen, J.; Hasse, G., Formation and application of porous silicon. *Materials Science and Engineering: R: Reports* **2002**, *39* (4), 93-141; (b) Haidary, S. M.; rcoles, E. P.; Ali, N. K., Nanoporous Silicon as Drug Delivery Systems for Cancer Therapies. *Journal of Nanomaterials* **2012**, *2012*, 15; (c) Osminkina, L. A.; Gongalsky, M. B.; Motuzuk, A. V.; Timoshenko, V. Y.; Kudryavtsev, A. A., Silicon nanocrystals as photo- and sono-sensitizers for biomedical applications. *Applied Physics B* **2011**, *105* (3), 665-668.

94. Vaccari, L.; Canton, D.; Zaffaroni, N.; Villa, R.; Tormen, M.; di Fabrizio, E., Porous silicon as drug carrier for controlled delivery of doxorubicin anticancer agent. *Microelectronic Engineering* **2006**, *83* (4–9), 1598-1601.

95. Kleps, I.; Ignat, T.; Miu, M.; Craciunoiu, F.; Trif, M.; Simion, M.; Bragaru, A.; Dinescu, A., Nanostructured Silicon Particles for Medical Applications. *Journal of Nanoscience and Nanotechnology* **2010**, *10* (4), 2694-2700.

96. Ashley, C. E.; Carnes, E. C.; Phillips, G. K.; Padilla, D.; Durfee, P. N.; Brown, P. A.; Hanna, T. N.; Liu, J.; Phillips, B.; Carter, M. B.; Carroll, N. J.; Jiang, X.; Dunphy, D. R.; Willman, C. L.; Petsev, D. N.; Evans, D. G.; Parikh, A. N.; Chackerian, B.; Wharton, W.; Peabody, D. S.; Brinker, C. J., The targeted delivery of multicomponent cargos to cancer cells by nanoporous particle-supported lipid bilayers. *Nat Mater* **2011**, *10* (5), 389-397.

97. (a) Bell, A. T., The Impact of Nanoscience on Heterogeneous Catalysis. *Science* **2003**, *299* (5613), 1688-1691; (b) Corma, A.; Serna, P., Chemoselective Hydrogenation of Nitro Compounds with Supported Gold Catalysts. *Science* **2006**, *313* (5785), 332-334; (c) Fujii, M., Chemical reaction mediated by excited states of Si nanocrystals—Singlet oxygen formation in solution. *Journal of Applied Physics* **2004**, *95* (7), 3689; (d) Fujii, M.; Kovalev, D.; Goller, B.; Minobe, S.; Hayashi, S.; Timoshenko, V., Time-resolved photoluminescence studies of the energy transfer from excitons confined in Si nanocrystals to oxygen molecules. *Physical Review B* **2005**, *72* (16); (e) Hughes, M. D.; Xu, Y.-J.; Jenkins, P.; McMorn, P.; Landon, P.; Enache, D. I.; Carley, A. F.; Attard, G. A.; Hutchings, G. J.; King, F.; Stitt, E. H.; Johnston, P.; Griffin, K.; Kiely, C. J., Tunable gold catalysts for selective hydrocarbon oxidation under mild conditions. *Nature* **2005**, *437* (7062), 1132-1135; (f) Kang, Z.; Liu, Y.; Lee, S.-T., Small-sized silicon

nanoparticles: new nanolights and nanocatalysts. *Nanoscale* **2011**, 3 (3), 777-791; (g) Kang, Z.; Tsang, C. H. A.; Wong, N.-B.; Zhang, Z.; Lee, S.-T., Silicon Quantum Dots: A General Photocatalyst for Reduction, Decomposition, and Selective Oxidation Reactions. *Journal of the American Chemical Society* **2007**, 129 (40), 12090-12091; (h) Turner, M.; Golovko, V. B.; Vaughan, O. P. H.; Abdulkin, P.; Berenguer-Murcia, A.; Tikhov, M. S.; Johnson, B. F. G.; Lambert, R. M., Selective oxidation with dioxygen by gold nanoparticle catalysts derived from 55-atom clusters. *Nature* **2008**, 454 (7207), 981-983; (i) Ye, H.; Titchenal, N.; Gogotsi, Y.; Ko, F., SiC Nanowires Synthesized from Electrospun Nanofiber Templates. *Advanced Materials* **2005**, 17 (12), 1531-1535.

98. (a) Li, J.; Dahn, J. R., An In Situ X-Ray Diffraction Study of the Reaction of Li with Crystalline Si. *Journal of The Electrochemical Society* **2007**, 154 (3), A156-A161; (b) Obrovac, M. N.; Christensen, L., Structural Changes in Silicon Anodes during Lithium Insertion/Extraction. *Electrochemical and Solid-State Letters* **2004**, 7 (5), A93-A96.

99. (a) Hu, Y.-S.; Demir-Cakan, R.; Titirici, M.-M.; Müller, J.-O.; Schlögl, R.; Antonietti, M.; Maier, J., Superior Storage Performance of a Si@SiO_x/C Nanocomposite as Anode Material for Lithium-Ion Batteries. *Angewandte Chemie International Edition* **2008**, 47 (9), 1645-1649; (b) Yu, Y.; Gu, L.; Zhu, C.; Tsukimoto, S.; van Aken, P. A.; Maier, J., Reversible Storage of Lithium in Silver-Coated Three-Dimensional Macroporous Silicon. *Advanced Materials* **2010**, 22 (20), 2247-2250.

100. (a) Martin, C.; Crosnier, O.; Retoux, R.; Bélanger, D.; Schleich, D. M.; Brousse, T., Chemical Coupling of Carbon Nanotubes and Silicon Nanoparticles for Improved Negative Electrode Performance in Lithium-Ion Batteries. *Advanced Functional Materials* **2011**, 21 (18), 3524-3530; (b) Zhou, X.; Yin, Y.-X.; Wan, L.-J.; Guo, Y.-G., Facile synthesis of silicon nanoparticles inserted into graphene sheets as improved anode materials for lithium-ion batteries. *Chemical Communications* **2012**, 48 (16), 2198-2200.

101. Ding, Z.; Quinn, B. M.; Haram, S. K.; Pell, L. E.; Korgel, B. A.; Bard, A. J., Electrochemistry and Electrogenenerated Chemiluminescence from Silicon Nanocrystal Quantum Dots. *Science* **2002**, 296 (5571), 1293-1297.

102. Hanessian, S.; Xie, F., Polymer-bound p-alkoxybenzyl trichloroacetimidates: Reagents for the protection of alcohols as benzyl ethers on solid-phase. *Tetrahedron Letters* **1998**, 39 (8), 733-736.

103. Wilcoxon, J. P.; Martin, J. E.; Provencio, P., Optical properties of gold and silver nanoclusters investigated by liquid chromatography. *The Journal of Chemical Physics* **2001**, *115* (2), 998-1008.
104. (a) Grabs, I.-M.; Bradtmöller, C.; Menzel, D.; Garnweitner, G., Formation Mechanisms of Iron Oxide Nanoparticles in Different Nonaqueous Media. *Crystal Growth & Design* **2012**, *12* (3), 1469-1475; (b) Saunders, A. E.; Sigman, M. B.; Korgel, B. A., Growth Kinetics and Metastability of Monodisperse Tetraoctylammonium Bromide Capped Gold Nanocrystals. *The Journal of Physical Chemistry B* **2003**, *108* (1), 193-199.
105. (a) Jayanth, T. T.; Jeganmohan, M.; Cheng, M.-J.; Chu, S.-Y.; Cheng, C.-H., Ene Reaction of Arynes with Alkynes. *Journal of the American Chemical Society* **2006**, *128* (7), 2232-2233; (b) Altable, M.; Filippone, S.; Martín-Domenech, A.; Güell, M.; Solà, M.; Martín, N., Intramolecular Ene Reaction of 1,6-Fullerenynes: A New Synthesis of Allenes. *Organic Letters* **2006**, *8* (26), 5959-5962.
106. (a) Canaria, C. A.; Lees, I. N.; Wun, A. W.; Miskelly, G. M.; Sailor, M. J., Characterization of the carbon–silicon stretch in methylated porous silicon—observation of an anomalous isotope shift in the FTIR spectrum. *Inorganic Chemistry Communications* **2002**, *5* (8), 560-564; (b) Mawhinney, D. B.; Glass, J. A.; Yates, J. T., FTIR Study of the Oxidation of Porous Silicon. *The Journal of Physical Chemistry B* **1997**, *101* (7), 1202-1206; (c) Jung, D. H.; Cho, S. Y.; Peck, D. H.; Shin, D. R.; Kim, J. S., Performance evaluation of a Nafion/silicon oxide hybrid membrane for direct methanol fuel cell. *Journal of Power Sources* **2002**, *106* (1–2), 173-177.
107. Thiel, P. A.; Madey, T. E., The interaction of water with solid surfaces: Fundamental aspects. *Surface Science Reports* **1987**, *7* (6–8), 211-385.
108. (a) Verdoni, L. P.; Fink, M. J.; Mitchell, B. S., A fractionation process of mechanochemically synthesized blue-green luminescent alkyl-passivated silicon nanoparticles. *Chemical Engineering Journal* **2011**, *172* (1), 591-600; (b) Hallmann, S. Hydrophilic Functionalized silicon Nanoparticles Produced by High Energy Ball Milling. Tulane University, 2011.
109. Zhang, N.; Chu, X.; Fathalla, M.; Jayawickramarajah, J., Photonic DNA-Chromophore Nanowire Networks: Harnessing Multiple Supramolecular Assembly Modes. *Langmuir* **2013**, *29* (34), 10796-10806.

110. Reppe, W.; Vetter, H., Carbonylierung VI. Synthesen mit Metallcarbonylwasserstoffen. *Justus Liebigs Annalen der Chemie* **1953**, 582 (1), 133-161.
111. Dasog, M.; De los Reyes, G. B.; Titova, L. V.; Hegmann, F. A.; Veinot, J. G. C., Size vs Surface: Tuning the Photoluminescence of Freestanding Silicon Nanocrystals Across the Visible Spectrum via Surface Groups. *Acs Nano* **2014**, 8 (9), 9636-9648.
112. Morris, G. A., Diffusion-Ordered Spectroscopy. In *eMagRes*, John Wiley & Sons, Ltd: 2007.
113. Reichardt, C., *Solvent effects in organic chemistry*. Verlag Chemie: 1979.
114. Delpuech, J. J., *Dynamics of solutions and fluid mixtures by NMR*. Wiley: 1995.
115. (a) Bond, A. M.; Colton, R.; Harvey, J.; Hutton, R. S., Voltammetric studies of ferrocene and the mercury dithiophosphate system at mercury electrodes over a temperature range encompassing the mercury liquid-solid state transition. *Journal of Electroanalytical Chemistry* **1997**, 426 (1-2), 145-155; (b) Bond, A. M.; Henderson, T. L. E.; Mann, D. R.; Mann, T. F.; Thormann, W.; Zoski, C. G., A fast electron transfer rate for the oxidation of ferrocene in acetonitrile or dichloromethane at platinum disk ultramicroelectrodes. *Analytical Chemistry* **1988**, 60 (18), 1878-1882.
116. (a) Provencher, S. W., A constrained regularization method for inverting data represented by linear algebraic or integral equations. *Computer Physics Communications* **1982**, 27 (3), 213-227; (b) Provencher, S. W., CONTIN: A general purpose constrained regularization program for inverting noisy linear algebraic and integral equations. *Computer Physics Communications* **1982**, 27 (3), 229-242.
117. (a) Alivisatos, P., The use of nanocrystals in biological detection. *Nat Biotech* **2004**, 22 (1), 47-52; (b) Bruchez, M.; Moronne, M.; Gin, P.; Weiss, S.; Alivisatos, A. P., Semiconductor Nanocrystals as Fluorescent Biological Labels. *Science* **1998**, 281 (5385), 2013-2016; (c) Michalet, X.; Pinaud, F. F.; Bentolila, L. A.; Tsay, J. M.; Doose, S.; Li, J. J.; Sundaresan, G.; Wu, A. M.; Gambhir, S. S.; Weiss, S., Quantum Dots for Live Cells, in Vivo Imaging, and Diagnostics. *Science* **2005**, 307 (5709), 538-544; (d) Pinaud, F.; Michalet, X.; Bentolila, L. A.; Tsay, J. M.; Doose, S.; Li, J. J.; Iyer, G.; Weiss, S., Advances in fluorescence imaging with quantum dot bio-probes. *Biomaterials* **2006**, 27 (9), 1679-1687.

118. He, Y.; Kang, Z. H.; Li, Q. S.; Tsang, C. H. A.; Fan, C. H.; Lee, S. T., Ultrastable, Highly Fluorescent, and Water-Dispersed Silicon-Based Nanospheres as Cellular Probes. *Angewandte Chemie-International Edition* **2009**, 48 (1), 128-132.
119. Erogbogbo, F.; Yong, K. T.; Roy, I.; Hu, R.; Law, W. C.; Zhao, W. W.; Ding, H.; Wu, F.; Kumar, R.; Swihart, M. T.; Prasad, P. N., In Vivo Targeted Cancer Imaging, Sentinel Lymph Node Mapping and Multi-Channel Imaging with Biocompatible Silicon Nanocrystals. *Acs Nano* **2011**, 5 (1), 413-423.
120. Bhadra, D.; Bhadra, S.; Jain, P.; Jain, N. K., Pegnology: a review of PEG-ylated systems. *Pharmazie* **2002**, 57 (1), 5-29.
121. (a) Medina, S. H.; El-Sayed, M. E. H., Dendrimers as Carriers for Delivery of Chemotherapeutic Agents. *Chemical Reviews* **2009**, 109 (7), 3141-3157; (b) Middel, O.; Verboom, W.; Reinhoudt, David N., Water-Soluble Cavitands – Synthesis, Solubilities and Binding Properties. *European Journal of Organic Chemistry* **2002**, 2002 (15), 2587-2597; (c) Tekade, R. K.; Kumar, P. V.; Jain, N. K., Dendrimers in Oncology: An Expanding Horizon. *Chemical Reviews* **2009**, 109 (1), 49-87.
122. (a) Gabizon, A.; Goren, D.; Horowitz, A. T.; Tzemach, D.; Lossos, A.; Siegal, T., Long-circulating liposomes for drug delivery in cancer therapy: a review of biodistribution studies in tumor-bearing animals. *Advanced Drug Delivery Reviews* **1997**, 24 (2-3), 337-344; (b) Kataoka, K.; Harada, A.; Nagasaki, Y., Block copolymer micelles for drug delivery: design, characterization and biological significance. *Advanced Drug Delivery Reviews* **2001**, 47 (1), 113-131; (c) Veronese, F. M., Peptide and protein PEGylation: a review of problems and solutions. *Biomaterials* **2001**, 22 (5), 405-417.
123. (a) Bateman, J. E.; Eagling, R. D.; Worrall, D. R.; Horrocks, B. R.; Houlton, A., Alkylation of Porous Silicon by Direct Reaction with Alkenes and Alkynes. *Angewandte Chemie International Edition* **1998**, 37 (19), 2683-2685; (b) Hovis, J. S.; Liu, H.; Hamers, R. J., Cycloaddition Chemistry of 1,3-Dienes on the Silicon(001) Surface: Competition between [4 + 2] and [2 + 2] Reactions. *The Journal of Physical Chemistry B* **1998**, 102 (35), 6873-6879; (c) Yang, L.; Lua, Y.-Y.; Lee, M. V.; Linford, M. R., Chemomechanical Functionalization and Patterning of Silicon. *Accounts of Chemical Research* **2005**, 38 (12), 933-942; (d) Yang, L.; Lua, Y.-Y.; Tan, M.; Scherman, O. A.; Grubbs, R. H.; Harb, J. N.; Davis, R. C.; Linford, M. R., Chemistry of Olefin-Terminated Homogeneous and Mixed Monolayers on Scribed Silicon. *Chemistry of Materials* **2007**, 19 (7), 1671-1678.

124. Worrell, B. T.; Malik, J. A.; Fokin, V. V., Direct evidence of a dinuclear copper intermediate in Cu(I)-catalyzed azide-alkyne cycloadditions. *Science* **2013**, *340* (6131), 457-60.
125. Özdemir, C.; Güner, A., Solubility profiles of poly(ethylene glycol)/solvent systems, I: Qualitative comparison of solubility parameter approaches. *European Polymer Journal* **2007**, *43* (7), 3068-3093.
126. Ross-Murphy, S. B., Dynamic Light Scattering. B. J. Berne and R. Pecora, John Wiley, New York, 1976, pp. 376. Price £16.50. *British Polymer Journal* **1977**, *9* (2), 177-177.
127. Koppel, D. E., Analysis of Macromolecular Polydispersity in Intensity Correlation Spectroscopy: The Method of Cumulants. *The Journal of Chemical Physics* **1972**, *57* (11), 4814-4820.
128. (a) Balasingam, S. K.; Lee, M.; Kang, M. G.; Jun, Y., Improvement of dye-sensitized solar cells toward the broader light harvesting of the solar spectrum. *Chemical Communications* **2013**, *49* (15), 1471-1487; (b) Tetreault, N.; Gratzel, M., Novel nanostructures for next generation dye-sensitized solar cells. *Energy & Environmental Science* **2012**, *5* (9), 8506-8516; (c) Zhang, Q.; Cao, G., Nanostructured photoelectrodes for dye-sensitized solar cells. *Nano Today* **2011**, *6* (1), 91-109.
129. Scholes, G. D.; Fleming, G. R.; Olaya-Castro, A.; van Grondelle, R., Lessons from nature about solar light harvesting. *Nat Chem* **2011**, *3* (10), 763-774.
130. Scholes, G. D.; Mirkovic, T.; Turner, D. B.; Fassioli, F.; Buchleitner, A., Solar light harvesting by energy transfer: from ecology to coherence. *Energy & Environmental Science* **2012**, *5* (11), 9374-9393.
131. (a) Kang, S.; Yasuda, M.; Miyasaka, H.; Hayashi, H.; Kawasaki, M.; Umeyama, T.; Matano, Y.; Yoshida, K.; Isoda, S.; Imahori, H., Light Harvesting and Energy Transfer in Multiporphyrin-Modified CdSe Nanoparticles. *ChemSusChem* **2008**, *1* (3), 254-261; (b) Li, L.-L.; Diau, E. W.-G., Porphyrin-sensitized solar cells. *Chemical Society Reviews* **2013**, *42* (1), 291-304.
132. (a) Dennler, G.; Scharber, M. C.; Brabec, C. J., Polymer-Fullerene Bulk-Heterojunction Solar Cells. *Advanced Materials* **2009**, *21* (13), 1323-1338; (b) Kotiaho, A.; Lahtinen, R.; Lehtivuori, H.; Tkachenko, N. V.; Lemmetyinen, H., Photoinduced

energy and charge transfer in layered porphyrin-gold nanoparticle thin films. *Journal of Physical Chemistry C* **2008**, *112* (27), 10316-10322; (c) Mandal, S.; Bhattacharyya, S.; Borovkov, V.; Patra, A., Porphyrin-Based Functional Nanoparticles: Conformational and Photophysical Properties of Bis-Porphyrin and Bis-Porphyrin Encapsulated Polymer Nanoparticles. *The Journal of Physical Chemistry C* **2011**, *115* (49), 24029-24036.

133. (a) Hasobe, T.; Imahori, H.; Kamat, P. V.; Ahn, T. K.; Kim, S. K.; Kim, D.; Fujimoto, A.; Hirakawa, T.; Fukuzumi, S., Photovoltaic Cells Using Composite Nanoclusters of Porphyrins and Fullerenes with Gold Nanoparticles. *Journal of the American Chemical Society* **2004**, *127* (4), 1216-1228; (b) Imahori, H.; Fujimoto, A.; Kang, S.; Hotta, H.; Yoshida, K.; Umeyama, T.; Matano, Y.; Isoda, S.; Isosomppi, M.; Tkachenko, N. V.; Lemmetyinen, H., Host-Guest Interactions in the Supramolecular Incorporation of Fullerenes into Tailored Holes on Porphyrin-Modified Gold Nanoparticles in Molecular Photovoltaics. *Chemistry – A European Journal* **2005**, *11* (24), 7265-7275; (c) Imahori, H.; Mitamura, K.; Shibano, Y.; Umeyama, T.; Matano, Y.; Yoshida, K.; Isoda, S.; Araki, Y.; Ito, O., A Photoelectrochemical Device with a Nanostructured SnO₂ Electrode Modified with Composite Clusters of Porphyrin-Modified Silica Nanoparticle and Fullerene. *The Journal of Physical Chemistry B* **2006**, *110* (23), 11399-11405.

134. (a) Imahori, H.; Fujimoto, A.; Kang, S.; Hotta, H.; Yoshida, K.; Umeyama, T.; Matano, Y.; Isoda, S., Structure and photoelectrochemical properties of nanostructured SnO₂ electrodes deposited electrophoretically with the composite clusters of porphyrin-modified gold nanoparticle with a long spacer and fullerene. *Tetrahedron* **2006**, *62* (9), 1955-1966; (b) Imahori, H.; Mitamura, K.; Umeyama, T.; Hosomizu, K.; Matano, Y.; Yoshida, K.; Isoda, S., Efficient photocurrent generation by SnO₂ electrode modified electrophoretically with composite clusters of porphyrin-modified silica microparticle and fullerene. *Chemical Communications* **2006**, *0* (4), 406-408.

135. (a) Liu, N.; Chen, H.-Z.; Chen, F.; Wang, M., Förster resonance energy transfer from poly(9-vinyl carbazole) to silicon nanoparticles in their composite films. *Chemical Physics Letters* **2008**, *451* (1-3), 70-74; (b) Staffilani, M.; Hoss, E.; Giesen, U.; Schneider, E.; Hartl, F.; Josel, H. P.; De Cola, L., Multimetallic ruthenium(II) complexes as electrochemiluminescent labels. *Inorganic chemistry* **2003**, *42* (24), 7789-98.

136. Marsh, D.; Mink, L., Microscale Synthesis and Electronic Absorption Spectroscopy of Tetraphenylporphyrin H₂(TPP) and Metalloporphyrins ZnII(TPP) and NiII(TPP). *Journal of Chemical Education* **1996**, *73* (12), 1188.

137. Clegg, R. M., Chapter 1 Förster resonance energy transfer—FRET what is it, why do it, and how it's done. In *Laboratory Techniques in Biochemistry and Molecular Biology*, Gadella, T. W. J., Ed. Elsevier: 2009; Vol. Volume 33, pp 1-57.
138. Lee, K. C. B.; Siegel, J.; Webb, S. E. D.; Lévêque-Fort, S.; Cole, M. J.; Jones, R.; Dowling, K.; Lever, M. J.; French, P. M. W., Application of the Stretched Exponential Function to Fluorescence Lifetime Imaging. *Biophys J* **2001**, *81* (3), 1265-1274.
139. Lakowicz, J. R., *Principles of Fluorescence Spectroscopy*, 3rd. Springer: New York, 2006.
140. Rosso-Vasic, M.; De Cola, L.; Zuilhof, H., Efficient Energy Transfer between Silicon Nanoparticles and a Ru–Polypyridine Complex. *The Journal of Physical Chemistry C* **2009**, *113* (6), 2235-2240.
141. Lakowicz, J. R., *Principles of Fluorescence Spectroscopy*. Springer: 2007.
142. Forster, T., 10th Spiers Memorial Lecture. Transfer mechanisms of electronic excitation. *Discussions of the Faraday Society* **1959**, *27* (0), 7-17.
143. Dexter, D. L., A Theory of Sensitized Luminescence in Solids. *The Journal of Chemical Physics* **1953**, *21* (5), 836-850.
144. Harris, D. C., *Quantitative Chemical Analysis*. W. H. Freeman: 2010.
145. Periasamy, A.; Day, R., *Molecular Imaging: FRET Microscopy and Spectroscopy*. Elsevier Science: 2011.
146. Sundström, V., Photosynthetic Light Harvesting, Charge Separation, and Photoprotection: The Primary Steps. In *Photobiology*, Björn, L., Ed. Springer New York: 2008; pp 289-319.
147. Fathalla, M.; Jayawickramarajah, J., Configurational Isomers of a Stilbene-Linked Bis(porphyrin) Tweezer: Synthesis and Fullerene-Binding Studies. *European Journal of Organic Chemistry* **2009**, *2009* (35), 6095-6099.
148. Hosseini, A.; Taylor, S.; Accorsi, G.; Armaroli, N.; Reed, C. A.; Boyd, P. D. W., Calix[4]arene-Linked Bisporphyrin Hosts for Fullerenes: Binding Strength, Solvation

Effects, and Porphyrin–Fullerene Charge Transfer Bands. *Journal of the American Chemical Society* **2006**, *128* (49), 15903-15913.

149. Hasobe, T.; Sandanayaka, A. S. D.; Wada, T.; Araki, Y., Fullerene-encapsulated porphyrin hexagonal nanorods. An anisotropic donor-acceptor composite for efficient photoinduced electron transfer and light energy conversion. *Chemical Communications* **2008**, *0* (29), 3372-3374.

150. Connors, K. A., *Binding Constants: The measurement of Molecular Complex Stability*. John Wiley & Sons: New York, 1987.

151. Guldi, D. M.; Ros, T. D.; Braiucă, P.; Prato, M.; Alessio, E., C₆₀ in the box. A supramolecular C₆₀-porphyrin assembly. *Journal of Materials Chemistry* **2002**, *12* (7), 2001-2008.

152. Ayabe, M.; Ikeda, A.; Shinkai, S.; Sakamoto, S.; Yamaguchi, K., A novel [60]fullerene receptor with a Pd(ii)-switched bisporphyrin cleft. *Chemical Communications* **2002**, (10), 1032-1033.

153. Dudic, M.; Lhotak, P.; Stibor, I.; Petrickova, H.; Lang, K., (Thia)calix[4]arene-porphyrin conjugates: novel receptors for fullerene complexation with C₇₀ over C₆₀ selectivity. *New Journal of Chemistry* **2004**, *28* (1), 85-90.

154. Tkachenko, N. V.; Lemmetyinen, H.; Sonoda, J.; Ohkubo, K.; Sato, T.; Imahori, H.; Fukuzumi, S., Ultrafast Photodynamics of Exciplex Formation and Photoinduced Electron Transfer in Porphyrin–Fullerene Dyads Linked at Close Proximity. *The Journal of Physical Chemistry A* **2003**, *107* (42), 8834-8844.

155. Wang, F.; Tang, J.; Liu, J.; Wang, Y.; Wang, R.; Niu, L.; Huang, L.; Huang, Z., Synthesis and photoinduced electron transfer characteristic of a bis (zinc porphyrin)-perylene bisimide array. *Journal of Physical Organic Chemistry* **2011**, *24* (11), 1101-1109.

156. Lee, K. C. B.; Siegel, J.; Webb, S. E. D.; Leveque-Fort, S.; Cole, M. J.; Jones, R.; Dowling, K.; Lever, M. J.; French, P. M. W., Application of the stretched exponential function to fluorescence lifetime imaging. *Biophys J* **2001**, *81* (3), 1265-1274.

157. Pettigrew, K. A. Solution Synthesis and Characterization of Silicon and Silicon/Germanium Nanoparticles. Bachelor of Science, California State University, Sacramento, 2004.
158. (a) Castano, A. P.; Mroz, P.; Hamblin, M. R., Photodynamic therapy and anti-tumour immunity. *Nature reviews. Cancer* **2006**, 6 (7), 535-45; (b) Brown, S. B.; Brown, E. A.; Walker, I., The present and future role of photodynamic therapy in cancer treatment. *The Lancet Oncology* **2004**, 5 (8), 497-508; (c) Sharman, W. M.; Allen, C. M.; van Lier, J. E., Photodynamic therapeutics: basic principles and clinical applications. *Drug Discovery Today* **1999**, 4 (11), 507-517; (d) Dougherty, T. J.; Gomer, C. J.; Henderson, B. W.; Jori, G.; Kessel, D.; Korbely, M.; Moan, J.; Peng, Q., Photodynamic Therapy. *Journal of the National Cancer Institute* **1998**, 90 (12), 889-905.
159. Nann, T., Nanoparticles in Photodynamic Therapy. *Nano Biomedicine and Engineering* **2011**, 3 (2).
160. (a) Bonnett, R., Photosensitizers of the porphyrin and phthalocyanine series for photodynamic therapy. *Chemical Society Reviews* **1995**, 24 (1), 19-33; (b) Ethirajan, M.; Chen, Y.; Joshi, P.; Pandey, R. K., The role of porphyrin chemistry in tumor imaging and photodynamic therapy. *Chemical Society Reviews* **2011**, 40 (1), 340-362; (c) Allison, R. R.; Sibata, C. H., Oncologic photodynamic therapy photosensitizers: A clinical review. *Photodiagnosis and Photodynamic Therapy* **2010**, 7 (2), 61-75.
161. (a) Secret, E.; Maynadier, M.; Gallud, A.; Gary-Bobo, M.; Chaix, A.; Belamie, E.; Maillard, P.; Sailor, M. J.; Garcia, M.; Durand, J.-O.; Cunin, F., Anionic porphyrin-grafted porous silicon nanoparticles for photodynamic therapy. *Chemical Communications* **2013**, 49 (39), 4202-4204; (b) Lilletvedt, M.; Tønnesen, H. H.; Høgset, A.; Sande, S. A.; Kristensen, S., Evaluation of physicochemical properties and aggregation of the photosensitizers TPCS_{2a} and TPPS_{2a} in aqueous media. *Die Pharmazie - An International Journal of Pharmaceutical Sciences* **2011**, 66 (5), 325-333.
162. (a) Yan, F.; Kopelman, R., The Embedding of Meta-tetra(Hydroxyphenyl)-Chlorin into Silica Nanoparticle Platforms for Photodynamic Therapy and Their Singlet Oxygen Production and pH-dependent Optical Properties¶. *Photochemistry and Photobiology* **2003**, 78 (6), 587-591; (b) Zhao, B.; Yin, J. J.; Bilski, P. J.; Chignell, C. F.; Roberts, J. E.; He, Y. Y., Enhanced photodynamic efficacy towards melanoma cells by encapsulation of Pc4 in silica nanoparticles. *Toxicology and applied pharmacology* **2009**,

241 (2), 163-172; (c) Kim, S.; Ohulchanskyy, T. Y.; Bharali, D.; Chen, Y.; Pandey, R. K.; Prasad, P. N., Organically Modified Silica Nanoparticles with Intraparticle Heavy-Atom Effect on the Encapsulated Photosensitizer for Enhanced Efficacy of Photodynamic Therapy. *The Journal of Physical Chemistry C* **2009**, *113* (29), 12641-12644; (d) Brevet, D.; Gary-Bobo, M.; Raehm, L.; Richeter, S.; Hocine, O.; Amro, K.; Loock, B.; Couleaud, P.; Frochot, C.; Morere, A.; Maillard, P.; Garcia, M.; Durand, J.-O., Mannose-targeted mesoporous silica nanoparticles for photodynamic therapy. *Chemical Communications* **2009**, (12), 1475-1477.

163. (a) Shi, L.; Hernandez, B.; Selke, M., Singlet Oxygen Generation from Water-Soluble Quantum Dot–Organic Dye Nanocomposites. *Journal of the American Chemical Society* **2006**, *128* (19), 6278-6279; (b) Tsay, J. M.; Trzoss, M.; Shi, L.; Kong, X.; Selke, M.; Jung, M. E.; Weiss, S., Singlet Oxygen Production by Peptide-Coated Quantum Dot–Photosensitizer Conjugates. *Journal of the American Chemical Society* **2007**, *129* (21), 6865-6871; (c) Narband, N.; Mubarak, M.; Ready, D.; Parkin, I. P.; Nair, S. P.; Green, M. A.; Beeby, A.; Wilson, M., Quantum dots as enhancers of the efficacy of bacterial lethal photosensitization. *Nanotechnology* **2008**, *19* (44), 445102; (d) Rakovich, A.; Savateeva, D.; Rakovich, T.; Donegan, J. F.; Rakovich, Y. P.; Kelly, V.; Lesnyak, V.; Eychmuller, A., CdTe Quantum Dot/Dye Hybrid System as Photosensitizer for Photodynamic Therapy. *Nanoscale research letters* **2010**, *5* (4), 753-60; (e) Duong, H. D.; Rhee, J. I., Singlet oxygen production by fluorescence resonance energy transfer (FRET) from green and orange CdSe/ZnS QDs to protoporphyrin IX (PpIX). *Chemical Physics Letters* **2011**, *501* (4–6), 496-501.

164. Kuruppuarachchi, M.; Savoie, H.; Lowry, A.; Alonso, C.; Boyle, R. W., Polyacrylamide Nanoparticles as a Delivery System in Photodynamic Therapy. *Molecular Pharmaceutics* **2011**, *8* (3), 920-931.

165. Bohn, P. W., Aspects of Structure and Energy Transport in Artificial Molecular Assemblies. *Annual Review of Physical Chemistry* **1993**, *44* (1), 37-60.

166. Maiti, N. C.; Mazumdar, S.; Periasamy, N., J- and H-Aggregates of Porphyrin–Surfactant Complexes: Time-Resolved Fluorescence and Other Spectroscopic Studies†. *The Journal of Physical Chemistry B* **1998**, *102* (9), 1528-1538.

167. (a) Czikkely, V.; Forsterling, H. D.; Kuhn, H., Extended dipole model for aggregates of dye molecules. *Chemical Physics Letters* **1970**, *6* (3), 207-210; (b) Nüesch, F.; Grätzel, M., H-aggregation and correlated absorption and emission of a merocyanine

dye in solution, at the surface and in the solid state. A link between crystal structure and photophysical properties. *Chemical Physics* **1995**, 193 (1–2), 1-17.

168. de Villiers, M. M.; Aramwit, P.; Kwon, G. S., *Nanotechnology in Drug Delivery*. Springer: 2008.

169. Baker, A.; Kanofsky, J. R., Direct observation of singlet oxygen phosphorescence at 1270 nm from L1210 leukemia cells exposed to polyporphyrin and light. *Archives of Biochemistry and Biophysics* **1991**, 286 (1), 70-75.

170. Su, Y.; He, Y.; Lu, H.; Sai, L.; Li, Q.; Li, W.; Wang, L.; Shen, P.; Huang, Q.; Fan, C., The cytotoxicity of cadmium based, aqueous phase – Synthesized, quantum dots and its modulation by surface coating. *Biomaterials* **2009**, 30 (1), 19-25.

171. Pawley, J., *Handbook of Biological Confocal Microscopy*. Springer: 2006.

172. (a) Buytaert, E.; Dewaele, M.; Agostinis, P., Molecular effectors of multiple cell death pathways initiated by photodynamic therapy. *Biochimica et Biophysica Acta (BBA) - Reviews on Cancer* **2007**, 1776 (1), 86-107; (b) Castano, A. P.; Demidova, T. N.; Hamblin, M. R., Mechanisms in photodynamic therapy: part one—photosensitizers, photochemistry and cellular localization. *Photodiagnosis and Photodynamic Therapy* **2004**, 1 (4), 279-293; (c) Tian, J.; Ding, L.; Xu, H.-J.; Shen, Z.; Ju, H.; Jia, L.; Bao, L.; Yu, J.-S., Cell-Specific and pH-Activatable Rubyrin-Loaded Nanoparticles for Highly Selective Near-Infrared Photodynamic Therapy against Cancer. *Journal of the American Chemical Society* **2013**, 135 (50), 18850-18858; (d) Lam, M.; Oleinick, N. L.; Nieminen, A.-L., Photodynamic Therapy-induced Apoptosis in Epidermoid Carcinoma Cells: REACTIVE OXYGEN SPECIES AND MITOCHONDRIAL INNER MEMBRANE PERMEABILIZATION. *Journal of Biological Chemistry* **2001**, 276 (50), 47379-47386.

173. Robert, A.; Miron, M. J.; Champagne, C.; Gingras, M. C.; Branton, P. E.; Lavoie, J. N., Distinct cell death pathways triggered by the adenovirus early region 4 ORF 4 protein. *The Journal of cell biology* **2002**, 158 (3), 519-28.

174. Berridge, M. V.; Herst, P. M.; Tan, A. S., Tetrazolium dyes as tools in cell biology: New insights into their cellular reduction. In *Biotechnology Annual Review*, El-Gewely, M. R., Ed. Elsevier: 2005; Vol. Volume 11, pp 127-152.

175. Mosmann, T., Rapid colorimetric assay for cellular growth and survival: Application to proliferation and cytotoxicity assays. *Journal of Immunological Methods* **1983**, 65 (1–2), 55–63.
176. Staudinger, H.; Meyer, J., Über neue organische Phosphorverbindungen III. Phosphinmethylderivate und Phosphinimine. *Helvetica Chimica Acta* **1919**, 2 (1), 635–646.
177. (a) Isenbügel, K.; Ritter, H.; Branscheid, R.; Kolb, U., Nanoparticle Vesicles Through Self Assembly of Cyclodextrin- and Adamantyl-Modified Silica. *Macromolecular Rapid Communications* **2010**, 31 (24), 2121–2126; (b) Mark, S. S.; Bergkvist, M.; Yang, X.; Teixeira, L. M.; Bhatnagar, P.; Angert, E. R.; Batt, C. A., Bionanofabrication of Metallic and Semiconductor Nanoparticle Arrays Using S-Layer Protein Lattices with Different Lateral Spacings and Geometries. *Langmuir* **2006**, 22 (8), 3763–3774; (c) Park, J. H.; Hwang, S.; Kwak, J., Nanosieving of Anions and Cavity-Size-Dependent Association of Cyclodextrins on a 1-Adamantanethiol Self-Assembled Monolayer. *Acs Nano* **2010**, 4 (7), 3949–3958; (d) López, C., Materials Aspects of Photonic Crystals. *Advanced Materials* **2003**, 15 (20), 1679–1704.
178. (a) Kamps, A. C.; Sanchez-Gaytan, B. L.; Hickey, R. J.; Clarke, N.; Fryd, M.; Park, S. J., Nanoparticle-Directed Self-Assembly of Amphiphilic Block Copolymers. *Langmuir* **2010**, 26 (17), 14345–14350; (b) Kretzschmar, I.; Reed, M. A., *Nanoparticle Arrays: Optical and Electronic Applications. In Dekker Encyclopedia of Nanoscience and Nanotechnology*. Second edition ed.; Taylor & Francis: 2009; p 2856–2867.
179. (a) Lodish, H., *Molecular Cell Biology*. W. H. Freeman: 2008; (b) Song, L. X.; Bai, L.; Xu, X. M.; He, J.; Pan, S. Z., Inclusion complexation, encapsulation interaction and inclusion number in cyclodextrin chemistry. *Coordination Chemistry Reviews* **2009**, 253 (9–10), 1276–1284; (c) Wan, P.; Xing, Y.; Chen, Y.; Chi, L.; Zhang, X., Host-guest chemistry at interface for photoswitchable bioelectrocatalysis. *Chemical Communications* **2011**, 47 (21), 5994–5996.
180. Del Valle, E. M. M., Cyclodextrins and their uses: a review. *Process Biochemistry* **2004**, 39 (9), 1033–1046.
181. (a) Hermkens, P. H. H.; Ottenheijm, H. C. J.; Rees, D., Solid-phase organic reactions: A review of the recent literature. *Tetrahedron* **1996**, 52 (13), 4527–4554; (b)

Hermkens, P. H. H.; Ottenheijm, H. C. J.; Rees, D. C., Solid-phase organic reactions II: A review of the literature Nov 95–Nov 96. *Tetrahedron* **1997**, 53 (16), 5643-5678.

182. (a) Liu, X.; Worden, J. G.; Dai, Q.; Zou, J.; Wang, J.; Huo, Q., Monofunctional Gold Nanoparticles Prepared via a Noncovalent-Interaction-Based Solid-Phase Modification Approach. *Small* **2006**, 2 (10), 1126-1129; (b) Huo, Q.; Worden, J., Monofunctional gold nanoparticles: synthesis and applications. *J Nanopart Res* **2007**, 9 (6), 1013-1025.

183. Kim, J. S.; Granström, M.; Friend, R. H.; Johansson, N.; Salaneck, W. R.; Daik, R.; Feast, W. J.; Cacialli, F., Indium–tin oxide treatments for single- and double-layer polymeric light-emitting diodes: The relation between the anode physical, chemical, and morphological properties and the device performance. *Journal of Applied Physics* **1998**, 84 (12), 6859-6870.

184. (a) Kofstad, P., *Nonstoichiometry, Diffusion, and Electrical Conductivity in Binary Metal Oxides*. R.E. Krieger Publishing Company: 1972; (b) Sørensen, O. T., *Nonstoichiometric oxides*. Academic Press: 1981; (c) Bak, T.; Nowotny, J.; Rekas, M.; Sorrell, C. C., Photo-electrochemical hydrogen generation from water using solar energy. Materials-related aspects. *International Journal of Hydrogen Energy* **2002**, 27 (10), 991-1022; (d) Nowotny, J.; Sorrell, C. C.; Bak, T.; Sheppard, L. R., Solar-hydrogen: Unresolved problems in solid-state science. *Solar Energy* **2005**, 78 (5), 593-602.

185. (a) Fujishima, A.; Hashimoto, K.; Watanabe, T., *TiO₂ Photocatalysis: Fundamentals and Applications*. BKC: 1999; (b) El Zayat, M. Y.; Saed, A. O.; El-Dessouki, M. S., Photoelectrochemical properties of dye sensitized Zr-doped SrTiO₃ electrodes. *International Journal of Hydrogen Energy* **1998**, 23 (4), 259-266; (c) Licht, S.; Wang, B.; Mukerji, S.; Soga, T.; Umeno, M.; Tributsch, H., Efficient Solar Water Splitting, Exemplified by RuO₂-Catalyzed AlGaAs/Si Photoelectrolysis. *The Journal of Physical Chemistry B* **2000**, 104 (38), 8920-8924; (d) Khaselev, O.; Bansal, A.; Turner, J. A., High-efficiency integrated multijunction photovoltaic/electrolysis systems for hydrogen production. *International Journal of Hydrogen Energy* **2001**, 26 (2), 127-132.

186. (a) Youngblood, W. J.; Lee, S.-H. A.; Maeda, K.; Mallouk, T. E., Visible Light Water Splitting Using Dye-Sensitized Oxide Semiconductors. *Accounts of Chemical Research* **2009**, 42 (12), 1966-1973; (b) O'Regan, B.; Gratzel, M., A low-cost, high-efficiency solar cell based on dye-sensitized colloidal TiO₂ films. *Nature* **1991**, 353 (6346), 737-740.

187. Hong, S.; Leroueil, P. R.; Majoros, I. J.; Orr, B. G.; Baker Jr, J. R.; Banaszak Holl, M. M., The Binding Avidity of a Nanoparticle-Based Multivalent Targeted Drug Delivery Platform. *Chemistry & Biology* **2007**, *14* (1), 107-115.
188. (a) Maus, L.; Dick, O.; Bading, H.; Spatz, J. P.; Fiammengo, R., Conjugation of Peptides to the Passivation Shell of Gold Nanoparticles for Targeting of Cell-Surface Receptors. *Acs Nano* **2010**, *4* (11), 6617-6628; (b) Maus, L.; Spatz, J. P.; Fiammengo, R., Quantification and reactivity of functional groups in the ligand shell of PEGylated gold nanoparticles via a fluorescence-based assay. *Langmuir* **2009**, *25* (14), 7910-7.
189. (a) Pujals, S.; Bastús, N. G.; Pereiro, E.; López-Iglesias, C.; Puentes, V. F.; Kogan, M. J.; Giralt, E., Shuttling Gold Nanoparticles into Tumoral Cells with an Amphipathic Proline-Rich Peptide. *ChemBioChem* **2009**, *10* (6), 1025-1031; (b) Sun, L.; Liu, D.; Wang, Z., Functional Gold Nanoparticle–Peptide Complexes as Cell-Targeting Agents. *Langmuir* **2008**, *24* (18), 10293-10297; (c) Pengo, P.; Baltzer, L.; Pasquato, L.; Scrimin, P., Substrate Modulation of the Activity of an Artificial Nanoesterase Made of Peptide-Functionalized Gold Nanoparticles. *Angewandte Chemie International Edition* **2007**, *46* (3), 400-404.
190. Ryan, J. A.; Overton, K. W.; Speight, M. E.; Oldenburg, C. N.; Loo, L.; Robarge, W.; Franzen, S.; Feldheim, D. L., Cellular Uptake of Gold Nanoparticles Passivated with BSA–SV40 Large T Antigen Conjugates. *Analytical Chemistry* **2007**, *79* (23), 9150-9159.
191. Kim, Y. H.; Jeon, J.; Hong, S. H.; Rhim, W. K.; Lee, Y. S.; Youn, H.; Chung, J. K.; Lee, M. C.; Lee, D. S.; Kang, K. W.; Nam, J. M., Tumor targeting and imaging using cyclic RGD-PEGylated gold nanoparticle probes with directly conjugated iodine-125. *Small* **2011**, *7* (14), 2052-60.

Biography

Zejing Xu was born on June 20, 1985, and raised in a small village in Shantou, China, where he attended and graduated from Jinshan Senior High School in 2004. He then attended Nanjing University, China, with studies in Chemistry and received his B.S. in Chemistry in 2008. He started his graduate studies at Tulane University in August 2008 and joined Prof. Mark J. Fink's research group in March 2009 for his graduate research. His graduate research involves the synthesis, characterization and functionalization of silicon nanoparticle based hybrid nanomaterials for photovoltaic and biological application.